Transport of non-spherical particles in microchannel flows

Tohme Tohme

Université Fédérale
Toulouse Midi-Pyrénées

THÈSE

En vue de l'obtention du
DOCTORAT DE L'UNIVERSITÉ DE TOULOUSE

Délivré par l'Université Toulouse 3 - Paul Sabatier

Présentée et soutenue par

Tohme TOHME

Le 8 décembre 2021

Transport of non-spherical particles in microchannel flows

Ecole doctorale : **MEGEP - Mécanique, Energétique, Génie civil, Procédés**

Spécialité : **Dynamique des fluides**

Unité de recherche :
ICA - Institut Clément Ader

Thèse dirigée par
Lucien BALDAS et Pascale MAGAUD

Jury

M. David NEWPORT, Rapporteur
M. Christophe SERRA, Rapporteur
M. Stéphane COLIN, Examinateur
Mme Maide BUCOLO, Examinatrice
M. Lucien BALDAS, Directeur de thèse
Mme Pascale MAGAUD, Co-directrice de thèse

Acknowledgments

Thank you, my two supervisors, Lucien BALDAS and Pascale MAGAUD, for your time, guidance, patience and support during this Ph.D. program.

Thank you, Stéphane COLIN, for helping me throughout all these years, from the day I applied for the master's program, until today. Thank you as well for accepting being a member of the jury.

Thank you, David NEWPORT and Christophe SERRA, for examining and reviewing this dissertation.

Thank you, Maide BUCOLO, for accepting being a member of the jury.

Thank you, my colleagues in the microfluidics team: Stéphane COLIN, Lucien BALDAS, Pascale MAGAUD, Ahmad BATIKH, Christine BARROT-LATTES, Marcos ROJAS-CARDENAS, Nicolas LAURIEN, Stéphane ORIEUX, Guillermo LOPEZ-QUESADA, Dominique FRATANTONIO, Daniel MARIUTA, Varun-Kumar YEACHANA, Yanfeng GAO, Georges SALIBA, Slaven BAJIC, Dingdong ZHANG and Zongwei ZHANG … I would like to thank you for your wonderful cooperation as well as the unforgettable moments that we spent together.

Thank you, Nicolas LAURIEN for helping me design and build the experimental setup.

Thank you, Christine LAFFORGUE-BALDAS and Micheline ABBAS for your helpful advices and continuous encouragement.

Thank you, all the members of Institut Clément Ader, for the help, advice and support, during these four years.

Thank you, Mohammad HOURANI for helping me in the image processing.

Thank you, my dear friends: GuillermoL, DingdongZ, ZhenhangW, FranciscoA, YaraS, SaidS, JosephT, HadiT, MarounK, PatriciaC, MohammadH, MarwanK, BachirS, ChadiJ, KhaledT, AmaniM and TatianaG … Thank you for your endless moral support. If I ever lost interest, you kept me motivated.

Thank you, Yara, my love, for always being there for me no matter what. Thank you for taking such good care of me during this journey.

Thank you, André, Mario, Minerva and Ibrahim. Without you, my family, I could not have achieved my current level of success. Your wise counsel, love and understanding, have, as always, served me well.

Thank you all for your unwavering support.

I hope you enjoy your reading.

Tohme Tohme

Toulouse, November 1, 2021

Patience, persistence and perseverance are the keys to success.

Abstract

Understanding the behavior of a particle flowing in a microchannel is a necessary step to design and optimize efficient microfluidic devices for the separation, concentration, counting, detecting, sorting or mixing of particles in suspension. Although the inertial migration of spherical particles has been deeply investigated in the last two decades, most of the targeted applications involve shaped particles whose behavior in microflows is still far from being completely understood. While traveling in a channel, a particle both rotates and translates: it translates in the streamwise direction driven by the fluid flow but also in the cross-section perpendicular to the streamwise direction due to inertial effects. In addition, particles rotation and translation motions are coupled. Most of the existing works investigating the transport of particles in microchannels decouple their rotational and lateral migration behaviors: particle rotation is mainly studied in simple shear flows where lateral migration is neglected and studies on lateral migration mostly focus on spherical particles whose rotational behavior is simple. Given the interest in the applications of inertial focusing, there is a need to better understand both rotational and migratory behaviors of non-spherical particles.

To address this objective, experiments have been conducted. In situ visualization of peanut and snowman shaped particles is performed by classical microscopy. Obtained images are post-processed and particles positions and orientations are identified. Parameters have been defined, extracted and analyzed in function of various geometrical and operating conditions, to understand the particles lateral migration, rotational behavior and longitudinal ordering in square microchannels, as well as the couplings between these three phenomena. The major results show that at low values of Reynolds number (less than 5), unlike spheres, the migration towards the channel centerline is not observed. At higher fluid inertia, the lateral migration and the longitudinal ordering seem to be qualitatively similar for the non-spherical case than the spherical ones, with larger focusing zones and a much lower fraction of particles in trains. Finally, it has been clearly found that the three studied phenomena (lateral migration, rotational behavior and longitudinal ordering) are strongly coupled.

Résumé

Comprendre le comportement d'une particule circulant dans un microcanal est une étape nécessaire pour concevoir et optimiser des dispositifs microfluidiques efficaces pour la séparation, la concentration, le comptage, la détection, le tri ou le mélange de particules en suspension. Bien que la migration inertielle de particules sphériques ait été étudiée en profondeur au cours des deux dernières décennies, la plupart des applications ciblées impliquent des particules non sphériques dont le comportement en microécoulement est encore loin d'être complètement compris. Lorsqu'elle se déplace dans un canal, une particule possède deux mouvements, un rotationnel et un migratoire : elle se déplace dans la direction de l'écoulement, entraînée par l'écoulement du fluide, mais aussi dans la section transversale perpendiculaire à la direction de l'écoulement, en raison d'effets inertiels. De plus, les mouvements de rotation et de translation des particules sont couplés. La plupart des travaux existants sur le transport des particules dans les microcanaux découplent leurs comportements rotationnel et migratoire : la rotation des particules est principalement étudiée dans des écoulements de cisaillement simple où la migration latérale est négligée et les études sur la migration latérale se concentrent principalement sur les particules sphériques dont le comportement rotationnel est simple. Compte tenu de l'intérêt pour les applications de la focalisation inertielle, il est nécessaire de mieux comprendre les deux comportements rotationnel et migratoire de particules non sphériques.

Pour atteindre cet objectif, des expériences ont été menées. La visualisation des particules en forme de cacahuète et de bonhomme de neige est réalisée par microscopie classique. Les images obtenues sont post-traitées et les positions et orientations des particules sont identifiées. Des paramètres ont été définis, extraits et analysés en fonction de diverses conditions géométriques et opératoires, afin de comprendre la migration latérale des particules, leur comportement rotationnel et la formation de trains dans des microcanaux carrés, ainsi que le lien entre ces trois phénomènes. Les principaux résultats montrent qu'à faibles valeurs du nombre de Reynolds (inférieur à 5), les particules non sphériques ne migrent pas vers le centre du canal comme le font les sphériques. À plus

forte inertie du fluide, la migration latérale et l'alignement longitudinal semblent qualitativement similaires pour les particules non sphériques que pour les sphériques, avec des zones de focalisation plus larges et à une fraction de particules en trains plus faible. Enfin, il a été clairement constaté que les trois phénomènes étudiés (migration latérale, comportement rotationnel et alignement longitudinal) sont fortement couplés.

Transport de particules non-sphériques dans des microcanaux

Introduction et état de l'art

Les suspensions solides-fluides sont présentes partout : dans le corps humain, dans les fluides environnementaux, dans les produits industriels, etc…. De nombreuses applications dans divers domaines, tels que l'agriculture, la biomédecine, les sciences environnementales et l'industrie pharmaceutique, nécessitent l'identification de particules (dont les formes et les tailles peuvent être différentes) et le contrôle de leurs trajectoires dans ces suspensions. La raison de cette demande peut être le besoin de : (i) identifier les différentes particules présentes dans la suspension, (ii) séparer les particules du fluide, (iii) trier les particules d'une suspension polydisperse, (iv) contrôler l'orientation des particules, (v) contrôler la concentration de la suspension et/ou (vi) déplacer les particules d'un fluide à un autre.

Les procédés de séparation classiques (centrifugation, filtration membranaire...) nécessitent de grands volumes d'échantillonage et ont un coût énergétique important. Au cours de la dernière décennie, des systèmes miniaturisés de séparation de particules utilisant des écoulements microfluidiques ont été développés : ils permettent de diminuer les volumes d'échantillons et le coût énergétique et d'augmenter l'adaptabilité à l'automatisation et la portabilité des dispositifs. Ces microsystèmes comprennent souvent une étape préliminaire dans laquelle les particules sont focalisées. Il existe de nombreuses techniques pour focaliser les particules. Ces méthodes peuvent être divisées en deux grandes catégories : actives et passives. Dans le cas de la focalisation active, les particules en suspension sont contrôlées à l'aide de champs de force externes (électrique, magnétique, optique, ou acoustique). Les techniques de séparation passives n'utilisent pas de champs externes pour contrôler la particule. Elles sont basées sur les interactions entre les particules, le fluide et la géométrie du canal. Le contrôle de la position d'une particule dans un canal peut se faire à l'aide d'un ou plusieurs fluides externes, en pinçant

la suspension et piégeant les particules dans une région de focalisation. Ce contrôle peut aussi se faire en se basant sur la différence de densité entre les particules et le fluide, ou même en introduisant un réseau de micro-obstacles à l'intérieur du canal pendant la fabrication. Ces méthodes présentent plusieurs inconvénients comme (i) la complexité dans la microfabrication (engendrant une élévation de coût), (ii) le risque de modifier les propriétés de la suspension, et (iii) le risque de colmatage.

Pour éliminer ces différents inconvénients, la technique de focalisation inertielle a été développée pour la focalisation des particules dans les microcanaux. Cette approche est basée sur le phénomène de migration inertielle. Ce dernier repose uniquement sur les forces hydrodynamiques induites dans le canal, dues aux interactions entre le fluide et les particules et entre les différentes particules. La technique de focalisation inertielle ne nécessite pas une force ou un écoulement externe et peut être appliquée dans un canal de géométrie simple. Cela en fait une opération simple et non invasive et un procédé peu coûteux. Elle peut également être décrite comme une technique portable, robuste et économe en énergie. En outre, elle nécessite de petits volumes d'échantillons et son temps d'analyse est réduit. Des revues récentes ont identifié cette technique comme prometteuse avec un grand potentiel pour le développement de dispositifs de micro-séparation pour des applications de laboratoire sur puce.

Le phénomène de migration inertielle a été observé pour la première fois par Poiseuille en 1836, alors qu'il étudiait les écoulements sanguins. Il a remarqué que les globules sanguins s'écoulant dans un tube semblaient former un anneau près des parois du tube. Ce phénomène a été confirmé quantitativement par les expériences de Segré et Silberberg sur des particules sphériques en 1962 et par d'autres études expérimentales, numériques et théoriques.

Il a été démontré que dans des conditions d'écoulement et de géométrie spécifiques, les particules migrent naturellement vers des positions d'équilibre latérales où elles se concentrent. Le nombre et les emplacements des positions d'équilibre varient en fonction de plusieurs paramètres, liés à la géométrie du canal, à la suspension (concentration,

polydispersité), à l'écoulement (le nombre de Reynolds, la viscoélasticité du fluide) et à la particule (forme, déformabilité, taille, densité).

Les mécanismes de la migration inertielle ont été mis en évidence par Matas et al. Dans un canal carré, trois forces latérales primaires entraînent les particules à travers les lignes de courant vers leurs positions d'équilibre. Ces forces sont induites par les parois du canal, le profil de vitesse parabolique de l'écoulement et la rotation de la particule. À un nombre de Reynolds modéré, des particules sphériques isodenses s'écoulant dans un microcanal carré migrent latéralement vers quatre positions d'équilibre situées au centre des parois du canal. Afin d'atteindre sa position d'équilibre, la particule suit une migration en deux étapes : d'abord, elle migre dans la direction latérale à travers les iso-contours de vitesse et atteint un anneau d'équilibre ; ensuite, elle se déplace transversalement le long de l'anneau choisi vers sa position d'équilibre. Dans la première étape, appelée migration transversale, les forces de soulèvement induites par le cisaillement et la paroi conduisent les particules vers une région en forme d'anneau rectangulaire où les effets des deux forces sont annulés. La force de portance induite par la rotation domine dans la deuxième étape de la migration (appelée migration transversale) et amène les particules à leurs positions d'équilibre avec une vitesse de migration plus faible.

La migration vers les positions d'équilibre se produit en même temps qu'un processus d'alignement longitudinal des particules, dans lequel les particules forment des trains et se suivent dans le canal avec un espacement interparticulaire constant. Ce phénomène a été observé par Segré et Silberberg, puis étudié et expliqué par Matas et al et Lee et al. Selon Gao, ce phénomène n'apparaît qu'après le développement complet de la migration latérale. L'alignement des particules est une conséquence des interactions entre le fluide et les particules, et entre les particules elles-mêmes. Il a été suggéré et confirmé que les zones de recirculation, créées autour de la particule dans l'écoulement, sont le principal facteur favorisant la formation de trains de particules.

En plus de leur migration inertielle, les particules ont un comportement rotationnel dans le canal. Selon Abbas et al. 2014, le comportement rotationnel d'une particule sphérique

isodense, s'écoulant dans un microcanal carré à un nombre de Reynolds modéré, est couplé au développement de la migration latérale de la sphère. Pendant le processus de migration, la vitesse angulaire de la particule a trois composantes le long des trois axes principaux du canal : elle tourne autour des deux directions de la section transversale (en raison de la présence de deux profils de vitesse paraboliques dans un écoulement de Poiseuille carré typique), ainsi qu'autour de l'axe de l'écoulement. Une fois que la particule est focalisée, seule la rotation dans la direction de la section transversale parallèle à la paroi la plus proche subsiste. La vitesse angulaire de la particule augmente avec l'augmentation du nombre de Reynolds.

La plupart des études théoriques, numériques et expérimentales menées sur la migration inertielle au cours des deux dernières décennies ont principalement porté sur des particules sphériques. Cette géométrie simple peut être facilement fabriquée pour les études expérimentales et rapidement représentée mathématiquement et numériquement. Ces travaux ont permis d'accroître les connaissances sur le transport des particules sphériques dans les microcanaux et de démontrer la capacité des méthodes de focalisation inertielle à séparer les particules en fonction de leur taille. Cependant, la plupart des applications ciblées impliquent des particules de forme complexe. Par exemple, un globule rouge adopte une forme de disque biconcave dans le corps, Escherichia coli est cylindrique, et Euglena gracilis a une géométrie ellipsoïdale. En outre, dans de nombreuses applications, on peut trouver des particules de même taille mais de géométries différentes, ce qui complique la séparation basée sur la taille, voire la rend impossible. Ainsi, la forme pourrait servir de marqueur spécifique dans l'identification et/ou la séparation des particules dans une suspension, ce qui soulève la question de savoir comment les particules non sphériques se déplacent dans un microcanal.

Dans le cas des particules sphériques, même si le couplage entre la migration latérale et le comportement rotationnel existe (surtout dans la deuxième étape de migration), la rotation a une influence limitée sur la migration latérale. Ce n'est pas le cas pour les particules non sphériques, où les mouvements de translation et de rotation peuvent être fortement couplés. Ainsi, les comportements rotationnels et migratoires doivent être

considérés lors de l'étude du transport de particules non-sphériques s'écoulant dans un microcanal. La plupart des travaux existants sur le transport de particules dans les microcanaux dissocient leurs comportements de rotation et de migration latérale : la rotation des particules est principalement étudiée dans des écoulements à cisaillement simple, où la migration latérale est négligée, et les études sur la migration latérale se concentrent principalement sur les particules sphériques dont le comportement rotationnel est relativement simple.

Le comportement rotationnel a d'abord été étudié dans un écoulement externe de cisaillement simple, puis a été étendu aux écoulements internes (Couette et Poiseuille) où intervient l'effet de paroi. La plupart de ces travaux sont numériques et théoriques. Les premières études sur l'effet de la forme d'une particule sur son comportement ont porté sur des particules ellipsoïdales (allongées et aplaties), puisque l'ellipsoïde est la forme non sphérique la plus proche de la sphère. En raison de plusieurs difficultés dans la fabrication d'ellipsoïdes pour les essais expérimentaux et du fait que les particules non sphériques qui s'écoulent dans les suspensions réelles ont des formes plus complexes, certaines études ont été étendues des ellipsoïdes aux particules non ellipsoïdales axisymétriques (principalement des tiges, des doublets et des disques). Ces travaux ont permis de comprendre l'effet de la forme de la particule sur son comportement.

En 1922, Jeffery a étudié théoriquement le comportement rotationnel d'un ellipsoïde rigide et isodense dans un écoulement externe à cisaillement simple, avec un taux de cisaillement constant. Jeffery a découvert qu'un ellipsoïde tourne autour de l'axe de vorticité (perpendiculaire au plan du gradient d'écoulement) le long d'un ensemble infini d'orbites fermées, appelées orbites de Jeffery, qui dépendent des conditions initiales, du taux de cisaillement et du rapport de forme du sphéroïde. Ce mode de rotation est appelé "kayak", car la trajectoire de la particule ressemble au mouvement d'une pagaie de kayak. Les deux orbites extrêmes sont appelées "tumbling", lorsque l'axe de révolution de la particule tourne dans le plan du gradient d'écoulement, et "log-rolling" lorsque la particule tourne autour de son axe de révolution aligné avec l'axe de vorticité. Jeffery a également montré que la vitesse angulaire de la particule n'est pas constante mais

périodique. Elle a une valeur maximale lorsque l'axe de révolution de la particule est perpendiculaire à la direction du mouvement du fluide et une valeur minimale lorsque la particule est alignée avec l'écoulement. La période de rotation de la particule est le temps nécessaire pour effectuer une orbite. Elle dépend du taux de cisaillement et du rapport de forme de la particule.

Bretherton et al. et Chwang ont montré que les résultats de Jeffery étaient applicables dans les écoulements internes, tant que la particule était éloignée des parois et que le taux de cisaillement utilisé dans les équations correspond à la valeur au centre de la particule étudiée. Concernant l'effet de l'inertie du fluide, Les études convergent sur le fait que les ellipsoïdes allongés (rapport de forme supérieur à 1) s'écoulant à faible inertie culbutent ("tumbling") et que les particules aplaties (rapport de forme inférieur à 1) roulent ("log-rolling"). Cependant, à des valeurs plus élevées du nombre de Reynolds, les résultats divergent, et différents modes de rotation sont observés.

Dans un canal carré, d'une façon similaire aux sphères, il a été observé que les particules non-sphériques suivent une migration latérale en deux phases vers les quatre positions d'équilibre (ellipsoïdes aplatis et cylindres). De plus, d'une façon similaire aux sphères, il a été trouvé que les petites particules ont besoin de canaux plus longs pour atteindre leur position d'équilibre (ellipsoïdes aplatis), que leurs positions d'équilibre sont plus proches des parois que les plus grandes particules et que ces positions d'équilibre se rapprochent des murs quand le nombre de Reynolds augmente (en forme de batonnets).

D'une façon similaire aux sphères, il a été montré que la migration latérale et le mode de rotation d'une particule non-sphérique sont fortement liés. Selon Lashgari et al. 2017 et Nizkaya et al. 2020, un ellipsoïde aplati commence à migrer avec un mouvement de kayak et passe lentement à un mouvement de "log-rolling" une fois qu'il atteint sa position latérale d'équilibre.

Enfin, à notre connaissance, il n'existe qu'une seule étude récente qui s'intéresse à l'alignement longitudinal des particules non-sphériques dans des écoulements en microcanaux. Il a été montré dans ce travail numérique (en 2D) que, comme les particules

sphériques, les ellipsoïdes interagissent entre eux pour former des trains. En outre, Hu et al. ont constaté que la formation de trains est renforcée en augmentant le rapport de forme des particules, la fraction volumique des particules ou le nombre de Reynolds, ou en diminuant le degré de confinement.

À propos de la thèse

Bien que plusieurs travaux numériques aient étudié les mouvements de rotation et de translation de particules non sphériques s'écoulant dans des canaux carrés, il y a un réel manque d'investigations expérimentales dans ce domaine. A notre connaissance, seuls Hur et al. ont publié des données expérimentales sur ce problème. De fait, l'analyse expérimentale du comportement des particules est beaucoup plus compliquée pour les particules non-sphériques que pour les particules sphériques, puisqu'une approche tridimensionnelle est nécessaire pour observer simultanément la position et l'orientation des particules.

Tous les résultats présentés dans ce travail bibliographique sont essentiels pour mieux comprendre le transport des particules dans un écoulement de Poiseuille et vérifier si la séparation basée sur la forme est possible. Cependant, pour cela, trois aspects importants restent à clarifier et devraient faire l'objet de prochains travaux dans ce domaine :

- Le comportement des particules (rotationnel et migratoire) à des nombres de Reynolds élevés (> 200), est encore un sujet de discussion dans la littérature ;
- Le rôle de l'interaction entre les particules non sphériques sur leur migration latérale et leur alignement longitudinal n'a été étudié que par Hu et al., bien qu'il ait été prouvé qu'il était essentiel dans le cas de particules sphériques ;
- Le couplage entre la migration latérale et la rotation de la particule pendant la phase de transition, qui n'est pas encore complètement compris.

Comme il a été expliqué, le comportement d'une suspension dans un microcanal est complexe car il dépend de nombreux paramètres, liés à la géométrie du canal, aux propriétés et à la concentration des particules, aux propriétés du fluide et aux conditions d'écoulement. Afin de concevoir des microdispositifs efficaces de type laboratoire sur

puce (pour des applications telles que la séparation ou le tri de particules dans des suspensions), une feuille de route a été tracée pour ce projet, afin de parvenir à une compréhension complète des mécanismes physiques régissant ce type d'écoulement. Ce plan est basé sur l'augmentation progressive de la complexité de l'écoulement et du type de la suspension.

La première étape a été d'étudier, dans un microcanal carré droit, le comportement de particules sphériques, rigides et isodenses. Ensuite, Gao a étudié l'influence de la bidispersité sur le comportement des sphères. Pour cela, il a étudié l'effet de la présence de sphères de deux tailles différentes -dans la même suspension- sur leur migration inertielle.

L'étape suivante consiste à comprendre l'effet de la forme des particules sur leur migration latérale, leur ordonnancement longitudinal et leur comportement rotationnel. Ceci correspond aux travaux présentés dans cette thèse.

La plupart des études, portant sur les particules non-sphériques, sont théoriques et numériques. Il a donc semblé pertinent de compléter et de valider ces travaux par une approche expérimentale. Dans un premier temps, un banc, basé sur la microscopie optique, a été conçu, construit et testé (Chapitre 2). Les données acquises à l'aide de ce banc ont été traitées et analysées, pour mieux comprendre la migration latérale (Chapitre 3), le comportement rotationnel (Chapitre 4) et la formation de trains (Chapitre 5) dans le cas de particules non sphériques, ainsi que les couplages entre ces trois phénomènes.

Matériels et méthodes

Comme mentionné précédemment, l'objectif de ce travail est d'étudier expérimentalement l'effet de la géométrie d'une particule sur son comportement dans le canal. Pour ce faire, il est nécessaire d'adopter une technique de visualisation qui permet le suivi des particules et la reconstruction 3D de la distribution des particules dans le canal. Ceci permettra également d'identifier les principaux paramètres définissant les migrations latérales et longitudinales ainsi que le comportement rotationnel des particules.

L'équipement constituant le dispositif expérimental peut être divisé en trois parties principales : le système fluidique, l'optique et le système mécanique :

- Le système fluidique : contient le microcanal de section carrée, la suspension et le pousse-seringue. La suspension contient des particules de polystyrène de forme de cacahuète ($5.1\mu m \times 3.4\mu m$ et $7.7\mu m \times 5.1\mu m$) et de bonhomme de neige ($15.3\mu m \times 12.8\mu m$), ainsi qu'un fluide, constitué d'eau distillée et de glycérol, de densité égale à celle des particules. La suspension s'écoule dans le canal à un débit volumique variant de 2 à $2000\mu L/min$, correspondant à un nombre de Reynolds compris entre $0{,}29$ et 290.
- L'optique : la visualisation est assurée par une source lumineuse et une caméra CCD (Sensicam QE), équipée d'un objectif ($\times 20$ ou $\times 40$). La caméra a une haute résolution et une fréquence d'images constante de 10 images par seconde. Lorsqu'une fréquence d'images élevée est requise (pour suivre la particule), cette caméra est remplacée par une Photron APX ou une Photron SA5, où une large gamme de fréquences d'images est couverte (entre 50 et 120000 images par seconde).
- Le système mécanique : le mouvement de l'équipement et la stabilité du système sont garantis par un rail optique, des chariots de rail, des platines linéaires équipées de têtes micrométriques, des ascenseurs de laboratoire, une équerre à 90 degrés et deux pieds de banc à hauteur variable.

Le dispositif expérimental et le protocole développés ont été validés grâce à des tests, tels que la mesure de la profondeur du canal et celle du plan focal, la vérification de l'orthogonalité et de l'alignement entre les différents composants du montage et l'effet des parois du canal sur la visualisation.

Afin d'obtenir les résultats de notre étude, différents tests ont été effectués, en modifiant le type de particules étudié, la concentration de la suspension, le débit, la profondeur du canal, et la distance de l'entrée du canal. Il convient de mentionner que, pour chaque test, 2000 images capturées sont considérées comme suffisantes.

Le traitement d'images est effectué à l'aide d'un code MATLAB. La première étape consiste à adapter toutes les images à un niveau de gris moyen commun. Ensuite, le fond de l'image est calculé. Une fois le fond obtenu, les particules sont isolées en extrayant le fond des images adaptées, ce qui produit une nouvelle image contenante idéalement uniquement les particules. Une façon simple d'isoler complètement les particules est de binariser l'image soustraite. Un seuil de niveau de gris est testé puis fixé. Deux types de particules sont identifiées : brillantes et non-brillantes. Une particule brillante comporte un point brillant à son centre, indiquant qu'elle se trouve dans le plan focal de la caméra. Puis, les particules et leurs caractéristiques sont identifiés dans les images binaires. Dans ce travail, les propriétés d'intérêt sont : les coordonnées du centre de masse, la longueur du grand axe, la longueur du petit axe et la surface de la particule, ainsi que l'angle entre le grand axe de la particule et l'axe horizontal. Après avoir identifié les particules, les parois du canal sont manuellement localisées et la position de chaque particule dans le canal est calculée. Cette position correspond à la distance entre le centre de la particule et la face interne de la paroi supérieure.

La catégorisation entre particules brillantes et non brillantes, ainsi que la position du centre de masse de la particule, permettent de tracer la distribution de particules dans plusieurs plans du canal. Cela permet de reconstruire la distribution de particules dans la section du canal.

Lors de la conception de microséparateurs dans des dispositifs microfluidiques, il est essentiel d'identifier la distance entre les parois du canal et les positions auxquelles les particules se concentrent. La position d'équilibre normalisée est la distance la plus fréquente par rapport à la paroi, normalisée par la hauteur du canal. Elle correspond à la valeur la plus fréquente dans la distribution de particules dans le plan médian du canal. L'identification des positions d'équilibre, sur lesquelles les particules sont focalisées, n'est pas suffisante pour concevoir un séparateur. L'efficacité du dispositif doit également être prise en compte. Elle est directement liée à la fraction de particules focalisées : plus cette fraction est élevée, plus l'efficacité est élevée. Gao a introduit le degré de focalisation, qui correspond au rapport entre le nombre de particules focalisées et le nombre total de

particules identifiées. Selon Gao, une particule est focalisée si son centre de masse est situé à une distance de la position d'équilibre inférieure au cinquième du diamètre rotationnel.

Le centre de masse de la particule ne donne pas seulement des informations liées à la migration latérale. Il permet également d'identifier les trains et d'analyser leur formation. En effet, le centre de masse de la particule est nécessaire pour calculer les distances entre la particule et les particules voisines. Un train est formé de trois particules ou plus. La distance entre les centres de deux particules consécutives, appelée espacement interparticulaire, est inférieure ou égale à cinq fois le diamètre rotationnel de la particule. De plus, après avoir vérifié visuellement les trains sur les images, une troisième condition est introduite : la différence entre les positions latérales de deux particules consécutives ne doit pas dépasser 5% de la hauteur du canal (7 pixels). Trois paramètres principaux caractérisent les trains pour une configuration donnée : la fraction de particules en trains (correspondant au nombre de particules en trains sur le nombre total de particules identifiées), l'espacement interparticulaire normalisé par le diamètre rotationnel (le plus probable pour une configuration donnée), et le nombre de particules dans un train.

Enfin, il faut noter que, l'orientation, la surface et le diamètre maximal détectés constituent une combinaison de paramètres utilisés pour déterminer le comportement rotationnel (mode, plan et/ou période de rotation) de la particule correspondante.

Principaux résultats

L'objectif principal de la présente thèse était d'étudier expérimentalement la migration latérale, le comportement rotationnel et l'alignement longitudinal de particules non sphériques s'écoulant dans des microcanaux droits carrés, ainsi que les couplages possibles entre ces trois phénomènes.

Une analyse, basée sur une étude bibliographique approfondie, a permis d'identifier les questions essentielles restées sans réponse dans la littérature. Ensuite, le dispositif expérimental et la technique de traitement des données, développés dans cette étude, ont été présentés. Grâce à cette technique de visualisation in-situ, la migration latérale,

le comportement rotationnel et l'ordonnancement longitudinal ont été caractérisés et évalués.

Les principaux résultats de ce travail de thèse ont été divisés en trois parties principales, une pour chacun des phénomènes mentionnés ci-dessus.

Les principales conclusions sont les suivantes :

- ***Migration latérale :***

- À une inertie modérée du fluide (le nombre de Reynolds entre 5 et 160) :
    - De manière similaire aux sphères, les particules non sphériques étudiées subissent une migration en deux étapes pour atteindre les quatre positions d'équilibre aux centres des quatre faces de la section carrée. Dans ce régime, l'évolution de la migration en fonction des conditions opératoires (inertie du fluide, concentration, degré de confinement, ...) est qualitativement similaire à ce qui a été observé pour les sphères.
    - Dans l'intervalle restreint couvert par cette étude, le rapport de forme des particules n'a pas d'effet significatif sur la position d'équilibre, ce qui signifie que les possibilités de séparation basées sur la forme sont limitées.
    - Les particules non sphériques se concentrent dans des zones plus grandes autour des quatre positions d'équilibre, par rapport aux sphères s'écoulant dans les mêmes conditions expérimentales, ce qui a également un effet limitant sur l'efficacité de la séparation.
- À des valeurs plus élevées du nombre de Reynolds, comme pour les sphères, une transition vers un nouveau régime de migration se produit.
- À faible inertie du fluide (le nombre de Reynolds inférieur ou égal à 5), contrairement aux sphères, la migration vers la ligne centrale du canal n'est pas observée et les particules continuent à migrer vers les quatre positions d'équilibre.

- ***Comportement rotationnel :***

- Le mode rotationnel, observé jusqu'un nombre de Reynolds égal 58, est directement couplé à la migration latérale. Une particule qui migre possède un mode "kayak", dans

lequel l'orientation du grand axe de la particule, par rapport à l'axe de vorticité, dépend du temps. Une fois que la particule a atteint sa position d'équilibre, le passage du mode "kayak" au mode culbute ("tumbling") se produit : la particule commence à tourner autour de l'axe passant par son centroïde et parallèle à la paroi de section transversale la plus proche.

- La particule culbutante ("tumbling") tourne à ses vitesses angulaires minimale et maximale lorsqu'elle est alignée avec et perpendiculaire à l'écoulement, respectivement, comme on le voit dans la littérature. La différence entre les valeurs extrêmes de la vitesse angulaire, ainsi que la proportion de temps (par une rotation) passée par la particule à l'orientation horizontale, augmentent avec le nombre de Reynolds. Cette dernière observation est intéressante pour les applications où l'orientation des particules est critique.
- La période de rotation diminue lorsque l'inertie du fluide augmente. De plus, dans les conditions de cette étude (pour un nombre de Reynolds inférieur ou égal à 29), l'expression théorique de la période de rotation de Jeffery est valide, tant que le taux de cisaillement utilisé dans cette équation est celui au centre de la particule sur sa position d'équilibre.

- ***Alignement longitudinal :***

- De manière similaire aux sphères, les particules non sphériques en écoulement forment des trains dans la direction de l'écoulement. Le phénomène d'alignement longitudinal se développe progressivement dans le canal, en raison des interactions entre les particules.
- La géométrie non sphérique de la particule influence les caractéristiques des trains (fraction de particules dans les trains, espacement interparticulaire, composition des trains), ainsi que leur dépendance aux conditions opératoires, telles que le degré de confinement et la concentration de la suspension. Une des observations majeures concerne la fraction de particules dans les trains, qui est beaucoup plus faible dans le cas non sphérique.

- Le phénomène d'alignement longitudinal est conditionné par la migration latérale. Contrairement au cas sphérique, le couplage entre ces deux phénomènes est complexe et dépend fortement des conditions d'écoulement.
- Les particules focalisées, en train de culbuter, semblent entrer dans une rotation en phase, établie progressivement le long du canal.

Perspectives

Des travaux futurs devraient être réalisés afin de compléter cette étude sur le transport de particules non sphériques dans les microcanaux :

- Pour vérifier si la distance entre les surfaces des particules consécutives dans les trains est le paramètre clé caractérisant le phénomène d'alignement longitudinal, le code de traitement existant devrait être adapté afin d'analyser ce paramètre sur les ensembles d'images déjà acquises.
- Pour vérifier si, de manière similaire aux sphères, à forte inertie du fluide, les particules non sphériques migrent vers huit positions d'équilibre (les quatre coins du canal carré et les quatre positions d'équilibre aux centres des quatre faces), des expériences doivent être réalisées à un nombre de Reynolds élevé (Re>200). Cela nécessite des temps d'exposition courts et une source lumineuse puissante.
- Pour isoler et caractériser clairement l'influence des rapports de forme et de confinement des particules sur leur transport dans le canal, un élargissement de la variété des géométries non sphériques étudiées devrait être envisagé. Il serait également intéressant de tester des particules asymétriques, afin d'étudier l'influence de l'asymétrie géométrique sur les comportements de translation et de rotation des particules.
- Afin d'approfondir l'analyse du comportement rotationnel (transition du "kayak" au "tumbling", rotation en phase dans les trains, ...), il serait nécessaire d'apporter des ajustements au dispositif expérimental, permettant une acquisition plus précise de la position et de l'orientation de la particule (par exemple, stéréovision).

L'objectif à long terme de ce projet est de prédire les trajectoires de microorganismes circulant dans des microcanaux. Comme mentionné précédemment, plusieurs étapes, de complexité croissante, ont été déterminées pour atteindre cet objectif. Dans la présente thèse, le transport de particules non sphériques monodispersées, rigides et isodenses se déplaçant dans des microcanaux droits a été étudié. Dans les travaux à venir, l'effet de la courbure du canal sur le transport des particules sera étudié. Ces travaux futurs seront suivis par l'étude du transport de particules déformables et de micro-organismes, dans des suspensions diluées puis modérément concentrées.

Table of Contents

List of Figures

List of tables

List of symbols and abbreviations

Roman symbols

$\boldsymbol{Symbol}$ $[\boldsymbol{unit}]$	
$\boldsymbol{A}$ $[\boldsymbol{pixels}]$	Particle surface area on the image
$\boldsymbol{A_c}$ $[\boldsymbol{m^2}]$	Channel cross-sectional area
$\boldsymbol{C_S}$ $[-]$	Lift coefficient
$\boldsymbol{C_W}$ $[-]$	Lift coefficient
$\boldsymbol{d_{i+1}^i}$ $[-]$	Normalized interparticle spacing between the particles i and $i+1$ of a train
$\boldsymbol{d_{min}}$ $[\boldsymbol{m}]$	Particle minor-axis length
$\boldsymbol{d_p}$, $\boldsymbol{d_{p1}}$, $\boldsymbol{d_{p2}}$ $[\boldsymbol{m}]$	Diameter of the particle
$\boldsymbol{d_r}$ $[-]$	Size ratio
$\boldsymbol{d_{rot}}$ $[\boldsymbol{m}]$	Particle rotational diameter
$\boldsymbol{d_v}$ $[\boldsymbol{m}]$	Equivalent volume diameter
$\boldsymbol{D_h}$ $[\boldsymbol{m}]$	Channel hydraulic diameter
$\boldsymbol{E_{12}}$, $\boldsymbol{E_{13}}$, $\boldsymbol{E_{23}}$ $[-]$	Errors
$\boldsymbol{f}$ $[-]$	Lift coefficient
$\boldsymbol{F}$ $[\boldsymbol{N}]$, $\vec{\boldsymbol{F}}$	Net inertial lift force
$\boldsymbol{F_S}$ $[\boldsymbol{N}]$, $\overrightarrow{\boldsymbol{F_S}}$	Shear-induced lift force
$\boldsymbol{F_W}$ $[\boldsymbol{N}]$, $\overrightarrow{\boldsymbol{F_W}}$	Wall-induced lift force
$\boldsymbol{F_\Omega}$ $[\boldsymbol{N}]$, $\overrightarrow{\boldsymbol{F_\Omega}}$	Rotation-induced lift force
$\boldsymbol{g}$ $[\boldsymbol{m/s^2}]$	Local acceleration of free fall
$\boldsymbol{H}[\boldsymbol{m}]$	Channel internal height
$\boldsymbol{H_T}$ $[\boldsymbol{m}]$	Channel's total heigh, including the borosilicate walls
$\boldsymbol{H_{wall}}[\boldsymbol{m}]$	Height of the channel's borosilicate walls
$\boldsymbol{l/d_{rot}}$, $\boldsymbol{l/d_p}$ $[-]$	Normalized interparticle spacing
$\boldsymbol{l_C}$ $[\boldsymbol{m}]$	Distance between the particles' centers

$\boldsymbol{l_s}$ $[\boldsymbol{m}]$	Distance between the particles' surfaces
$\boldsymbol{L_f}$ $[\boldsymbol{m}]$	Focusing length
$\boldsymbol{n_{air}}$ $[-]$	Refractive index of air
$\boldsymbol{n_{glass}}$ $[-]$	Refractive index of glass
$\boldsymbol{n_{glycerol}}$ $[-]$	Refractive index of glycerol
$\boldsymbol{n_i}$ $[-]$	Refractive index of the medium in which the lens is immersed
$\boldsymbol{n_{mixt}}$ $[-]$	Refractive index of the suspending fluid
$\boldsymbol{n_o}$ $[-]$	Refractive index of the observed object.
$\boldsymbol{n_{water}}$ $[-]$	Refractive index of water
$\boldsymbol{n_x}$ $[-]$	x-component of the orientation vector
$\boldsymbol{n_y}$ $[-]$	y-component of the orientation vector
$\boldsymbol{P, P_1, P_2, P_3}$ $[-]$	Pixels
$\boldsymbol{P_c}$ $[\boldsymbol{m}]$	Channel wetted cross-sectional perimeter
$\boldsymbol{Q}$ $[\boldsymbol{m^3/s}]$	Volume flow rate
$\boldsymbol{R}$ $[\boldsymbol{m}]$	Channel radius of curvature
$\boldsymbol{t}$ $[\boldsymbol{s}]$	Time
$\boldsymbol{t_T}$ $[\boldsymbol{s}]$	Travel time
$\boldsymbol{T}$ $[\boldsymbol{s}]$	Period of rotation
$\boldsymbol{U}$ $[\boldsymbol{m/s}]$	Average fluid velocity
$\boldsymbol{V_{12}, V_{13}, V_{23}}$ $[-]$	2000-element-vectors containing grey level values
$\boldsymbol{V_p}$ $[\boldsymbol{m^3}]$	Volume of the particle
$\boldsymbol{W}$ $[\boldsymbol{m}]$	Channel smallest dimension
$\boldsymbol{W_i}$ $[\boldsymbol{pixels}]$	Image width
$\boldsymbol{x}$ $[-]$	Flow direction
$\boldsymbol{y}$ $[-]$	Cross-sectional direction/ gradient direction
$\boldsymbol{x_r}$ $[-]$, $\boldsymbol{y_r}$ $[-]$	Relative coordinates in the channel coordinate system
$\boldsymbol{x_t}$ $[\boldsymbol{pixels\ and\ m}]$	Longitudinal distance travelled by the particle between two consecutive images
$\boldsymbol{Y_{eq}}$ $[\boldsymbol{m}]$	Equilibrium position

$\boldsymbol{Y_{eq}/H}$ $[-]$	Normalized equilibrium position
$\boldsymbol{z}$ $[-]$	Cross-sectional direction/ vorticity direction/ aligned with camera's optical axis

Greek symbols

$\boldsymbol{Symbol}$ $[\boldsymbol{unit}]$	
$\boldsymbol{\alpha}$ [°]	Channel inclination
$\boldsymbol{\beta}$ $[-]$	Curvature ratio
$\boldsymbol{\delta}$ $[\boldsymbol{m}]$	Displacement of the focal plane
$\boldsymbol{\delta_{fp}}$ $[\boldsymbol{m}]$	Depth of the focal plane
$\boldsymbol{\delta_l}$, $\boldsymbol{\delta_{linside}}$, $\boldsymbol{\delta_{lwall}}[\boldsymbol{m}]$	Displacement of the lens
$\boldsymbol{\Delta\varphi}$ [°]	Difference between the orientations of two consecutive particles of a train
$\boldsymbol{\Delta_i}$ $[-]$	Difference between the $GLMV$ of the first image and that of an image i
$\boldsymbol{\Delta Y}$ $[\boldsymbol{m}]$	Maximum oscillation amplitude
$\boldsymbol{\varphi}$ [°]	Particle orientation in the plane of the camera
$\boldsymbol{\Phi}$ [%]	Particle volume fraction / Suspension concentration
$\boldsymbol{\Phi_{eq}}$ [%]	Equivalent concentration
$\boldsymbol{\gamma}$ $[\boldsymbol{s^{-1}}]$	Shear rate
$\boldsymbol{\eta}$ $[-]$	Focusing degree
$\boldsymbol{\eta_{max}}$ $[-]$	Maximum focusing degree at a fixed X/H and varying Re
$\boldsymbol{\eta_{Re}}$ $[-]$	Maximum focusing degree at a fixed Re and varying X/H
$\boldsymbol{\kappa}$ $[-]$	Blockage ratio/ confinement ratio
$\boldsymbol{\lambda}$ $[-]$	Particle aspect ratio
$\boldsymbol{\lambda_e}$ $[-]$	Particle equivalent aspect ratio
$\boldsymbol{\mu}$ $[\boldsymbol{Pa.s}]$	Suspending fluid dynamic viscosity
$\boldsymbol{\rho_f}$ $[\boldsymbol{kg/m^2}]$	Suspending fluid density
$\boldsymbol{\rho_p}$ $[\boldsymbol{kg/m^2}]$	Particle density
$\boldsymbol{\psi}$ $[-]$	Fraction of particles in trains

Non-dimensional numbers

$\boldsymbol{K}$	Dean number
$\boldsymbol{Re}$	Channel Reynolds number
$\boldsymbol{Re_{cr}}$	Critical Reynolds number
$\boldsymbol{Re_p}$	Particle Reynolds number

Abbreviations and Acronyms

$\boldsymbol{2D}$	Two-dimensional
$\boldsymbol{3D}$	Three-dimensional
$\boldsymbol{\mu TAS}$	Miniaturized Total Chemical-Analysis Systems
$\boldsymbol{AR_c}$	Channel aspect ratio
$\boldsymbol{CCD}$	Charged Coupled Device
$\boldsymbol{DLD}$	Deterministic Lateral Displacement
$\boldsymbol{DNC}$	Do not converge
$\boldsymbol{fps}$	Frames Per Second
$\boldsymbol{FR}$	Frame Rate
$\boldsymbol{GLMV}$	Grey Level Mean Value
$\boldsymbol{Ka}$	Kayaking
$\boldsymbol{LR}$	Log-Rolling
$\boldsymbol{PDF}$	Probability Density Function
$\boldsymbol{PFF}$	Pinched Flow Fractionation
$\boldsymbol{PNT35}$	Peanut particle (3.4μm x 5.1μm)
$\boldsymbol{PNT57}$	Peanut particle (5.1μm x 7.7μm)
$\boldsymbol{SNW}$	Snowman particle (12.8μm x 15.3μm)
$\boldsymbol{SPLITT}$	Split-flow thin cell fractionation
$\boldsymbol{SS}$	Steady State
$\boldsymbol{Tu}$	Tumbling

1. Introduction

1.1. General context

Solid-fluid suspensions are found everywhere: the human body, environmental fluids, industrial products, consumer applications, etc. Many applications in various fields, such as agriculture, biomedicine, environmental sciences, food technology, and the pharmaceutical industry, need identifying particles (whose forms and sizes can be different, as shown by the examples given in Figure 1.1) and controlling their trajectories in such suspensions [1,2]. The reason behind this request can be the need to:

- Identify various particles in the suspension. This allows determining the states of stem cells and detect anomalies like cancer for example [3–5]. It is also used to detect pollutants in environmental fluids (air and water) and pathogenic bacteria in other fluids (milk for example).
- Separate the particles from the fluid. Depending on the application, the aim can be to capture the particles if they are the target, or simply “clean” the fluid (i.e., depolluting air or water).
- Sort the particles of a polydisperse suspension. In fact, several real-life suspensions contain particles of different sizes and/or shapes, like blood for example. The aim of the sorting could be linked to a need for a treatment of a specific particle type in this suspension.
- Control the particles orientation. For example, while producing paper, the orientation distribution of the cellulose fibers in the flow is one of the basic parameters to control the quality of the final product [6].
- Control the concentration of the suspension by generating particle-rich and particle-free regions or streams.
- Move the particles from one suspending fluid to another. This is used in cell analysis studies for example [7].

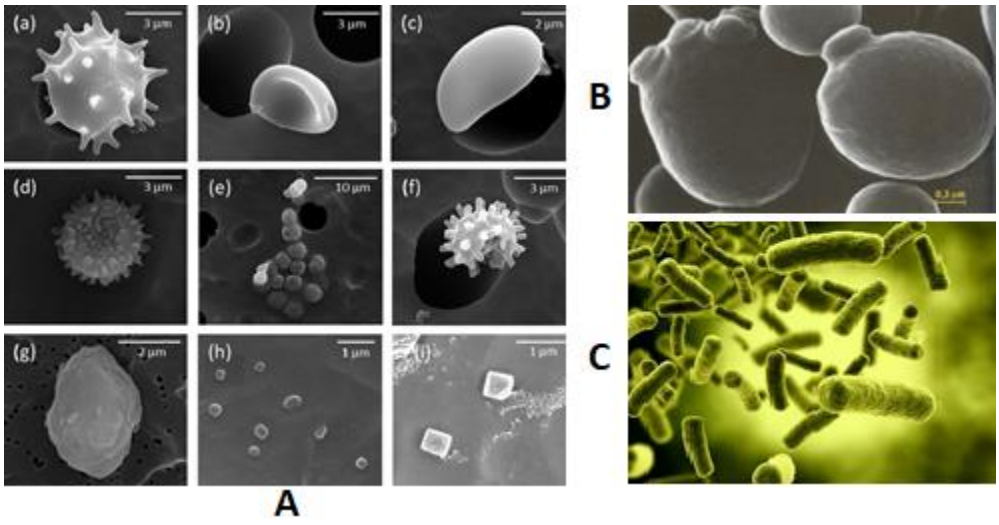

Figure 1.1. (A) Aerosol particles (reprinted from [8]), (B) yeast and (C) Escherichia coli

The conventional separation processes (settling, centrifugation, membrane filtration…) require large volumes and have an important energetic cost. In the past decade, miniaturized particle separation systems using microfluidic flows have been developed: they allow lowering the sample volumes and the energetic cost and increasing the adaptability to automation and the portability of the devices. These microsystems often include a preliminary stage in which the particles are focused into a tight stream. There exist many techniques to focus the particles. These methods can be divided into two large categories: the active techniques and the passive ones.

In the case of active focusing, particles in a suspension are controlled using external force fields, that are often applied perpendicularly to the main flow direction. The choice of the force field is based on the particles' properties. The force can be: (i) electrical [9,10] (Figure 1.2.a), (ii) magnetic [11,12] (Figure 1.2.b), (iii) optical [13,14], or (iv) acoustic [15].

Using an external force field makes the separation process faster and more efficient. However, the requirement of an additional outer force demands additional equipment, which increases the cost and complicates the operations. In addition, this technique could have an effect on biological samples, like damaging living cells.

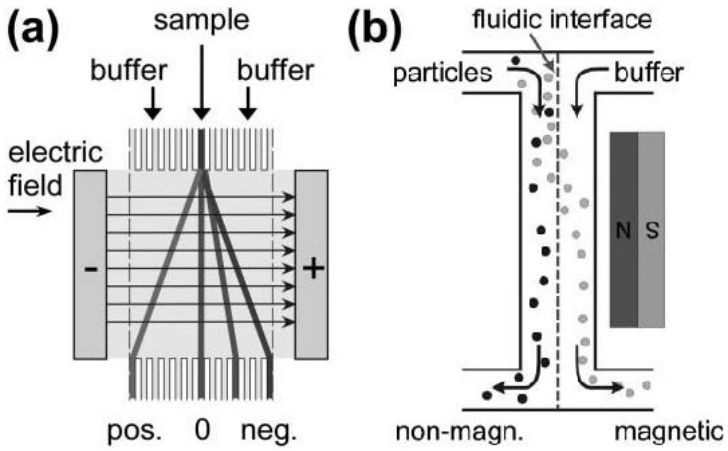

Figure 1.2. Active techniques: (a) electrophoresis and (b) magnetophoresis. Reprinted from [16].

Passive separation techniques do not use external fields to control the particle. They take advantage of the forces induced by the interactions between the particles, the flow and the channel structure.

The control of the position of a particle in a channel can be done using one or multiple external particle-free sheath flows [17,18]. This method is called the pinched flow fractionation (PFF) when more than one sheath flow is used to pinch the sample solution, trapping the particles in one focusing region [13,19–21]. A schematic illustration is shown in Figure 1.3.

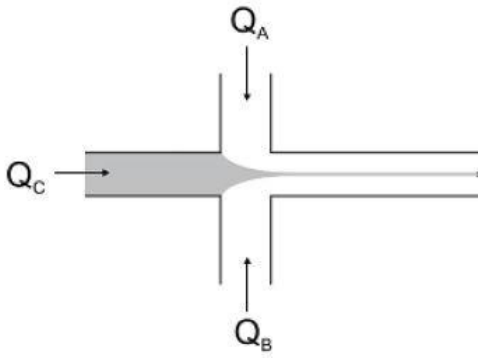

Figure 1.3. Particle focusing using sheath flows. The index C refers to the central inlet, while A and B refer to the sheath flows. Reprinted from [22].

The choice of the sheath fluid, its inlet inclination with respect to the suspension, and the flow rates, affect the particle focusing at the outlet. The final result depends also on the width of the outlet and the particle's diameter. Thus, by changing these parameters, the

position and width of the focused stream can be tuned [23]. This advantage makes of PFF a practical method for several applications like flow cytometers for cell counting and sorting [24–27], cell patterning [28], microflow switches [29–32], microfluidic injection systems [33], diffusion-based mixers [34–36], etc.

Nonetheless, this method has several restraints. The use of the sheath fluid demands extra inputs and additional equipment, which complicates the fabrication process and increases the cost. In addition to that, mixing this pinching fluid with the original suspension can dilute the sample flow and modify its properties. Finally, if the studied suspension contains living bio-cells, the flow rates should be limited to avoid damaging the cells.

There exist sheathless passive techniques that do not require any external force or flow. These methods are based on the interactions between the particles, the suspending fluid and the channel walls to focus the particles.

Density-based techniques for example rely on the difference between the density of the particle and that of the suspending fluid to generate sedimentation or flotation in the channel [37]. These methods are reasonably efficient, cheap, easily maintained, and do not require special-environment conditions. However, they have one major drawback which is the incapability to manipulate neutrally buoyant particles, that have the same density as the suspending fluid.

The deterministic lateral displacement (DLD) is another sheathless passive technique to control the positions of the particles in the channel [38–40]. This method consists of introducing an array of internal micro-scale obstacles in the channel during the fabrication (Figure 1.4). The DLD technique is based on the interactions between the particles and the obstacles. The shape, angle and size of the obstruction affect the flow, influencing the trajectory of the particle in the channel. The size of the particle also has a crucial role in determining the chosen path. The DLD method is efficient and speedy. However, integrating internal obstacles in a channel complicates the fabrication, increases the fabrication costs and raises the risk of clogging.

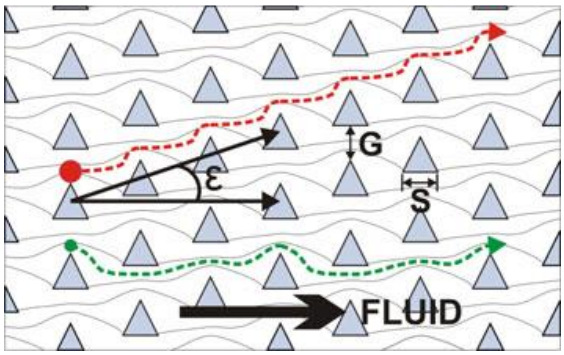

Figure 1.4. The deterministic lateral displacement technique using triangular obstacles. Reprinted from [38].

As seen above, a diverse set of methods has emerged to help achieve focusing at the microscale [41]. To improve the outcome, two or more of these techniques can be combined. For example, electrophoresis could be supported by an array of internal obstacles [42]. Also, the external fields can be strengthened by a pinching flow, like in the case of the split-flow thin cell fractionation ($SPLITT$) [43].

However, these techniques present few drawbacks like the requirement of sheath flows and/or external forces, a high fabrication cost, difficulties in miniaturization… To eliminate these obstacles, the inertial focusing technique has been developed for particle focusing in microchannels. This approach is based on the inertial migration phenomenon. This latter relies only on hydrodynamic forces induced in the channel, due to interactions between the fluid and the particles and between the different particles flowing together. The inertial focusing technique does not require any sheath flow, external force or complex channel geometry. This makes it a simple non-invasive operation and a low-cost process. It can be also described as a highly-portable, robust, power-efficient, and continuous high-throughput technique. In addition, it demands small sample volumes and it has low analysis time. Recent reviews have identified this technique as promising with great potential for the development of micro-separation devices for Lab-on-a-Chip applications [44].

The work done in this thesis aims to bring new insights on the inertial migration phenomenon, that will be presented in details in Section 1.2.

1.2. Transport of particles in microchannel flows: state of the art

1.2.1. Introduction

For more than 50 years now, and for multiple purposes, techniques are being developed to control the behavior of particles flowing in microchannels (Section 1.1), among which the inertial focusing technique. This technique is based on the inertial migration phenomena, described in Section 1.2.2. The effects of several parameters on the particles' transport are presented in Section 1.2.3. Next, based on previous works, Section 1.2.4. covers a detailed analysis of the influence of the particle's shape on its transport. Finally, an overview of the shape-based separation is covered in Section 1.2.5.

1.2.2. Mechanisms of inertial migration and rotational behavior

1.2.2.1. Lateral migration

As explained in the first section of this chapter, the inertial focusing could be an effective technique for particle focusing in a channel. This method is based on the inertial migration phenomenon which was first observed by Poiseuille in 1836 [45], while studying blood flows. He noticed that blood corpuscles flowing in a tube seemed to concentrate radially close to the walls of the tube. This phenomenon was quantitatively confirmed by the experiments of Segré and Silberberg on spherical particles [46,47] in 1962 and by other experimental [48–51], numerical [52–54] and theoretical [55–58] studies.

It has been shown that under specific flow and geometrical conditions, flowing particles naturally migrate toward lateral equilibrium positions where they concentrate. The number and the locations of the equilibrium positions vary in function of several parameters (Section 1.2.3).

The mechanisms of inertial migration were highlighted by Matas et al. [59]. In a square channel, three primary lift forces carry neutrally-buoyant particles across the streamlines

toward their equilibrium positions: the wall-induced lift force F_W, the shear-induced lift force F_S and the rotation-induced lift force F_Ω.

The presence of the channel walls generates F_W. In fact, when the particle is next to the wall, it causes an asymmetry in the streamlines of the flow. This generates a difference of pressure around the particle, repulsing it away from the wall towards the channel's centerline (Figure 1.5.a) [1,60–62].

Due to the curvature in Poiseuille's velocity profile, the fluid's relative velocities (with respect to the particle) at both sides of the particle (the wall side and the centerline side) are not the same. This dissymmetry causes a lower pressure on the wall side of the particle, , i.e., the area with increasing shear gradient, creating the shear-induced lift force F_S and directing the particle towards the wall [59,60,63] (Figure 1.5.b).

This difference in the magnitude of the velocities creates a torque, making the particle rotate, generating by that the rotation-induced lift force F_Ω. Since the neutrally buoyant particles always lag behind the fluid in a Poiseuille flow [64], this rotation-induced lift force acts against the flow velocity gradient in the direction of the center of the channel [55,60,65,66] (Figure 1.5.c), and its magnitude depends on the particle's diameter, its angular velocity, the velocity of the flow and the fluid's density.

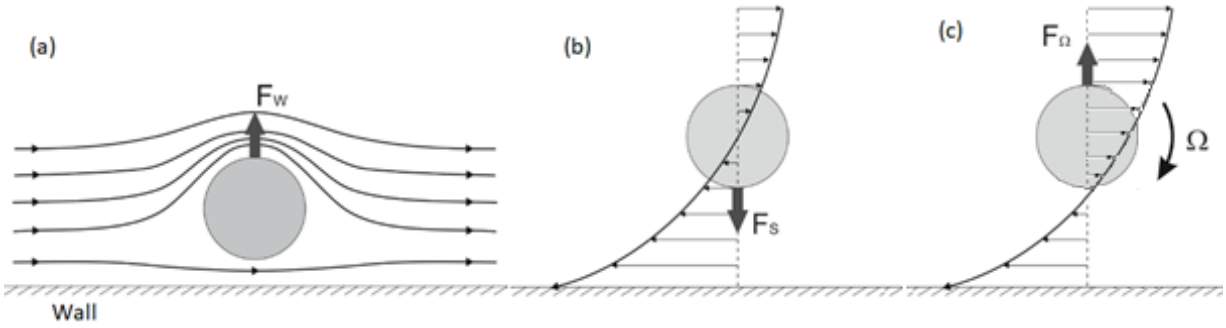

Figure 1.5. Illustration of (a) the wall-induced lift force F_W, (b) the shear-induced lift force F_S, and (c) the rotation-induced lift force F_Ω. Figures (a) and (b) are reprinted from [67].

Neutrally buoyant spherical particles flowing at moderate fluid inertia in a square microchannel laterally migrate toward four equilibrium positions located at the centers of the channel walls [53,67]. In order to attain its equilibrium position, the particle follows a two-stage migration: first, it migrates in the lateral direction through the velocity iso-contours and reaches an equilibrium ring; then, it moves cross-laterally along the chosen

ring toward its equilibrium position [53,59,67–69]. In the first stage, called the cross-streamline migration, the shear-induced and the wall-induced lift forces drive the particles to a rectangular ring-like region where the effects of both forces are canceled. The rotation-induced lift force dominates in the second stage of migration (called the cross-lateral migration) and drives the particles to their equilibrium positions with a smaller migration velocity.

In the case of a rigid particle flowing in a Newtonian straight flow, and in the first stage of the migration, the Magnus effect has been shown to be negligible compared to the wall-induced and the shear-induced lift forces [60,66]. Few studies show derived theoretical and empirical expressions of the net inertial lift force $\vec{F} = \overrightarrow{F_W} + \overrightarrow{F_S}$. Two main results emerged, depending on the confinement ratio κ. This parameter, also called blockage ratio, is the ratio between the diameter of the particle d_p and the smallest dimension in the channel cross-section.

For very low values of κ ($\kappa \ll 1$), Asmolov [58] theoretically found that the net lift force can be calculated using the expression: $F = f\rho_f U^2 d_p^4/D_h^2$, where f is a lift coefficient that depends on the particle lateral position and channel Reynolds number Re.

Reynolds number is calculated as follows: $Re = \rho_f U D_h/\mu$, where ρ_f is the fluid density, U is the average fluid velocity, μ is the dynamic fluid viscosity and D_h is the channel hydraulic diameter ($D_h = 4A_c/P_c$, with A_c being the cross-sectional area and P_c the "wetted" cross-sectional perimeter).

For finite-sized particles ($0.05 < \kappa < 0.2$), it has been shown by Di Carlo et al. [62] that F scales as $F \propto \rho_f U^2 d_p^3/D_h$ near the channel center, while it scales as $F \propto \rho_f U^2 d_p^6/D_h^4$ next to the channel walls.

The wall-effect is weak near the channel center, so the net lift force is equal to the shear-induced lift force. However, next to a wall, F_S is negligible and $F = F_W$. This means that the wall-induced lift-force can be calculated as follows:

$$F_W = C_W \rho_f U^2 d_p^6/D_h^4 \quad (1.1),$$

while the shear-induced lift force can be found using:

$$F_S = C_S \rho_f U^2 d_p^3/D_h \quad (1.2),$$

where C_W and C_S are lift coefficients depending on the particle position and Reynolds number Re [1,62].

Even with these expressions for the lift forces on finite-sized particles (Equations 1.1 and 1.2), finding the forces magnitudes theoretically is still not possible since no clear analytical or empirical expressions linking the lift coefficients to the particle position and Reynolds number are identified yet.

1.2.2.2. Longitudinal ordering

The migration toward the equilibrium positions occurs together with a particle longitudinal ordering process, in which the particles form trains and follow each other in the channel with a constant interparticle spacing (Figure 1.6.a). This was observed by Segré and Silberberg [46,47], then investigated and explained by Matas et al. [70] and Lee et al. [68]. According to Gao [67], this phenomenon only appears after the lateral migration is fully developed.

The particle alignment is a consequence of the interactions between the fluid and the particles, and between the particles themselves. Matas et al. [70] suggested that the recirculation zones, created around the particle in the flow, are the main factor helping the particles align in trains. This proposition was confirmed by Morris and this team [71,72] using lattice-Boltzmann simulations. It was demonstrated, numerically by Humphry et al. [73] and experimentally by Lee et al [68] in 2010, that the particles move in an oscillatory trajectory in order to ensure the steady axial spacing. When one particle is following another one in the channel, this lagging particle is faster than the leading one. Once they approach each other, the lagging particle is dragged by the recirculation zones created by the leading one, and the drag force will act to slow down the faster one until it reaches the average intersected fluid speed. So, the quick particle will be pushed by the streamlines in the opposite direction, and will move slightly toward the channel walls to slow down, following the opposite direction streamline. The leading particle with a slower speed will also be dragged by the recirculation zones caused by the quick one, which accelerates and directs it slightly towards the channel center, following the streamline in the main flow direction. In addition to the recirculation zones drag forces, the inertial lift

forces direct the two particles back to their sharp focusing positions when they are far from their equilibrium positions as shown in Figure 1.6.b.

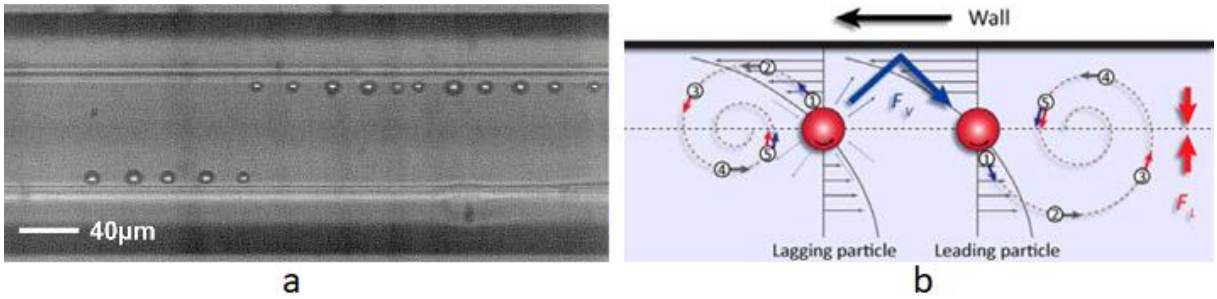

Figure 1.6. (a) A captured image representing the longitudinal ordering of spherical particles in a square channel at $Re = 210$ (reprinted from [67]); (b) Schematic drawing of the interaction between two aligned particles (reprinted from [68]).

1.2.2.3. Rotational behavior

In addition to their inertial migration, particles have a rotational behavior in the channel. According to [53], the rotational behavior of a spherical neutrally buoyant particle flowing in a square microchannel at moderate Reynolds numbers is coupled to the sphere's lateral migration development. During the migration process, the particle's angular velocity has three components along the three main axes of the channel: it rotates around both cross-sectional directions (due to the presence of two parabolic velocity profiles in a typical square Poiseuille flow), as well as around the flow axis. Once the particle is focused, only the rotation in the cross-sectional direction parallel to its closest wall remains. The particle's angular velocity increases with increasing Re. Figure 1.7 shows particles focused on their equilibrium positions in a square cross-section with their rotational axes.

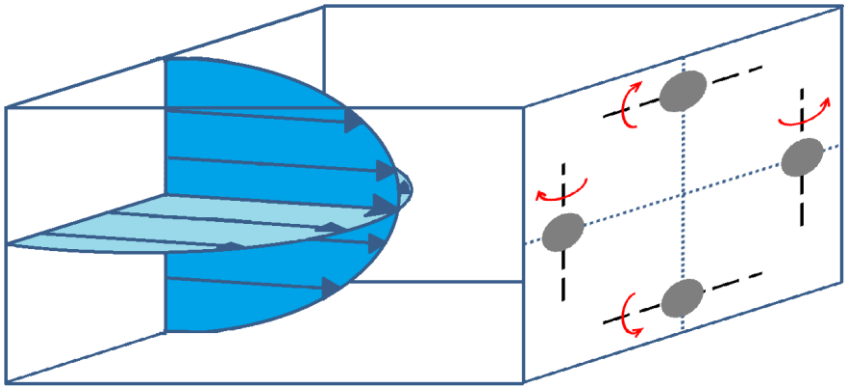

Figure 1.7. A schematic representing a square microchannel in which particles are focused on their equilibrium positions and are rotating around their rotational axis (dashed black lines).

1.2.3. Effects of the various geometrical and operating parameters on the inertial migration

1.2.3.1. Channel properties

1.2.3.1.1. Length

The focusing length L_f is the distance needed for the lateral migration to be finished. In other words, it is the necessary distance for the particle to reach its equilibrium position. The calculation of L_f was obtained for different configurations [44,48,65].

If the channel's length is greater than L_f, most of the particles will be at the equilibrium position at the outlet of the channel. The longer is the channel, the higher will be the number of focused particles.

The same logic applies on the longitudinal ordering. In fact, as mentioned earlier, trains form while the focused particles are flowing in the channel. This means that, when the channel length increases, the trains have more time and chance to be formed, which enhances the longitudinal ordering and increases the percentage of particles in trains [67].

1.2.3.1.2. Cross-section

The channel's cross-section is an important parameter influencing the migration of particles in microchannels. When the geometry and/or the aspect ratio is changed, the velocity field is modified, affecting the number and the locations of the equilibrium positions (Figure 1.8). The most commonly used geometries are circular [59], rectangular [2,65] and square [53,67]. Less frequent cross-sectional geometries are triangular [74], trapezoidal [75], and semi-circular [74].

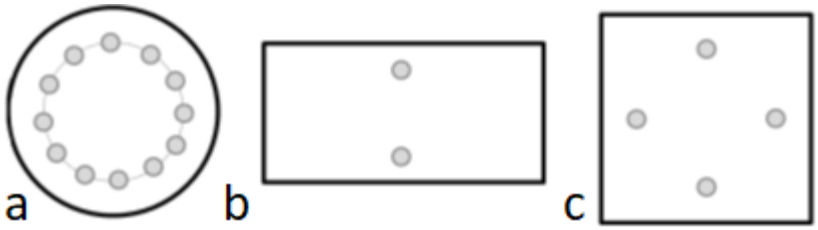

Figure 1.8. Equilibrium positions at moderate fluid inertia in a (a) circular cross-section (annulus); (b) high-aspect-ratio rectangular cross-section (the centers of the long faces); and (c) square cross-section (also applicable for a low-aspect-ratio rectangular cross-section) (the centers of the four faces).

1.2.3.1.3. Curvature

In order to reduce the space needed on Lab-on-chip devices, recent works have been investigating the inertial migration of particles in curved channels. Serpentines, helicoidal and sinusoidal channels are being used. However, it has been shown that, by curving the channel, secondary recirculating flows are created in the channel's cross-sectional plane (Figure 1.9). These flows, also called Dean's vortices, induce an extra force (Dean's force) acting on the locations of the equilibrium positions [76–78]. The magnitude of this force highly depends on the Dean number K, which is equal to $K = Re\sqrt{\beta}$, with β being the curvature ratio ($\beta = D_h/2R$, D_h is the channel's hydraulic diameter and R its radius of curvature).

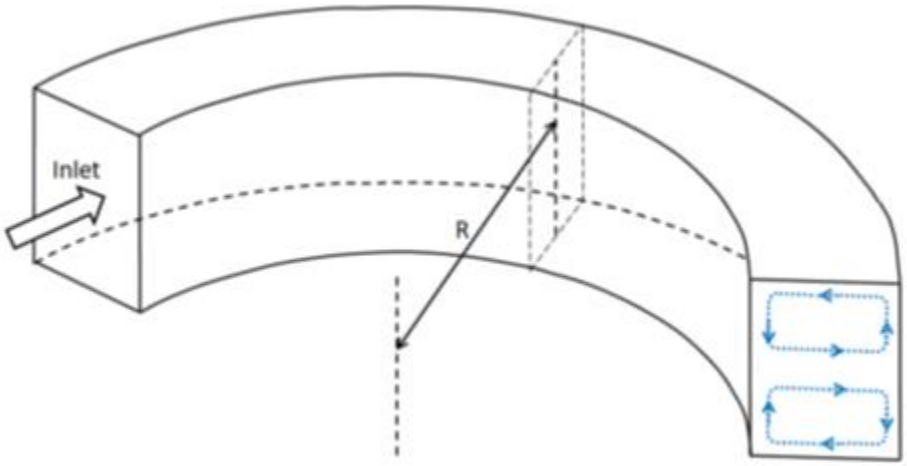

Figure 1.9. A schematic representing a curved channel with the Dean vortices in blue.

1.2.3.2. Fluid and flow properties

1.2.3.2.1. Reynolds number Re

Fluid inertia, represented by Reynolds number, is an essential parameter influencing the inertial migration. In a square channel, depending on Reynolds number, three different migration regimes can be observed. At low Re ($Re < 5$ in the experimental conditions of [53]), spheres laterally migrate toward the centerline of the channel. At moderate Re ($5 < Re < 150$), particles migrate toward the four equilibrium positions described earlier. At high Reynolds numbers ($Re > 450$, according to [69]), secondary equilibrium positions appear at the corners of the channel, increasing the total number of equilibrium positions from four to eight. At intermediate Reynolds number ($150 < Re < 450$), in

function of the operating conditions, a transitory regime exists between four and eight equilibrium positions.

At moderate fluid inertia, increasing the Reynolds number accelerates the migration process and thus decreases the focusing length (the channel length required to focus the particles) [67].

Other than affecting the migration velocity, fluid inertia has an effect on the distance between a face-centered equilibrium position and its nearest wall. An increase in Re in the moderate range gets the spheres closer to the walls [53]. However, at high values of Re, an increase in fluid inertia, increases the distance between the face-centered equilibrium positions and the walls, and the four equilibrium positions are observed to be closer to the channel centerline [69].

Fluid inertia also influences the train formation. The fraction of particles in trains, defined as the number of particles in trains over the total number of particles, increases with Reynolds number at moderate inertia [67]. This increase can be explained in two ways. It can be related to the focusing length, which decreases when the Reynolds number increases, giving the particles more time to rearrange themselves in trains before reaching a fixed distance from the channel inlet. The second explanation is that increasing the Re makes the recirculation zones wider [71,79] increasing the chance to trap particles and enhancing the train formation. At high Reynolds numbers, the fraction of particles in trains is shown to decrease [67]. The reason behind this finding is assumed to be related to the transition from four to eight equilibrium positions at high Reynolds numbers.

Reynolds number is shown to have another effect on the longitudinal ordering. With an increasing Re, the average distance between the particles in a train decreases [80]. Morris and co-authors [71,79,81] showed that when the Reynolds number increases, the recirculation zones, responsible for setting the interparticle distance, get closer to the surface of the particle which makes the particles of a train closer to each other.

1.2.3.2.2. Non-Newtonian and viscoelastic fluids

When the suspending fluid is non-Newtonian, a viscoelastic force is added to the particle's free body diagram, joining the other existing forces. This changes the locations and the number of equilibrium positions. The magnitude and the direction of this force depend on the size of the particle and the properties of the suspending fluid [82–91]. In some configurations [87], the magnitude of this force is so considerable, that the particles are pushed towards the channel centerline.

1.2.3.3. Suspension properties

1.2.3.3.1. The number of particles: the particle volume fraction Φ

The suspension concentration, also called the particle volume fraction Φ, is the ratio between the total volume of the particles and the volume of the whole suspension. A change in Φ is shown to have an effect on the particle's migration in the channel.

Lim et al. [92] observed that an increase in the value of Φ changes the particle distribution in the channel cross-section. In fact, they showed that, in a rectangular channel, cancer cells flowing in a diluted blood suspension, focus on the two centers of the long faces. However, for a concentrated blood suspension, the equilibrium positions correspond to the centers of the short faces.

Gao et al. [67,80,93] experimentally investigated the effect of Φ on the inertial migration of spherical particles in square channels. While increasing Φ ($0.02\% < \Phi < 1\%$), they did not notice any modification in the particle distribution: at moderate inertia, regardless of the suspension concentration, the particles focused at the four faced-centered positions. However, it was shown that, the four equilibrium positions are slightly pushed away from the wall, when Φ is increased. The physical phenomenon behind this observation is still unclear.

They also showed that increasing Φ widens the regions in which the particles are focused [67,93]. They attributed this finding to the increase in the particle-particle interactions. In fact, for a certain channel length, only a certain number of particles can occupy the four

face-centered equilibrium positions with a corresponding interparticle spacing in the streamwise direction regulated by interparticle forces.

Concerning the longitudinal ordering, Gao et al. [67,80,93] observed that, at a fixed moderate Re, if Φ increases in the range of $0.02\% - 1\%$, the train formation is enhanced, thanks to the increase in the number of particle-particle interactions.

1.2.3.3.2. Polydispersity

In order to have a closer configuration to real-life suspensions, where different types of particles are present, few works were done on the effect of the polydispersity on the inertial migration [94–97]. A suspension is considered polydisperse when it contains particles of different types and/or sizes.

Gao et al. [94] experimentally studied bidisperse suspensions. They mixed polystyrene spheres of two different sizes and studied the effect of the size ratio $d_r = d_{p1}/d_{p2}$ (where d_{p1} and d_{p2} are the diameters of the large and small particles respectively) on the migration of these particles.

No clear effect of the bidispersity was identified for small size ratios (close to 1): both types of particles migrated similarly to the monodisperse case ($d_r = 1$) and mixed trains were observed.

However, for high size ratios (up to 4), the migration of the small particles was influenced by the presence of the big ones, that migrated normally. The small particles could not finish the lateral migration and concentrated along the channel perimeter. In addition, the observed trains were mainly composed of big particles, showing that the small particles did not form or integrated any trains.

1.2.3.4. Particle properties

1.2.3.4.1. The particle's density

In the non-neutrally-buoyant case, where the density of the particle ρ_p is different than the density of the suspending fluid ρ_f, a new force arises, resulting from the vector sum of the weight of the particle and the buoyancy force. This force is equal to $|\rho_p -$

$\rho_f| \times V_p \times g$, where V_p is the volume of the particle and g is the local acceleration of free fall. This resulting force is oriented upwards or downwards if the particle is lighter ($\rho_p < \rho_f$) or heavier ($\rho_p > \rho_f$) than the fluid respectively.

1.2.3.4.2. The particle's size: the confinement ratio κ

As defined earlier, κ is the ratio between the diameter of the particle and the smallest cross-sectional dimension. This parameter is shown to have an effect on the sphere's inertial migration. In the case of neutrally buoyant particles, increasing κ accelerates the migration process and thus decreases the channel length needed to reach the final stage of migration. In addition, bigger spheres (i.e., higher κ) focus at an equilibrium position closer to the channel centerline than smaller particles [53].

The longitudinal ordering is also altered by the confinement ratio. In fact, an increase in the particle's size (in a fixed geometry) results in larger recirculation zones [71,79]. This rises the chance of capturing a particle and forming a train, and decreases the interparticle distance.

1.2.3.4.3. The particle's deformability

In some real-life applications, the particles are not perfectly rigid. For this reason, studies have been done, investigating the inertial migration of deformable particles. These works confirm the existence of a deformability-induced lift force acting on the particles, and modifying the particle distribution in the channel [2,85,98–103]. Recently, Connolly et al. [104,105] confirmed these findings and found that the deformability of the particle, determined by its elastic modulus, is one of the crucial parameters that influences the particles migration in the channel. In fact, they showed that an increase in the particle's deformability (a decrease in the Young's modulus), resulted in a migration toward the channel center, where the velocity gradient effects are lower than those at the channel wall.

1.2.3.4.4. The particle's shape

The shape of the particles can also have an influence on their transport in the channel. This parameter, which constitutes the main object of this study, will be described in detailed in the next section.

1.2.4. Behavior of rigid non-spherical particles in a flow

1.2.4.1. Introduction

Most of the theoretical, numerical, and experimental studies conducted on inertial migration during the last two decades have mainly investigated spherical particles. This simple geometry can be easily fabricated for experimental studies and quickly represented mathematically and numerically. These works have increased the knowledge on the transport of spherical particles in microchannels and demonstrated the ability of inertial focusing methods to separate particles based on their sizes. For example, Di Carlo [106] highlighted the possibility to separate particles of different sizes within the transverse plane of the channel. The separation was experimentally proven by Bhaghat et al. [107] by extracting 590nm particles from a mixture of 1.9µm and 590nm particles using inertial migration.

However, most of the targeted applications (Chapter 1) involve complex-shaped particles. For instance, a human red blood cell adopts a biconcave disk-like shape in the body, Escherichia coli is cylindrical, and Euglena gracilis has an ellipsoidal geometry. Furthermore, in many applications, particles of the same size but different geometries can be found, which complicates the size-based separation or even makes it impossible. Thus, shape could serve as a specific marker in the identification and/or separation of particles in a suspension, which raises the question of how do non-spherical particles travel in a microchannel.

In the spherical case, even if the coupling between the lateral migration and the rotational behavior exists (especially in the second migration stage), the rotation has a limited influence on the lateral migration. This is not the case for non-spherical particles, where the translational and rotational motions are strongly coupled [108,109]. Thus, both rotational and migratory behaviors should be considered when studying the transport of non-spherical particles flowing in a microchannel. In this section, a bibliographic analysis, based on multiple studies concerning these two behaviors, is presented.

Most of the existing works investigating the transport of particles in microchannels decouple their rotational and lateral migration behaviors: particle rotation is mainly studied in simple shear flows, where the lateral migration is neglected, and studies on lateral migration mostly focus on spherical particles whose rotational behavior is relatively simple.

The rotational behavior was first studied in a simple shear flow, and then was extended to bounded shear and Poiseuille flows where the wall-effect intervenes. Most of these works are numerical and theoretical.

Since an ellipsoid is the closest non-spherical shape to a sphere, the first studies, on the effect of the shape of a particle on its behavior, investigated ellipsoidal particles. Later on, works were done on particles with more complex geometrical shapes.

Different geometries have been studied in the literature. They can be classified into three main categories: ellipsoids, non-ellipsoidal axisymmetric particles, and asymmetrical ones (Figure 1.10). Based on the aspect ratio of the particle (λ = radial diameter/equatorial diameter), an ellipsoid can be a prolate or an oblate ($\lambda > 1$ and $\lambda < 1$, respectively). Similarly, non-ellipsoidal axisymmetric particles are subclassified into rod-shaped particles ($\lambda > 1$) and disc-shaped ones ($\lambda < 1$).

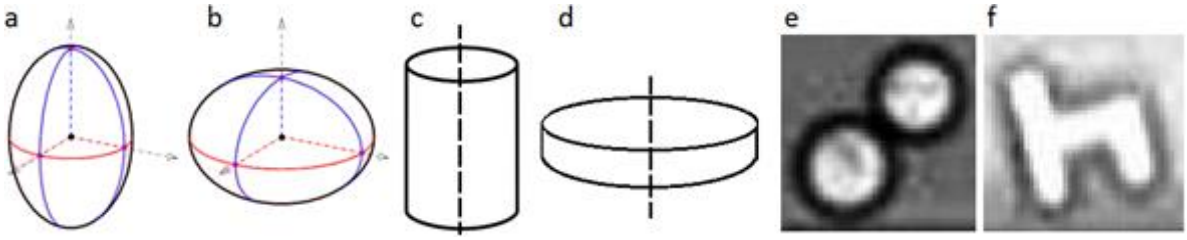

Figure 1.10. Non-spherical geometries: (a) prolate (ellipsoid); (b) oblate (ellipsoid); (c) cylinder (non-ellipsoidal axisymmetric); (d) disc (non-ellipsoidal axisymmetric); (e) axisymmetric doublet; (f) h-particle (asymmetric). Figures (e) and (f) are reprinted from [110].

1.2.4.2. Rotational behavior of a Non-Spherical Particle in a Shear Flow

1.2.4.2.1. Ellipsoidal Particle

Jeffery's Theory

In 1922, Jeffery [111] theoretically studied the rotational behavior of an ellipsoid in a simple shear flow. The particle was rigid, isolated, and neutrally buoyant; the fluid was

Newtonian, and the suspension flowed in a simple shear, creeping, unbounded flow (i.e., with a constant shear rate and with neglected fluid inertia and wall effects).

Jeffery found that an ellipsoid rotates around the vorticity axis (perpendicular to the flow-gradient plane) along one of an infinite set of closed orbits, the so-called Jeffery orbits, which are dependent on the initial conditions, the shear rate, and the spheroid's aspect ratio. This mode of rotation is called "kayaking", since the particle's trajectory resembles the motion of a kayak paddle (Figure 1.11a,b1–b3). The two extreme orbits are called "tumbling", when the axis of revolution of the particle is rotating in the flow-gradient plane (Figure 1.11a,c1–c3), and "log-rolling" when the particle rotates around its axis of revolution aligned with the vorticity axis (Figure 1.11a,d1–d3).

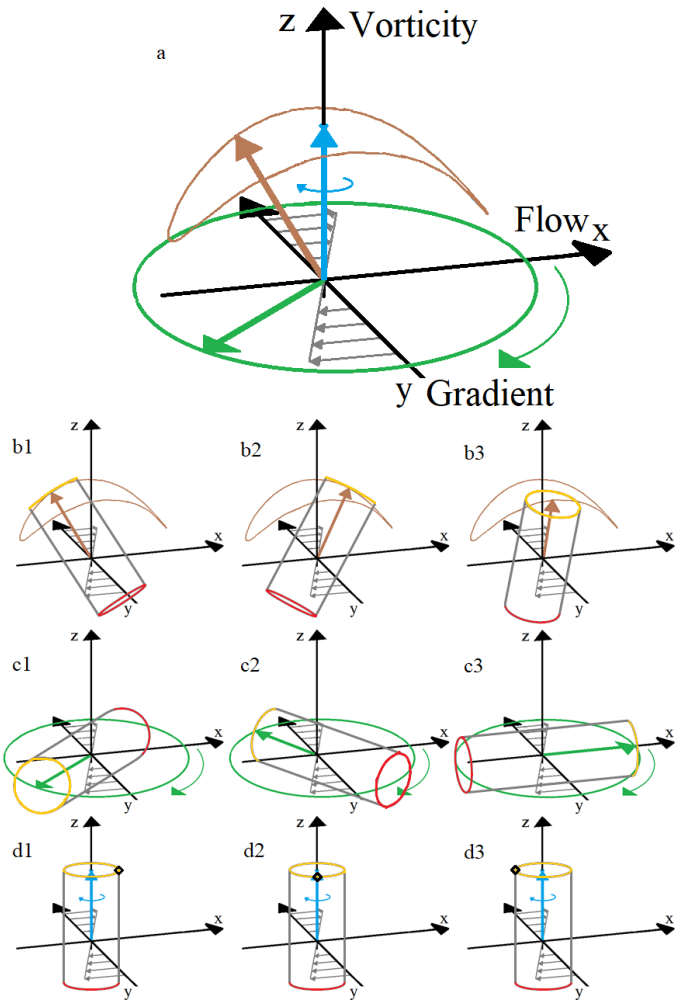

Figure 1.11. Schematics of Jeffery's orbits: (a) the log-rolling motion (blue), the tumbling motion (green), and the kayaking motion (brown); (b1–b3): kayaking at three different moments for a cylindrical particle; (c1–c3): tumbling at

three different moments for a cylindrical particle and (d1-d3): log-rolling at three different moments for a cylindrical particle.

Jeffery also showed that the particle's angular velocity is not constant but periodic. It has a maximum value when the particle's axis of revolution is perpendicular to the direction of the fluid motion and a minimum value when the particle is aligned with the flow. The period of rotation T is the time needed to complete one orbit. It depends on the shear rate γ and the particle's aspect ratio λ, and it can be calculated as follows:

$$T = \left(\lambda + \frac{1}{\lambda}\right) 2\pi/\gamma \qquad (1.3).$$

Extension of Jeffery's Theory for General Shear Flows

Bretherton et al. [112] extended Jeffery's theory. They theoretically investigated the rotational behavior of an ellipsoid flowing in a general shear flow, where the shear rate γ changes with the position. The results validated Jeffery's analysis: the particle orbits around the vorticity axis and has a period of rotation T that can be calculated using Equation (1.3), with γ equal to the shear rate at the center of the studied particle.

Effect of Fluid Inertia

Fluid inertia is shown to have a significant influence on the dynamics of particles suspended in a fluid: it makes ellipsoids adopt a rotational behavior that is different from the one found by Jeffery [111].

For a small non-zero Reynolds number, a prolate particle gradually turns its axis of revolution into the flow-gradient plane in order to tumble [113] (Figure 1.12a1,a2). The tumbling mode corresponds to the orbit with the maximal energy dissipation [114,115]. At high Reynolds numbers, other rotational modes have been observed by several authors. Ding and Aidun [116] found that above a critical Reynolds number ($Re \approx 29$ for neutrally buoyant particles), a prolate can cease rotating in a steady-state flow. According to them, this change in the particle's rotational motion is due to modifications in the recirculation zones created around the moving particle. In the absence of inertia, the streamlines are fully attached, and therefore, the torque on the ellipsoid is always forcing it to rotate, creating a time-periodic state. This rotating state is stable. However, at $Re > 0$, the streamlines detach, creating recirculation zones that influence the particle's behavior by generating an opposing torque and thus decreasing the net torque exerted

on the particle. Beyond the critical Reynolds number, the opposing torque becomes high enough to stop the particle from rotating. This steady-state mode has not been observed by other authors. Qi and Luo [117,118] identified in lieu three different rotational modes with increasing inertia: at low Re *(*$Re < 205$*)*, the prolate tumbles in the flow-gradient plane; at intermediate Re ($205 < Re < 345$), the axis of the spheroid deviates from the flow-gradient plane, and at higher Re ($345 < Re < 467$), the prolate rolls with its revolution axis aligned with the vorticity axis. According to Yu et al. [119], a prolate spheroid flowing in a simple shear flow with *Re* increasing from 0 to 256 undergoes the following transitions: Jeffery's orbit, tumbling, kayaking, log-rolling, and inclined rolling (log-rolling around a tilted axis with respect to the vorticity axis). Huang et al. [120] also found numerically an additional rotational mode that they called inclined kayaking. Both Yu et al. [119] and Huang et al. [120] found that some of these solutions co-exist for a given set of parameters and that the final rotational mode depends on the initial conditions.

In the case of an oblate and in the presence of fluid inertia, Saffman [113] theoretically showed that the axis of symmetry of the particle gradually aligns with the vorticity axis imposing a log-rolling rotational mode (Figure 1.12b1,b2). For high Reynolds numbers ($220 < Re < 467$), Qi and Luo [117,118] showed that the inclined log-rolling is the dominant rotational regime. According to Yu et al. [119], an oblate spheroid in a simple shear flow with *Re* increasing from 0 to 192 undergoes the following transitions: Jeffery orbit, log-rolling, inclined rolling, and steady-state. During this last rotational mode, the oblate does not rotate and has its axis of revolution aligned with the gradient axis.

To summarize, the studies converge on the fact that prolate ellipsoids flowing in low-inertia shear flows tumble and oblate particles log-roll. However, at higher values of Re, the results diverge, and different rotational modes are observed.

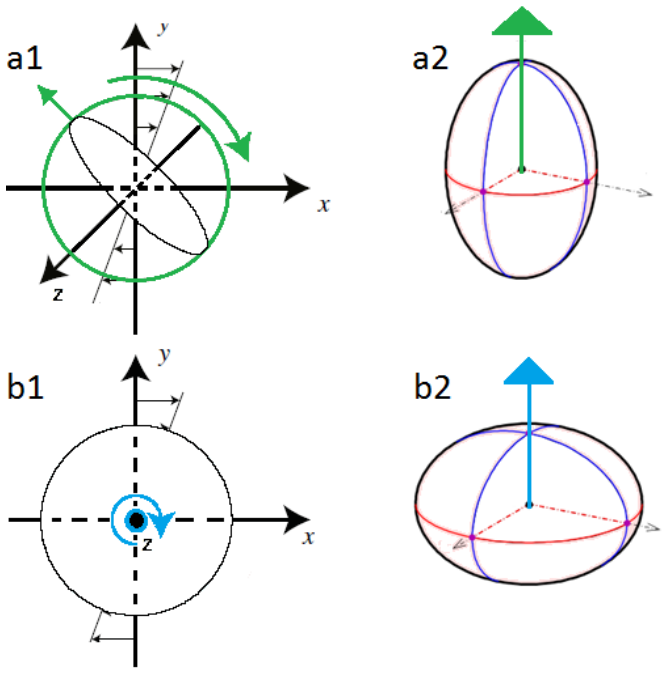

Figure 1.12. (a1) A tumbling prolate; (a2) a prolate with its axis of revolution in green; (b1) a log-rolling oblate; (b2) an oblate with its axis of revolution in blue. Figures (a1) and (b1) are adapted from [121].

Extension of Jeffery's Theory for Bounded Flows

In Jeffery's theory, the particle is flowing in an unbounded flow where no wall effect on the particle is considered. Chwang [122] theoretically studied the rotational behavior of ellipsoids in bounded Couette and Poiseuille flows and showed that Jeffery's results were applicable as long as the particle is far from the walls.

Effect of Buoyancy (Sometimes Called "Particle Inertia")

Jeffery's theory [111] is based on a neutrally buoyant condition, where the particle and the fluid have the same density. While increasing the particle-to-fluid density ratio, Ding and Aidun [116] observed that the ellipsoid's rotational modes are conserved and that only the transition Reynolds numbers between the different modes are increased.

Effect of the Particle's Aspect Ratio

In the absence of fluid inertia, Equation (1.3) shows that an increase in the particle's aspect ratio causes an increase in the rotation period. This phenomenon has been shown to be still valid in the presence of fluid inertia in [123].

Moreover, the variation in the rotational rate is shown to increase when the ellipsoid's aspect ratio is increased: the maximum angular velocity (when the particle is perpendicular to the flow) becomes higher, and the minimum angular velocity (when the

particle is aligned with the flow) becomes lower [124]. This was also reported by Bretherton [112], who observed that an elongated prolate with a high value of λ spends most of its time almost parallel to the streamlines, and it reverses itself periodically.

Effect of the Particle's Initial Orientation

In the absence of inertia, Jeffery's theory [111] considered that the particle's initial orientation has a determinant effect on its trajectory and the choice of the orbit. When the inertial effects start taking place, the conclusions are more controversial. Yu et al. [119] showed theoretically that the trajectories of prolates and oblates flowing in a Couette flow at a given Reynolds number are determined by their initial orientations. However, the results of Huang et al. [120] and Rosén et al. [125] indicate that the rotational mode of an ellipsoid is influenced by its initial orientation only within certain intervals of Re.

1.2.4.2.2. Axisymmetric Non-Ellipsoidal Particle

Due to several challenges in the fabrication of ellipsoids for experimental testing and since the non-spherical particles that flow in real suspensions have more complex shapes, some of the studies were extended from ellipsoids to axisymmetric non-ellipsoidal particles (mainly rods, doublets, and discs). These works helped understand the effect of the shape of the particle on its behavior, especially when the particle has sharp edges and/or is more flattened or elongated than an ellipsoidal particle.

Extension of Jeffery's Theory to Axisymmetric Non-Ellipsoidal Particles

Bretherton [112] showed that Jeffery's equations are also valid for almost any axisymmetric particle, provided that an equivalent aspect ratio λ_e is used. This latter is determined experimentally by measuring the orbital period [112,126]. So, it can be deduced that an axisymmetric non-ellipsoidal neutrally buoyant particle in simple, creeping, and unbounded flows kayaks around the vorticity axis in a closed orbit. The orbit is determined by the particle's initial orientation, and the rotational period depends on the equivalent aspect ratio.

Effect of Fluid Inertia

As seen previously, in the presence of inertia, a prolate particle gradually turns into the flow-gradient plane in order to tumble, whereas an oblate particle gradually aligns its axis with the vorticity axis in order to log-roll. With increasing Reynolds number, other rotational modes can appear.

In the same way, in the presence of fluid inertia, a rod-like particle ($\lambda_e > 1$) tumbles in the flow-gradient plane, while a disc-like particle ($\lambda_e < 1$) rolls with its axis of revolution perpendicular to this same plane [127–130]. A Reynolds number $Re \sim O(10^{-3})$ is sufficient to force rods and discs to drift from kayaking to a new rotational behavior [127,131,132].

Ku and Lin [133] obtained similar results for fibers that are rod-like particles with a large aspect ratio. At $Re = 0$, a fiber in a simple shear flow far from the walls rotates with a constant period that can be accurately calculated using Jeffery's equations. At weak inertia, the fiber still rotates periodically, but it slowly drifts toward the flow direction. Similar to the case of prolates and rod-like particles, low inertia forces the fiber to tumble in the shearing plane perpendicular to the vorticity.

Above a critical Reynolds number ($4 < Re_C < 13$, varying with the particle's aspect and confinement ratios), Zettner and Yoda [124] showed experimentally that a cylindrical particle can cease rotating, resting at a nearly horizontal equilibrium orientation. Ku and Lin [133] obtained similar results for fibers, for a particle Reynolds number $Re_p \geq 6$ (Re_p is the Reynolds number based on the length of the particle and the flow average velocity). In addition, they showed that the stable stationary orientation is established with the fiber's axis tilted by a small angle about the flow direction.

Walls and Confinement Effects

The experimental study of Poe and Acrivos [134] and the numerical simulations of Aidun [135] on the transport of rods in simple shear flows revealed that low confinement ratios ($\kappa < 0.32$) have negligible effects on the particle's behavior. This parameter is the ratio between the diameter of the particle and the smallest dimension in the channel cross-section. However, κ has a marked effect at higher values [116,124].

Increasing the confinement degree causes an increase in the value of the critical Reynolds number above which a fiber changes its rotational behavior from a periodic tumbling to a steady state, meaning that it delays the transition from time-periodic rotation to stationary state. It also decreases the angle between the fiber stationary equilibrium orientation and the streamwise direction [133]. However, for a highly confined flow, a fiber has a stable stationary orientation through the whole range of Reynolds numbers studied in this analysis.

Effect of the Particle's Aspect Ratio λ

As explained previously, an increase in the aspect ratio of an ellipsoid increases its period of rotation and can also alter its rotational behavior.

Similar results were obtained in the case of cylinders. Trevelyan and Mason [136], Kittipoomwong et al. [137], and Skjetne et al. [138] showed that when the aspect ratio of a cylinder λ increases at a constant shear rate, the cylinder's angular velocity decreases and its period of rotation increases (Figure 1.13). However, the measured period of rotation was less than the one predicted by Jeffery [111] when the actual aspect ratio λ was inserted in Jeffery's equations. For example, Trevelyan and Mason [136] observed that the period of rotation of a cylindrical particle is equal to two-thirds the period of rotation of a prolate with the same aspect ratio. This deviation is due to the non-spheroidal form and can be taken into consideration by replacing the aspect ratio λ by the equivalent ellipsoidal axis ratio λ_e [112,126,127,136,139]. For rod-like particles, it was found experimentally and numerically that $\lambda_e/\lambda \approx 0.7$ [136,140].

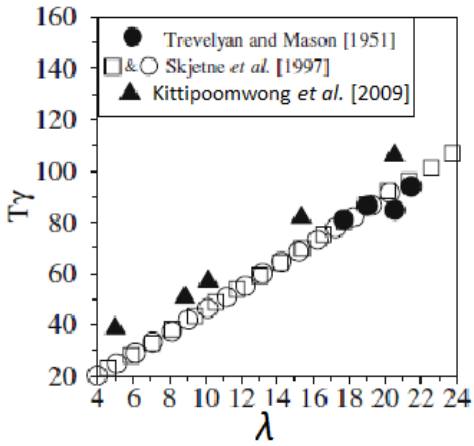

Figure 1.13. Normalized period of rotation as a function of the aspect ratio of a cylindrical rod. Reprinted from [137].

An increase in the particle's aspect ratio also modifies the rotational mode [124]. It increases the critical Reynolds number above which the particle adopts a steady state, i.e., stops rotating. In addition, the maximum value of the angular velocity (when the particle is perpendicular to the flow) increases, and its minimum value (when the particle is aligned with the flow) decreases.

Effect of the Solid Volume Fraction Φ (Suspension's Concentration)

Anczurowski et al. [129,130] showed that the drift from Jeffery's orbits to a tumbling motion occurred faster (i.e., at a smaller Re) by increasing the suspension's concentration.

1.2.4.2.3. Asymmetric Particles

On a higher level of complexity, few works investigated the effect of the particle asymmetry on its rotational behavior in a shear flow. Gierszewski and Chaffey [141] ran numerical simulations to study the rotation of a triaxial ellipsoid in a simple shear flow. They showed that if the particle is asymmetric, its motion is qualitatively different from that of an axisymmetric particle, and it has no fixed period of rotation around the fluid's vorticity axis. In fact, once the symmetry is broken, the period of rotation is altered, and the more the particle is asymmetric, the more the period is modified. As a function of the asymmetry in the particle's geometry, particles can tumble periodically, quasi-periodically (also called doubly periodic), or in a chaotic way [142]. The behavior can be chaotic in both space and time references.

1.2.4.3. Rotational and Migratory Behaviors of a Non-spherical Particle Flowing in a Square Microchannel

In this section, we present several studies investigating the behavior of a non-spherical particle in a square microchannel and the possible alterations once a parameter -related to the particle, the channel, the suspension, and or the flow- is modified.

The main difference between a Poiseuille and a simple shear flow is that in the first one not only the rotational behavior but also the inertial migration should be considered while studying the behavior of a particle in the channel.

1.2.4.3.1. Rotation Behavior and Inertial Migration at Moderate Reynolds Numbers

The main difficulty in the study of non-spherical particles is that their migration is strongly coupled with their orientation and rotational regime [109]. For example, the lift component induced by the particle's rotation has an obvious influence on the transverse focusing position of the particles, which cannot be neglected [143].

In 2017, Lashgari et al. [108] were the first to study the motion of oblate particles in a microfluidic configuration where not only the equilibrium position but also the entire migration dynamics of the particle from the initial to the final position, including particle trajectory, velocity, rotation, and orientation, were investigated. The results of their numerical simulations reveal phenomena similar to those observed for spherical particles. In particular, an oblate particle experiences at moderate Re a lateral motion toward a face-centered equilibrium position so that four face-centered equilibrium positions are observed as for spheres (Figure 1.14). Likewise, oblates migrate in a two-stage process: they first migrate laterally toward a square annulus in the vicinity of the walls, and they secondly move cross-laterally in the annulus toward the four-centered equilibrium positions.

More recently, Nizkaya et al. [109] studied inertial focusing of oblate spheroidal particles in channel flow at moderate Reynolds numbers $Re = 11-44$ using lattice Boltzmann simulations. They found also that all spheroids focus on the four face-centered equilibrium positions.

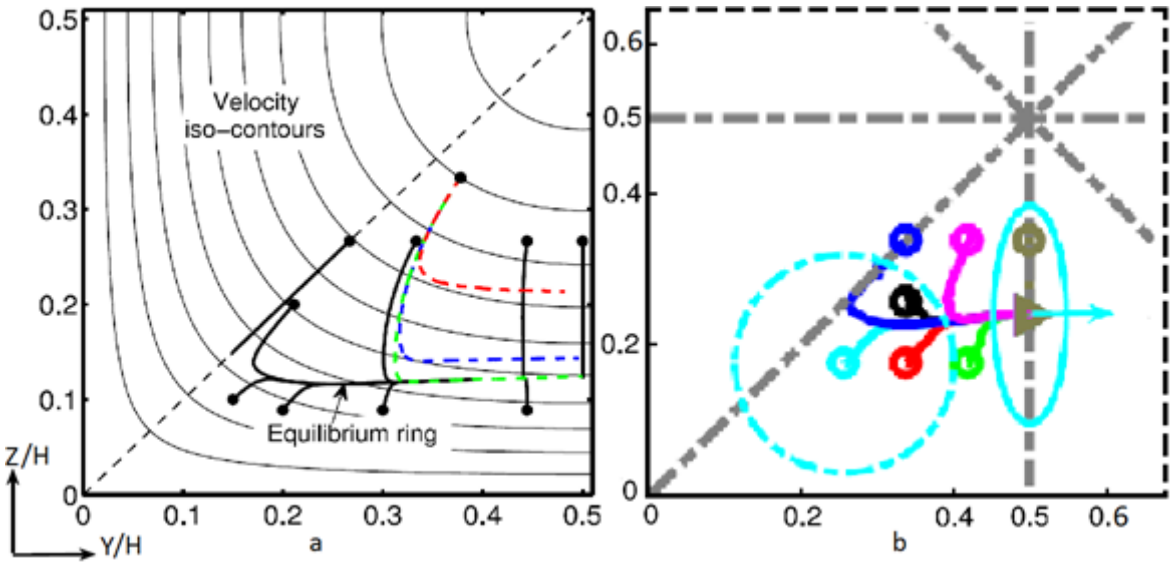

*Figure 1.14. Stages of inertial lateral migration of: (a) a sphere. The solid circles are the initial positions of each trajectory. The thick black lines are the projection of particle trajectories for $Re = 120$. The dark, mid, and light gray dashed lines (red, blue, and green) are the respective trajectories for $Re = 12{,}60$ and 120 launched from the same initial position (reprinted from [53]); (**b**) an oblate at $Re = 100$. The open circles and triangles show the initial position and final equilibria, respectively. The initial and final orientations of the oblate are shown for a particular case with the light blue solid line (reproduced from [108]).*

For cylindrical particles flowing in a square channel as well, Su et al. [144] demonstrated numerically that there are always four stable equilibrium positions for Re varying from 50 to 200. The two-stage process (cross-streamline and cross-lateral migrations) was also observed for these cylindrical particles.

While the particles migrate toward their equilibrium positions, their rotational mode changes. Pan et al. [145] showed that an ellipsoidal particle in a Poiseuille flow has a stable orientational behavior after reaching its equilibrium position: a prolate ellipsoid tumbles and an oblate ellipsoid log-rolls, as they do in a shear flow at moderate Re (Section 1.2.4.2.1.). According to [108,109], the streamwise motion of an oblate spheroid, from its initial to its final equilibrium position is coupled to a rotation around its axis of revolution (log-rolling) and a tumbling around its equatorial axis creating the already described kayaking mode. As the particle gets closer to the equilibrium position, the tumbling motion vanishes gradually, and the particle just rotates around its axis of revolution (Figure 1.15). This means that oblates start to migrate with a kayaking motion and slowly move to a log-rolling motion while getting closer to their equilibrium lateral positions. The kayaking motion is responsible for oscillations of the trajectories.

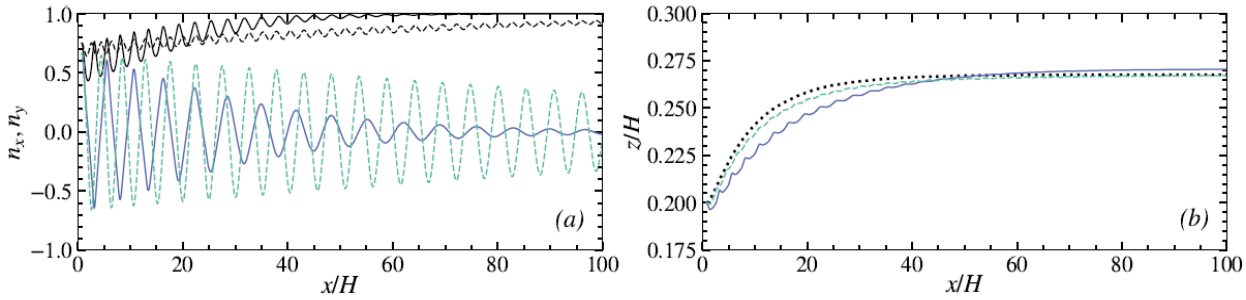

Figure 1.15. (a) x-components (colored curves) and y-components (black curves) of the orientation vector of an oblate and (b) trajectories for spheroids with $\kappa = 0.15$ and $\lambda = 0.5$ (solid), 0.8 (dashed), and 1 (dotted). Reprinted from [109].

Lashgari et al. [108] found that, on its final equilibrium position, the orientation vector of an oblate particle is parallel to the nearest wall, perpendicular to the flow. This is in agreement with the experimental findings of Di Carlo et al. [50] on the inertial focusing of particles in microchannels. Finally, at the equilibrium position, an oblate particle rotates around its axis of revolution (with zero streamwise and wall-normal rotation rates).

According to [108], the focusing length in square channels is slightly longer for oblate particles compared to spherical particles of the same volume starting from the same initial lateral position. This is mainly attributed to the presence of a tumbling motion during the migration, which reduces the lateral velocity of the oblates. However, this is not the case in rectangular channels where the focusing length is slightly shorter for oblates than for spheres. Tumbling is negligible in that case, and it has been numerically found that the lateral velocity for oblate particles is higher than that of spheres in a rectangular cross-section [108].

Unlike spherical particles [53,108], non-spherical ones oscillate while being transported in a microchannel flow. Hur et al. [110], Masaeli et al. [146], and Su et al. [144] observed that an elongated particle ($\lambda > 1$) will keep oscillating regardless of its position in the channel (still migrating or focused on an equilibrium position) (Figure 1.16). This might be due to the fact that a prolate particle prefers to tumble (see Section 1.2.4) and that, while adopting this type of rotation, the angular velocity, the sweeping area, and the distance from the wall continuously change, leading to periodical variations of the wall-induced lift force and thus a periodic motion of the particle toward and away from the wall [144]. In

the same way, Nizkaya et al. [109] showed that an oblate particle oscillates while kayaking, since the kayaking motion is a combination of tumbling and log-rolling but stopped oscillating once it is focused on its equilibrium position.

Despite this oscillatory behavior, the magnitudes of the observed oscillations are very small: around 1.25% of the particle's length [144]. It can be deduced that similarly to spheres, non-spherical particles have well-defined equilibrium positions.

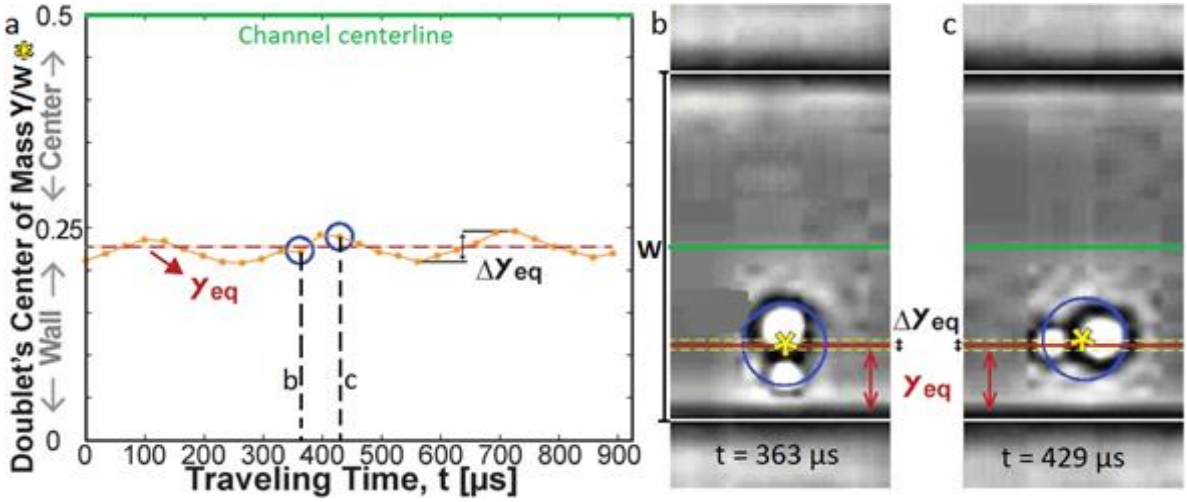

Figure 1.16. The oscillations of the center of mass of a doublet around its equilibrium position Y_{eq}. This latter is determined by averaging the values of the positions of the particle's center. Blue circles in (a) indicate the data points retrieved from the high-s speed microscopic images ((b) and (c)) taken at the corresponding times. Reprinted from [110].

Finally, to our knowledge, there exist only one study [147] that investigates the longitudinal ordering of non-spherical particles in microchannel flows. It has been shown in this recent $2D$ numerical work that, similar to spherical particles [67,80], ellipsoids interact with each other to form trains. In addition, Hu et al. [147] found that the longitudinal ordering is enhanced by increasing the particle aspect ratio, the particle volume fraction or Re, or by decreasing the confinement ratio κ.

1.2.4.3.2. Influence of Reynolds number Re

Similar to spherical particles, Hur et al. [110] experimentally observed that neutrally buoyant discs, rods, and doublets migrate toward the channel center at low Reynolds numbers ($Re < 14$). However, this behavior was observed for only a few particles so it was considered to be an unstable behavior.

For an oblate particle flowing in a square microchannel at moderate and high Reynolds numbers, Lashgari et al. [108] identified three migration regimes, as seen in Figure 1.17:

- For $Re < 150$, particles log-roll and migrate toward the four face-centered equilibrium positions, with the particles being closer to the wall with increasing Re;
- For $150 < Re < 200$, an oblate particle still focuses close to a face-centered equilibrium position but with its axis not perpendicular to the closest wall. This rotational mode resembles the inclined rolling mode reported in the dynamical system analysis of the motion of an oblate spheroid in a simple shear flow [116,121]. In that range of Re, particles still get closer to the wall when *Re* increases;
- For $Re > 200$, an oblate particle approaches one of the four standard equilibrium positions, but its orientation and rotation are time-dependent and chaotic. The rotational mode seems to be a combination of the tumbling and the log-rolling motions. This behavior of oblates was also observed by Rosén et al. [121], who showed that above a certain particle Reynolds number, the tumbling motion can be found in addition to the already existing log-rolling mode. At $Re > 300$, the particle focuses closer to the channel center.

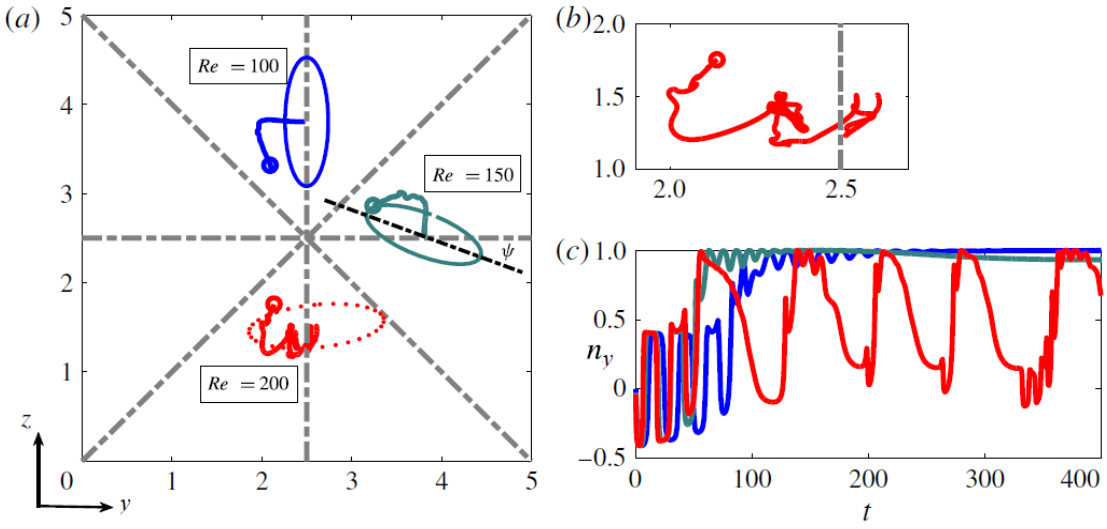

Figure 1.17. (a) Lateral trajectories of a rigid oblate particle in a square channel at different Reynolds numbers. Open circles and triangles show the initial and final equilibrium positions, respectively. The final orientation of the oblate spheroid is shown with solid and dashed (for unstable cases) lines. (b) Zoom on a particle trajectory at $Re = 200$. (c) The x-component of the orientation vector, n_x, as a function of time for the different Reynolds numbers under investigations (same color coding as in panel a). Reproduced from [108].

Similar results have been obtained for rod-like particles. In a square channel, while increasing the fluid inertia, Su et al. [144] ($Re = 50-400$) did not observe any modification in the distribution of cylindrical particles in the channel. The non-spherical particles kept their four equilibrium positions at the centers of the channel walls regardless of Re. In addition, no works showed the transition from four to eight equilibrium positions, which was observed for spherical particles (previous sections).

Moreover, Masaeli et al. [146] observed that at a fixed distance from the channel inlet, the percentage of tumbling prolate particles increased from 39% at $Re \approx 8$ to 84% at $Re \approx 20$. So, an increase in the Reynolds number increases the probability of finding a prolate particle with a tumbling rotational mode. It might be deduced from this observation that an increase in Re accelerates the transition phase from the kayaking mode to other modes (tumbling for prolates and log-rolling for oblates), lowering by that the channel length needed to reach the equilibrium rotational mode. Note that the Reynolds number has the same effect on the focusing length: when Re increases, the equilibrium positions are reached faster [110].

Finally, it has been observed that the effect of the Reynolds number on the distance between the equilibrium positions of spheres and the closest wall is the same in the case of non-spherical particles. The experimental results in [146] showed that the equilibrium positions of rod-like particles move closer to the channel wall while increasing the Reynolds number up to 200. The numerical simulations of Huang et al. [148] showed also that the focusing positions of oblate particles tend to get closer to the channel centerline while increasing Re above 200 (Figure 1.18).

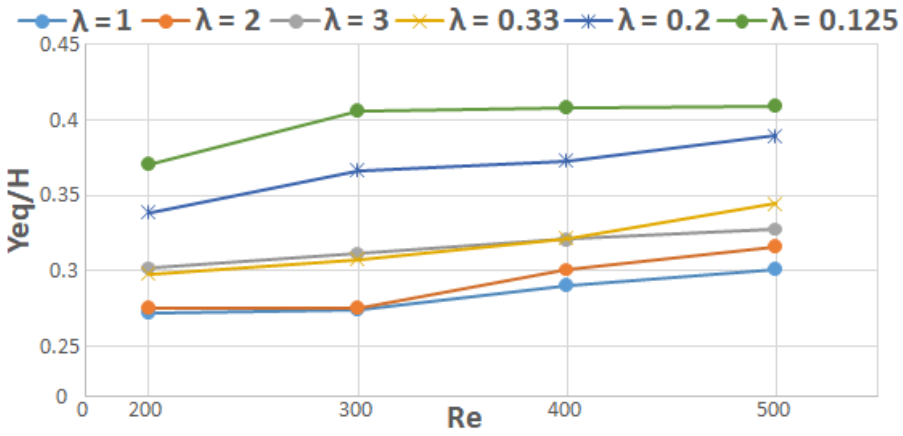

Figure 1.18. The results of Huang et al. [148] represented as the evolution of the normalized equilibrium position of an ellipsoidal particle (prolate and oblate) as a function of the Reynolds number. H is the channel's height.

1.2.4.3.3. Influence of the Confinement Ratio κ

At moderate Reynolds numbers, when spherical particles migrate toward the four face-centered equilibrium positions, it is seen that spheres get closer to the centerline when the confinement degree increases.

An "equivalent diameter" definition is needed to quantify the confinement for particles of different shapes. The definitions of this diameter vary among the different studies. Hur et al. [110] experimentally observed that the particle's equilibrium position Y_{eq} is determined by its rotational diameter d_{rot} (the longest distance between two points on the particle, which corresponds to the particle's longest axis of symmetry for most of the cases), regardless of its geometrical shape. This was shown to be true for all the tested geometries (spheres, cylinders, discs, symmetric and asymmetric doublets) except for the case of asymmetric disks (h-particles). The observations of [110] were later numerically confirmed by Masaeli et al. [146]. Thus, we chose the rotational diameter as an equivalent diameter.

Figure 1.19 represents some of the works done on the effect of the confinement ratio ($\kappa = d_{rot}/W$) on the equilibrium distance from the nearest wall normalized by the channel smallest dimension W (Y_{eq}/W). It can be deduced that the normalized equilibrium position increases with the confinement ratio, which means that non-spherical particles get closer to the channel centerline, as do spheres in the same conditions [49,67].

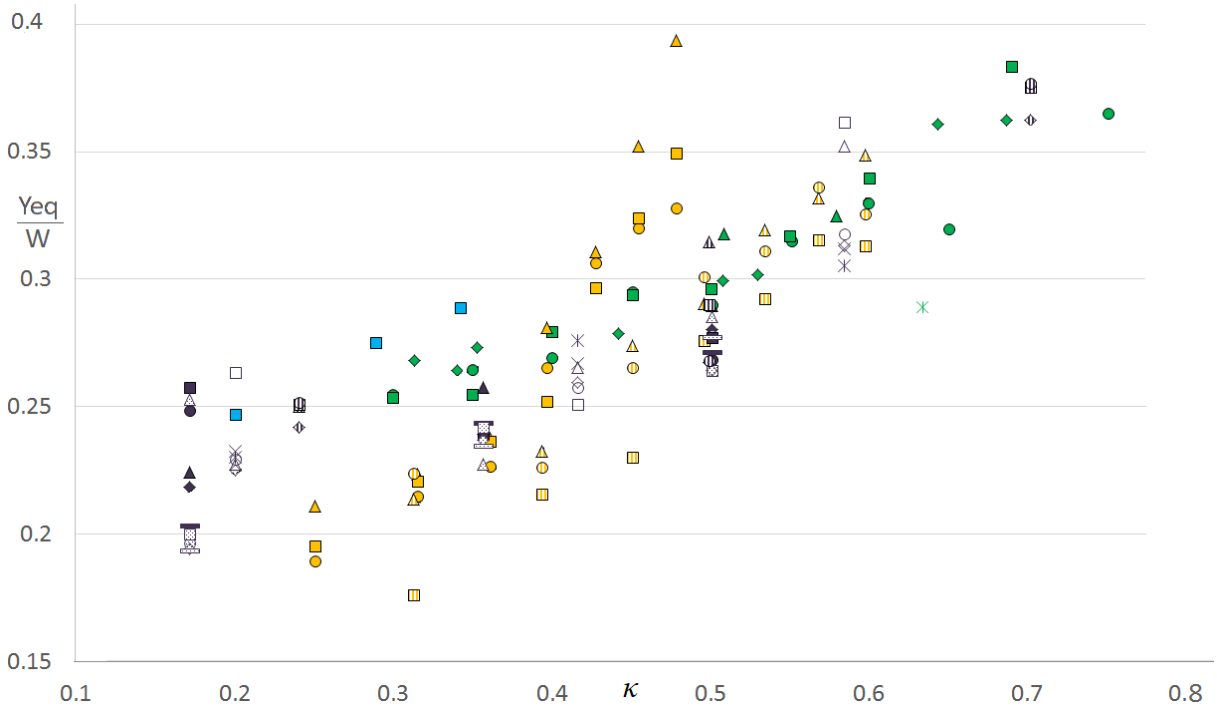

Figure 1.19. The evolution of the normalized equilibrium position Y_{eq}/W as a function of the confinement ratio κ (the normalized rotational diameter d_{rot}/W). The results are obtained by Lashgari et al. 2017 [108] (blue) [Oblate $-$ $Re = 100 - AR_c = 0.5$ (channel aspect ratio)(filled square)], Hur et al. 2011 [110] (green) [Sphere $-$ $Re = 200 - 0.6 < AR_c < 0.66$ (filled square), Disc $-$ $Re = 200 - 0.6 < AR_c < 0.666$ (filled triangle), Cylinder $-$ $Re = 200 - 0.6 < AR_c < 0.66$ (filled rhombus), Doublet $-$ $Re = 200 - 0.6 < AR_c < 0.66$ (filled circle), Asymmetric disc $-$ $Re = 200 - 0.6 < AR_c < 0.66$ (asterisk)], Li et al. 2017 [149] (yellow) [E. gracilis $-$ $Re = 205 - AR_c = 0.55$ (filled square), E. gracilis $-$ $Re = 128 - AR_c = 0.55$ (filled circle), E. gracilis $-$ $Re = 77 - AR_c = 0.55$ (filled triangle), E. gracilis $-$ $Re = 205 - AR_c = 0.45$ (dashed square), E. gracilis $-$ $Re = 128 - AR_c = 0.45$ (dashed circle), E. gracilis $-$ $Re = 77 - AR_c = 0.45$ (dashed triangle)] and Masaeli et al. 2012 [146] (purple) (Sphere/Rod $-$ $Re = 13.09 - AR_c = 0.74$ (filled triangle), Sphere/Rod $-$ $Re = 19.64 - AR_c = 0.74$ (filled square), Sphere/Rod $-$ $Re = 26.18 - AR_c = 0.74$ (filled rhombus), Sphere/Rod $-$ $Re = 32.73 - AR_c = 0.74$ (filled circle), Sphere/Rod $-$ $Re = 39.27 - AR_c = 0.74$ (dotted triangle), Sphere/Rod $-$ $Re = 45.82 - AR_c = 0.74$ (filled rectangle), Sphere/Rod $-$ $Re = 52.36 - AR_c = 0.74$ (dotted square), Sphere/Rod $-$ $Re = 58.91 - AR_c = 0.74$ (dotted rhombus), Sphere/Rod $-$ $Re = 65.45 - AR_c = 0.74$ (dotted rectangle), Sphere/Rod $-$ $Re = 72 - AR_c = 0.74$ (dotted circle), Sphere/Rod $-$ $Re = 14 - AR_c = 0.64$ (empty triangle), Sphere/Rod $-$ $Re = 21 - AR_c = 0.64$ (empty square), Sphere/Rod $-$ $Re = 28 - AR_c = 0.64$ (empty rhombus), Sphere/Rod $-$ $Re = 35 - AR_c = 0.64$ (empty circle), Sphere/Rod $-$ $Re = 42 - AR_c = 0.64$ (X), Sphere/Rod $-$ $Re = 49 - AR_c = 0.64$ (asterisk), Sphere/Rod $-$ $Re = 14.8 - AR_c = 0.53$ (dashed triangle), Sphere/Rod $-$ $Re = 22.2 - AR_c = 0.53$ (dashed rectangle), Sphere/Rod $-$ $Re = 29.6 - AR_c = 0.53$ (dashed rhombus), Sphere/Rod $-$ $Re = 37 - AR_c = 0.53$ (dashed circle)).

Concerning the effect of the confinement degree on the focusing length, Lashgari et al. [108] numerically found that the focusing length of an oblate particle decreases with increasing κ. In other words, large particles focus faster than smaller ones. This is similar to the spherical case where smaller particles need longer channels to reach their focusing positions.

Finally, Lashgari et al. [108] observed that in a square channel and for a high value of confinement ($\kappa = 1/2.43$), the migration dynamics of an oblate are completely

different. The equilibrium position is along the diagonal symmetry line, between the corner and the center of the channel (Figure 1.20). In order to explain the peculiar behavior of the large oblate in a square channel, the authors examine the rotation rate of the oblate around the streamwise direction during the migration process. Typically, during the migration stages, the angular velocity increases and then decreases. It increases due to the fast motion of the particle toward the equilibrium wall and then decreases due to the particle's slow motion toward the equilibrium position under the action of the rotation-induced lift force. The magnitude of this force is reduced when the angular velocity decreases, and the particle eventually focuses at a face-centered equilibrium position. This behavior is not observed for the largest oblates presented here. In this case, the streamwise rotation does not reduce to zero as the particle moves toward the vertical symmetry line, which accelerates the particle motion. This might occur because large oblates are more susceptible to tumbling. As a result of this acceleration, the particle crosses the vertical symmetry line and focuses on the diagonal where the streamwise rotation rate becomes zero and the shear-induced and wall-induced lift forces balance each other. This strange behavior was not observed by Hur et al. [110], who studied the inertial migration in highly confined rectangular channels and confirmed that the particles focus at the centers of the longest channel sides similarly to the cases of low κ values.

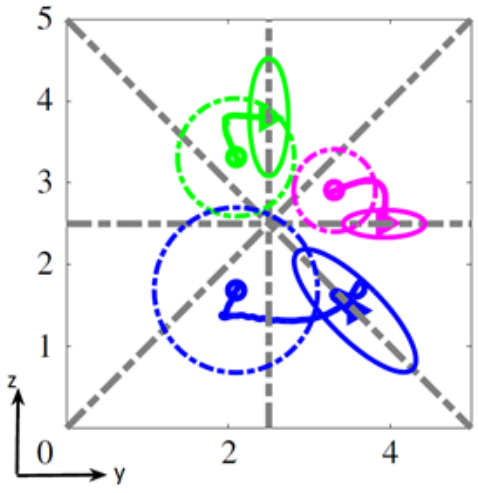

Figure 1.20. Lateral trajectories of oblate rigid particles of different sizes in a square duct at $Re = 100$. The particles have the same aspect ratio (ratio between the particle axes, $\lambda = 1/3$) and different volumes. The confinement ratios κ

are equal to 1/6.93, 1/3.47, and 1/2.43 for the pink, green, and blue particles, respectively. The values of κ are calculated using the particles aspect ratio and the equivalent volume diameters d_v (diameter of the sphere of the same volume). Open circles and triangles show the initial and final equilibrium positions, respectively. The initial and final orientations of the oblates are shown with dashed and solid lines. Reproduced from [108].

1.2.4.3.4. Influence of the Particle's Aspect Ratio λ

Figure 1.15 reprinted from Nizkaya et al. [109], present the streamwise component (colored curves) and the vorticity component (black curves) of the orientation vector (Figure 1.15a) as well as the trajectories of three oblate particles with the same rotational diameter but different aspect ratios ($\lambda_1 = 0.5$ (solid), $\lambda_2 = 0.5$ (dashed), and $\lambda_3 = 1$ (sphere) (dotted)) (Figure 1.15b). As seen in Figure 1.15a, the streamwise component of the orientation vector experiences decaying oscillations, while the vorticity component converges to unity. This confirms that oblates start with a kayaking motion (responsible for oscillations) and slowly converge to a log-rolling motion with the revolution and rotational axes aligned with the vorticity direction. As seen in Figure 1.15b, the equilibrium positions for the three oblates are very close, indicating that the equilibrium positions and the log-rolling motions are controlled by the particle's rotational diameter with a weak dependence on the aspect ratio. This result is in full agreement with the experimental findings of [110,146].

Concerning the rotational behavior, it can be observed that the oscillations vary with the value of λ, showing that the particle's aspect ratio influences the kayaking motion. For example, the oscillations of the less-oblate spheroid ($\lambda = 0.8$) decay much slower than those for $\lambda = 0.5$ (more oblate). Moreover, it can be noted that in the case studied by Nizkaya et al. [109], the particles reach their equilibrium position (Figure 1.15b) before the stabilization of their rotational mode (Figure 1.15a). This phenomenon is more pronounced when the particle aspect ratio λ is closer to 1 (spherical case).

Equation (1.3), proposed by Jeffery for the calculation of the period of rotation, indicates that an increase in the aspect ratio of the ellipsoid increases its period of rotation T. This was shown to be true by Masaeli et al. [146], who studied the behavior of elongated particles ($\lambda = 3$ and 5) in a rectangular Poiseuille flow. However, this result was not obtained by Hur et al. [110], who claimed that T is independent of λ and that it increases with the confinement ratio κ (Figure 1.21). However, the study presented in [110] was

performed on a small range of λ ($2 < \lambda < 4$). In our opinion, the work should be done on a larger interval in order to validate the obtained results.

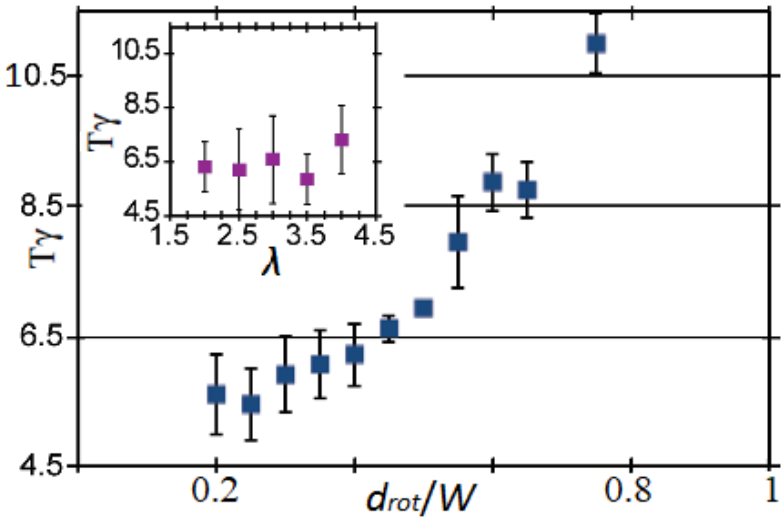

Figure 1.21. Normalized period of rotation of doublets with various size and asymmetry as a function of the aspect ratio λ (purple) and the confinement ratio d_{rot}/W (blue). Reprinted from [110].

1.2.4.3.5. Effect of Other Parameters

Other parameters, such as the particle asymmetry and its initial position and orientation, have been shown to have an influence on the rotational behavior, but the relative literature summarized hereafter is still poor regarding confined flow.

Effect of asymmetry in the particle's geometry: In the case of a shear flow (cf. Section 1.2.4.2.3), asymmetry in the particle's geometry generates chaos in its rotational behavior [141,142]. This was confirmed by Einarsson et al. in a Poiseuille flow [150,151]. However, the findings of Hur et al. [110] in a rectangular channel show that h-shaped particles (Figure 1.10.f) and axisymmetric discs log-roll in a similar way, and no chaotic behavior is observed.

Effect of the particle's initial conditions: As shown earlier, in a shear flow, when inertia is present, the effect of the particle's initial conditions is still unclear. In a Poiseuille flow, with a Reynolds number varying between 11 and 44, Nizkaya et al. [109] numerically found that oblates choose to log-roll regardless of their initial position and orientation.

1.2.5. "Shaped-based" separation

Works conducted during the last two decades on inertial focusing have shown that this technique has a great potential in terms of practical applications. The most developed application of inertial focusing of non-spherical particles is separation.

Mach and Di Carlo [152] designed an inertial microfluidic device to separate pathogenic bacteria cells from diluted blood. After two passes of the single channel system, the device removed 80% of the pathogenic bacteria and enriched red blood cells concentration four times. Two similar works were done using more sophisticated separator designs, permitting the separation of yeast cells [146] and E. gracilis [149] of different aspect ratios, with high levels of purity (more than 90%).

Although the separation in these works is presented as a "shape-based" separation, it is still not clear if the difference in the equilibrium positions is due to a change in the aspect ratio λ or in the confinement degree κ. Particles of different shapes (hence different λ) but the same volume, have indeed different rotational diameters, which thus modifies the corresponding confinement ratio. As seen in Section 1.2.4.3.3, an alteration in κ induces a change in the particle equilibrium position. Some works took advantage of this effect to perform a so-called "shape-based" separation of biological particles. Thus, complementary experiments should be performed on particles with identical κ but different aspect ratios λ to verify if they have the same Y_{eq} or not. In the case where the equilibrium positions of particles of different shapes are identical, kinetic separation based on the migration velocity could be considered, exploiting for example the observations from Nizkaya et al. [109] regarding the relation between the transitory rotational mode of the particles and their aspect ratio.

1.2.6. Summary and conclusions

Randomly introduced particles migrate laterally towards equilibrium positions and order longitudinally in the channel. These two phenomena are directly influenced by the characteristics of the flow, the particles, the fluid and the channel.

The majority of the studies investigating the inertial migration focus on spherical particles, while many real-life applications involve complex-shaped particles. So, it is necessary to understand the effect of the particle's shape on its migratory behavior in the channel. However, the transport of non-spherical particles in a microchannel is indeed much more complicated than the transport of spherical ones, since the translational and rotational behaviors are strongly coupled. Thus, it is necessary to study both migratory and rotational behaviors of non-spherical particles flowing in microchannels.

The aim of Section 1.2.4. is, by analyzing and comparing works in the literature investigating the transport of rigid non-spherical particles in a flow, to identify and summarize the main findings and remaining questions related to the behavior of complex shape particles flowing in microchannels. Table 1.1 summarizes the references dealing with suspensions of non-spherical particles cited in this chapter. These works are classified according to the studied phenomena (rotational behavior, inertial migration), the type of flow (unbounded and bounded shear flows, Poiseuille flow), and the approach adopted by the researchers (theoretical, numerical, or experimental approach).

Table 1.1. References dealing with suspensions of non-spherical particles cited in this chapter.

Studied Phenomenon	**Rotational Behavior**			**Inertial Migration**
Type of flow *Type of study*	Unbounded shear	Bounded shear	Poiseuille	
Theoretical	[111,112,114,122, 131,132,141,142]	[113,115,127,128,136]	[122,127]	-
Numerical	[117,118,132,137, 140–142]	[116,119–121,123,125,133,135,138]	[108,109,144,145, 148,150]	[108,109,144,146–148]
Experimental	-	[113,115,124,126–130,134,136]	[110,127,129,150, 151]	[110,146,149,152]

Section 1.2.4.2. covers the studies done on the rotational motions of different non-spherical particles in straight shear flows (bounded and unbounded) to identify the main parameters influencing their behavior. Table 1.2 summarizes the key conclusions.

Table 1.2. Summary of the key conclusions concerning the rotational behavior of ellipsoidal and axisymmetric non-ellipsoidal particles. Ka means "kayaking", Tu means "tumbling", LR means "log-rolling", SS means "steady state", DNC means "studies do not converge", and X means "no work identified in the literature". The papers analyzed to produce this table are listed in the second and third columns of Table 1.1.

Particle	**Ellipsoid**		**Axisymmetric**
	Prolate ($\lambda > 1$)	Oblate ($\lambda < 1$)	Rod/cylinder ($\lambda > 1$)
$\boldsymbol{Re}$ (increasing)	*Ka→Tu→DNC **	*Ka→LR→*DNC *	*Ka→Tu→SS*
Walls/$\boldsymbol{\kappa}$	No effect, if the particle is far from the wall		Low κ: no effect High κ: effect on the transition Re
Buoyancy	Effect on the transition Re		X
$\boldsymbol{\lambda}$ (getting far from 1)	Period of rotation increases		
Initial orientation	Effect is present for $Re = 0$ DNC * for $Re > 0$		X
Concentration (increasing)	X		The transition (*Ka→Tu*) occurs faster

In Section 1.2.4.3., we present the studies investigating the transport of non-spherical particles flowing in a straight square microchannel, where the lateral migration has to be considered. These different works have highlighted that in a Poiseuille flow, a particle simultaneously rotates and translates.

At moderate Reynolds numbers ($0 < Re < 150-200$ depending on the configuration), near the channel entrance, the particle undergoes a transition phase. During this transition phase, it laterally migrates toward one of the equilibrium positions located near the channel walls, and its rotational mode gradually shifts from kayaking to tumbling if its aspect ratio is above 1 (prolate spheroids, rods, fibers…) or to log-rolling if its aspect ratio is below 1 (oblate spheroids, discs…). At the end of the transition period, the particle that is focused on its equilibrium position translates solely in the streamwise direction and tumbles or log-rolls with its axis of rotation parallel to the closest wall. The channel length needed for a particle to reach its equilibrium position can be different, depending on the particle aspect ratio, from that needed to reach its equilibrium rotational mode. The particles symmetry, aspect ratio, volume fraction, confinement ratio, and Reynolds number play a major role in both the rotational behavior and the translational migration of the particles.

At higher Reynolds numbers, other rotational modes (steady state, inclined rolling…) and focusing positions can appear, but the different existing studies do not converge on these points.

Although several numerical works have studied both the rotational and translational motions of non-spherical particles flowing in square channels, there is a real lack of experimental investigations in that field. To our knowledge, solely Hur et al. [110] have published experimental data on this problem. De facto, the experimental analysis of the particles' behavior is much more complicated for non-spherical particles than for spherical ones, since a three-dimensional approach is needed to observe simultaneously the particles' position and orientation.

All the results presented in this work are essential to better understand the particles' transport in a Poiseuille flow and demonstrate that shape-based separation is possible. However, for that purpose, three important aspects still need to be clarified and should be the object of the coming works in that field:

- The particles' behavior (rotational and translational) at high Reynolds numbers (over 200), which is still a subject of discussion in the literature;
- The role of the interaction between non-spherical particles on their lateral migration and longitudinal ordering, which has been studied only by Hu et al. [147], although it has been proven to be essential in the case of spherical particles;
- The coupling between the lateral migration and the rotation of the particle during the transitional phase, which is not yet completely understood.

1.3. About the thesis

The first section of this chapter highlights the need to understand the behavior of a suspension in a microchannel flow, in order to design efficient Lab-on-chip microdevices for applications like separation or sorting of particles in suspensions.

In Section 1.2, it has been explained that this behavior is complex as it depends on many parameters, related to the channel geometry, the particles properties and concentration, the fluid properties and the flow conditions. Thus, a roadmap has been drawn for this project to reach a complete understanding of the physical mechanisms governing this

type of flow. This plan is based on progressively increasing the complexity of the studied particle-laden flows (Figure 1.22).

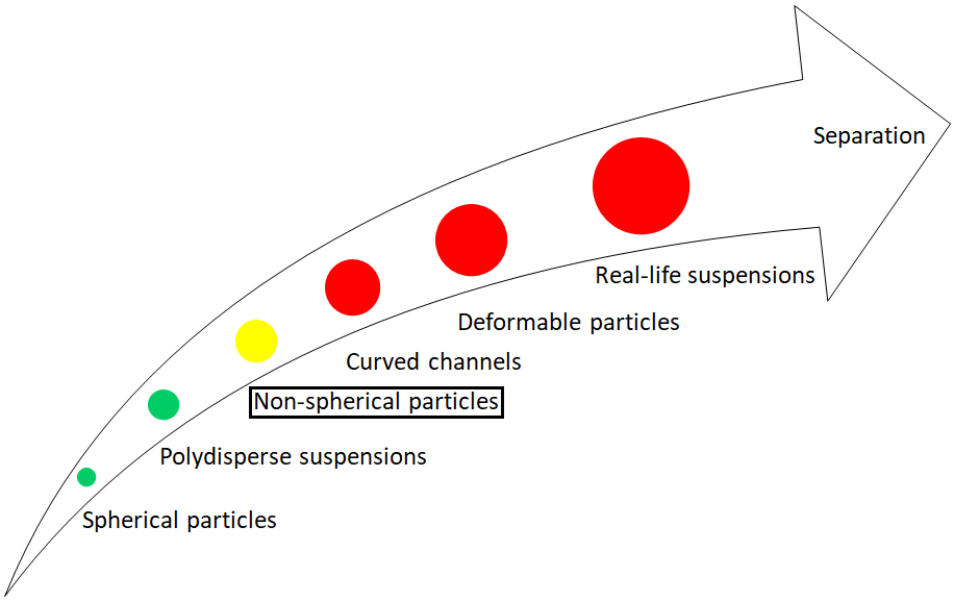

Figure 1.22. The different steps of the project.

The first step was to study, in a straight square microchannel, the behavior of spherical rigid particles in a neutrally-buoyant condition [67,80,93]. Then, Gao [67,94] studied the influence of bidispersity on the spheres' behavior. This was done by investigating the effect of the presence of spheres of two different sizes on their inertial migration.
The next stage consists of understanding the effect of the shape of the particles on their lateral migration, longitudinal ordering and rotational behavior. This corresponds to the works presented in the next chapters of this thesis.

Most of the studies, investigating non-spherical particles, are theoretical and numerical (cf. Section 1.2). So, it seemed pertinent to complete and validate these works using an experimental approach. First, a setup, based on optical microscopy, has been designed, built and tested (Chapter 2). Data acquired using this bench were processed and analyzed, with the objective to better understand the lateral migration (Chapter 3), rotational behavior (Chapter 4) and longitudinal ordering (Chapter 5) of non-spherical particles, as well as the couplings between these three phenomena.

2. Experimental setup and image processing

2.1. Introduction

As mentioned previously, the objective of this work is to experimentally study the effect of the geometry of a particle on its behavior in the channel. In order to do so, it is necessary to adopt a visualization technique which allows the particle tracking and the 3D reconstruction of the particle distribution in the channel. This will also allow to identify the main parameters defining the lateral and the longitudinal migrations as well as the rotational behavior of the particles.

2.2. Visualization technique

2.2.1. Introduction

Flowing particles can be identified and located using different techniques, depending on the properties of the particles and the objective of the study. Among the great variety of existing techniques to visualize particles in a flow [67], our team chose two methods. These methods are optical, using a light source and a camera, to illuminate the particles and capture images respectively. The choice of these techniques is based on numerous advantages that they present such as the precision and the ability to find the 3D particle distribution in the channel.

The first technique is the particle projection method [153]. In this technique, a membrane is placed under the vertical exit of the channel (Figure 2.1a). Once the flowing fluorescent particles reach the channel outlet, they mark their lateral positions on the membrane (Figure 2.1b). This technique gives information concerning the cross-sectional distribution of the particles in the channel. However, it demands fluorescent particles and cannot give information concerning the longitudinal ordering and the rotational behavior of the particles.

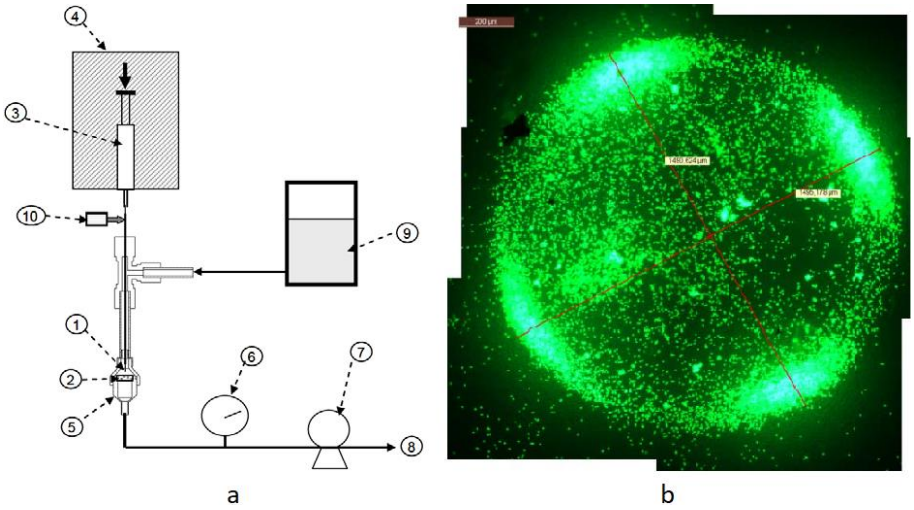

Figure 2.1. (a) Experimental setup of the particle projection method: (1) microchannel, (2) membrane, (3) stainless steel syringe, (4) syringe pump, (5) membrane holder, (6) manometer, (7) pump, (8) liquid outlet, (9) filtered water and (10) micrometric screw [153]; (b) Fluorescent image illustrating the distribution of particles in the channel cross section, a high light intensity corresponds to a high concentration of particles.

The second technique, has been developed and used by Gao [67], to visualize spherical particles and detect their locations in the channel [67]. It is an *in-situ* technique, in which the channel is placed horizontally under a microscope equipped with a CCD camera and a light source (Figure 2.2). Images are captured at different channel depths in order to reconstruct a $3D$ particle distribution in the channel.

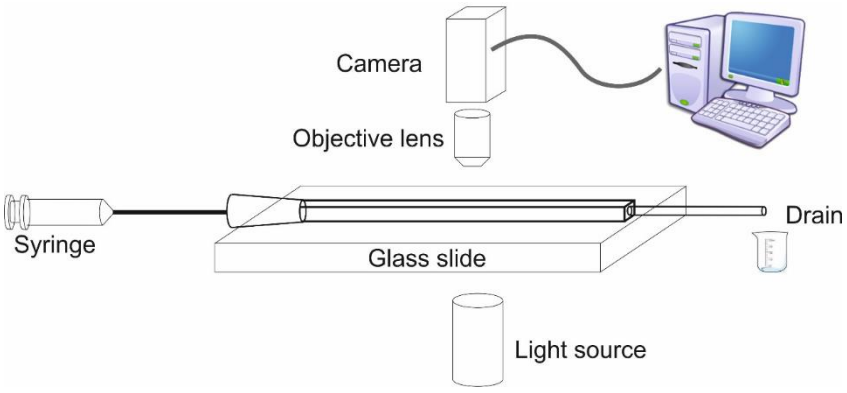

Figure 2.2. Experimental setup of the in-situ visualization method [67].

The *in-situ* technique, developed by Gao in 2017 [67] is precise and can be applied on a large range of Re. However, it has two major limitations. The first one concerns the light source which is normally a part of the microscope, and does not always supply enough light to illuminate the flow. The other constraint is the difficulty in identifying the orientation and rotational behavior of the particles.

To surpass these limitations, a new experimental setup, based on the previously described technique, has been developed and tested. This new setup does not require any microscope, which makes the apparatus flexible and adaptable to different experimental conditions. In addition, the new setup allows to modify the utilized camera, in function of the type of the study, such as implementing a fast camera capable of tracking the rotational behavior of the particle in the channel.

2.2.2. Apparatus

The equipment constituting the experimental apparatus can be divided into three main parts: the fluidic system, the optics, and the mechanical system.

In the fluidic system are found the microchannel, the suspension and the pump. Each straight borosilicate microchannel (VitroTubes™) has a square cross-section, an internal height of 80µm and a length in the range 10 to 60cm. It is glued to glass slides and to 1mm diameter tubes at its inlet and outlet (Figure 2.3).

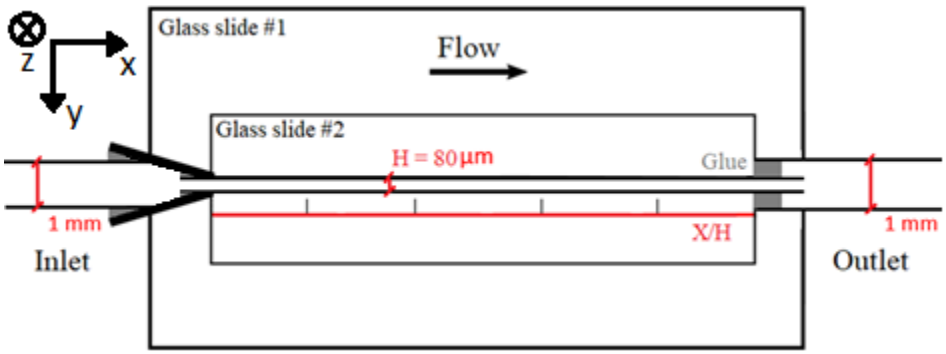

Figure 2.3. Schematic representing the channel, that is glued to the glass slides and the larger tubes.

The neutrally-buoyant suspension contains polystyrene particles ($\rho_p = 1050\ kg/m^3$) and a suspending fluid. Table 2.1 shows the properties of different particles studied in this work. The suspending fluid is a mixture of 80.27% distilled water and 19.73% glycerol (in volume fraction). The result of this combination is considered a Newtonian incompressible fluid that has a density ρ_f equal to that of the particles ρ_p, and a dynamic viscosity $\mu_f = 0.0015cP$ at room temperature [64] (Appendix B).

Table 2.1. Properties of the studied particles. See Appendix A for more details.

Name	Type	Geometry	d_{rot} (μm)	d_{min} (μm)	λ	Figure
$PNT35$	Peanut	Symmetric doublet	5.1	3.4	1.5	
$PNT57$			7.7	5.1	1.509	2.4.a
SNW	Snowman	Asymmetric doublet	15.4	12.8	1.195	2.4.b

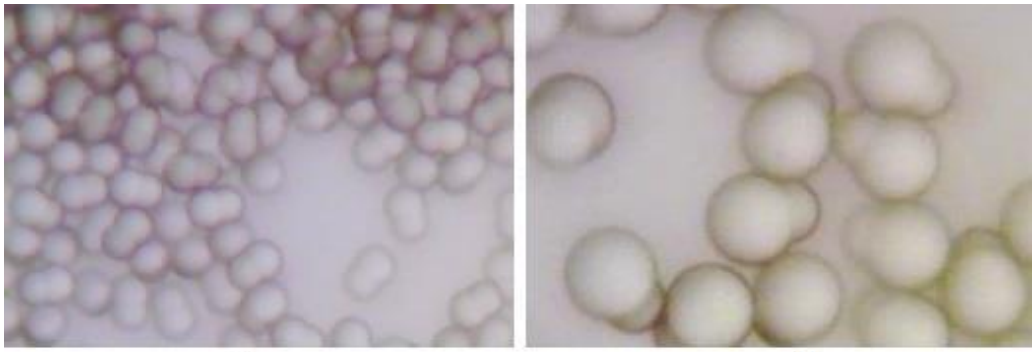

Figure 2.4. (a) $PNT57$ and (b) SNW particles. The images are provided by the supplier (Magsphere Inc.).

A Harvard Apparatus PHD 400 syringe pump generates a laminar flow at a volume flow rate Q varying from 2 to 2000$\mu L/min$, corresponding to Reynolds number Re values ranging between 0.29 and 290. In function of the desired flow rate, one of three stainless steel syringes is used. These syringes have different volume capacities (8, 20 and 50mL), corresponding to a syringe's diameter of 9.525, 19.13 and 28.6mm respectively.

The visualization is ensured by a high intensity illuminator (Fiber-Lite MI-150) and a CCD camera (Sensicam QE), equipped with an objective lens (x20 or x40). The total magnification can be increased by placing an optic tube between the lens and the camera. This last one has a high resolution (1376 x 1040 pixels) and a constant frame rate FR of 10 frames per second (fps). In addition, this camera is recommended for experiments with a wide range of Re, thanks to its wide range of exposure time (500ns to 3600s). The camera is linked to a computer on which the corresponding software (Camware) is installed. The captured images are saved, then processed using MATLAB (detailed in the next section). When a high value of FR is required, the Sensicam QE camera is replaced by a Photron APX or a Photron SA5, where a large range of frame rates is covered (FR between 50 and 120,000fps).

The motion of the equipment and the stability of the system are guaranteed by a four-sided aluminum structural optical rail, three rail carriages, three ball bearing linear stages equipped with micrometer heads, two lab jacks, a 90 degrees angle bracket, an optical mount and two variable-height bench legs. These tools were supplied by Newport™.

The experimental apparatus consists of three main parts (Figure 2.5). Each one is attached to a rail carriage which allows big displacements on the optical rail (Z direction). The whole system stays perfectly horizontal thanks to the bench legs.

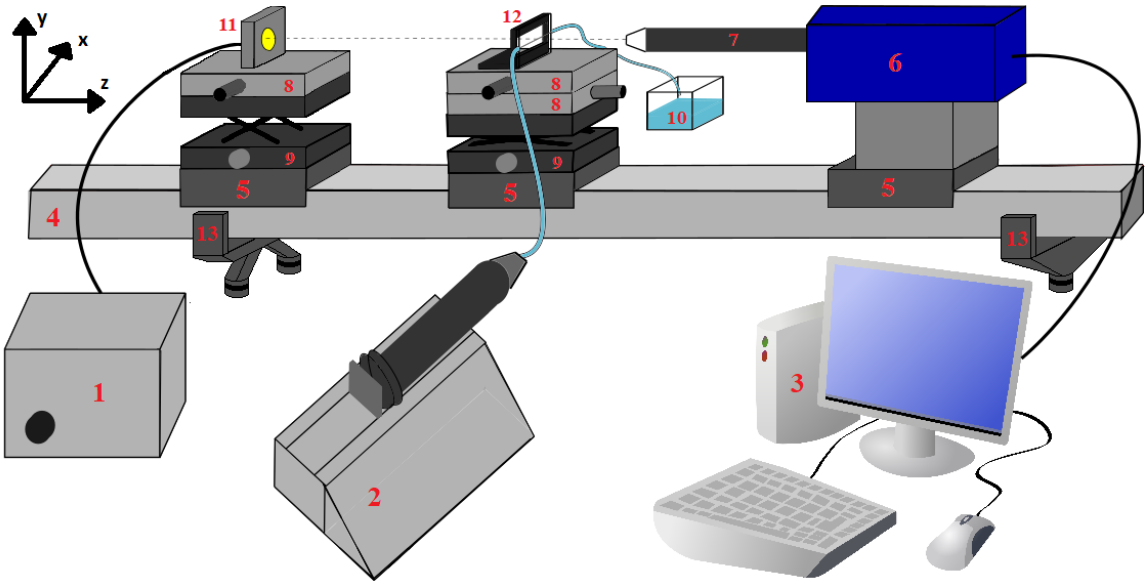

Figure 2.5. Schematic illustration of the experimental apparatus: (1) the light source, (2) the syringe pump, (3) the computer with the corresponding software, (4) the rail, (5) the rail carriages, (6) the camera, (7) the optic tube, (8) the linear stages and their micrometer heads, (9) the lab jacks, (10) the drain, (11) the optical mount, (12) the 90° angle bracket (on which the channel is fixed) and (13) the bench legs.

In the first part is found the camera.

The second unit consists of the lab jack, two linear stages, the bracket and the channel. The jack is used to change the channel's vertical position (Y direction), in order to get it in the frame of the camera. On this jack, the linear stages are mounted. These two are linked to micrometer heads controlling the channel's micrometric fine displacements along the X and Z directions. The bracket holding the microchannel is fixed on the top stage. Its role is to ensure the orthogonality between the channel's flow axis and the

camera's axis, as well as the parallelism between the channel's (XY) plane and the camera's plane of focus.

On the last carriage figures the mount holding the light source's cable. The X and Y positions of the optical post are respectively controlled by the lab jack and the linear stage (linked to a micrometer head).

2.2.3. Protocol

Tests are done on suspensions of different types of non-spherical particles and volume fractions Φ, at different flow rates Q, channel depths Z/H, and distances X/H from the channel's inlet. The concentrations in this study are chosen in a way to have the same number of particles per volume as the spherical suspensions used by Gao et al. [67,80,93].

The equivalent concentration Φ_{eq} indicates the particle volume fraction of the spherical suspension, that has the same number of particles. Using Φ_{eq} simplifies the comparison between the spherical and non-spherical results.

The calculation of the suspension composition as well as the suspension preparation are detailed in Appendix B.

Once the experimental apparatus is ready, the prepared suspension is inserted in the syringe. Then, the luminosity is increased progressively to avoid causing any damage to the camera. After choosing the flow rate and turning on the pump, a certain time should be considered before the image acquisition starts. This waiting time is necessary for the suspension to fill the channel (and the inlet linking tube). It varies between few seconds and one hour, in function of the chosen flow rate.

As mentioned earlier, the objective of this experimental study is to understand the effect of the particle's geometry on the lateral migration, the longitudinal ordering and the rotational behavior in the channel. Studies done using the apparatus described above can be either statistical or for particle tracking. The type of the study does not require any alteration in the apparatus other than the choice of the camera and its frame rate. If the

study is statistical, the same particle should not appear on more than one image. However, if the objective is to observe the behavior of the particle by following it, then it should appear on more than one image. Thus, it can be deduced that FR should be chosen in function of the particle's velocity and the type of the study.

Another parameter to take into consideration is the exposure time, i.e., the time during which the camera captures light to collect data (Figure 2.6). Decreasing the exposure time gives a neater image, in which the particle seems to be immobile in the channel (Figure 2.7b). However, at a low exposure time, a loss in the image's brightness occurs, requiring a stronger amount of light from the light source.

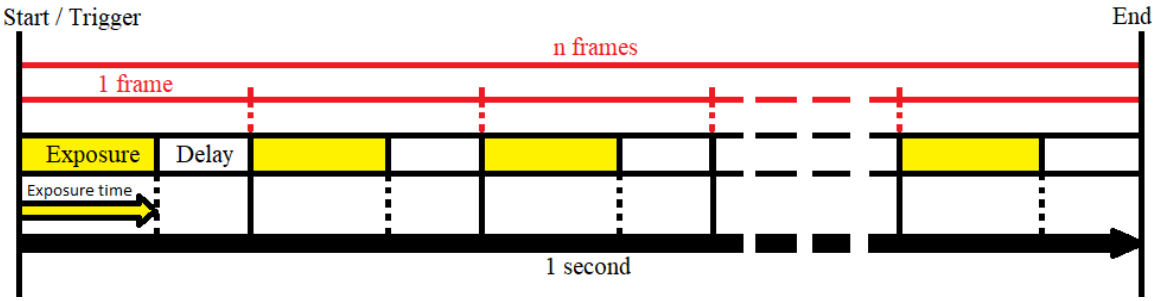

Figure 2.6. Schematic illustrating the process of image capturing during one second ($FR = n\ fps$).

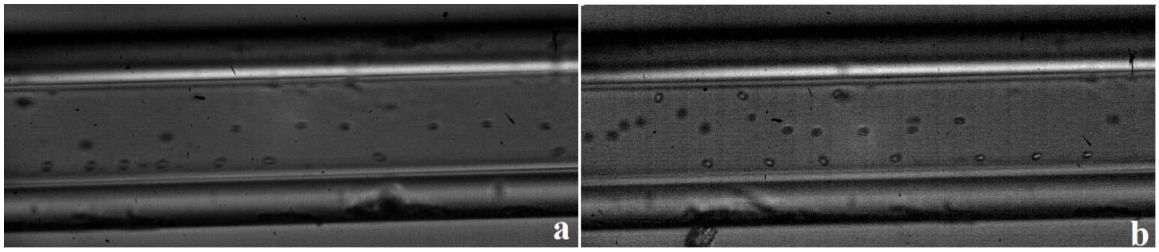

Figure 2.7. Images captured at (a) high (5µs) and (b) low (2µs) exposure times, for a PNT57 suspension flowing at $Re = 58.4$

Finally, it should be mentioned that, for each test, 2000 captured images are considered enough for the statistical study. This value was found by Gao in 2017 [67], for similar experimental conditions. In fact, for a fixed configuration, he observed that the statistical analysis of the particle distribution in the channel was converging from a number of images equal to 2000.

2.2.4. Validation tests

Various tests have been done to validate the developed experimental apparatus and protocol, such as the measurement of the depth of the channel and that of the focal

plane, the verification of the orthogonality and the alignment between the different components of the setup and the effect of the channel's walls on the visualization.

2.2.4.1. Channel depth

The objective of this test is to experimentally validate the relation between the displacement of the channel (Z axis) and that of the focal plane. This would help locate the midplane of the channel ($Z/H = 0.5$), in which the majority of the tests are done.

For a fixed channel and a moving lens, based on Descartes-Snell's refraction law, Barrot et al. [154] deduced a relation between the displacement of the focal plane δ and that of the lens δ_l:

$$\delta = \delta_l n_o / n_i \qquad (2.1),$$

with n_i being the refractive index of the medium in which the lens is immersed ($n_i = n_{air} = 1$) and n_o the refractive index of the observed object.

In this study, the channel focal plane has to pass through layers of different heights and refractive indexes (Figure 2.8). The total depth of the channel is 160μm, corresponding to $H = 80\mu m$ for the inside and $H_{wall} = 40\mu m$ for each borosilicate wall ($n_{glass} = 1.517$).

The test was done using only the suspending fluid inside of the channel. In fact, it is supposed that the particles have no effect on the refractive index of the suspension, since the particle concentration is relatively low (less than 0.2%). The suspending fluid is a mixture of distilled water ($n_{water} = 1.333$ and 80.27% volume fraction) and glycerol ($n_{glycerol} = 1.472$ and 19.73% volume fraction). The refractive index of this mixture is found to be $n_{mixt} \approx 1.36$ [155].

By applying the equation (2.1) on the walls and the inside of the channel, the displacement of the lens for a 160μm focal-plane displacement is obtained:

$$H_{wall} = \delta_{l\text{wall}} n_{glass} / n_{air} \rightarrow \delta_{l\text{wall}} = 26.37\mu m,$$
$$H = \delta_{linside} n_{mixt} / n_{air} \rightarrow \delta_{linside} = 58.82\mu m,$$
$$\delta_{lT} = \delta_{l\text{wall}} + \delta_{linside} + \delta_{l\text{wall}} = 111.56\mu m.$$

It can be deduced that, to move the focal plane a distance of 160μm, the channel needs to be moved by 111.56μm in the Z direction.

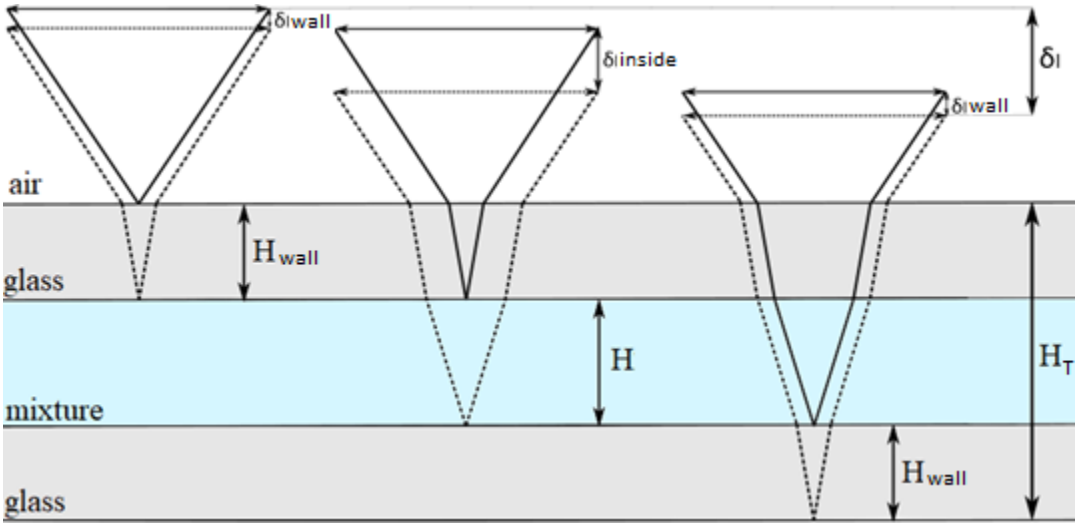

Figure 2.8. Schematic representing the link between the channel displacement and that of the focal plane.

This calculation was verified experimentally. Two marks were drawn, perpendicularly to the channel, one on the top wall of the channel and another one on the glass slide on which the channel is fixed. In order to be able to differentiate between the bottom of the channel and the surface of the slide, the second mark covers all the width of the channel and some millimeters of the slide (Figure 2.9). Three zones are defined: (a) on the channel, (b) under the channel and (c) on the glass slide. The distance between the two zones (a) and (c) is equal to that between (a) and (b), corresponding to the channel's total height $H_T = 160\mu m$.

Validating the theory, it was observed that, a total displacement of the channel of 162μm was needed to pass from (a) to (c), while 112μm were sufficient to scan the whole channel (from zone (a) to (b)) (Figure 2.9).

Note that, the same test was done using an empty channel ($\delta_{linside} = H = 80\mu m, n_{air} = 1$), and a total displacement of 134μm was needed to scan the channel.

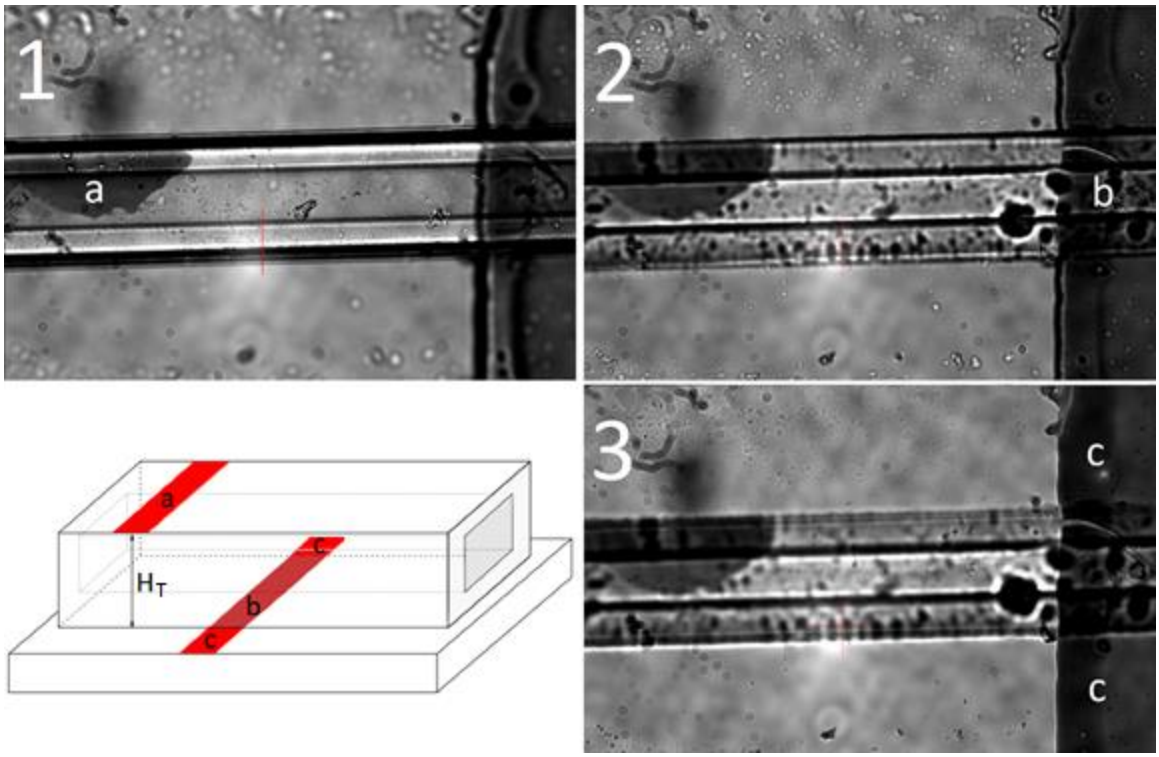

Figure 2.9. Schematic showing the three marks on the channel. The zones (a), (b) and (c) are in the plane of focus in the images (1), (2) and (3) respectively.

2.2.4.2. Focal plane

On the captured images, particles with and without central bright points are observed (cf. Figure 2.7.b). According to many previous experimental studies [156], particles with a bright point are in focus and those without a bright point are out of focus. In other words, the brightness of the particle represents its relative position with respect to the focal plane.

In the case of spherical suspensions, Gao [67] experimentally found that the bright point is located at the particle's edge that is opposing the light source. This means that the identified bright plane is shifted from the focal plane by a distance equal to the particle's radius, in the opposite direction of the light source (Figure 2.10).

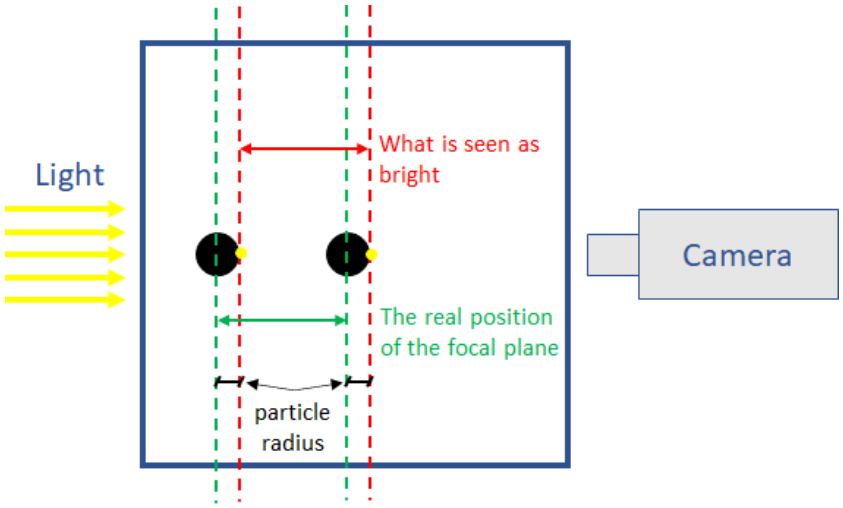

Figure 2.10. Schematic showing the location of bright points in the spherical case, and illustrating the relative positions of two spheres with respect to the focal plane. The two spheres are located on the left of the edges of the focal plane. The distance between two lines of the same color correspond to the depth of measurement (explained later).

For the tested non-spherical particles (PNT and SNW), it has been observed that the characteristics of the bright points are in direct link with the orientation of the particle's main axis with respect to the focal plane. For example, two bright points are present when the particle is parallel to the focal plane (Figure 2.11). The sizes of these two bright points, as well as the distance separating them, change in function of the particle's location and orientation. When the particle is perfectly perpendicular to the focal plane, only one bright point, in the center of the circular projection of the particle, is identified, similarly to the spherical case.

A more detailed study on the link between the characteristics of the bright point(s) and the position and orientation of the non-spherical particle could not be done due to the difficulty in the control of the particle's orientation in the channel during the image acquisition. So, for non-spherical particles, it has been assumed that, in a similar way to spheres, the bright point is also at the particle's edge that is opposing the light source.

As defined by Gao in 2017 [67], the depth of measurement is the maximal distance between the nearest and the farthest simultaneously identified in-focus particles (Figure 2.10). Knowing the depth of measurement gives the number of planes required to scan

all the channel. Using an experimental approach, Gao [67] found that, in his operational conditions, the depth of measurement is equal to 10µm.

Using the same channel, suspending fluid, camera and optical technique, the experiment of Gao is reproduced by scanning a static non-spherical particle in the channel and identifying the depth of the plane, in which the particle is not blurry (Figure 2.11). The obtained depth of measurement is also equal to 10µm.

*Figure 2.11. Scan of a static $PNT57$ (5.1µm*7.7µm) particle in the channel. The difference between two consecutive images is equal to a lens displacement of 2µm. The particle appears to be non-blurry for a lens displacement corresponding to a depth of field approximately equal to 10µm.*

2.2.4.3. Orthogonality and alignment

The orthogonality between the channel and the camera's axis is first checked by verifying, without calculation, the heights of the channel walls. In fact, a clear difference of heights between the upper wall and the lower one means that the channel's axes Y and Z do not align with the experimental setup's axes Y and Z respectively. On the other hand, a difference of heights between the right side and the left one indicates a deviation of the X and Z axes of the channel from those of the setup (cf. Figures 3.3 and 3.5).

Once the images are captured, the orthogonality is validated, by evaluating, on a captured image, the height of both walls (upper and lower) from both sides (right and left). The channel, supposed perfectly fixed to the glass slide, is considered orthogonal to the camera's axis when the four heights are equal.

Once the orthogonality between the channel and the camera is verified, the alignment between the light source and the camera's optical axis is checked. At the distances between the light source and the camera that the apparatus imposes, the contour of the light source appears on the image. It creates four black arc-shaped spots on the corners of the image (or a black contour if the light source is far enough from the camera). These

spots have to be identical and symmetrical in order to consider the camera and the light source aligned.

It can be noted that, this alignment can be also manually checked with a small lab laser. This latter is placed at the lens of the camera, parallel to the main rail, and the optical mount ((11) in Figure 2.5) is moved using the lab jack and the linear stage, until it is aligned with the light of the laser.

2.2.4.4. Image distortion

As explained in the previous chapter, the spacing between the particles is an important parameter in the study of the longitudinal ordering. So, it is essential to verify that the channel borosilicate walls, have no effect on the (XY) plane. In other words, it is necessary to check that the presence of the channel walls does not influence the distances between the particles by distorting the images.

This test was done by Gao in 2017 [67], using the same microchannels. A grid distortion test target was placed behind the channel, and an image of the target was captured. Then, this image is compared to another one, taken in the absence of the channel. The two captured images were identical, confirming that the channel walls do not affect the visualized suspension in the (XY) plane.

2.3. Image processing

2.3.1. Introduction

In this section, the image processing technique, used to extract data from the captured images, is presented. The objective of this technique is to identify all the particles as well as their positions and orientations in the channel. Transforming this data into plots and histograms (next section) is needed to study the translational and rotational behaviors.

The position of the particle in the plane of the camera ((XY) plane) can be easily identified. By comparing the location of the particle's centroid to that of the channel wall, the particle's position in the channel is calculated. The brightness of the particle gives

information concerning its relative position with respect to the camera's focal plane (Z direction).

The angle between the projection of the particle in the (XY) plane and the flow direction can be also identified.

The image processing is done using a developed MATLAB code, mainly based on the image processing toolbox and other basic functions. This code can be divided into seven essential parts: (i) the grey level mean value adaptation, (ii/iii) the background calculation and extraction, (iv) the binarization, (v/vi) the particles and the walls identification, and (vii) the particle localization.

2.3.2. Grey level mean value adaptation

As a consequence to the change in the luminosity, the captured images are found to have different grey level mean values ($GLMV$). This instability complicates the image processing, especially during the image-background comparison step (explained later). To avoid this problem, a transformation is applied to the 2000 images, by setting one common $GLMV$. The simplest and fastest way to do so is by translating all the images to the $GLMV$ of the first image: the difference Δ_i between the $GLMV$ of the first image and that of an image i is added to the grey level of every pixel of this image ($\Delta_i = GLMV_1 - GLMV_i$).

Two questions have been raised: can the luminosity variation be recovered with a simple translation as described above? Due to the difference in mediums crossed by the light, is the transformation needed for the channel area different than that needed outside of it?

In fact, to be sure that a translation is sufficient, it is necessary to verify that the difference between the grey levels of two chosen pixels on the same image, remains constant on all the other images. Figure 2.12 resumes the test done on three chosen pixels: P_1 (outside the channel), P_2 (on one of the walls) and P_3 (inside the channel).

As a first step, the grey level of each one of these pixels is identified on the 2000 images. Then, three 2000-element-vectors are created (V_{12}, V_{13} and V_{23}). In these vectors are

found the differences between the grey levels of the chosen pixels on the 2000 images (step 2). Note that, there is a possibility that a particle occupies the pixel P_3 in some images. This would affect the calculation, since the grey level of a pixel occupied by a particle is very high or very low, depending on the relative position of the particle with respect to the plane of focus. To eliminate this error, the elements of the influenced vectors (V_{13} and V_{23}, where P_3 is present) are sorted from smallest to largest, then the first and last 25% of these values are removed (step 3). Next, the mean values of the three vectors are determined (step 4). Finally, for each element of the three vectors, the error is calculated by subtracting the vector's mean value from the value of the element (in absolute value), and dividing the result by the highest attainable grey level value (255) (step 5).

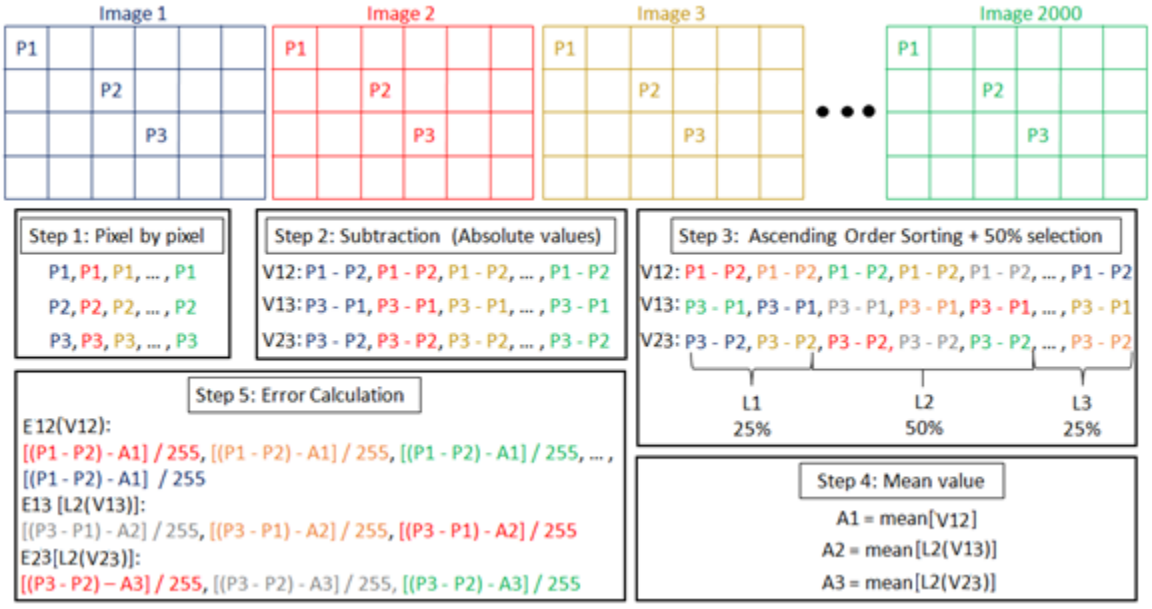

Figure 2.12. Schematic resuming the error calculation test, done for the pixels P_1, P_2 and P_3, over the 2000 images.

Figure 2.13 shows three histograms representing the normalized number of elements in function of the calculated error for the three vectors. The mean errors of V_{12}, V_{13} and V_{23} are relatively 0.99%, 0.41%, and 0.46%, while the maximum errors are 3.4%, 0.89% and 1.04% respectively. It can be also shown that, the highest calculated errors belong to V_{12}, the vector comparing the grey levels of P_1 and P_2. This is considered acceptable, since the main objective of the image processing is to study the inside of the channel, and since

selection criteria are imposed in further steps to remove all remaining non-particle areas. Concerning the elements of V_{13} and V_{23}, the calculated errors are low and do not affect the image processing. Thus, it is deduced that a simple translation is sufficient to adapt the images at the same $GLMV$.

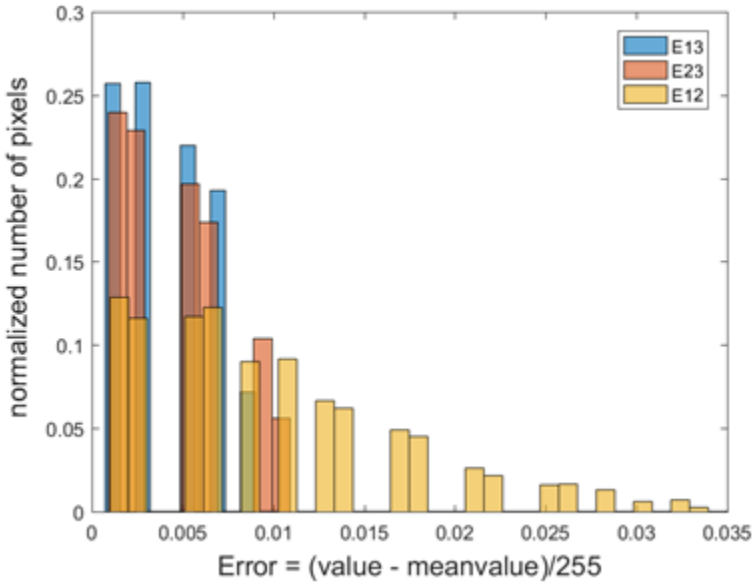

Figure 2.13. The pixel distribution in function of the calculated errors E_{12}, E_{13} and E_{23}.

2.3.3. Background calculation

The second step of the code is the background calculation. The background corresponds to an image of the microchannel without particles (Figure 2.14b). The grey level of a pixel P of the background is equal to the mean value of the grey levels of this same pixel on the 2000 images. The background is calculated by adding all the adapted images, then dividing the result by the number of images (2000).

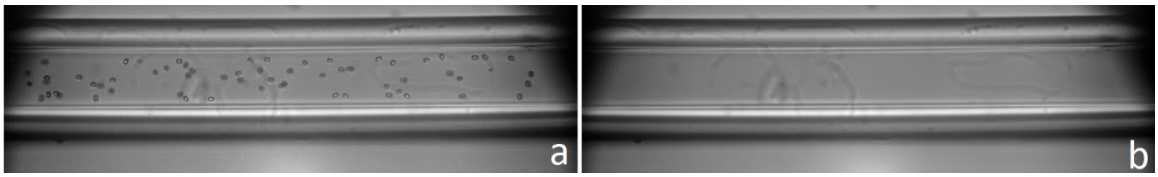

Figure 2.14. (a) A random captured image and (b) the corresponding calculated background.

An important question concerns the effect of the presence of the particles in the channel on the background's calculation. In fact, the grey levels of the pixels occupied by a particle are higher or lower than the channel's "ordinary" grey levels. These extreme values can

influence the calculation of the mean value, thus changing the resulting grey level of the background's pixel.

To check if this influence is significant, the following test was done. First, 2000 images of a highly concentrated suspension were captured. Then, the 2000 grey levels of each pixel are identified and sorted. Next, the mean, the 25% truncated mean and the error are calculated for each pixel. The error is equal to the difference between the two means (in absolute value) over 255.

It should be mentioned that, this test consumes a huge amount of time, since 2000 grey levels should be identified and sorted for each pixel of the image. To reduce the calculation time, the test was done on half of the pixels of the channel region (total number of studied pixels = 50544).

Figure 2.15 shows the distribution of the studied pixels based on the calculated error. It can be observed that the maximum error is around 0.3%. Thus, it can be deduced that the influence of the particles on the background calculation can be neglected. In addition, it is concluded that finding the background by adding the images and dividing the resulting image by 2000, is precise (low error) and faster than the truncated-mean calculation since there is no need to identify and sort the grey level values.

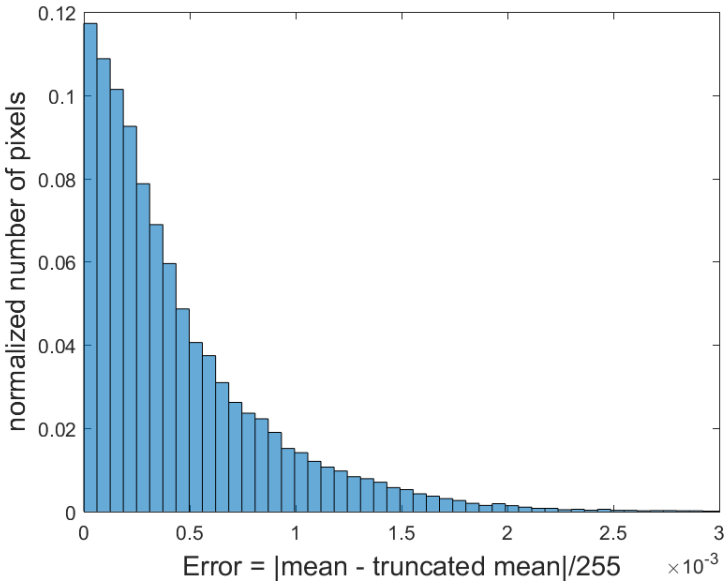

Figure 2.15. The pixel distribution in function of the calculated error.

2.3.4. Background extraction (Image/Background comparison)

Once the background is obtained, the particles are isolated by extracting the background from the adapted images. This is done by subtracting the calculated background from the adapted image, producing a new image ideally containing only the particles (Figure 2.16).

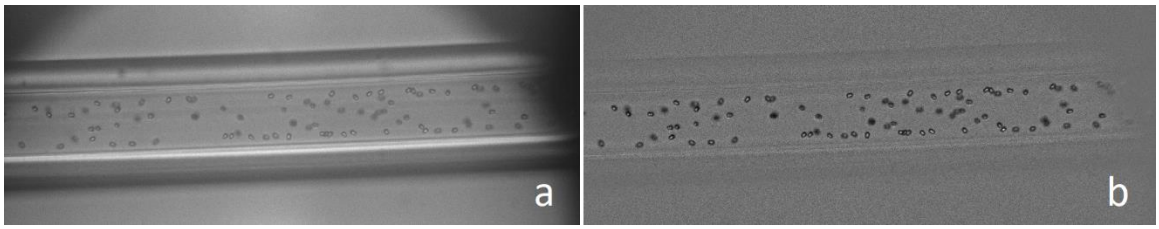

Figure 2.16. (a) A random captured image and (b) the corresponding subtracted image.

2.3.5. Binarization

An easy way to fully isolate the particles is by binarizing the subtracted image. A threshold grey level is tested then fixed. Pixels with grey levels higher than this critical value are transformed into white pixels, while those with grey levels lower than the threshold, become black. Following this strategy, the new image has a white background with black particles on it (Figure 2.17b). Some of the particles have white spots in them, indicating that they are in the camera's focal plane (bright particles). The rest of the particles are considered non-bright particles).

It should be mentioned that, the particles that are very far from the plane of focus, have normally grey levels close to those of the background. This might causes eliminating them while binarizing. The threshold is adapted in a way that the maximum number of these particles still exist on the binarized images.

2.3.6. Particle identification

To identify the particles, the function *regionprops* is used. It gives a set of characteristics of identified objects/regions in binary images. In this work, the properties of interest are: the location of the center of mass (centroid), the major axis length, the minor axis length, the area (the number of black pixels), the filled area (filled area = area + white pixels inside the region) and the angle between the major axis and the horizontal.

However, not all of the identified regions are particles. Some of them are spots caused by a local luminosity variation or by a sudden vibration of the system. In addition, the interactions between the particles enhance the formation of aggregates (bigger solids), that should not be taken into consideration while identifying the particles. To eliminate these regions, size and shape criteria are imposed. The identified region should have an area and an aspect ratio (major axis length/minor axis length) falling in certain intervals that vary in function of the studied particles. If it is not the case, the identified object is not considered as a particle and is eliminated (Figure 2.17).

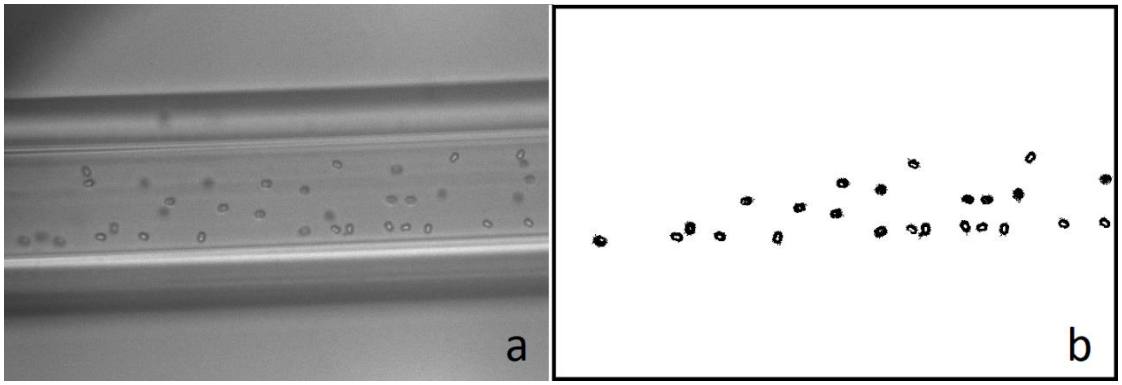

Figure 2.17. (a) A random captured image and (b) the corresponding binarized image.

The remaining identified regions are considered as particles. They can be with or without bright points, which is respectively decided by the presence or absence of white pixels inside the particle. To quantitively differentiate between them, the ratio (area/filled area) is calculated. Its highest value is 1, corresponding to out-of-focus particles (no bright point). If this ratio is lower than 0.9, the particle is considered to be in the focal plane. In other words, a bright particle has a white point that occupies more than 10% of its filled area. Otherwise, the particle is considered to be out-of-focus. This value was chosen after looking at different particles, and judging if they were considered bright or not.

Centroid identification

When the main axis of a SNW particle is inclined with respect to the focal plane (Figure 2.18), the projection (green triangle) of the particle's centroid (C, black X) might be different from the centroid of the particle's projection (red asterisk, identified during the image processing). This is due to the asymmetry along one of the axes of the SNW, and might induce errors in locating the particles, which modifies the particle distribution.

Using the geometrical properties of the SNW particle (Appendix A), the angle between the line (AB) and the particle's main axis (DE) is calculated (around 31°), and the position of the centroid of the particle is found ($CD = 6.96\mu m$, $DE = 15.3\mu m$)(Figure 2.18). The deviation between the triangle and the asterisk is calculated and found to be equal to $0.288\mu m$, negligible in front of d_{rot} ($d_{rot} = 15.3\mu m$).

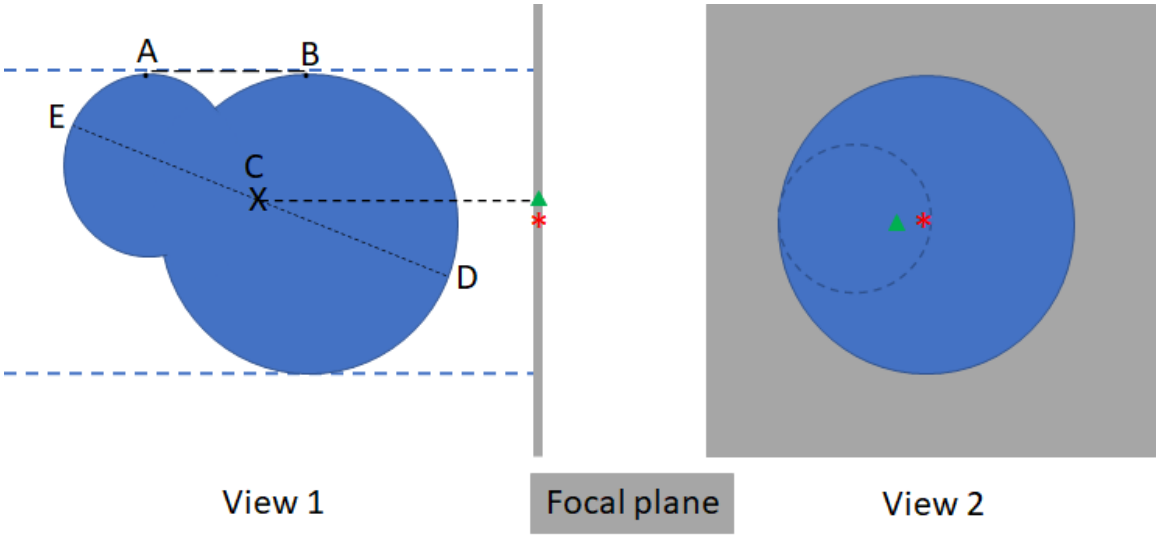

Figure 2.18. Schematic showing a SNW inclined particle, projected on the focal plane.

2.3.7. Wall identification

To identify the position of the particle in the channel, it is necessary to locate the channel walls. This is done by locating manually four points A, B, C and D on the calculated background (Figure 2.19). The points A and C belong to the upper wall, while B and D are on the lower one. These points are chosen to be on the outer sides of the walls, due to the complexity in the visual identification of the inner sides. The walls are considered well identified when the distances AB and CD are identical, and when the slopes of the lines AC and BD are equal.

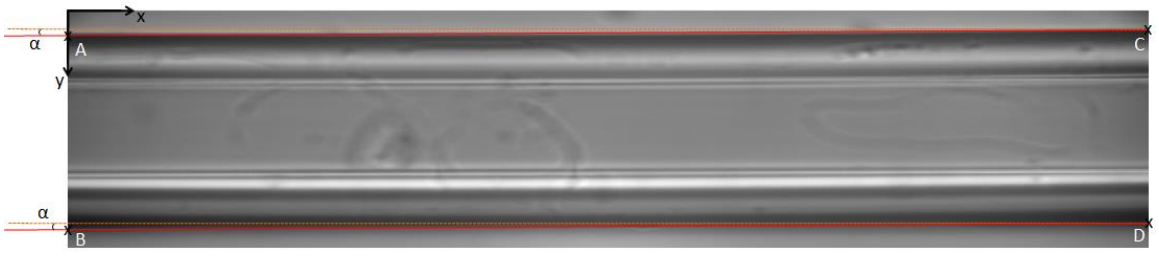

Figure 2.19. The identification of the external walls (AC and BD) as well as the inclination of the channel α, using the calculated background. The orange line is horizontal, while the red line is inclined by α.

2.3.8. Particle localization

Once the channel walls are identified, the location of the particle in the channel can be calculated. It corresponds to the distance between the particle centroid and the inner side of the upper wall.

The height of the wall is equal to the quarter of that of the whole channel ($H_{wall} = 40\mu m$ and $H_{channel} = 160\mu m$). Since the channel is not perfectly horizontal, its inclination α should be taken into account in the calculation. The angle α is measured by calculating and averaging the slopes of the lines (AC) and (BD), and it is found to vary between -3° and 3°. So, the height of the channel is equal to $ABcos\alpha$, and that of the wall is $ABcos\alpha/4$. Let x_r and y_r be the relative coordinates of the centroid $K(x, y)$ of an identified particle in the channel coordinate system, and L the point of (AC) with the same x value (Figure 2.20). In the flow direction, x_r is equal to $x/cos\alpha$. In the lateral direction, the distance between K and the outer side of the upper wall is equal to $(y - y_L)cos\alpha$. By subtracting the wall height from this distance, y_r is obtained: $y_r = (y - y_L - AB/4)cos\alpha$, where $(y_L - y_A)/x_L = (y_C - y_A)/x_C$, with x_C being equal to the W_i, the image width. The normalized particle position in the channel corresponds to the ratio between y_r and the height of the inside of the channel ($AB/2$, corresponding to $H = 80\mu m$).

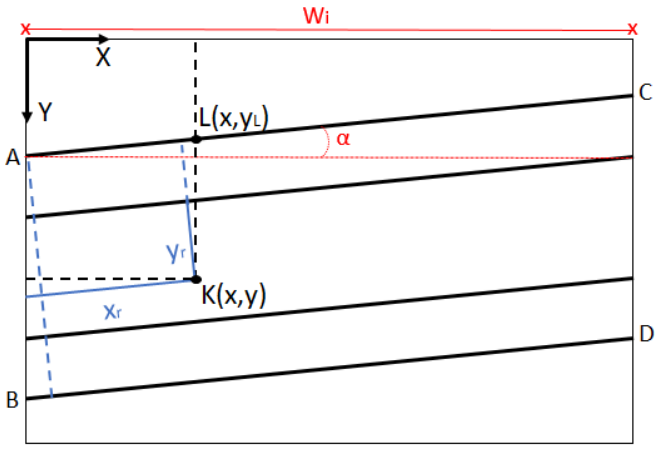

Figure 2.20. Schematic of the particle localization in the channel.

Finally, using the value of y_r/H, one last selection criterion is applied. In fact, the closest normalized distance between the particle's center and the inner wall is equal to

$d_{min}/(2H)$. So, y_r/H must fall in the interval $[d_{min}/(2H)\,;1-d_{min}/(2H)]$. If it is not the case, the falsely identified particle is eliminated.

2.4. Data post-processing

Once the image processing is done, raw data is collected. It consists of all the identified particles as well as their parameters: the centroid position, the area, the filled area, the maximum diameter and the orientation. The identified orientation corresponds to the angle between the main axis of the particle projection, in the camera's plane, and the horizontal.

As described in the previous section, a bright particle has a bright point that occupies at least 10% of its area. This categorization between bright and non-bright particles, along with the centroid position, allow plotting the particle distribution. This latter is a probability density function PDF, represented in function of y/H, the normalized lateral position in the channel (Figure 2.21).

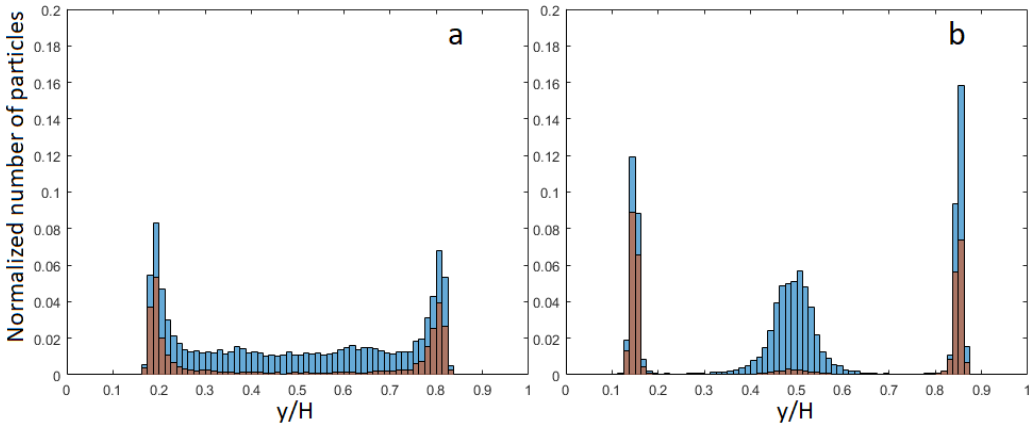

Figure 2.21. Two examples of the particle distribution. In each case, two histograms are plotted (blue and red). They show the normalized number of particles as a function of the normalized positions (y/H). The normalized number of particles is the ratio between the number of particles and the total number of identified ones. The blue histogram corresponds to all the identified particles, while the red one represents the distribution of the in-focus particles (with a bright point). Both examples correspond to midplane PDFs ($Z/H = 0.5$), obtained for a suspension of $PNT57$ particles flowing at (a) $Re = 10$ and (b) $Re = 116$, with an equivalent particle volume fraction of 0.1% and a distance from the wall $X/H = 750$.

In the design of microseparators in microfluidic devices, it is essential to identify the distance between the channel walls and the positions at which the particles focus. The normalized equilibrium position Y_{eq}/H is the most frequent distance from the wall,

normalized by the channel height. It corresponds to the y/H value of the highest red bin, in a midplane PDF ($Z/H = 0.5$). Due to the symmetry and the four face-centered equilibrium positions in a square cross-section (Chapter 1), Y_{eq}/H appears on both sides of the centerline. So, to get a more precise value of the equilibrium position, Y_{eq}/H is identified from both sides, then averaged. After finding Y_{eq}/H, curves describing its evolution in function of other parameters (Re, X/H, Φ, κ, λ) are plotted and explained (Chapter 3).

Identifying the equilibrium positions, on which the particles are focused, is not sufficient to complete a design. The efficiency of the device should be also taken into consideration. It is directly related to the fraction of focused particles: the higher this fraction is, the higher the efficiency is.

Gao [67] introduced the focusing degree η. It was mainly used to quantify the migration development and follow its dependence on several parameters (Re, Φ, X/H and κ). In a given configuration, the focusing degree corresponds to the ratio between the number of focused particles and the total number of identified ones.

Gao [67] considered that a particle is focused if its centroid is located at a distance shorter than $0.2d_{rot}$ from the equilibrium position. Based on this estimation, he considered that, at moderate Reynolds numbers, a particle is focused when it is located in one of the four virtual rectangles centered at the equilibrium positions [67]. These rectangles have a width of $0.4d_{rot}/H$ (y direction) and a height equal to the depth of the focal plane δ_{fp} (z direction, $\delta_{fp} = 10\mu m$ in this study and that of [67]).

By definition, at moderate Reynolds numbers, a particle is considered focused when it is located in one of the four virtual rectangles centered at the equilibrium positions [67]. For Gao [67], these rectangles have a width of $0.4d_{rot}/H$ (y direction) and a height equal to the depth of the focal plane δ_{fp} (z direction, $\delta_{fp} = 10\mu m$ in this study and that of [67]).

Based on this definition and on midplane PDFs ($Z/H = 0.5$), Gao [67] considered that the focused particles are the bright ones with $|y/H - Y_{eq}/H| \leq 0.2d_{rot}/H$ (or $|y/H +$

$Y_{eq}/H - 1| \leq 0.2d_{rot}/H$) and the non-bright ones with $|y/H - 0.5| \leq 0.2d_{rot}/H$ (Figure 2.22).

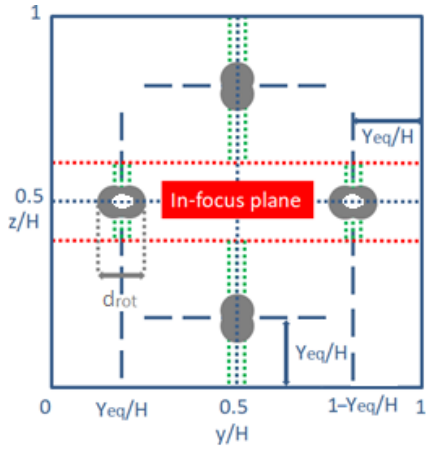

Figure 2.22. A square cross-section with the four equilibrium positions and the rectangles in which the particles are considered focused (in green), based on the definition of Gao [67]. The left and right walls are the ones that appear on the captured images.

However, by using only midplane PDFs to calculate η, the two out-of-focus rectangles, at $Y/H = 0.5$, have a height of $(H - \delta_{fp})/2 = 35\mu m$ and not 10µm as defined earlier (Figure 2.22). But as seen in Chapter 1, the inertial migration consists of two stages, during which the particle migrates to an equilibrium ring then moves towards the equilibrium position. Thus, it was assumed that the probability of having a particle at $Y/H = 0.5$ and $|z/H - Y_{eq}/H| > \delta_{fp}/2$ (or $|z/H + Y_{eq}/H - 1| > \delta_{fp}/2$) is very low. Based on this assumption, the initially proposed definition of the focusing degree η is considered acceptable. Moreover, this definition will be applied in this study, in order to simplify the comparison between the obtained non-spherical results (Chapters 3 and 5) and the spherical ones of Gao et al. [67,80,93].

The centroid of the particle does not only give information linked to the lateral migration. It also helps identify trains and analyze the longitudinal ordering. In fact, the centroid is needed to calculate the distances between the particle and nearby particles. Having these distances help identify trains.

A train is formed of three or more particles. The distance between the centers of two consecutive particles, called the interparticle spacing, is smaller than or equal to five times

the rotational diameter d_{rot}. It has been verified (See Chapter 5 Section 5.3.2.2) that this range of interparticle spacing permitted the detection of the quasi-totality of the trains. Moreover, after visually checking the trains on the images, a third condition is introduced: the difference in the lateral positions of two consecutive particles should not exceed 5% of the channel height (7 pixels).

Three main parameters characterize the longitudinal ordering for a given configuration: the fraction of particles in trains ψ (corresponding to the number of particles in trains over the total number of identified particles), the normalized interparticle spacing l/d_{rot} (the most probable interparticle spacing for a given configuration), and the number of particles per train.

Finally, it should be noted that, the detected orientation, area and maximum diameter constitute a combination of parameters used to determine the rotational behavior (mode, plane and/or period of rotation) of the corresponding particle (Chapter 4).

2.5. Summary and conclusions

In this chapter, the developed in-situ visualization technique is presented. This method, inspired by the one developed by Gao in 2017 [67], is approved thanks to few simple validation tests.

Once the images are captured, a developed image-processing MATLAB code helps obtain raw data such as the position of the particles in the channel, their areas, diameters and orientations. This serves as an input to identify parameters linked to the lateral migration (Y_{eq}/H, η), the rotational behavior and the longitudinal ordering (ψ, l/d_{rot}) of the particles in the channel.

3. Lateral migration

3.1. Introduction

In this chapter, the lateral migration of non-spherical particles (PNT and SNW) is studied at moderate and low inertia, while varying Reynolds number, the particle volume fraction, the distance from the channel inlet, the confinement ratio and/or the particle aspect ratio. To quantify the effect of these parameters, the equilibrium position and the focusing degree are studied and compared for different configurations.

3.2. Lateral migration at moderate and high inertia

3.2.1. Particle distribution and migration stages

To identify the particle distribution, the channel is scanned along the z axis. This is done by changing the position of the channel with respect to the camera's plane of focus (Figure 3.1b). This scan is executed on two types of particles ($PNT57$ and SNW) at two different values of Reynolds number (5.84 and 58) (Figure 3.1a).

It can be remarked that, regardless of the type of the particle, at a fixed Re, the blue histograms (representing all the particles) are very similar and only the red histograms are altered when Z/H is modified. This confirms that the fraction and distribution of in-focus particles are changing while scanning the channel, while the overall distribution does not depend on the position of the plane of focus.

The histograms corresponding to $0.5 < Z/H < 1$ are not represented, since they can be obtained by mirroring, thanks to the symmetry with respect to the plane $Z/H = 0.5$.

For fixed experimental conditions, the equilibrium positions are the most probable locations that the particles will occupy. In other words, these positions correspond to the peaks present on the histograms.

At $Re = 5.84$, two peaks are present, one from each side of the channel centerline ($Y/H = 0.5$). At $Z/H = 0.5$ and 0.375, the bright particles (red bins) are located at the two peaks. At $Z/H = 0.25$, the majority of the bright particles are positioned at the

peaks, while a small proportion resides between the two peaks. A uniform distribution of the bright particles is observed at $Z/H = 0.125$.

This suggests that the particles form a ring in the square cross-section and have an equal distance from the wall (Figure 3.1c). One edge of this ring is located at $Z/H = 0.125$, and the plane $Z/H = 0.25$ covers a part of the zone occupied by this ring. This observation indicates the development of the first stage of migration (cross-streamline) explained in the first chapter.

At $Re = 58$, one extra peak, located at $Y/H = 0.5$, appears. For $PNT57$ particles, at $Z/H = 0.5$, the bright particles are located at the two side peaks. At $Z/H = 0.375$, the bright particles are also positioned at the two side peaks, but with a smaller proportion. At $Z/H = 0.25$ a small number of bright particles is identified. These particles are roughly equally distributed on the three peaks. At $Z/H = 0.125$, the bright particles occupy the central peak. Finally, at $Z/H = 0$, a small number of bright particles is located at the central peak.

This confirms the appearance of four equilibrium positions located at the centers of the four faces of the square cross-section (Figure 3.1d). The particles migrate along the ring towards the closest equilibrium position, finishing by that the second stage of migration (cross-lateral).

The same observation applies on SNW particles for $Re = 58.4$. The only difference is that the SNW particles appear to focus at equilibrium positions, closer to the midplane. In fact, SNW particles focus around the plane $Z/H = 0.25$, while $PNT57$ particles focus around the plane $Z/H = 0.125$.

Based on these observations, it can be deduced that, at moderate fluid inertia, PNT and SNW particles follow the same two-stage lateral migration described in the literature [50,53,67,108,144] (cf. Chapter 1).

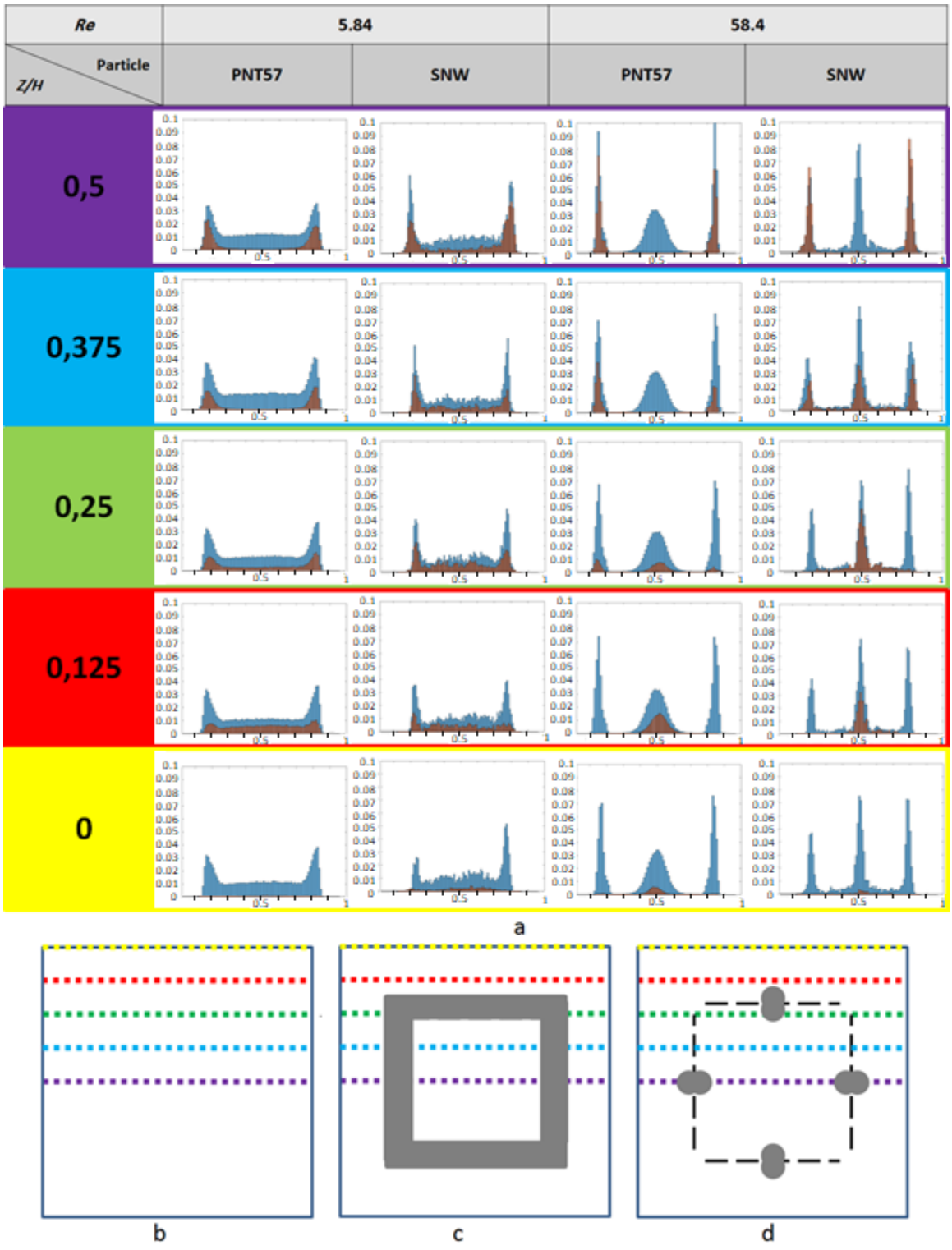

Figure 3.1. (a) Channel scan for $PNT57$ and SNW particles at $X/H = 1000$ and at two different values of Reynolds number (5.84 and 58); (b) a square cross-section with different positions of the focal plane (same colors as in (a)); (c) the ring formation, also known as the cross-streamline migration and (d) the four face-centered equilibrium positions in a square microchannel. In the $PDFs$ of figure (a), the horizontal axis represents the normalized lateral position of the particles (y/H) and varies between 0 and 1; the vertical axis corresponds to the normalized number of particles and varies between 0 and 0.1 (10%).

3.2.2. Evolution of the lateral migration in the channel (Effect of the channel length)

For the study of the evolution of the lateral migration in the channel, midplane PDFs ($Z/H = 0.5$) are generated at different distances from the channel inlet. The tests are done on a $PNT57$ suspension at fixed Reynolds number.

Figure 3.2 represents four midplane PDFs of a $PNT57$ suspension at different distances from the channel inlet. It can be observed that an increase in X/H enhances the particle lateral migration towards the four equilibrium positions: most of the particles are still in the first migration phase at $X/H = 250$ and 500 (ring formation), while they attain the face-centered equilibrium positions at $X/H = 750$. This effect was also highlighted for spherical particles by Gao [67]. In fact, by increasing the distance from the inlet, more particles will have the necessary channel length to finish their two-phase lateral migration and attain their equilibrium position.

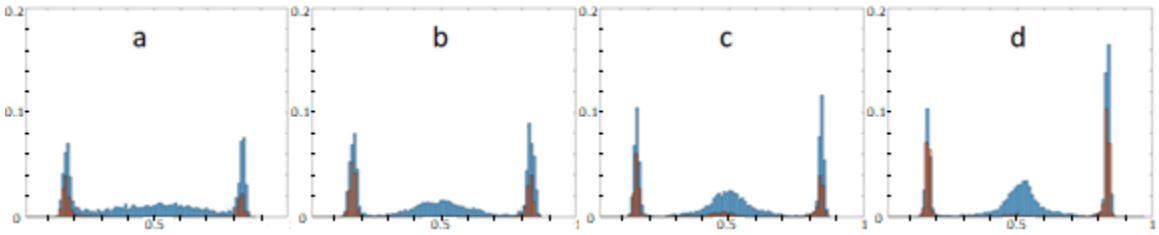

Figure 3.2. Midplane PDFs of a $PNT57$ suspension at different distances from the channel inlet: (a) 250, (b) 500, (c) 750 and (d) 1000. The suspension has a concentration of 0.0175% and flows at $Re = 58$. The horizontal axis varies between 0 and 1, while the vertical axis varies between 0 and 0.2 (20%).

This enhancement in the lateral migration is also quantitively confirmed by the increase of the focusing degree η with X/H, regardless of the value of Reynolds number (Figure 3.3). It can be also remarked from Figure 3.3 that, for a fixed Reynolds number, the evolution of η is not linear. This suggests the presence of a plateau that the focusing degree attains at higher values of X/H. The value of η corresponding to this plateau appears to be a function of Re, but no conclusions can be drawn concerning these values due to the short range of X/H. The rise in the value of η in function of X/H, as well as the formation of a plateau was also observed by Gao et al. [67,93] for spherical particles.

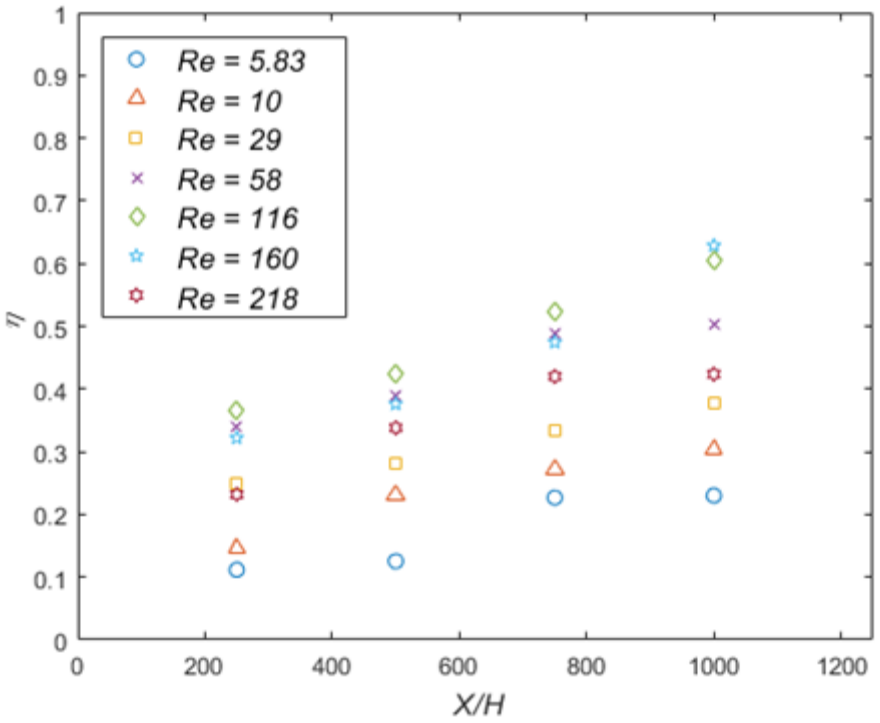

Figure 3.3. Focusing degree in function of the distance from the channel inlet for different values of Reynolds number. The tests are done on a suspension of $PNT57$ particles ($\lambda = 1.5$ and $\kappa = 0.09625$), having an equivalent particle volume fraction of 0.1%.

In Figure 3.4, the normalized equilibrium position is plotted in function of the distance from the channel inlet, for different values of Re. It can be observed that Y_{eq}/H does not depend on X/H. In other words, once the particle attains its equilibrium position, it will remain there, as long as no modifications in the flow occur (change in Re or the channel geometry). This is coherent with the results of numerical simulations done on spherical [53] and oblate [108] particles in square microchannels, where it has been shown that, a focused particle does not change its equilibrium position while flowing in the channel (Figure 3.5).

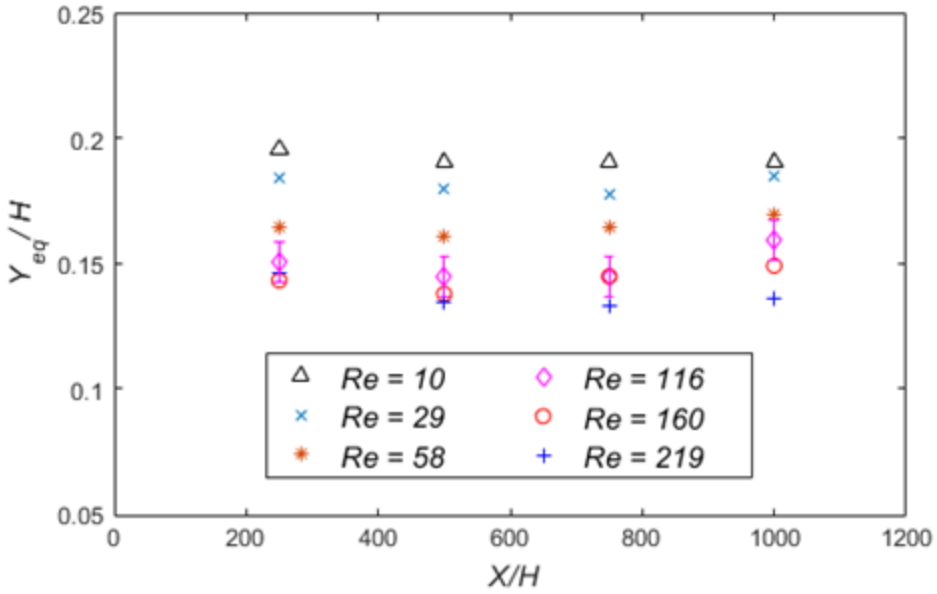

Figure 3.4. Normalized equilibrium position in function of the distance from the inlet, for different values of Reynolds number. The suspension contains $PNT57$ particles at an equivalent volume fraction of 0.1%. Error bars are added only for $Re = 116$ for visualization reasons. For the other values of Re, the error bars are of the same order of magnitude.

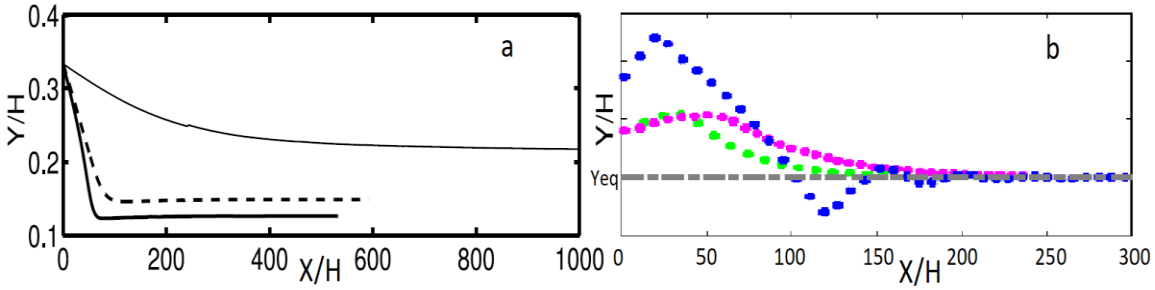

Figure 3.5. Normalized lateral position in function of the normalized distance from the inlet for (a) spherical [53] and (b) oblate particles [108]. It can be observed that once the particle is focused at a fixed Y/H, it maintains this equilibrium position regardless of the value of X/H. Figures a and b are reprinted from [53] and [108] respectively.

3.2.3. Effect of fluid inertia (Reynolds number Re)

Fluid inertia, represented by Reynolds number, is one of the most important parameters controlling the migration velocity and the particle distribution in the channel cross-section. To put into evidence this effect, midplane PDFs ($Z/H = 0.5$) of a $PNT57$ suspension are identified at different Re (Figure 3.6). The tests are done at a fixed distance from the channel inlet ($X/H = 500$).

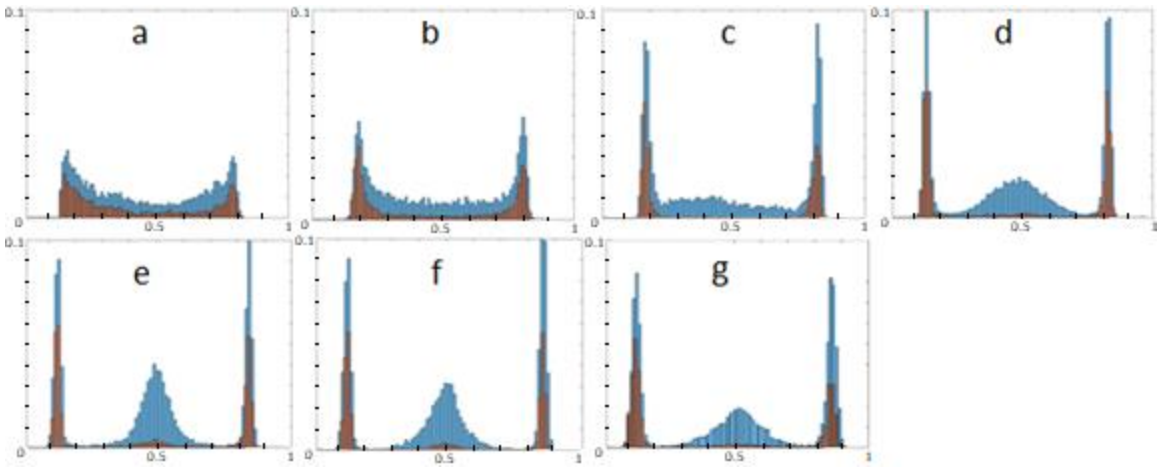

Figure 3.6. Midplane $PDFs$ of a $PNT57$ suspension at different values of Reynolds number: (a) 5.84, (b) 10, (c) 29, (d) 58, (e) 116, (f) 160 and (g) 218. The suspension has a concentration of 0.035% ($\Phi_{eq} = 0.1\%$) and the test is done at $X/H = 500$. The horizontal axis varies between 0 and 1, while the vertical axis varies between 0 and 0.1 (10%).

Figure 3.6 shows that fluid inertia enhances the lateral migration. In fact, it can be clearly observed that, at low values of Reynolds number ($Re \leq 29$), the particles form a ring (first migration phase), while at higher Re, the face-centered equilibrium positions appear. In addition, the central peak becomes sharper when increasing Re from 58 to 116, meaning that the zone in which the particles are concentrated, is becoming narrower. These observations indicate that the higher Reynolds number is, the faster the migration towards the equilibrium position is. In other words, increasing Re shortens the required focusing lengths.

These results are similar to the ones found for spherical particles, which showed that the particle attains its equilibrium position faster at higher Re [53,67] and that the focusing length is inversely proportional to the flow velocity [44,65,107], and thus to Reynolds number.

The lateral migration enhancement, induced by fluid inertia, is linked to the increase in the magnitudes of the three main lateral forces acting on the particle (c.f. Chapter 1). This drives the particles faster towards the equilibrium positions, resulting in a faster migration.

However, for high values of Re, a defocalization from the equilibrium positions is observed. It can be remarked from Figure 3.6 that, when Re transitions from 160 to 218,

the bright peaks seem to become larger and lower. In the spherical case, this same phenomenon was observed and attributed to the existence of a new migration regime [54,69,93] (cf. Chapter 1). The results of this present study can be explained in the same way.

For all the configurations, it has been observed that fluid inertia has the same effect on the lateral migration of non-spherical particles, regardless of the type of the particle ($PNT57$, $PNT35$ and SNW). The only identified difference concerned the values of Reynolds number at which the distribution transitions from the ring to the four face-centered positions, and then to the defocalization at high inertia. These differences are highlighted in the next sections (effect of κ and λ).

The findings from Figure 3.6 are quantitatively confirmed by plotting the evolution of the focusing degree in function of Reynolds number (Figure 3.7). It can be observed that, when Re increases, η increases to a maximum value η_{max} (reached at a critical Reynolds number Re_{cr}), then decreases.

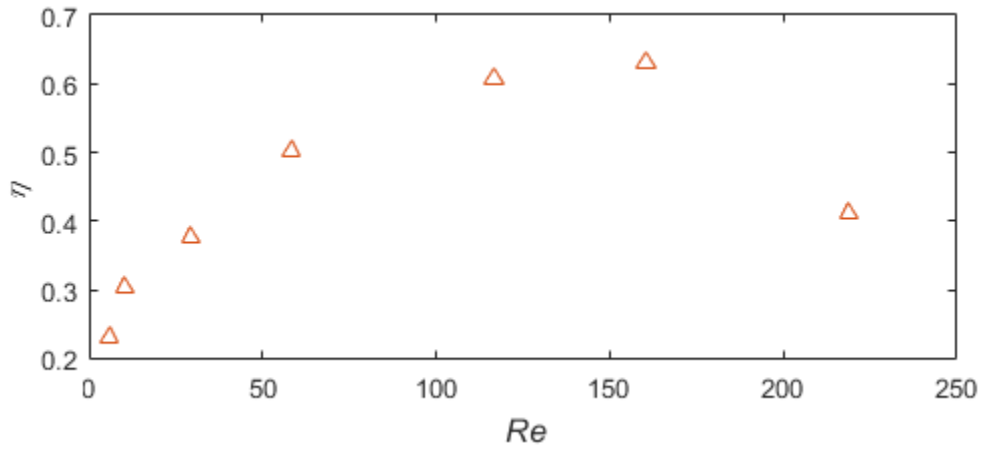

Figure 3.7. Focusing degree in function of the channel Reynolds number for $PNT57$ particles ($\lambda = 1.5$ and $\kappa = 0.09625$). The equivalent particle volume fraction is 0.1% and the tests are done at $X/H = 1000$ in an 80µm square microchannel.

The same effect of fluid inertia on the focusing degree was obtained in the case of spherical particles [67,93]. Concerning the decreasing part of the curve ($Re > Re_{cr}$), Gao

et al. [93] appropriated this drop to the alteration of the migration regime from four to eight equilibrium positions. Although none of the studies dealing with non-spherical particles mention a shift to a new migration regime at high fluid inertia (to our knowledge), the results of this study put into evidence a modification of the face-centered migration regime at high values of Re.

Concerning the effect of fluid inertia on the equilibrium position, it can be observed from Figure 3.8 that, Y_{eq}/H decreases with Re. This means that the particle gets closer to the wall when fluid inertia is increased. Our results are in agreement with other experimental [146] and numerical [108] works done on non-spherical particles.

The same behavior is observed in the case of spherical particles [93]. In fact, when fluid inertia increases, the shear-induced lift force increases more than the wall-induced one [157,158], pushing the particle towards the wall and thus decreasing the distance between the equilibrium position and the wall.

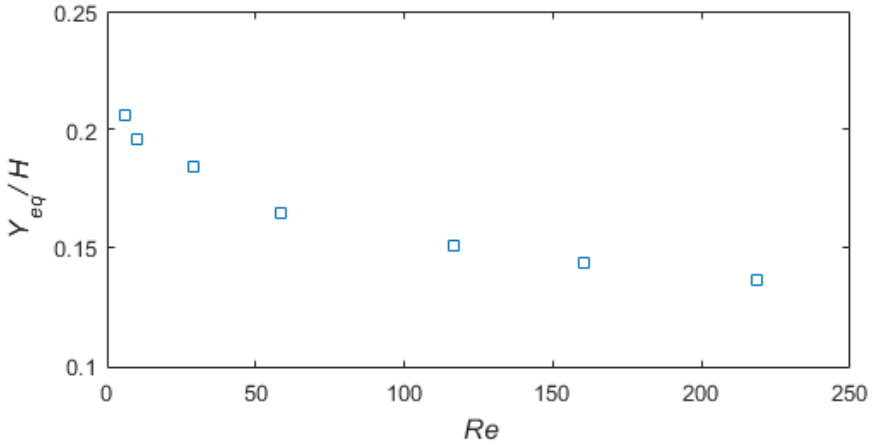

Figure 3.8. Normalized equilibrium position in function of the channel Reynolds number. The suspension contains $PNT57$ particles at an equivalent volume fraction of 0.1% and the tests are done at $X/H = 1000$.

3.2.4. Effect of the particle volume fraction Φ

In this subsection, the effect of the particle volume fraction Φ is studied. For this purpose, $PNT57$ suspensions of different concentrations were tested at a fixed Re and X/H (Figure 3.9). It can be remarked from Figure 3.9 that when the particle volume fraction is

increased, the peaks become slightly less sharp and the particles seem to occupy a larger volume around the equilibrium positions. The same effect is observed in the case of $PNT35$ and SNW particles and for different Re and X/H values.

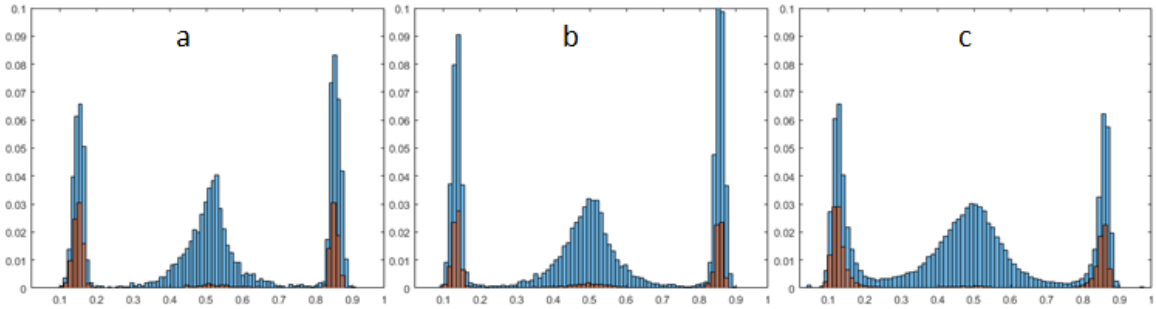

Figure 3.9. Midplane PDFs of a $PNT57$ suspension at different particle volume fractions: (a) 0.0175%, (b) 0.035% and (c) 0.07%. The suspension is flowing at $Re = 160$ and the test is done at $X/H = 500$. The horizontal axis varies between 0 and 1, while the vertical axis varies between 0 and 0.1 (10%).

These qualitative observations are quantitatively confirmed in Figure 3.10. In fact, increasing Φ, for a fixed Re, induces a decrease in the value of η. This was also found by Gao et al. [93] while studying spherical particles. They linked this phenomenon to the "space constraint" effect. In fact, according to [93], for a given channel length, there isn't enough space to focus all the particles on the faced-centered equilibrium positions, due to the interparticle spacing imposed in the streamwise direction and regulated by interparticle forces.

Moreover, it can be observed from Figure 3.10 that, an increase in the suspension concentration decreases the value of Re_{cr}. This was also obtained in the spherical case [93], in a more pronounced way, for $0.02\% \leq \Phi \leq 1\%$. The reason behind this alteration of the critical Reynolds number is still unclear.

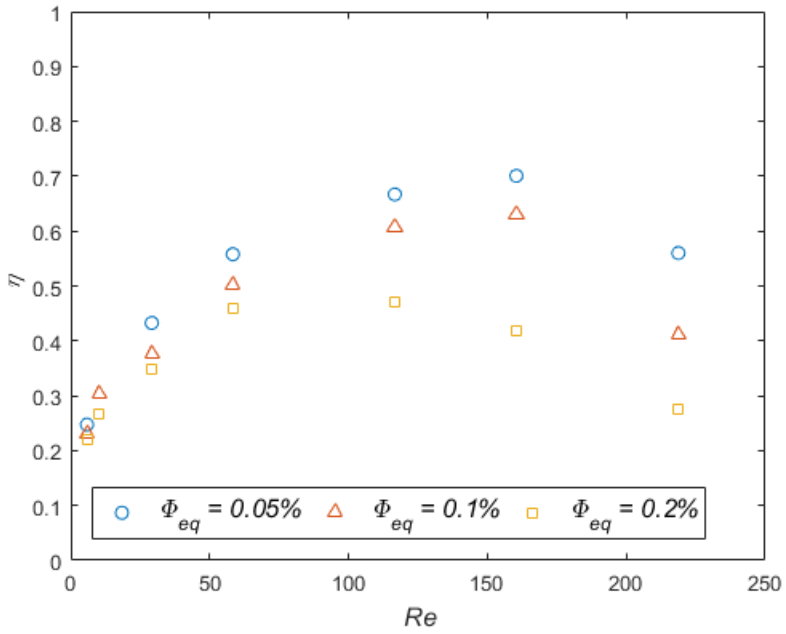

Figure 3.10. Focusing degree in function of the channel Reynolds number for three different equivalent particle volume fractions. The tests are done on $PNT57$ particles ($\lambda = 1.5$ and $\kappa = 0.09625$) at $X/H = 1000$.

To study the effect of the suspension's concentration on the normalized equilibrium position, the evolution of Y_{eq}/H is plotted in function of Reynolds number, for different particle volume fractions (Figure 3.11).

Regardless of the value of Φ, the normalized equilibrium position is shown to decrease with Re. This means that, in this range of Φ, the effect of fluid inertia on the equilibrium position is the same, independently from the value of Φ.

However, for a fixed Reynolds number, the distance between the equilibrium position and the wall seems to decrease with the concentration. In other words, an increase in Φ pushes the equilibrium positions towards the channel walls. This effect was also experimentally observed by Gao et al. [93] on spherical particles. The physical phenomenon behind this effect is still unclear.

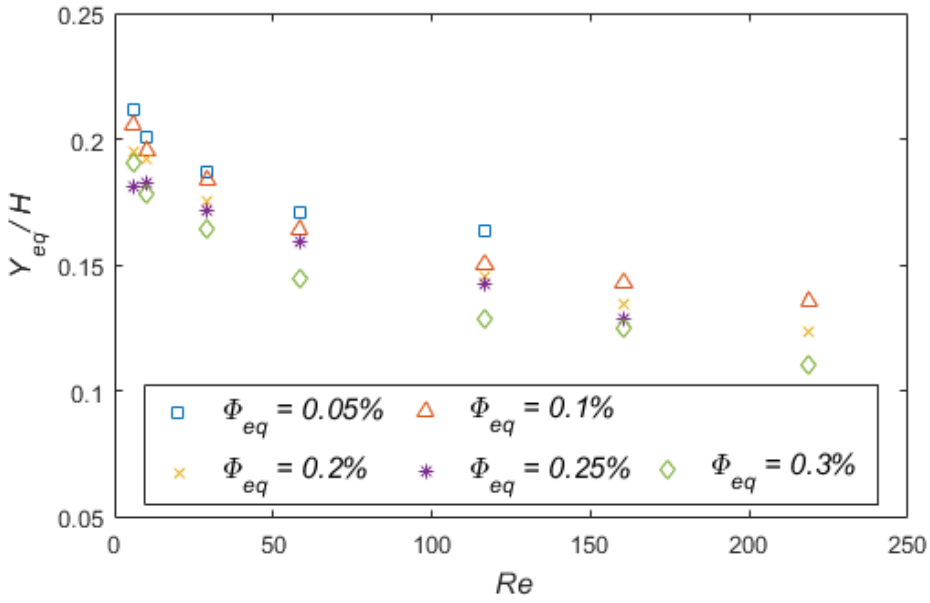

Figure 3.11. Normalized equilibrium position in function of the channel Reynolds number for different concentrations. The suspension contains $PNT57$ particles and the tests are done at $X/H = 1000$.

3.2.5. Effect of the particle aspect ratio λ

As mentioned in Chapter 2, the available particle aspect ratios are limited to the values 1.5 and 1.2 corresponding to PNT and SNW particles respectively. So, in this section, in order to extend the range of λ, the comparison between spherical particles ($\lambda = 1$) and the non-spherical ones is added.

To identify the effect of the particle aspect ratio on the lateral migration, midplane PDFs are obtained for particles of very close κ but different λ. Precisely, the non-spherical results of this study are compared to the spherical ones obtained by Gao [67] in the same configurations.

It can be observed from Figure 3.12 that, for a fixed Re and X/H, the spherical and non-spherical particles, of very close κ, seem to have the same equilibrium position. It can be also remarked that the bright peaks are larger and lower in the non-spherical case. This means that the non-spherical particles are focused in larger zones around the equilibrium positions than spheres.

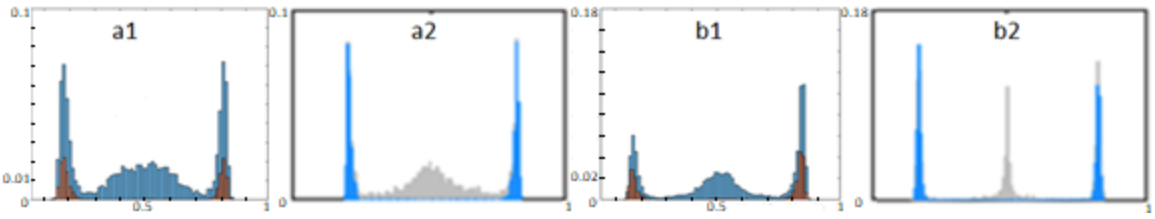

Figure 3.12. Midplane PDFs of PNT57 ($\lambda = 1.5$) (a1 and b1) and spherical ($\lambda = 1$) (a2 and b2) [67] suspensions ($\kappa \approx 0.1$). The tests are done at $X/H = 1000$. The suspensions are flowing at $Re = 29$ (a1 and a2) and 58 (b1 and b2). In addition, the suspensions have the same number of particles ($\Phi_{eq} = 0.1\%$). In the spherical case (a2 and b2), the blue bins correspond to the in-focus particles and the grey bins represent all the identified particles. The y-axis varies between 0 and 0.1 for (a1) and (a2), while it ranges from 0 to 0.18 for (b1) and (b2).

Concerning the equilibrium position, Figure 3.13 shows the evolution of Y_{eq}/H in function of Re, for non-spherical (symbols) and spherical (lines) [93] particles in square microchannels.

At moderate fluid inertia, an increase in the value of Re decreases the value of Y_{eq}/H, indicating that the particles are pushed towards the channel walls. This is the case for spherical [93] and non-spherical particles.

At high fluid inertia, according to Gao et el. [93], the equilibrium positions of the spherical particles (mainly for $\kappa = 0.11$) are pushed towards the channel centerline when Re is increased. In fact, at these values of Re, the new migration regime starts taking place, where eight equilibrium positions are present: the four centers of the faces (already existing) and the four corners of the square cross-section [93]. The results represented for spheres at high values of Re correspond to the four face-centered equilibrium positions.

In these experimental conditions, the increase in the value of Y_{eq}/H, at high values of Re, is not observed for non-spherical particles.

It can be also observed from Figure 3.13 that two particles of close κ but different λ values have roughly the same Y_{eq}/H. This means that, in the range of λ studied here, the normalized equilibrium position does not vary with the particle aspect ratio and is determined by the confinement ratio κ. If λ has an effect on Y_{eq}/H, it is not sufficiently pronounced here to be detected.

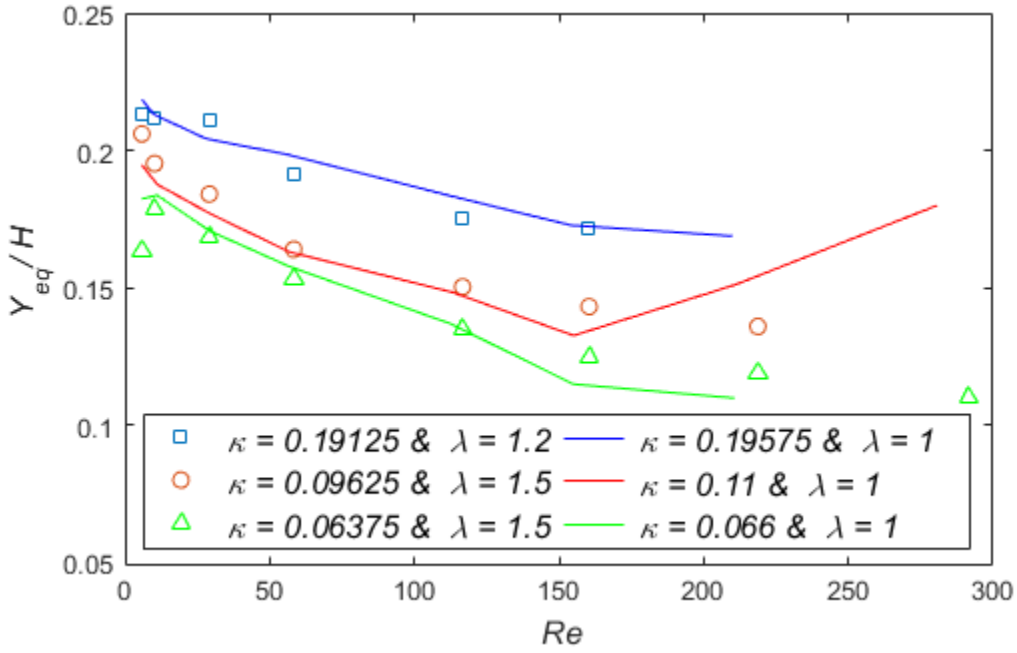

Figure 3.13. Normalized equilibrium position in function of the channel Reynolds number for spherical (lines) [93] and non-spherical particles (symbols). All the suspensions have the same number of particles ($\Phi_{eq} = 0.1\%$) and the tests are done at $X/H = 1000$ in an 80µm square microchannel.

To quantify the second observation from Figure 3.12, the focusing degree η is evaluated for non-spherical particles, and compared to the spherical results of Gao et al. [67,93] (Figure 3.14). It can be shown from Figure 3.14 that λ does not have any effect neither on the shape of the curve nor on the critical Reynolds number. However, the particle aspect ratio seems to have a clear impact on the value of η. For a fixed κ and Re, the focusing degree is lower for non-spherical particles. This is coherent with the observation from Figure 3.12, where non-spherical particles are focused in larger zones around the equilibrium positions. In fact, for a fixed definition of η, where the focusing zone corresponds to an estimated zone of $\pm 0.2 d_{rot}$ around Y_{eq} (Chapter 2), a more dispersed distribution around Y_{eq} would automatically induce a drop in the calculated value of the focusing degree η.

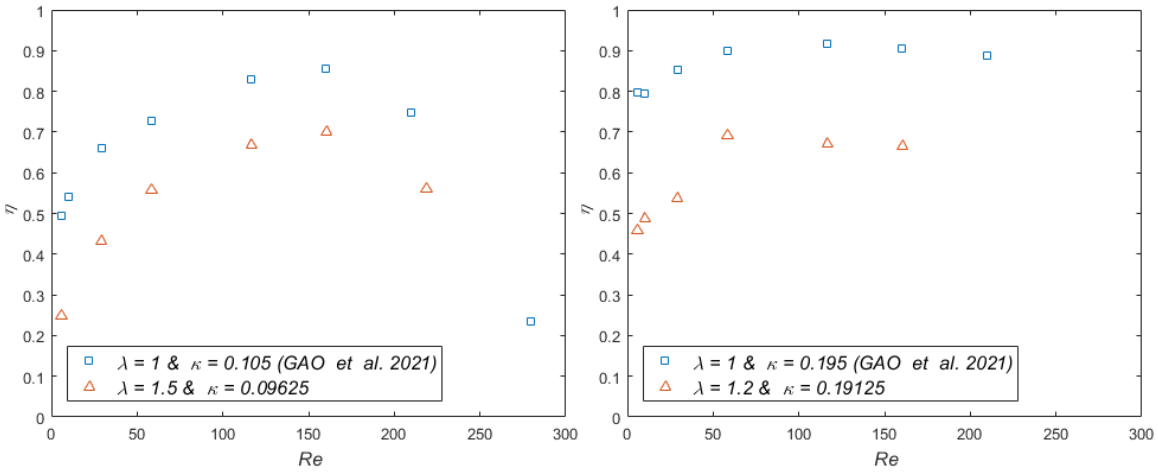

Figure 3.14. Focusing degree in function of Reynolds number for spherical (squares) [93] and non-spherical (triangles) particles. The left and right plots correspond to particles with $\kappa \approx 0.1$ and 0.19 respectively. All the suspensions have the same number of particles ($\Phi_{eq} = 0.05\%$) and the tests are done at $X/H = 1000$ in an 80µm square microchannel.

The reason behind the wider dispersion around the equilibrium positions in the non-spherical case, cannot be attributed to image processing. In fact, as shown in Chapter 2, even though the particle rotates and changes its area and orientation in the plane (Chapters 1 and 4), the distance between the projection of the particle's centroid and the identified centroid of the particle's projection is so small, and the induced error is negligible. This means that the wider distribution of non-spherical particles is due to a physical phenomenon occurring in the channel.

A possible hypothesis, that can explain the effect of λ on the distribution of the particles around the equilibrium positions (and thus on η), is related to the particle oscillation in the non-spherical case. As seen in Chapter 1, non-spherical isolated particles oscillate about the equilibrium position. This is due to the particle tumbling mode, shown in Chapter 1 and confirmed in Chapter 4. While rotating, the distance between the edge of the particle and the wall, periodically changes, inducing a periodic modification in the balance between the wall-induced and the shear lift forces. This generates a lateral oscillation of the particle's centroid in the channel cross-section.

High-frame rate images were studied, in order to confirm the presence of this behavior and determine the amplitudes of the oscillations. Focused tumbling isolated particles were tracked on several successive images and their positions Y/H were measured and plotted in function of time (Figure 3.15).

It can be observed from Figure 3.15 that, the particle is oscillating about a mean value, considered to be the particle's equilibrium position. It has been verified that this value is close to the normalized equilibrium position deduced from the statistical analysis of the lateral migration, that was presented earlier. It should be noted that, the results are validated by studying about 20 particles per configuration (only two of them are represented on Figure 3.15).

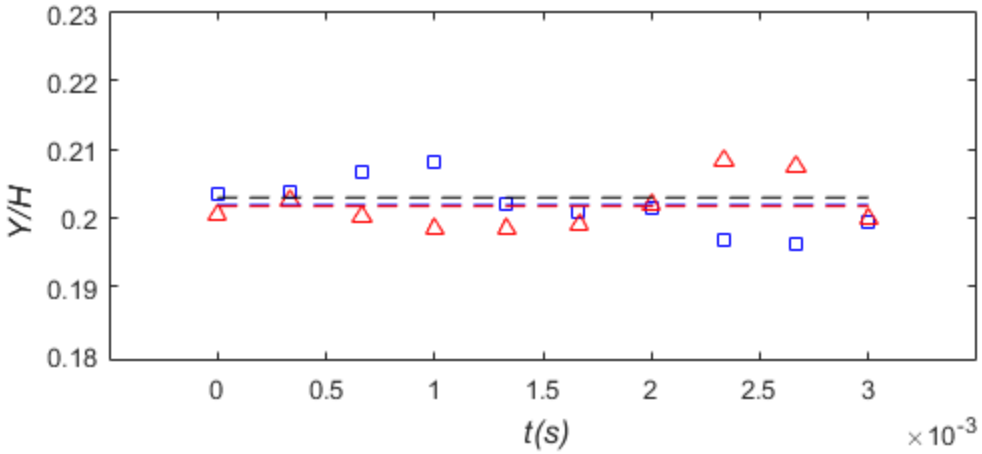

Figure 3.15. Trajectories (Y/H) of two SNW particles (red triangles and blue squares) in function of time at $X/H = 1000$. The suspension ($\Phi_{eq} = 0.05\%$) is flowing at $Re = 5.84$. The normalized equilibrium position is equal to 0.203 (dashed black line). The mean values about which the particles oscillate are represented by the dashed red and blue lines, that are approximately superposed.

For a fixed configuration, the oscillation amplitude ΔY is calculated for every identified particle, then averaged. Figure 3.16 shows the variation of $\Delta Y/d_{rot}$ in function of Reynolds number for SNW and $PNT57$ particles. It can be noticed that, $\Delta Y/d_{rot}$ does not vary with Re. However, this amplitude is not the same for the two studied particles, for which κ and λ are different. The amplitude of the oscillations of the SNW particles is around $0.044d_{rot}$ ($d_{rot} = 15.3\mu m$), while that of the $PNT57$ particles is approximately equal to $0.036d_{rot}$ ($d_{rot} = 7.7\mu m$) (Figure 3.16).

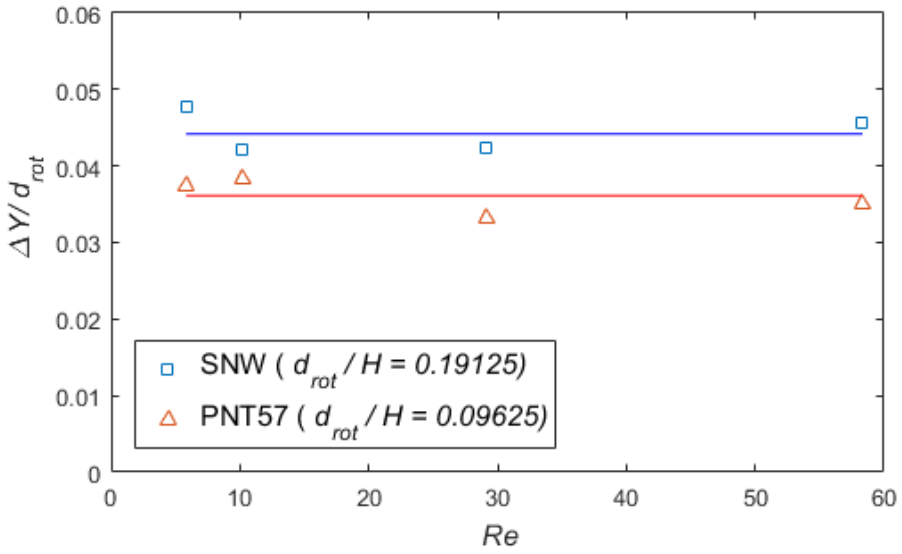

Figure 3.16. The variation of $\Delta Y/d_{rot}$ in function of Reynolds number for SNW ($\kappa = 0.19125$, $\lambda = 1.2$) and $PNT57$ ($\kappa = 0.09625$, $\lambda = 1.5$) particles.

The dependence of the oscillation amplitude ΔY on the confinement ratio κ was also observed by Hur et al. [110] in rectangle microchannels. Their results show that a non-spherical particle of $\kappa = 0.3$ (and a geometry similar to the SNW particles), oscillates around the equilibrium position with an amplitude of $0.058d_{rot}$. They also found that, ΔY becomes smaller when the confinement ratio is decreased.

Even though the results of this study appear to confirm the results of Hur et al. [110], the SNW and $PNT57$ particles have different values of λ. To dissociate the effect of κ from that of λ, other types of particles, having the same κ but different λ, should be studied.

The periodically-changing wall-induced force F_W, is a function of the distance between the edge of the particle and the wall. The shorter this distance is, the strongest F_W is. The two extreme distances from the wall are obtained when the main axis of a rotating particle is parallel and perpendicular to the flow. For a fixed λ, increasing κ (i.e., d_{rot}) rises the difference between these extreme edge positions. This grows the difference between the corresponding values of F_W, which increases the oscillation amplitude. The same logic applies in the case of a fixed κ and an increasing λ.

Since the maximum oscillation amplitude is around $0.04d_{rot}$, which is much less than $0.2d_{rot}$, the oscillations of the non-spherical particles ($Y_{eq} \pm 0.04d_{rot}$) are considered to

be taken into account while calculating the focusing degree ($Y_{eq} \pm 0.2d_{rot}$). So, it can be deduced that the oscillations of non-spherical particles are not behind the wider distribution around the equilibrium position.

Another hypothesis that can explain the wider particle distribution in the non-spherical case, is linked to the particle-particle interactions. The recirculation zones, induced around the particle, are the origin of the train formation and the particle-particle interactions.

In the spherical case, these zones are not a function of the orientation of the sphere, due to the symmetry in the spherical geometry. This allows the formation of aligned trains, at the studied range of κ [67,80].

However, in the non-spherical case, due to the rotation of the particle, the size and the shape of the recirculating zones are periodically modified, moving by that the attraction point on which the lagging particle will focus. In other words, the formed trains might not be perfectly aligned in the non-spherical case, making the zone in which the particles are focused wider.

If this hypothesis is true, unlike the spherical case [67,80], unaligned trains should be identified in this study. However, after visually inspecting the non-spherical trains, formed at different configurations, it has been observed that no obvious staggered or unaligned trains are formed. This observation does not totally disprove the proposed hypothesis. Numerical simulations should be done to confirm or deny it.

To resume, the physical phenomenon behind the wider distribution of non-spherical particles is still unknown. Numerical simulations should be done and a larger range of λ should be tested.

3.2.6. Effect of the confinement ratio κ

The PDFs of $PNT35$ ($\kappa = 0.06375$) and $PNT57$ ($\kappa = 0.09625$) suspensions of the same number of particles are compared at a fixed Re and X/H (Figure 3.17). Both particles have an aspect ratio $\lambda = 1.5$. The goal of this study is to identify the effect of the confinement ratio κ on the lateral migration.

Figure 3.17 shows that the large particles ($PNT57$) migrate faster than the smaller ones ($PNT35$): at $Re = 116$, the apparition of the four equilibrium positions happens at X/H smaller than 500 for $PNT57$ particles, while, at this distance from the inlet, $PNT35$ particles are still in the cross-streamline migration phase.

This was also observed in the case of spherical particles [67] and oblate spheroids [108]. In fact, Lashgari et al. [108] numerically studied the migration of two oblates having different volumes but identical aspect ratios, and found that the required focusing length is longer in the case of the smaller spheroid. So, it can be deduced that, while conserving λ, Re, X/H and Φ_{eq}, an increase in κ accelerates the lateral migration.

As presented in Section 1.2.2.1. (Chapter 1), the forces acting on the particle are proportional to the particle's diameter to the power 6 for F_W (Equation 1.1), 3 for F_S (Equation 1.2) and 3 for F_Ω [55]. So, it is logical that the larger the particle's diameter is, the stronger the net lift force is, which induces a faster migration towards the equilibrium position.

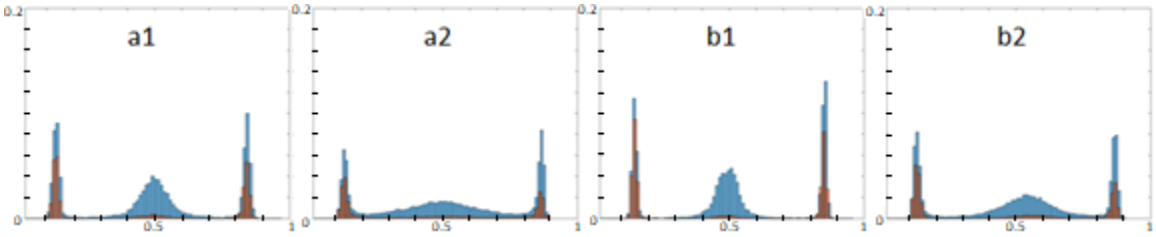

Figure 3.17. Midplane PDFs of $PNT57$ ($\kappa = 0.09625$, $\lambda = 1.5$) (a1 and b1) and $PNT35$ ($\kappa = 0.06375$, $\lambda = 1.5$) (a2 and b2) suspensions flowing at $Re = 116$. The tests are done at $X/H = 500$ (a1 and a2) and 750 (b1 and b2). In addition, the suspensions have the same number of particles ($\Phi_{eq} = 0.1\%$). The y-axis varies between 0 and 0.2.

This effect of the confinement ratio on the migration velocity, is also revealed in the alteration in the focusing degree. Figure 3.18 illustrates the evolution of η in function of Re, for $PNT35$ and $PNT57$ suspensions. It can be observed that both curves increase to η_{max}, then decrease. However, when the particle is smaller, the maximum focusing degree is lower and attained at a smaller Re_{cr}.

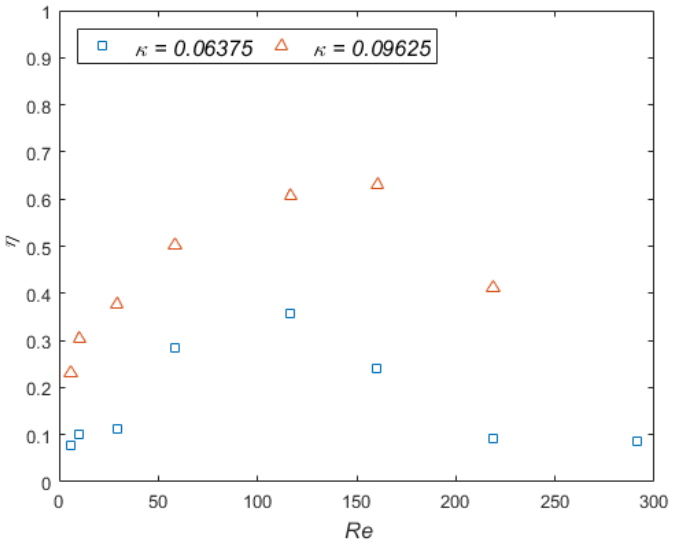

Figure 3.18. Focusing degree in function of Reynolds number for PNT particles ($\lambda = 1.5$). The triangles and squares correspond to $PNT57$ and $PNT35$ particles respectively. Both suspensions have the same number of particles ($\Phi_{eq} = 0.1\%$) and the tests are done at $X/H = 1000$ in an 80µm square microchannel.

Gao et al. [93] experimentally observed the same effect of κ on η, for spherical suspensions. They explained that, at a fixed X/H, when κ is increased, the number of focused particles rises, since larger particles focus faster than smaller ones. This increase induces a raise in the focusing degree η. However, even though the reason behind the alteration of the value of η is determined, the physical explanation describing the modification of Re_{cr} with κ is still unclear.

It should be noted that, similarly to the spherical case ([93], squares in Figure 3.14), κ has an effect on the shape of the curve $\eta = f(Re)$. In fact, at low κ, a well-marked peak is present. This peak expands by increasing the value of κ (Figure 3.20), then transforms into a plateau for higher confinement ratios (Figure 3.14 (right) in the previous subsection). This finding suggests that, the range of Re, in which most of the particles are

focused (η is close or equal to η_{max}), becomes wider by increasing the confinement ratio κ (the size of the particle). This also shows that, larger particles are stable at their equilibrium positions for a wider range of Re.

Concerning the effect of κ on the equilibrium position, it can be observed from Figure 3.13 (shown earlier), that Y_{eq}/H increases with κ. In other words, large particles are closer to the channel centerline than small particles. This confirms the findings on spherical and non-spherical particles, presented in Chapter 1.

Moreover, it can be observed from Figure 3.13 that, the curves for the smallest spherical and non-spherical particles ($\kappa \approx 0.06$) seem to increase (for $5.83 < Re < 10$) then decrease. This was also observed by Kim et al. in 2008 [51] on spheres for $\kappa \approx 0.071$. The declining part was explained in Section 3.2.3. The inclining segment, only observed for the small particles, is more difficult to explain. It might be due to an error in the identification of the equilibrium position. In fact, as explained in Chapters 1 and 3, for small Re and κ values, the particles require long focusing distances. So, in these configurations, the number of particles located on the equilibrium positions is low and the peaks of the particle distribution are flat and wide (approximately around $0.1H$ at $Re = 5.83$ for $PNT57$ particles in Figure 3.1), which increases the possibility of misidentifying Y_{eq}/H.

Although all studies converge on the fact that the normalized equilibrium position increases with κ, the equation describing this evolution is still unknown. To our knowledge, for non-spherical particles, only one fitting equation was proposed in the literature. This model, obtained by Hur et al. [110], is linear ($Y_{eq}/\mathrm{H} = 0.27\kappa + 0.17$), with a determination coefficient $R^2 = 0.92$. It is based on experimental studies on non-spherical particles (of different geometries) flowing in a rectangular channel at $Re = 200$, for κ varying between 0.3 and 0.75. The equation was proposed based on the results, and no physical explanation of the choice of a linear fitting model was given.

Note that, it is not possible to find theoretically the relation between Y_{eq} and κ, by simply equalizing the lateral lift forces ($F_W = F_S$), using the equations presented in Chapter 1. In

fact, the position of the particle appears in the expressions of the lift coefficients C_W and C_S, which have not been theoretically found yet (Section 1.2.2.1. in Chapter 1).

The obtained values of Y_{eq}/H for the non-spherical particles (c.f. Figure 3.13) are represented on Figure 1.19 from Chapter 1 (Figure 3.19), for three values of Reynolds number. The results are presented regardless of the type of the non-spherical particle (SNW or PNT), since λ has no effect on Y_{eq}/H in this study's conditions (Figure 3.13). The fitting model of Hur et al. [110] is added to the figure.

It can be observed from Figure 3.19 that, similar to the findings of Hur et al. [110], the results of this this study show that, for a fixed Re, the equilibrium position seems to progress linearly with the confinement ratio. It can be also noticed that, the equation describing this evolution is certainly a function of the Reynolds number.

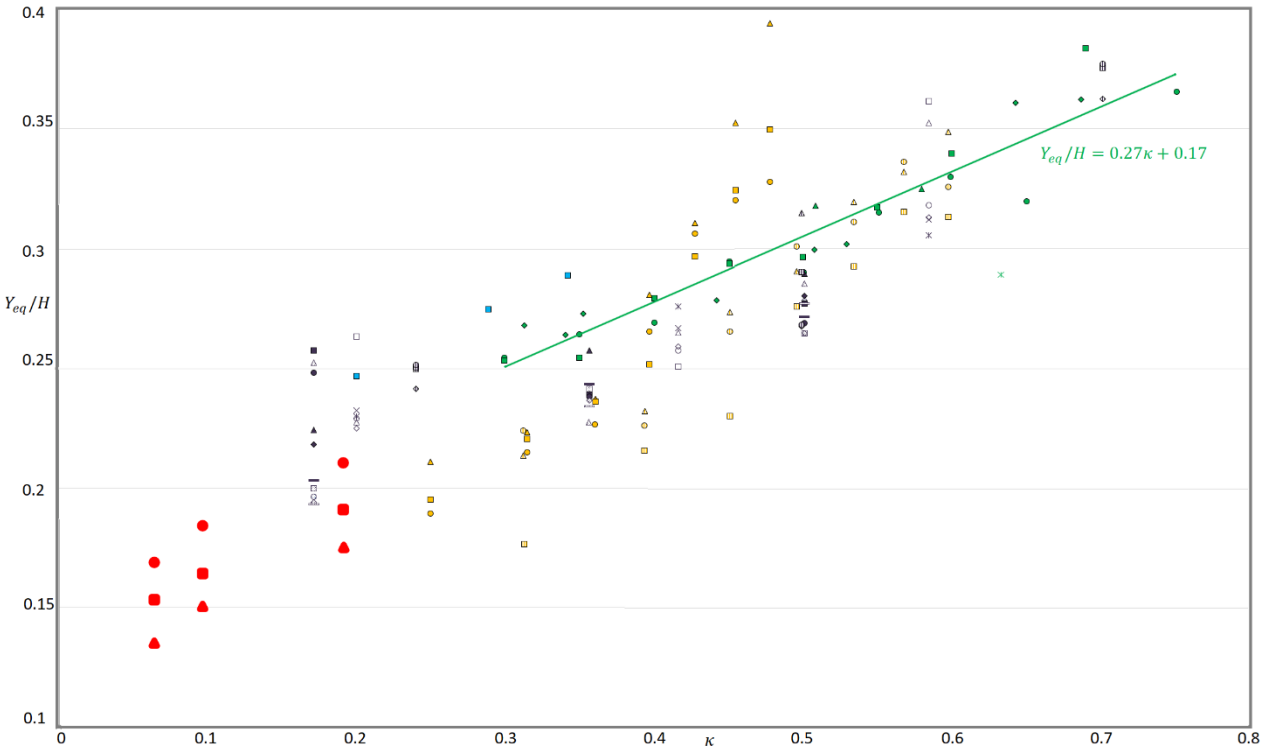

Figure 3.19. Evolution of the normalized equilibrium position in function of the confinement ratio κ. The linear fitting of Hur et al. [110] is represented by the green line ($Re = 200$ and $0.3 \leq \kappa \leq 0.75$). The red symbols correspond to the results of this study (circles for $Re = 29$, squares for $Re = 58$, and triangles for $Re = 116$). The other points correspond to configurations explained in details in Figure 1.19 (Chapter 1). In the configurations where the cross-section of the channel is a rectangle (check Figure 1.19), the height H is replaced by W, the channel's shortest dimension.

3.3. Lateral migration at low inertia

Figure 3.20 shows different PDFs of $PNT57$ and spherical suspensions ($\kappa \approx 0.1$) [67] of the same number of particles. Both experiments are done in 80µm square channels at the same distance from the inlet ($X/H = 7125$).

It can be remarked that, at low inertia, unlike spheres, which migrate towards the channel centerline [67], non-spherical particles keep migrating towards the four equilibrium positions (Figure 3.20). The same behavior is observed for $PNT57$ suspensions of different concentrations ($\Phi_{eq} = 0.2\%$) and for SNW suspensions.

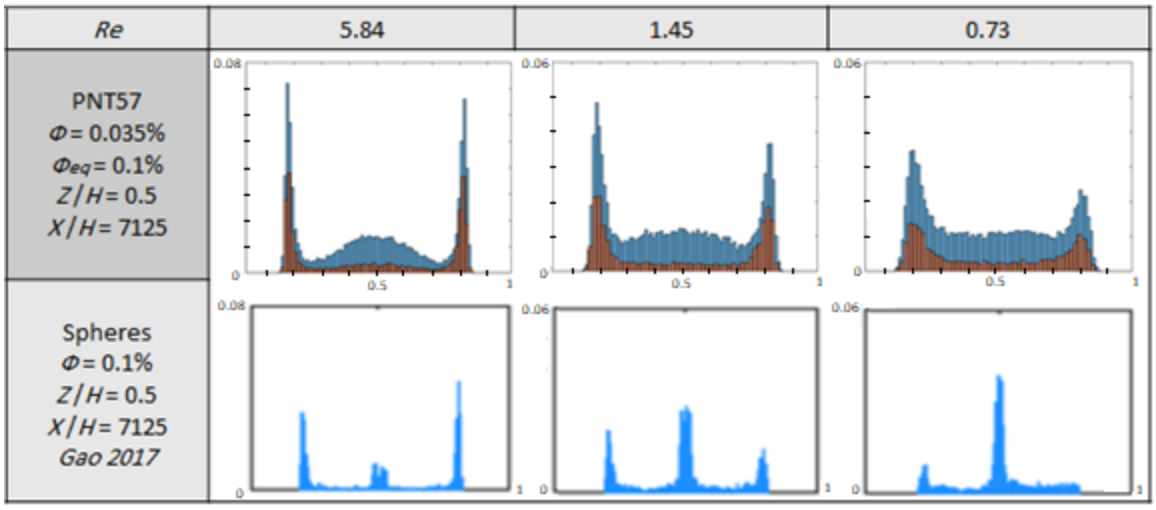

Figure 3.20. Midplane PDFs of $PNT57$ and spherical [67] suspensions ($\kappa \approx 0.1$) at different Re. The tests are done at the same X/H and the suspensions have the same number of particles. In the non-spherical case (up), blue bins represent all the identified particles, while red bins correspond to in-focus particles. In the spherical case (down), only the in-focus particles are represented in blue. The y-axis varies between 0 and 0.08 for $Re = 5.84$ and between 0 and 0.06 for the other values of Re.

Hur et al. [110], who experimentally studied the lateral migration of non-spherical particles, observed that, for $Re < 14$, only a small percentage of the particles flowed at the centerline of the channel. So, it was deduced that this migration regime is unstable. No further explanation was given.

To our knowledge, even at low values of Re, the channel centerline was never numerically found to be a stable equilibrium position. According to Abbas et al. [53], the migration towards the center might be due to interactions between the particles. Their conclusion was drawn after running numerical simulations at $Re = O(1)$ on a sphere, initially

positioned close to the channel centerline, and observing that the particle migrated towards a face-centered equilibrium position.

The interactions between non-spherical particles are surely more complicated than those between spheres. Due to the non-spherical particle geometry and the periodic rotation (c.f. Chapter 1), the sizes and the shapes of the recirculating zones induced by the particles change periodically during the period of rotation. This makes the interactions with other particles more fluctuating, which might explain the absence of the migration towards the channel centerline.

3.4. Summary and conclusions

In this chapter, the lateral migration of neutrally buoyant non-spherical particles in square microchannels has been experimentally studied. The results show that:

- At moderate fluid inertia, non-spherical particles migrate in a similar way as spheres. A two-stage migration is needed to attain the four face-centered equilibrium positions in a square channel.
- At high fluid inertia, similar to the spherical case, a transition to a new migration regime occurs, represented in a drop in the focusing degree.
- At low fluid inertia ($Re \leq 5$), unlike spheres [67], the migration towards the channel centerline is not observed and the particles keep on migrating towards the face-centered equilibrium positions (even at $Re \approx 1$).
- The dependence of the equilibrium position and focusing degree on Re, Φ, X/H and κ is the same for spherical and non-spherical particles.
- Concerning the effect of the particle aspect ratio λ on the equilibrium position, for the experimental conditions of this study, Y_{eq} is not a function of λ. In fact, two particles, with different aspect ratios but the same confinement ratio, have similar equilibrium positions.
- Non-spherical particles focus in larger zones around the four equilibrium positions, when compared to spheres flowing at the same experimental conditions.

4. Rotational behavior

4.1. Introduction

As explained in the previous chapters, it is essential to understand the rotational behavior of a non-spherical particle flowing in a microchannel, and link it to the particle's inertial migration. In this chapter, the evolution of the particle rotational mode in function of the lateral migration is presented qualitatively and quantitatively (Section 4.2), and the dynamics of the tumbling mode are investigated (Section 4.3).

4.2. Rotational mode

4.2.1. Qualitative observations

In this subsection, in order to follow the particle and identify its rotational mode, images captured at high frame rates are studied. For each configuration, around 20 particles were identified and tracked. Only particles with sharp and clear contours were taken into account, since it is complicated to determine the orientations of blurry particles.

In this study, the Reynolds number varies between 0.7 and 58. At higher fluid inertia, this study was not possible, due to the drop in the image quality (low brightness and contrast, small field of view).

Figures 4.1a and 4.1b show the evolution of the orientation of a peanut and a snowman particle, respectively, while flowing in the channel midplane ($Z/H = 0.5$), along their equilibrium positions. These two particles rotate around a common axis, parallel to the closest cross-sectional wall. This rotation is the tumbling motion described in the literature (and presented in Chapter 1).

In addition, the two particles tumble with the same sense of rotation: they rotate clockwise in the right-handed Cartesian coordinate system formed by the flow direction, the normal to the closest wall (directed from the wall towards the channel center), and the normal to the visualization plane.

Visualizations done on midplanes, over the studied range of Re $(0.7 - 58)$, show that, all of the focused particles were tumbling, with the same sense of rotation, regardless of Reynolds number and the type of the particle (SNW or PNT).

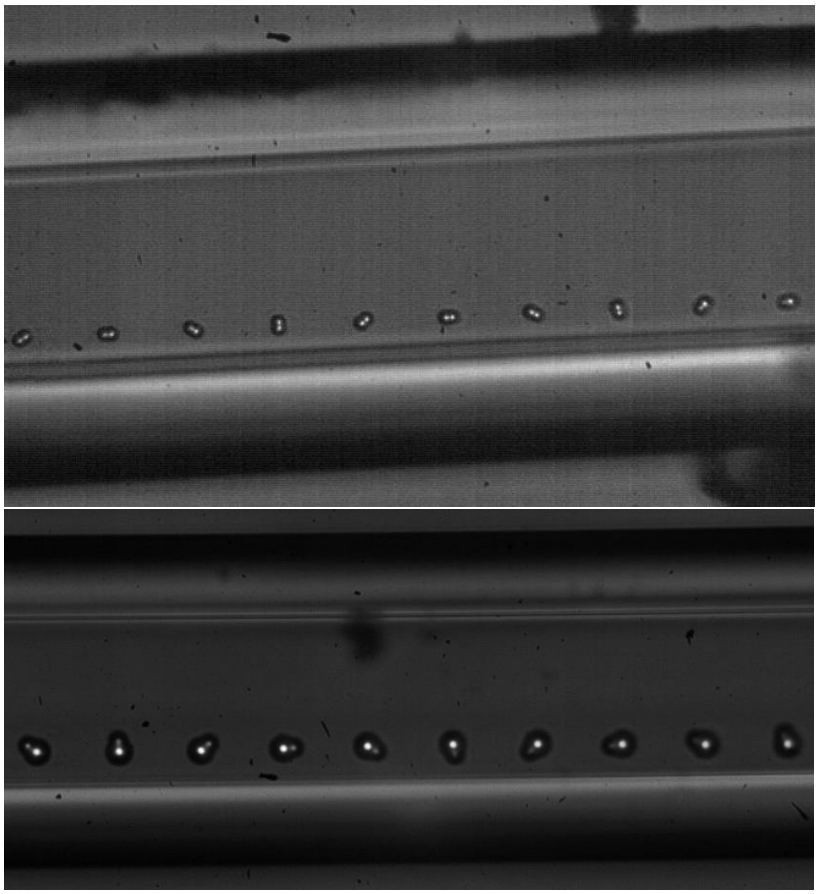

Figure 4.1. The tumbling mode of two focused bright tumbling $PNT57$ (up) and SNW (down) particles, at $Re = 5.84$ and $Z/H = 0.5$. These figures are obtained by superposing 10 consecutive images with the background. The suspension is flowing from left to right.

To check if all the particles in the channel have this rotational mode, and to find the coupling between the rotational behavior and the lateral migration, a channel scan has been done. The chosen configuration had a ring-shaped distribution ($Re = 5.84$). Five planes were studied: the midplane ($Z/H = 0.5$), two intermediate planes ($Z/H = 0.375$ and 0.625), and two farther planes ($Z/H = 0.25$ and 0.75). Only the bright particles were tracked in each plane.

In the midplane, the bright focused particles tumbled as described earlier.

In the intermediate planes, two types of bright particles were identified: the ones that are located on the ring and are in their second phase of migration (located at $Y/H = Y_{eq}/H$ and $Z/H \neq 0.5$) (Figure 4.2 up), and the other ones that are still in their first phase of migration ($Y/H \neq Y_{eq}/H$)(Figure 4.2 down). None of the studied particles tumbled, since the orientation between the particles' major axes and the vorticity axis Z, the camera's axis, was time-dependent (c.f. Figure 1.11. in Chapter 1). The type of this rotation is complex to guess using only one camera, but it resembles the kayaking motion described in the literature (Chapter 1).

Figure 4.2. The trajectories of two SNW particles. The upper particle is focused on the ring and is in its second phase of migration. The lower particle is still in the first phase, reaching the equilibrium ring. The test is done at $Re = 5.84$ and $Z/H = 0.625$.

In the farther planes ($Z/H = 0.25$ and 0.75) (Figure 4.3), bright particles were distributed all over the channel, indicating that these planes were located on the ring (c.f. Figure 3.1 Chapter 3). At the center of the channel ($Y/H = 0.5$), all the focused particles were rotating about the axis parallel to the closest cross-sectional wall (Figure 4.3 up). The other particles of the ring ($Y/H \neq 0.5$) were kayaking (Figure 4.3 down).

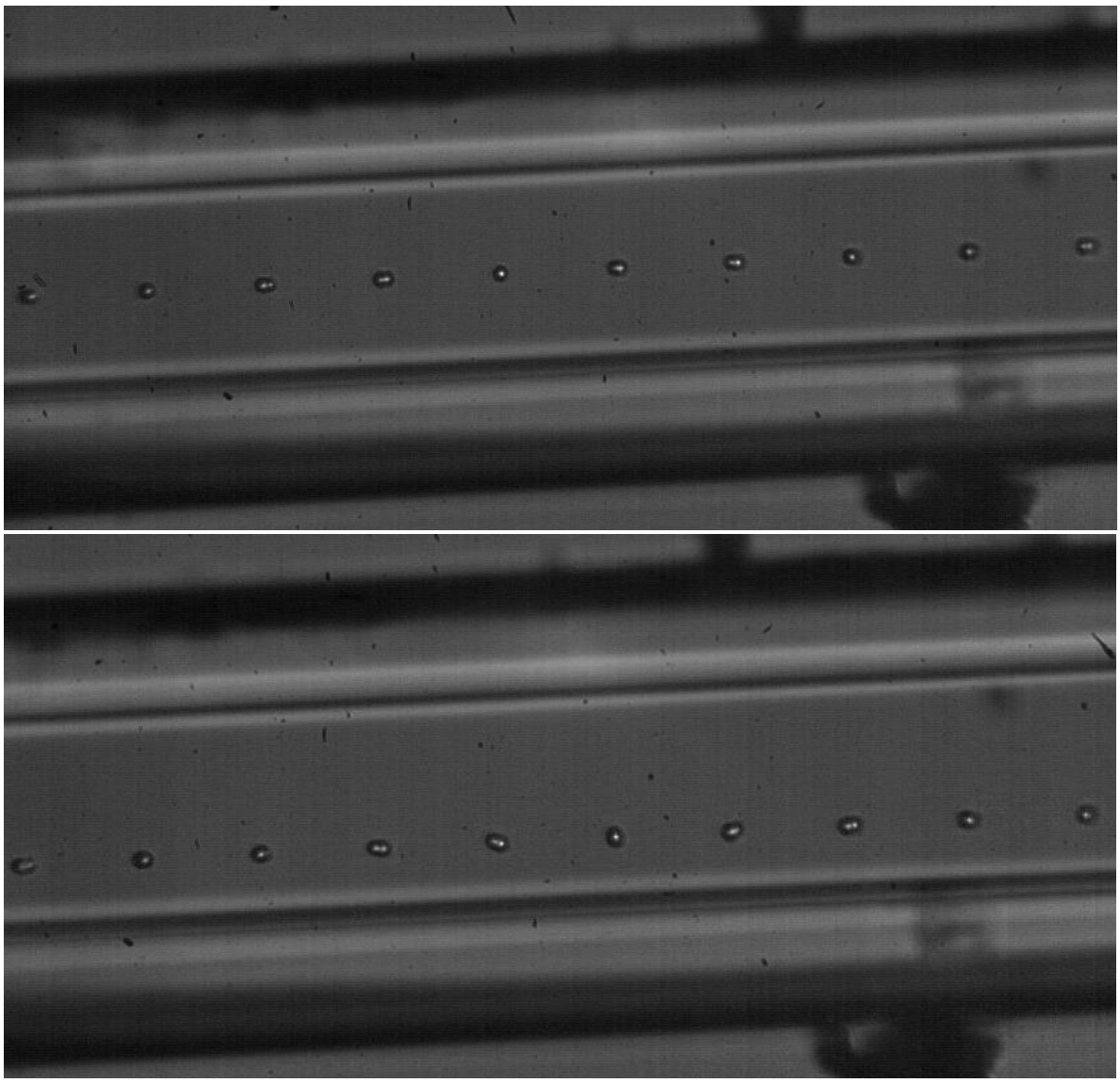

Figure 4.3. The trajectories of two $PNT57$ particles. The upper particle is focused on the equilibrium position and tumbling perpendicularly to the plane of the camera. The lower particle is located at the edge of the ring and having a kayaking rotational mode. The test is done at $Re = 5.84$ and $Z/H = 0.75$.

The observations from this channel scan permit to assume that a kayaking particle will switch to its equilibrium rotational mode (tumbling here), once it attains its equilibrium position. This was also found by Pan et al. [145] while studying prolate ellipsoids (c.f. Section 1.2.4.3.1). The same analogy was numerically observed in the case of spherical particles flowing in square channels [53]. Abbas et al. [53] numerically found that a migrating sphere has a three-component angular rotation, that drifts to a rotation around a unique axis parallel to the closest cross-sectional wall, once the particle is focused at the equilibrium position.

As shown in Chapter 3, at moderate Re, the lateral migration is enhanced with fluid inertia. Thus, by increasing Re, the fraction of focused particles increases and the fraction of tumbling ones too, which is in agreement with the results of Masaeli et al. [146], who found that the percentage of tumbling particles rose when Reynolds number was increased from 8 to 20.

The reason behind this drift in the rotational mode is linked to the velocity profiles. In fact, in a square channel, the velocity gradient has two components (in the y and z directions) (c.f. Figure 1.7 in Chapter 1) which depend on the position in the channel. This velocity gradient induces the rotation of the particle, where the orientation of the particle's major axis, with respect to the vorticity axis, is time-dependent (Kayaking mode, c.f. Figure 1.11 in Chapter 1), if the particle is not focused yet.

However, at the equilibrium position, the effect of one of the velocity gradient components is eliminated due to symmetry. The difference in the magnitude of the relative fluid velocity (in the reference of the particle) at the edges of the particle (the wall and center sides) creates a rotation along the axis passing by the particle centroid and parallel to the wall with which the particle is interacting (Tumbling mode) (Figures 4.1 and 4.3 up). The relative fluid velocity being greater on the wall-side edge, imposes the rotational sense described earlier for Figure 4.1, and schematized in Figure 4.4.

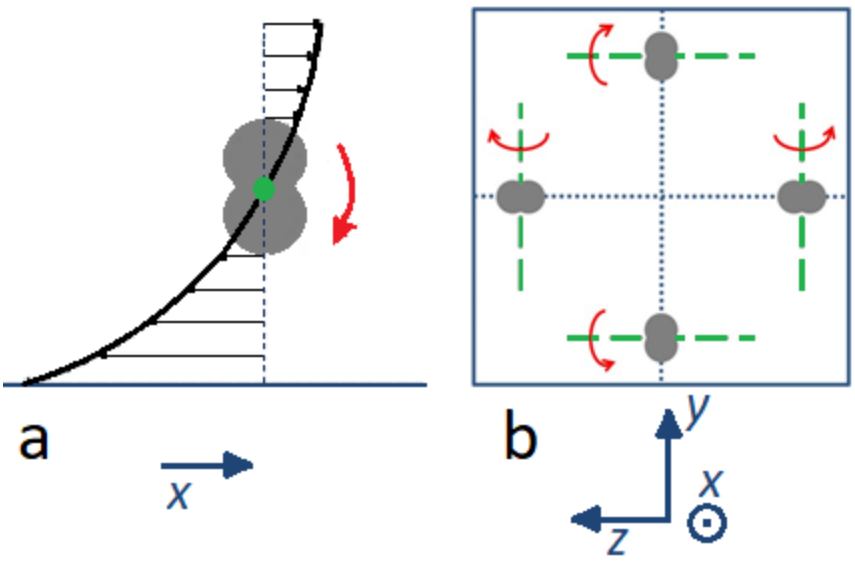

Figure 4.4. The tumbling behavior of focused elongated particles ($\lambda > 1$) in a square microchannel, observed from (a) the longitudinal and (b) the lateral cross-sections. The green dot in (a) and the dashed green lines in (b) represent the rotational axes. The red arrows correspond to the sense of rotation.

4.2.2. Quantitative results

In the previous subsection, the qualitative observations were done on around 20 particles per configuration. In order to confirm the results by statistical analysis, the number of studied particles should be increased. So, it has been decided to study the images that previously served to investigate the lateral migration, where more different particles can be identified within a relatively small number of images. However, in these images, a given particle appears on one image only, which makes impossible following it and detecting its rotational mode. To check if the particle is in a tumbling mode or not, a determinant geometrical parameter is needed.

A particle tumbling in the plane of the camera will conserve its identified surface A and rotational diameter d_{rot}. On another hand, a particle with an out-of-plane rotation (mainly kayaking) will periodically change its surface and rotational diameter with respect to the plane of the camera.

To make sure that the image processing code is sufficiently precise to categorize the particles into tumbling and non-tumbling ones, based on their surfaces and rotational diameters, high frame rate images are used. From these images, particles are visually sorted into tumbling and non-tumbling modes, based on 10 consecutive images per

particle. The distribution of A and d_{rot} is plotted for all the identified particles (Figure 4.5). The blue and red bins correspond to particles with non-tumbling and tumbling modes respectively.

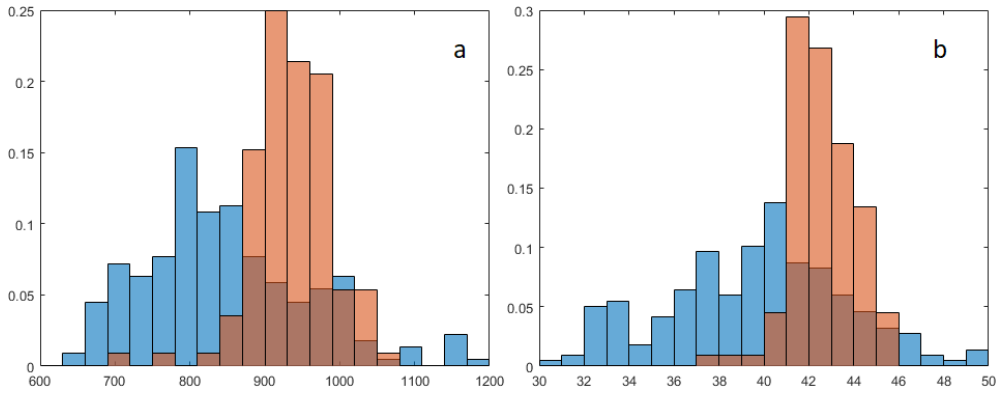

Figure 4.5. (a) Surface area A and (b) rotational diameter d_{rot} distribution of visually identified tumbling (red) and non-tumbling particles (blue). The x-axis is in pixels and the y-axis corresponds to the number of particles over the total number of particles.

Theoretically, the tumbling particles should have the same A and d_{rot}. However, it can be observed from Figure 4.5 that, the red histograms representing the tumbling particles form a gaussian curve around a peak. The width of this distribution is verified to be in the same order of magnitude as the fabrication error.

It can be also remarked from Figure 4.5 that, for both parameters, the blue and red histograms overlap. This overlapping is firstly caused by the fabrication error. It is also enhanced by out-of-plane rotating particles, that are in the plane of the camera at the moment of the capture of the image. This means that choosing an interval for A or d_{rot}, in which the particle is considered tumbling, will: (i) take into consideration non-tumbling particles that fall in this interval and (ii) neglect the tumbling particles that are not in the determined interval.

For two chosen intervals for A and d_{rot}, the error is calculated as being the number of wrongfully identified rotational modes over the total number of particles (Figure 4.6). In other words, the numerator corresponds to the sum of: (i) the number of particles visually identified as tumbling particles but numerically considered as non-tumbling particles, and

(ii) the number of particles visually classified as non-tumbling particles but numerically selected as tumbling particles.

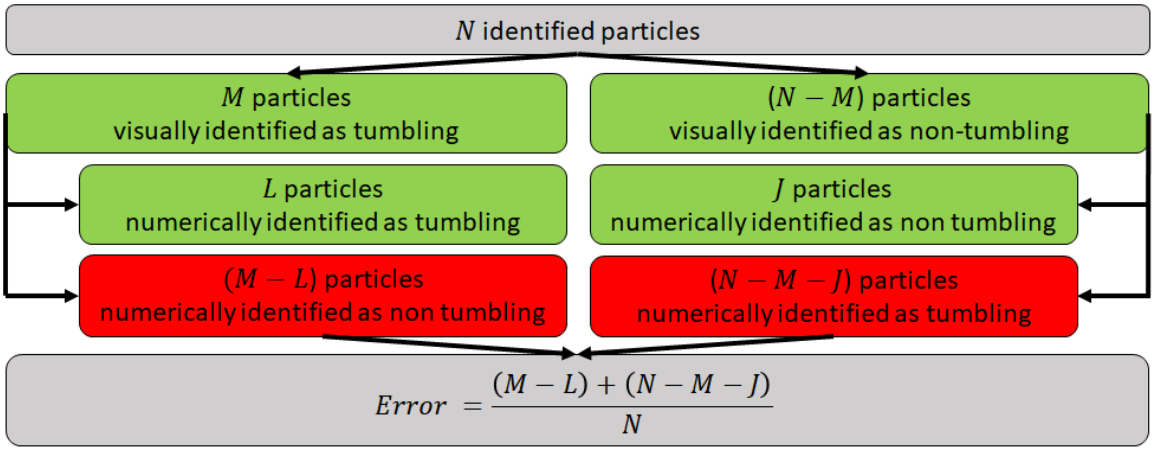

Figure 4.6. Schematic summarizing the error calculation.

For the same chosen intervals, but different configurations (high frame rate images of other planes and values of Reynolds number), it has been found that all the obtained errors were around 20% (±3%). So, since the calculated errors were very close, it was confirmed that the surface of the particle and its rotational diameter, are two parameters that can be used to determine if a particle is tumbling in the plane of the camera or not, with an 80% accuracy.

This method is now applied on low-frame-rate images, where the particle appears on one image only. However, since the two cameras (Sensicam and Photron) are different, the chosen intervals for A and d_{rot} were adapted, by analyzing highly focused configurations, acquired by the Sensicam camera, and considering that all the focused particles are tumbling.

Once the ranges of A and d_{rot} are defined for the low-frame-rate images, a channel scan is done (Figure 4.7). A non-fully developed focusing configuration is chosen (here a ring-distributed configuration, $Re = 5.84$), in order to detect particles in different migration phases. The blue bins correspond to the bright particles identified in the plane. The red

bins represent the bright particles that are considered having an in-plane tumbling rotational mode (with A and d_{rot} falling in the defined intervals).

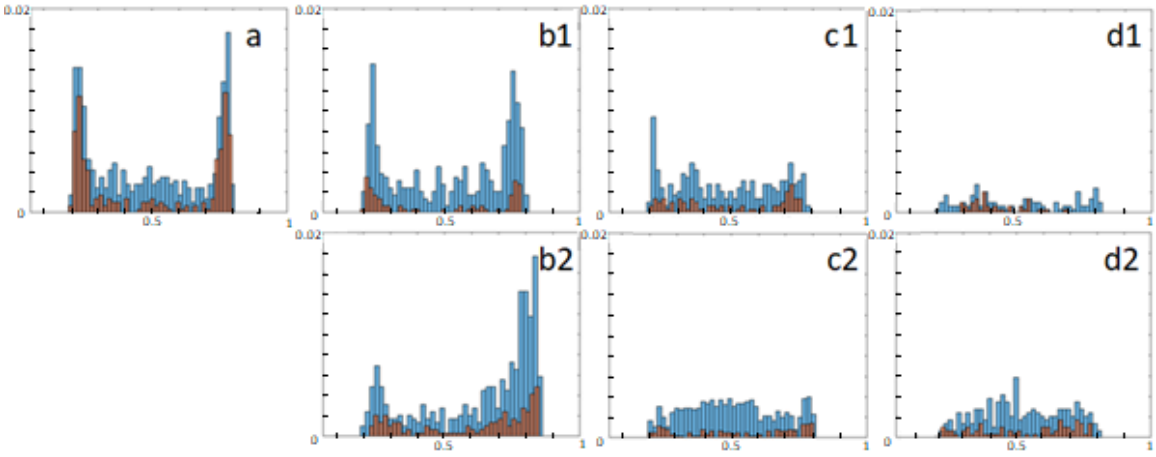

Figure 4.7. Histograms representing the distributions of bright PNT57 particles (blue) and in-plane bright tumbling particles (red) at different channel depths: (a) midplane (b1) and (b2) $Z/H = 0.625$ and 0.375; (c1) and (c2) $Z/H = 0.75$ and 0.25; (d1) and (d2) $Z/H = 0.875$ and 0.125. The x-axis represents Y/H and the y-axis varies between 0 and 0.02.

In the midplane (Figure 4.7a), the majority of the focused particles is tumbling. In addition, the fraction of non-focused particles, considered as tumbling ones, is low. In the other planes (Figure 4.7b1,b2,c1,c2,d1,d2), a relatively small fraction of tumbling particles is identified. These minor fractions, of non-tumbling focused particles and tumbling non-focused ones, are surely due to the error of considering the area and the rotational diameter as the determinant parameters to differentiate tumbling particles from non-tumbling ones.

In addition to this error, a fraction of the small red peaks that appear on the ring (at Y_{eq}/H) at $Z/H = 0.375$ and 0.625 (Figure 4.7b1,b2) might represent tumbling focused particles, located on the edges of these planes, close to the midplane ($Z/H = 0.5$).

It should be also mentioned that, in this channel scan, only the tumbling in the plane of the camera is identified. This explains why, on the ring, at $Z/H = 0.25$ and 0.75, practically no tumbling was detected, since the tumbling at $Y/H = 0.5$ is done perpendicularly to the plane of the camera (Figure 4.3 up).

To conclude, for the elongated particles of this study, the link between the lateral migration and the rotational mode is confirmed: focused particles tumble, while the non-focused particles do not tumble. This means that the particles switch to the tumbling mode once they attain their equilibrium positions.

4.3. Tumbling mode dynamics

In this section, the tumbling of focused particles is studied, as well as its dependence on some parameters such as fluid inertia.

For this study, images are captured at high frame rates, in order to track the change in the particle orientation. This latter is the angle that forms the particle main axis with the flow (x axis). It can be detected using the function *regionprops* described in Chapter 2.

Using our experimental setup and image processing technique, it is hard to precisely follow the rotation of a particle tumbling in the (xz) plane. For this reason, it has been decided to base the study on the already-identified bright focused particles tumbling in the (xy) midplane.

Since the same particle appears on different images, it is possible to get accurate particle tracking and orientation identification, using the developed post-processing code. On two successive images (i) and ($i+1$), a focused bright in-plane tumbling particle is located respectively at (X_i, Y_i) and (X_{i+1}, Y_{i+1}), with ideally: $X_{i+1} = X_i + x_t$ and $Y_{i+1} = Y_i$, where x_t is the x-distance travelled by the particle between two captured images. The theoretical calculation of x_t allows the determination of the position of the particle on the next image, with an uncertainty, evaluated using preliminary trial and error tests. The incertitude in the direction of Y is equal to ΔY, the maximum oscillation amplitude, calculated in Section 3.2.5 of Chapter 3.

Once the particle is well tracked, its orientation φ is identified on each image. The evolution of this angle in function of time is plotted for a SNW particle for three values of Reynolds number (Figure 4.8). For a fixed Re, it was verified that the obtained curve is

identical for 20 particles, but only one curve per Re was presented on Figure 4.8, for readability reasons.

For the three presented values of Re, the orientation of the particles seems to increase from 0° to 360°, representing a full rotation of the particle. This increase in φ seems to be non-linear in function of time. A plateau appears at the angles $0°$, $180°$ and $360°$, while inflection points are present at $\varphi = 90°$ and $270°$. A fitting example is added to Figure 4.8b to illustrate this non-linear evolution in function of time.

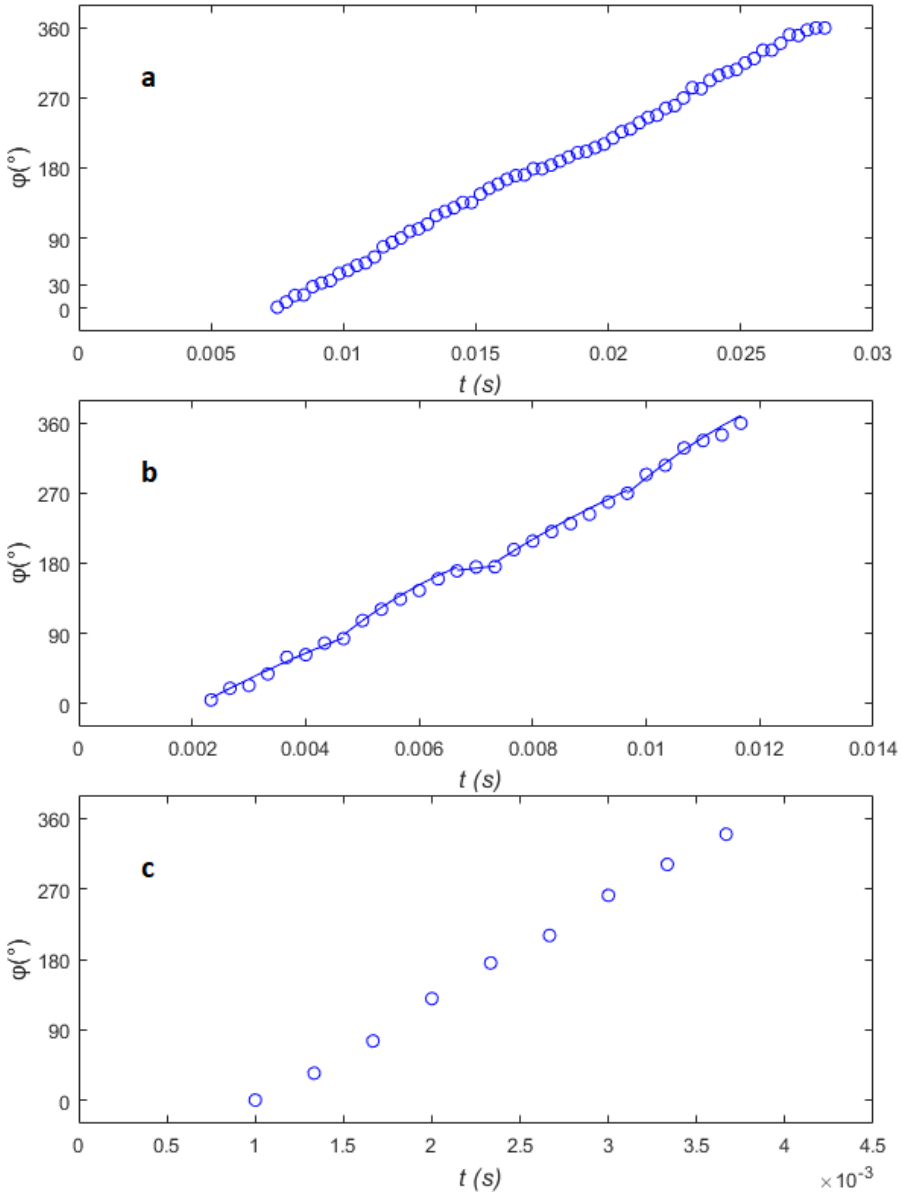

Figure 4.8. Evolution of the orientation of a SNW particle in function of time, at (a) $Re = 0.73$ (up), (b) 1.46 (center) and (c) 5.84 (down). The tests are done on the same suspension, at $X/H = 1000$.

Two main observations emerge from Figure 4.8.

Observation #1 from Figure 4.8: The slope of the curve $\varphi = f(t)$ is not constant, it has a maximum value around the angles 90° and 270°, and a minimum value for $\varphi = 0°, 180°$ and $360°$.

This means that the angular velocity ($d\varphi/dt$) is not constant in function of time; having its minimum and maximum values when the particle is aligned with and perpendicular to the flow respectively. This confirms the characteristics of the tumbling mode found in the literature (Chapter 1).

To deepen this study, a quantitative approach is developed, by investigating the statistical orientation distribution of focused bright particles in the midplane. The particles are identified using low-frame rate images, where the particle appears on one image only. The absolute value of the particle's orientation can vary between 0° (horizontal particle) and 90°, in nine intervals of 10° each. (Figure 4.9).

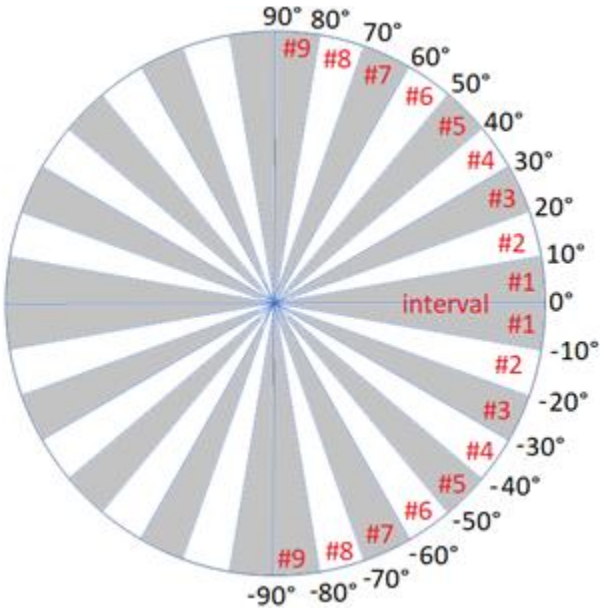

Figure 4.9. Schematic showing the decomposition into 9 intervals.

Figure 4.10 shows the orientation distribution, by interval, for the three previously presented values of Reynolds number 0.73, 1.46 and 5.84. The y-axis represents the

fraction of particles $f(i)$: the number of particles in an interval i $(1 \leq i \leq 9)$ over the total number of particles. Theoretically, for a particle rotating at a constant angular velocity, the nine fractions should be equal to 0.11 (10/90, or 20/180 or 40/360). However, it can be seen from Figure 4.10 that, for a fixed Re, the fractions of particles in the nine intervals are not equal. This means that the particle is tumbling with a varying angular velocity and not rotating at a constant angular velocity.

In addition, regardless of Re, the maximum and minimum fractions of particles are found near the horizontal (interval #1) and vertical (interval #9) orientations respectively. This indicates that the particle's angular velocity is minimum when the particle is aligned with the flow ($\varphi = 0°, 180°$ or $360°$), and has its maximum value when the particle is perpendicular to the flow direction. This finding confirms the observation #1 from Figure 4.8, and supports the theoretical results of Jeffery [111]. The phenomenon behind this behavior can be explained by the fact that, due to the velocity profile in the channel, the difference in the fluid's relative velocity (with respect to the center of the particle) at the edges of the particle is minimum and maximum when the particle is aligned with and perpendicular to the flow respectively. The higher this difference is, the faster the particle will rotate.

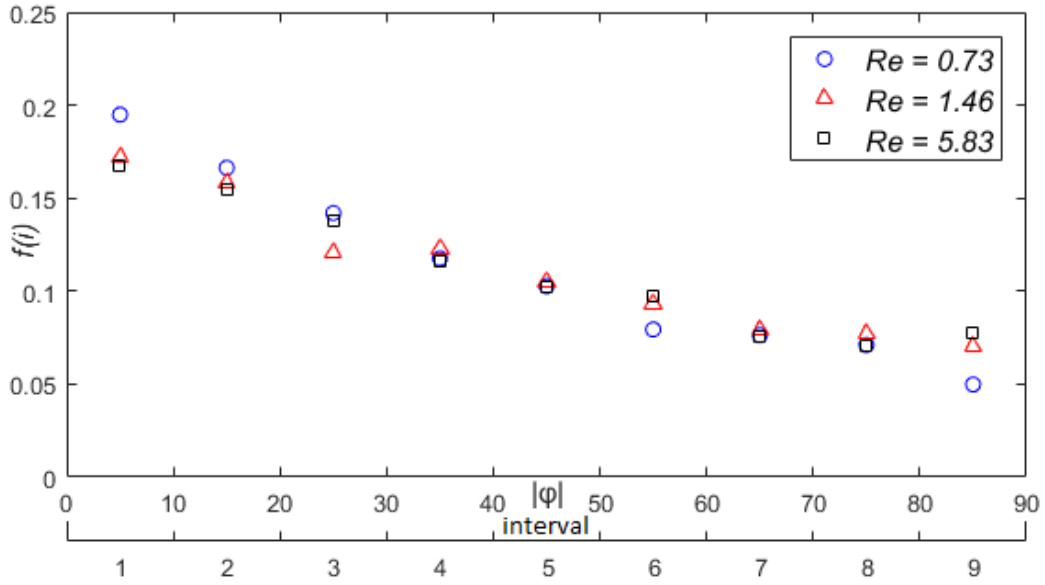

Figure 4.10. The orientation distribution for three different values of Reynolds number, at $X/H = 7125$. On the x-axis, the nine intervals are present. On the y-axis, the fraction of particles $f(i)$ is found.

The same study has been done at a larger range of Re ($Re \leq 58$), and showed that the focused particles tumble while flowing in the channel, with maximum and minimum angular velocities at $\varphi = k\pi/2$ and $k\pi$ respectively (with k being an integer) (Figure 4.11). The last results are thus still valid at higher values of Reynolds number.

It can be also noticed from Figure 4.11 that by increasing fluid inertia, the difference between the fractions rises: the fraction of roughly horizontal particles (interval #1) increases while the fraction of vertical particles (interval #9) decreases. This means that, by increasing Re, the difference between the maximum and minimum velocities of the particle increases. This also indicates that, in one period of rotation, the proportion of time, during which the particle will stay horizontal, increases.

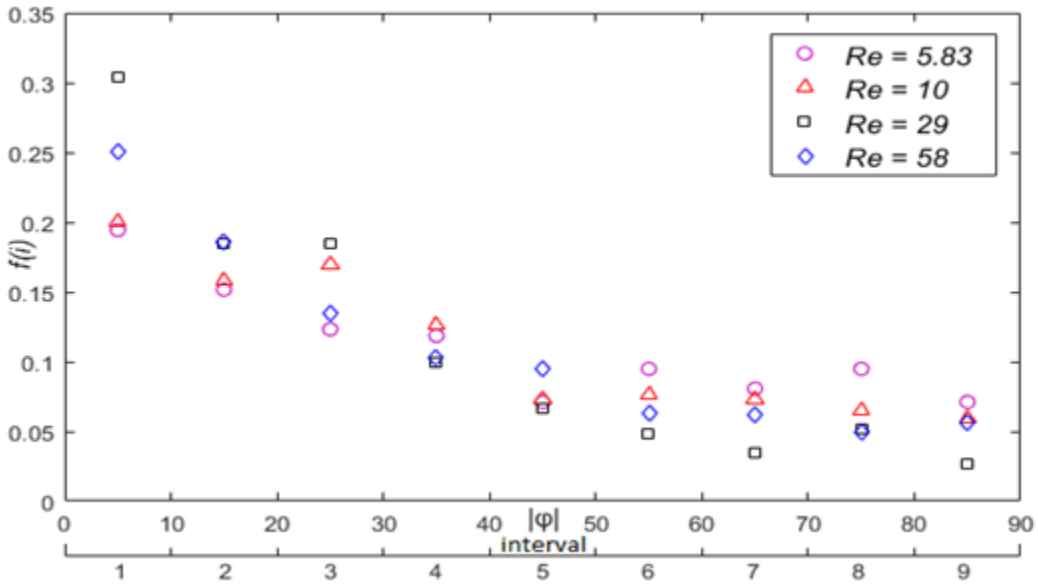

Figure 4.11. Orientation distribution for four different values of Reynolds number, at $X/H = 750$.

Finally, the same study is done at different distances from the channel inlet (X/H). Figure 4.12 represents the orientation distribution at a fixed Reynolds number ($Re = 29$ (Figure 4.12a) and 58 (Figure 4.12b)) for four different values of X/H. It can be observed that, the four curves are very close, meaning that the characteristics of the tumbling mode are not modified along the channel.

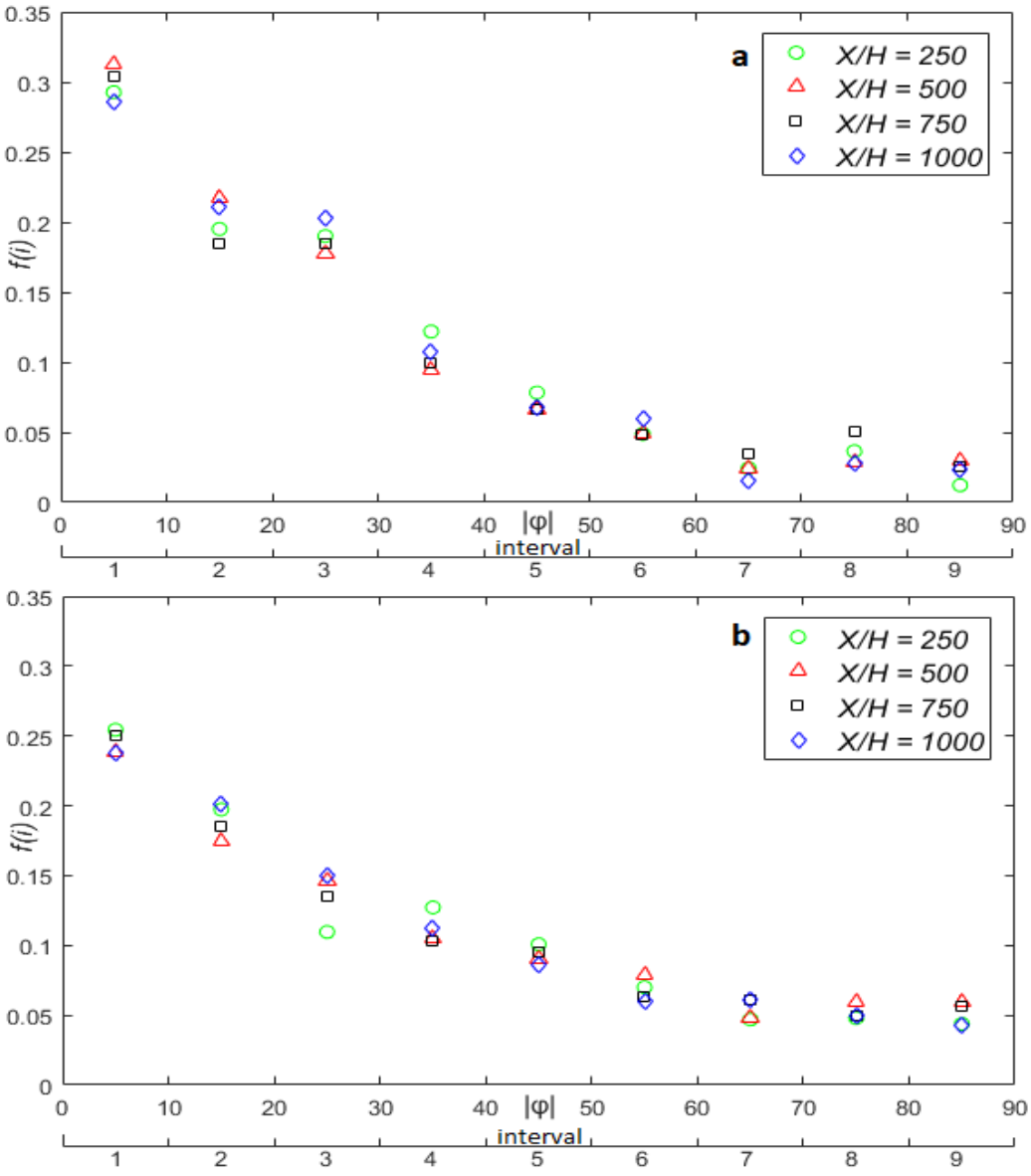

Figure 4.12. The orientation distribution for four different values of X/H, for (a) $Re = 29$ and (b) $Re = 58$.

Observation #2 from Figure 4.8: When Reynolds number increases, the time needed to complete one full rotation becomes shorter, indicating a decrease in the period of rotation.

The experimental values of the period of rotation, obtained from the curves $\varphi = f(t)$ (Figure 4.8), are plotted in function of Reynolds number (Figure 4.13), along with the theoretical ones deduced from an analytical study, based on Jeffery's equation (Equation

1.3 in Chapter 1) (detailed in Appendix C). The shear rate used in the theoretical calculation corresponds to the one at the center of the particle.

Although the tumbling motion was observed for Re varying from 0.7 to 58, it was only possible to identify the period of rotation up to $Re = 29$. At $Re = 58$, there were not enough experimental points to clearly measure the period of rotation.

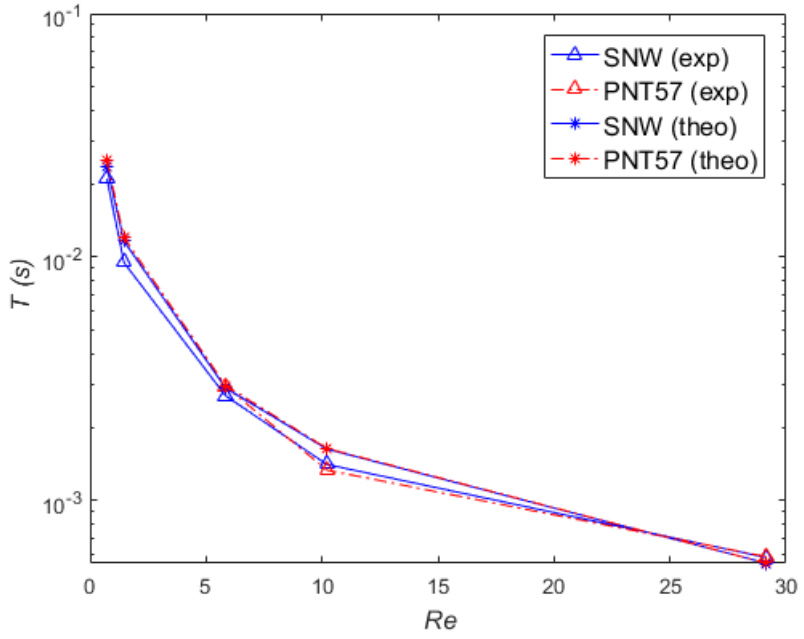

Figure 4.13. Experimental and theoretical periods of rotation as a function of Reynolds number, for two types of particles (SNW and $PNT57$). The experimental tests are done at $X/H = 1000$. The maximum error in the measured period of rotation is equal to $3.3 \times 10^{-4} s$.

Figure 4.13 shows a clear agreement between the measured periods of rotation and the theoretical ones. So, it can be confirmed that Jeffery's calculation of the period of rotation [111] is valid in the configuration of this study: nearly ellipsoidal particles flowing at $Re \leq 29$ in a square microchannel, with $\lambda = 1.2$ and 1.5 and respective $\kappa = 0.19125$ and 0.09625. This is in agreement with the findings of Bretherton [112] and Chwang [122] that showed that Jeffery's theory, designed for a simple unbounded shear flow, is applicable in Couette and Poiseuille bounded flows, as long as: (i) the particle is far from the wall and (ii) the shear rate used in Jeffery's equation (Equation 1.3) corresponds to the one at the center of the particle.

Regardless of the particle type, the period of rotation decreases when Re is increased. In fact, by raising fluid inertia in the channel, Poiseuille's velocity profile becomes sharper. This increases the difference between the relative velocities of the fluid (with respect to the particle) at the particle edges, which creates a greater torque, leading the particle to rotate faster (shorter period of rotation).

It can be also observed from Figure 4.13 that, the experimental curves of both types of particles (of different κ and λ) are almost superposed. The absence of the effect of λ on the period of rotation is surely linked to the closeness in the aspect ratios of the particles ($\lambda = 1.2$ and 1.5 for SNW and $PNT57$ respectively), which is in agreement with Jeffery's equation (Equation 1.3 in Chapter 1). From this equation, it can be also observed that the κ does not intervene in the calculation of T, which is coherent with the findings of this study, since the two particles have different values of κ and roughly the same value of T. However, these results are different from the findings of Hur et al. [110] ($2 < \lambda < 4, \kappa > 0.2$), who found that the rotational period increases with κ and is independent from λ.

4.4. Summary and conclusions

In this chapter, two main rotation-related parameters have been investigated: the rotational mode (qualitatively and quantitatively) and the period of rotation (theoretically and experimentally).

Concerning the rotational mode, it has been shown that, in the case of a migrating particle, the orientation of the major axis with respect to the vorticity axis is time-dependent, and the particle rotates with a three-component angular velocity (kayaking). Once the particle attains its equilibrium position, a switch from the kayaking mode to a tumbling one occurs. The particle starts rotating about the axis passing by its centroid and parallel to the closest cross-sectional wall.

The tumbling particle rotates at its minimum and maximum angular velocities when it is aligned with and perpendicular to the flow respectively. The difference between these

extreme values, as well as the proportion of time (per one rotation) spent at a horizontal orientation increase with Reynolds number. This last finding is interesting for applications where the orientation of the particles is critical (c.f. Chapter 1).

Regarding the period of rotation, it has been shown that T decreases when fluid inertia is increased. In addition, it has been confirmed that Jeffery's theoretical expression of T [111] is valid in bounded Poiseuille flows for Reynolds number less than or equal to 29, as long as the shear rate used in the formula corresponds to the one at the center of the particle.

Finally, it should be mentioned that, these findings are applicable for Re ranging between 0.7 and 58. Above $Re = 58$, the image quality was not sufficient to confirm the presence of tumbling at the equilibrium positions (small frame, low contrast and brightness). An amelioration of the experimental setup, in terms of the camera and the light source, is needed to widen the studied interval of Re. This would also help identify, if it exist, other rotational modes at higher values of Re, as found in the literature (Chapter 1).

5. Longitudinal ordering and train formation

5.1. Introduction

One of the main three phenomena occurring in the channel, is the longitudinal ordering, during which the particles interact with each other and form trains in the flow direction (c.f. Section 1.2.2.2 in Chapter 1). For several years now, the train formation is being deeply studied for spherical particles [67,68,70,80,93,159]. However, to our knowledge, only one recent numerical study exists in the non-spherical case [147], where the confinement ratio is relatively high ($\kappa \geq 0.24$), compared to the range of κ in our study ($\kappa < 0.2$).

The longitudinal ordering can be characterized by the fraction of particles in trains ψ, the normalized interparticle spacing l/d_{rot}, and the number of particles per train (c.f. Section 2.4 in Chapter 2).

In this chapter, the longitudinal ordering of non-spherical particles is analyzed and compared to that of spheres [67,80,93], by studying the evolution of the three characteristics mentioned above in function of κ, λ, Re, Φ and X/H (Section 5.3). In addition, the possible coupling between the longitudinal ordering phenomenon and the lateral migration (Section 5.2) as well as the one between the longitudinal ordering and the rotational behavior (Section 5.4) are investigated.

5.2. Longitudinal ordering and lateral migration

The fraction of particles in trains ψ, introduced in Chapter 2 is used in this section to quantify and evaluate the evolution of the longitudinal ordering of particles, in different configurations.

Figure 5.1 shows the evolution of ψ in the channel with respect to the distance from the inlet. It can be remarked that the fraction of particles in trains increases while advancing in the channel, indicating that trains form progressively.

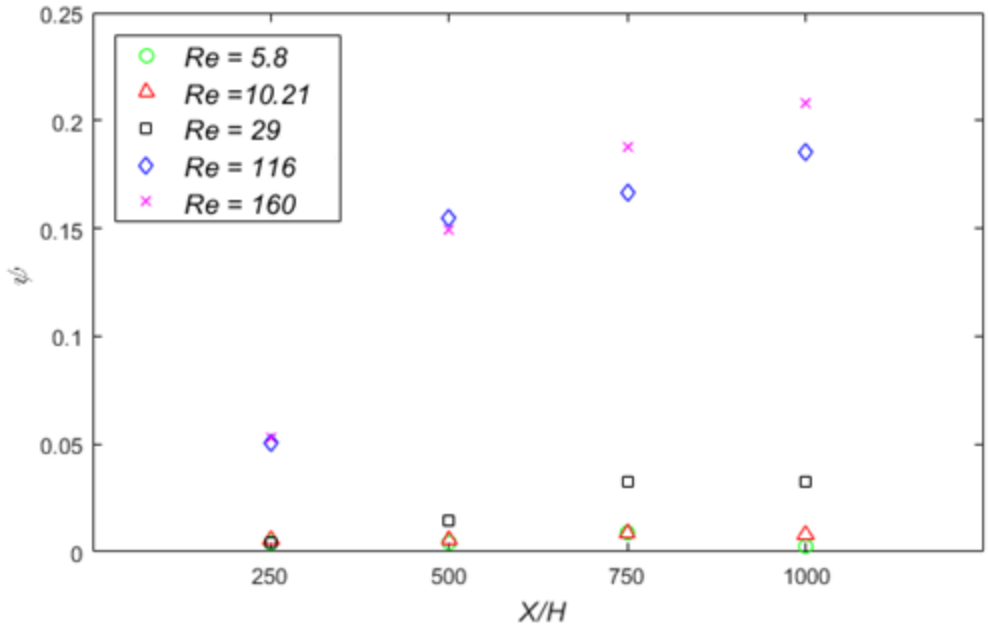

Figure 5.1. Evolution of the fraction of $PNT57$ particles in trains in function of the distance from the channel inlet (X/H), for different values of Reynolds number.

In previous works, done on spherical particles, Gao et al. [67,80] showed that the longitudinal ordering begins after the lateral migration: the trains are only formed once the particles have attained their equilibrium positions. To verify this coupling between the two phenomena, the fraction of particles in trains ψ and the focusing degree η are plotted in function of Re, for $PNT57$ and SNW particles (Figure 5.2). It can be observed from Figure 5.2 that the two parameters have close evolutions in function of Re: an increase to a maximum value at a critical Reynolds number Re_{cr}, then a decrease. The value of Re_{cr} is the same for η and ψ (Figure 5.2 (up)). This shows a coupling between the longitudinal ordering and the lateral migration. However, this coupling is complex, and appears to depend on the flow configuration (Re), since for the same value of η (red triangles at $Re = 29$ and $Re = 218$, for $PNT57$ particles), two different values of ψ (blue circles) are obtained.

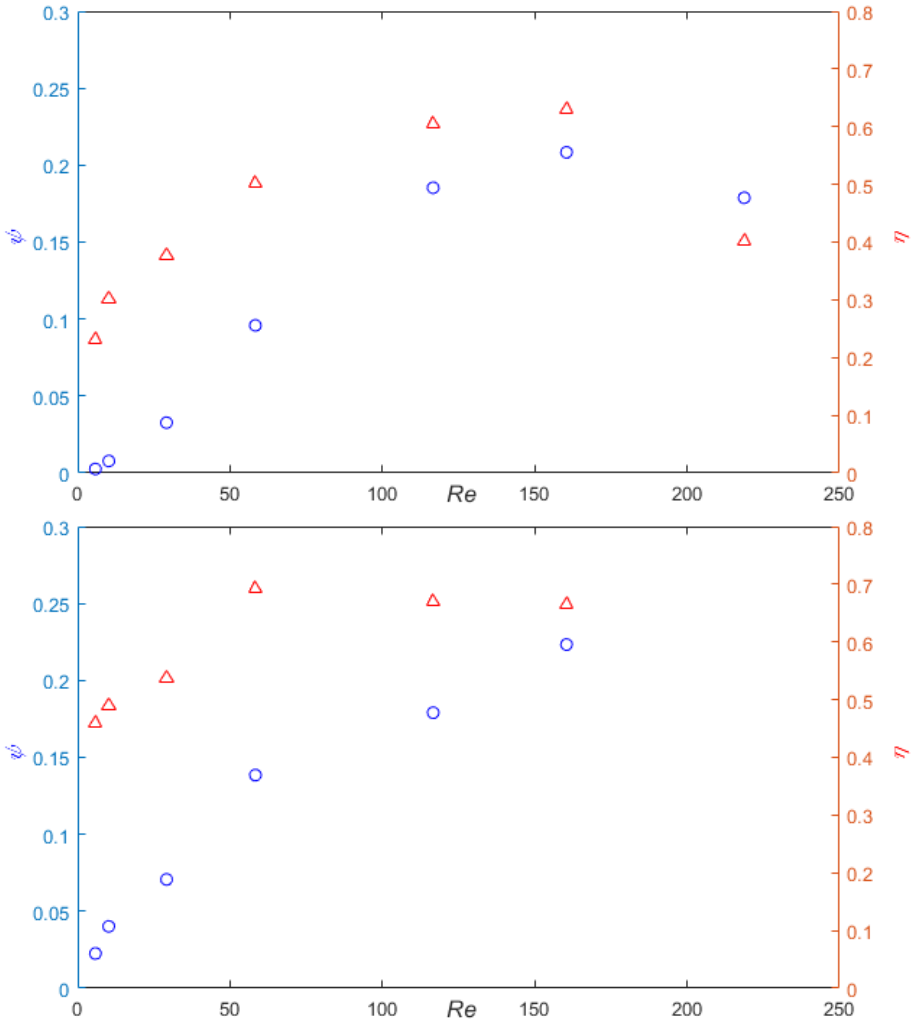

Figure 5.2. Evolution of the fraction of particles in trains ψ (blue circles, left y-axis) and the focusing degree η (red triangles, right y-axis) in function of Reynolds number, for $PNT57$ (up) and SNW (down) particles.

To get more deeply into the nature of this connection, a channel scan is done, in order to locate the trains and identify the particles migratory status. This helps understand which phenomenon occurs first. Figure 5.3 shows the distribution of trains in the channel at a low Reynolds number ($Re = 5.83$), for $PNT57$ particles, where most of them are still in their second stage of migration (ring-shaped distribution).

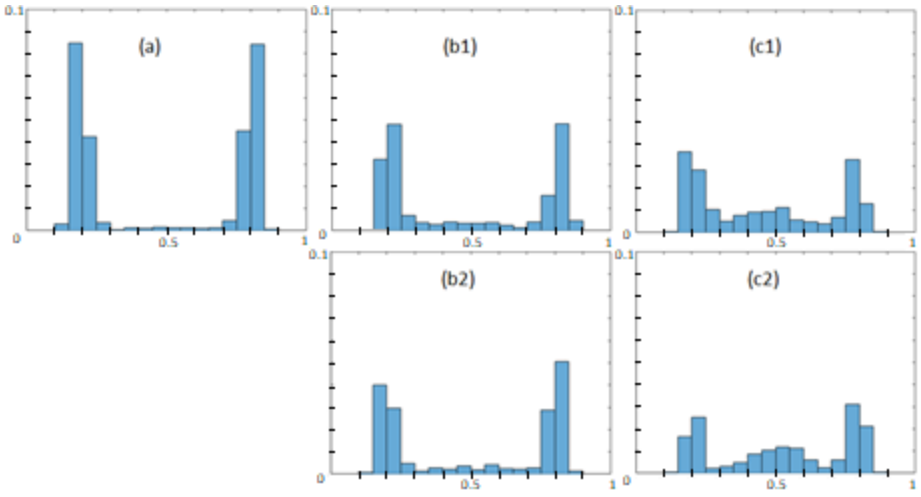

Figure 5.3. Histograms representing the distributions of bright $PNT57$ particles in trains, at $Re = 5.83$ and different channel depths: (a) midplane (b1) and (b2) $Z/H = 0.75$ and 0.25; (c1) and (c2) $Z/H = 0.875$ and 0.125. The x-axis represents Y/H and varies between 0 and 1. The y-axis corresponds to the fraction of bright particles in trains and varies between 0 and 0.1.

It can be observed from Figure 5.3 that the trains are mainly located on the ring. This means that the trains are formed before attaining the equilibrium positions. This is different from the findings of Gao et al. [67,80,93] on spherical particles, where trains were only found at the four face-centered equilibrium positions.

This result is preliminary, since the test has been done on one type of particles ($PNT57$) and at one Reynolds number, where the value of ψ is very low (c.f. Figure 5.2). To confirm and generalize this finding, other tests should be done in other configurations (other Re, λ, κ, X/H, Φ…).

So, based on what was presented in this section, it can be concluded that, the train formation is conditioned by the lateral migration. In fact, the lateral migration is developed through the channel and is enhanced by fluid inertia (Chapter 3). The more the migration is advanced, the closer the particles are from each other (on the ring and in the focusing zones), which increases the particle-particle interactions and the chance of forming trains. At higher fluid inertia, the focalization on the four face-centered equilibrium positions is less pronounced (new migration regime, Chapter 3), which explains the drop in the focusing degree and in the fraction of particles in trains.

5.3. Characteristics of trains

As defined in Chapter 2, three main criteria characterize the longitudinal ordering: the fraction of particles in trains ψ, the normalized interparticle spacing l/d_{rot} and the train composition, represented by the number of particles per train. In this section, the effects of κ, λ, Re, and Φ on the longitudinal ordering phenomenon, using these criteria, are investigated.

5.3.1. Effect of the confinement ratio κ

5.3.1.1. Fraction of particles in trains ψ

Two $PNT57$ ($\kappa = 0.09625$, $\lambda = 1.5$) and $PNT35$ ($\kappa = 0.06375$, $\lambda = 1.5$) suspensions, of the same number of particles, are studied at $X/H = 1000$, and their corresponding ψ is plotted in function of the channel Reynolds number Re (Figure 5.4a) and the particle Reynolds number Re_p ($Re_p = Re \times \kappa^2$) (Figure 5.4b).

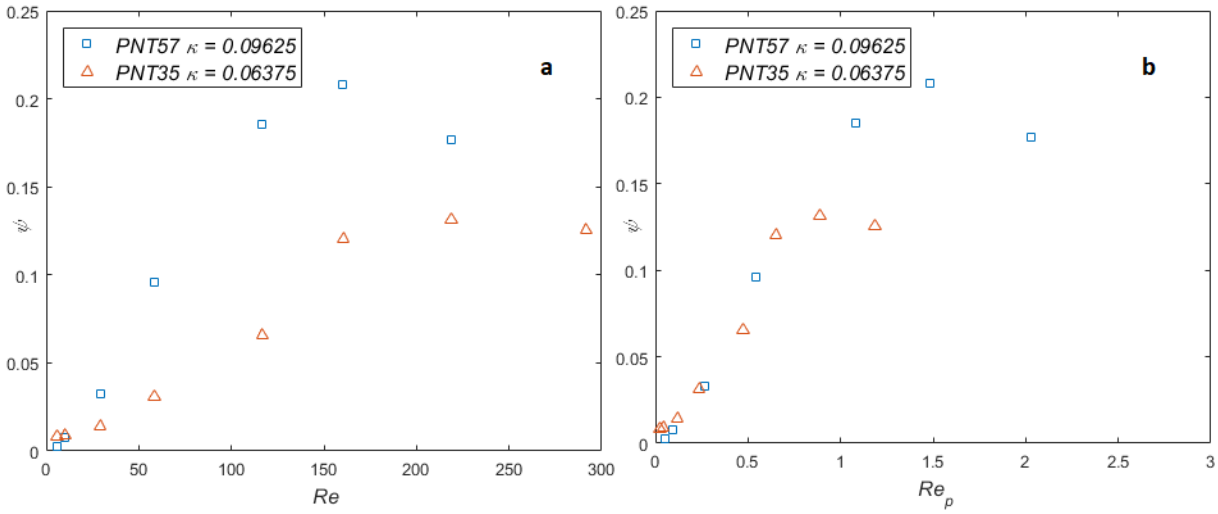

Figure 5.4. Evolution of the fraction of particles in trains ψ in function of (a) the channel Reynolds number and (b) the particle Reynolds number, for $PNT35$ ($\kappa = 0.06375$, red triangles) and $PNT57$ ($\kappa = 0.09625$, blue square) particles. Both suspensions have the same number of particles ($\Phi_{eq} = 0.1\%$) and the tests are done at $X/H = 1000$.

Figure 5.4a shows that, for both particles, ψ increases to a maximum value at a critical Reynolds number then decreases. A greater κ induces a decrease in the value of Re_{cr} and an increase in the values of ψ.

Concerning Figure 5.4b, it can be clearly observed that the increasing parts of both curves overlap. This means that the particle Reynolds number, characterizing the shear flow seen by the particle, controls the train formation.

These results are similar to the ones obtained by Gao et al. [67,80] on spherical particles.

The effect of κ on the values of ψ could be explained by the fact that larger particles create larger recirculation zones [71,79], increasing the chance of capturing other particles and forming trains.

5.3.1.2. Train composition

In this study, regardless of the experimental conditions (Re, λ, κ, Φ, X/H), the majority of the trains are formed of three particles, a smaller fraction corresponds to trains of four particles, and a roughly null fraction represents trains of more than four particles, as shown for example in Figure 5.5. This is in full agreement with the experimental results of Gao et al. 2021 [93] (square cross-section) and Matas et al. 2004 [70] (circular cross-section) on spherical particles. This is also coherent with the numerical work of Gupta et al. [159] on spheres, who found that, the maximum number of stable particles per train is equal to three, for our range of κ and Re. They explained that the maximum length of stable train structures is approximately equal to the channel hydraulic diameter (H for square channels), and that a decrease in κ increases the number of particles stable in a train.

Figure 5.5 compares the train composition of $PNT35$ and $PNT57$ suspensions. These particles have the same geometrical shape ($\lambda = 1.5$) but different confinement ratios. It can be remarked that, when κ is increased, the fraction of three-particle trains gets lower while the other fractions increase (especially four-particle trains). In other words, longer trains are found for the larger particles ($PNT57$). This is different from the spherical result of Gupta et al. [159] explained above, and might be linked to the non-spherical geometry of the studied particles.

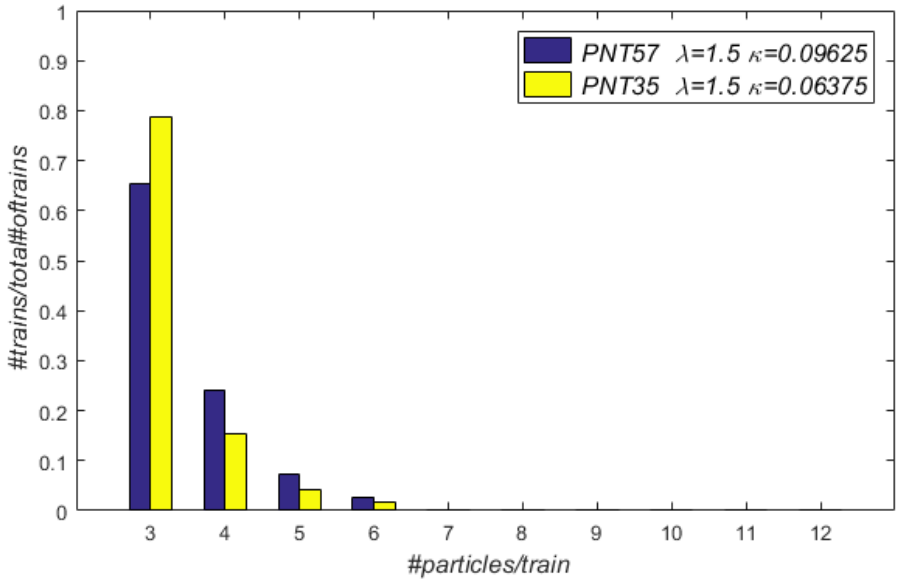

Figure 5.5. Fraction of trains as a function of the number of particles per train, for $PNT57$ ($\kappa = 0.09625$) and $PNT35$ ($\kappa = 0.06375$) particles, at $Re = 58$. Both suspensions have the same equivalent concentration ($\Phi_{eq} = 0.1\%$).

5.3.2. Effect of the particle aspect ratio λ

5.3.2.1. Fraction of particles in trains ψ

Figure 5.6 shows the evolution of the fraction of particles in trains ψ in function of the channel Reynolds number (Figure 5.6a) and the particle Reynolds number (Figure 5.6b), for three $PNT57$ ($\kappa = 0.09625$, $\lambda = 1.5$), SNW ($\kappa = 0.19125$, $\lambda = 1.2$) and spherical ($\kappa = 0.11$, $\lambda = 1$, magenta circles) [67] suspensions.

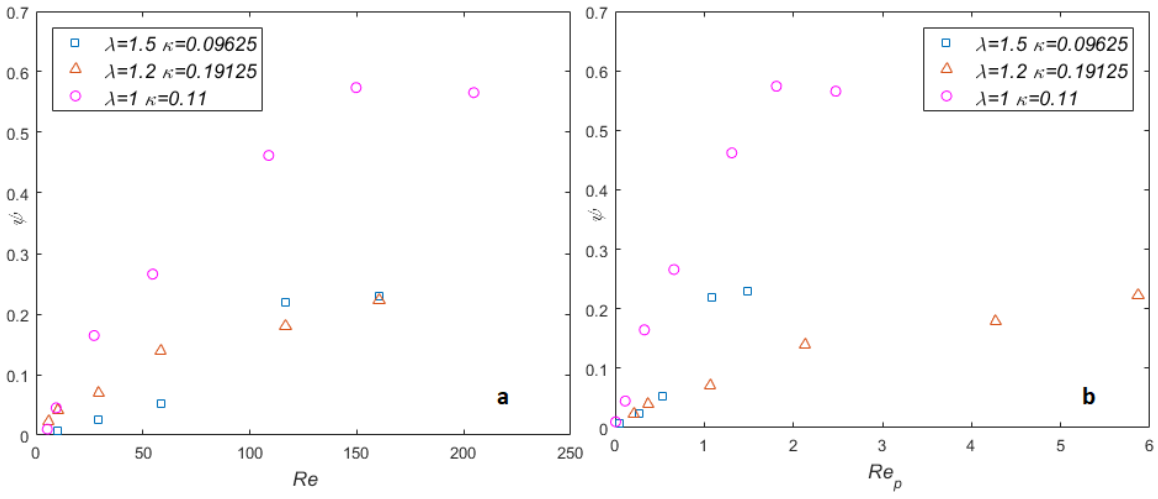

Figure 5.6. Evolution of the fraction of particles in trains ψ in function of (a) the channel Reynolds number and (b) the particle Reynolds number, for $PNT57$ ($\kappa = 0.09625$, $\lambda = 1.5$, blue square), SNW ($\kappa = 0.19125$, $\lambda = 1.2$, red triangle)

and spherical ($\kappa = 0.11$, $\lambda = 1$, magenta circles) [67] particles. The three suspensions have the same number of particles ($\Phi_{eq} = 0.05\%$) and the tests are done at $X/H = 1000$.

It can be observed from Figure 5.6a that all the curves increase with Re, to a maximum value at a critical Reynolds number. The $PNT57$ and spherical curves are seen to decrease after attaining Re_{cr}.

Based only on the effect of κ found in Section 5.3.1, the spherical ($\kappa = 0.11$) and the $PNT57$ ($\kappa = 0.09625$) curves would overlap in Figures 5.6a and 6.6b. In addition, the SNW ($\kappa = 0.19125$) curve would be the highest curve in Figure 5.6a, and its increasing part would overlap with the increasing parts of the two other curves in Figure 5.6b.

However, it can be observed from Figure 5.6a that, for a fixed Re and κ (spherical and $PNT57$), when λ increases (from 1 to 1.5), the fraction of particles in trains ψ decreases. This shows a clear effect of λ on ψ. This result might be linked to the rotation of the non-spherical particles. When a sphere rotates, the recirculating zones in front and behind the particle conserve the same size, thanks to the symmetry in the spherical geometry. However, when a non-spherical particle rotates, the sizes of these zones periodically change in function of the orientation of the particle's main axis. Due to this instability, it becomes harder to capture particles and form trains, which explains the low values of ψ, when the non-spherical case is compared to the spherical one.

Based on the effects of κ and λ on ψ, the curve representing the evolution of the SNW suspension in function of Re (Figure 5.6a) would be higher than that of the $PNT57$ suspension, since $\kappa(SNW) > \kappa(PNT57)$ and $\lambda(SNW) < \lambda(PNT57)$. This is the case only for low values of Re (Figure 5.6a). In addition, it can be observed from Figure 5.6b that the curve representing the evolution of ψ for the SNW particles overlaps with the $PNT57$ curve only for very low Re_p. For the rest of the range of Re_p, the SNW curve is lower than the $PNT57$ curve. This means that the shape of the particle has an effect on the train formation. In fact, the $PNT57$ particles are symmetric doublets, while the SNW particles are asymmetric doublets. This asymmetry along one of the axes of the SNW,

along with the particle's periodic rotational behavior, complexifies the time-dependent recirculating zones around the particle, and thus the interactions with other particles, which might reduce the possibility of forming trains, and thus decrease ψ.

5.3.2.2. Normalized interparticle spacing l/d_{rot}

The second important criterion to investigate is the interparticle spacing. It corresponds to the most probable distance between the centers of two consecutive particles of a train, in a given configuration (Re, Φ, X/H, κ). The normalized interparticle spacing is equal to this distance normalized by the rotational diameter of the particle d_{rot} (or the diameter d_p in the case of a spherical particle).

For the spherical case, in order to determine the value of l/d_p, Gao [67] plotted a histogram of all the identified interparticle distances in a given configuration, and chose l/d_p corresponding to the highest bin. The same method is used in the case of SNW particles, for which a peak is also identifiable (Figure 5.7), whatever the flow conditions and the distance from the channel inlet.

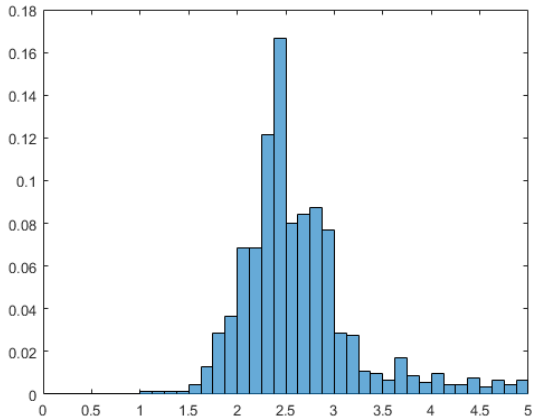

Figure 5.7. Example of the distribution of the normalized interparticle spacing in the case of SNW particles, flowing at $Re = 160$ and $X/H = 750$. The y-axis represents the number of spacings over the total number of spacings. The x-axis corresponds to the normalized interparticle spacing (l/d_{rot}).

Figure 5.8a represents a histogram of the normalized interparticle spacing l/d_{rot} in the case of a $PNT57$ particle. It can be remarked that no sharp peak is observed, meaning that there is no unique preferential spacing between the centers of $PNT57$ particles of a

train. This was observed for all the $PNT35$ and $PNT57$ configurations, regardless of X/H, Φ and Re.

This finding rose the question of whether or not, the choice of $5d_{rot}$, the longest possible spacing between the centers of the particles of a train, should be increased in order to identify a peak in the histogram of l/d_{rot}. To answer this question, a $PNT57$ configuration is studied and trains are identified by imposing the same criteria described in Section 2.4 of Chapter 2, while increasing the critical interparticle spacing from $5d_{rot}$ to $10d_{rot}$. A small but negligible increase in the fraction of identified trains is observed (from 0.185 to 0.203). Concerning the distribution of l/d_{rot}, the identification of the preferential interparticle spacing was still impossible due to the absence of a clear sharp peak (Figure 5.8b).

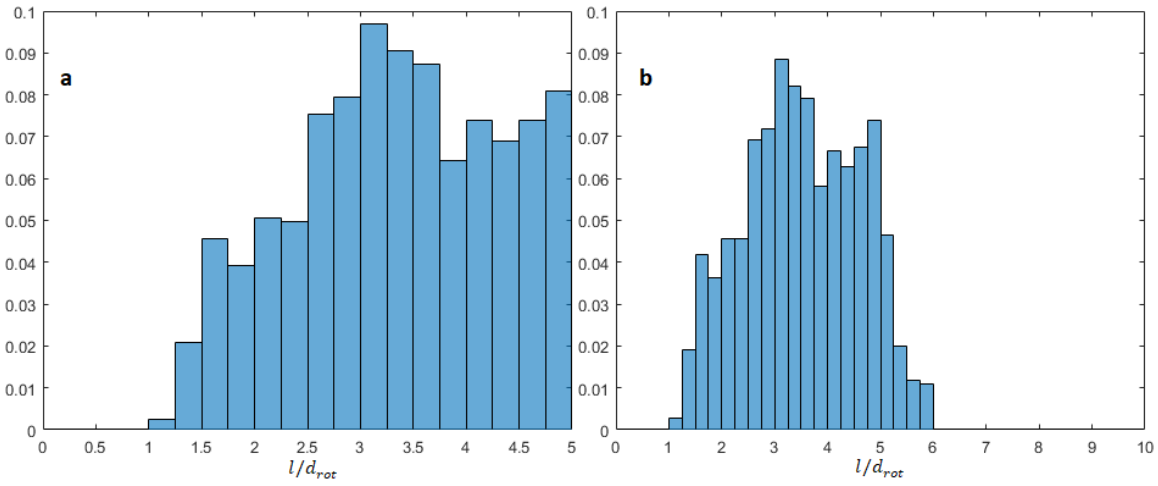

Figure 5.8. Distribution of the interparticle spacing in the case of $PNT57$ particles for $Re = 116$ and $X/H = 1000$, for two different values of the critical interparticle spacing ((a) $5d_{rot}$ and (b) $10d_{rot}$). The y-axis represents the number of spacings over the total number of spacings. The x-axis corresponds to the normalized interparticle spacing (l/d_{rot}).

In the monodisperse spherical case, Gao [67] found that the key parameter is the distance between the surfaces of two consecutive particles and not the distance between their centers. He showed that this distance, which is equal to $(l - d_p)$ (d_p being the diameter of the sphere), is constant. His finding was based on his experimental results, as well as those of Matas et al. [70] and Humphry et al. [73]. This can explain why, in the non-

spherical case (especially for PNT), the distance between the centers of the particles is not constant.

In fact, rotating non-spherical particles in train, with a constant distance l_S between their surfaces, will necessarily have a non-constant distance l_C between their centers (Figure 5.9). The distance separating the extreme values (l_{C1} and l_{C2}), between which l_C fluctuates during one period of rotation, increases with the particle aspect ratio λ (Figure 5.9). This might explain why a peak appears in the histograms representing l_C/d_{rot} in the case of SNW particles ($\lambda = 1.2$), and disappears in the case of $PNT35$ and $PNT57$ particles ($\lambda = 1.5$).

Additional analysis is necessary to confirm these conclusions. In fact, the distances between the surfaces of the particles of the trains should be identified on the acquired images. However, given the non-spherical geometry of the particles and their rotational behavior, this study implies an additional development in the image processing code that we did not have time to develop.

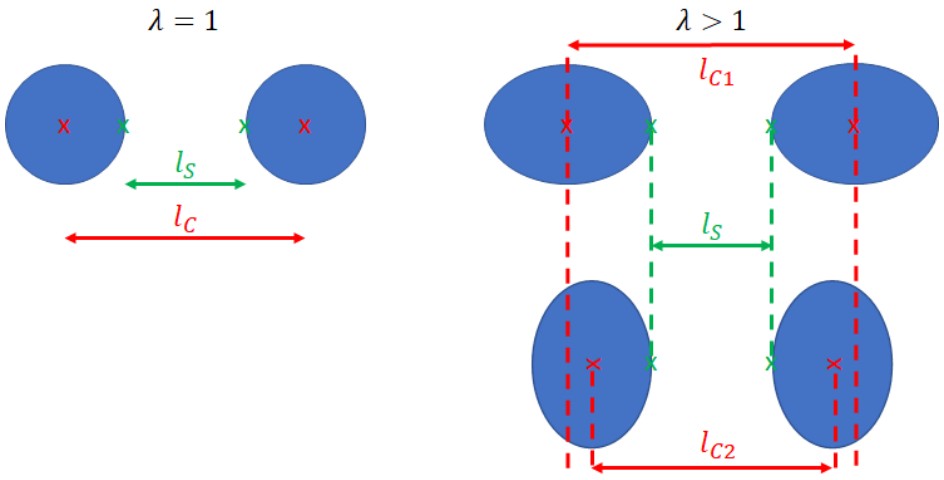

Figure 5.9. The distances l_S and l_C between two consecutive particles in a train, for $\lambda = 1$ and $\lambda > 1$.

5.3.2.3. Train composition

Figure 5.10 shows the train composition for SNW ($\kappa = 0.19125$, $\lambda = 1.2$), $PNT57$ ($\kappa = 0.09625$, $\lambda = 1.5$) and spherical ($\kappa = 0.11$, $\lambda = 1$) [67,93,159] suspensions, having the same number of particles and flowing at the same Re.

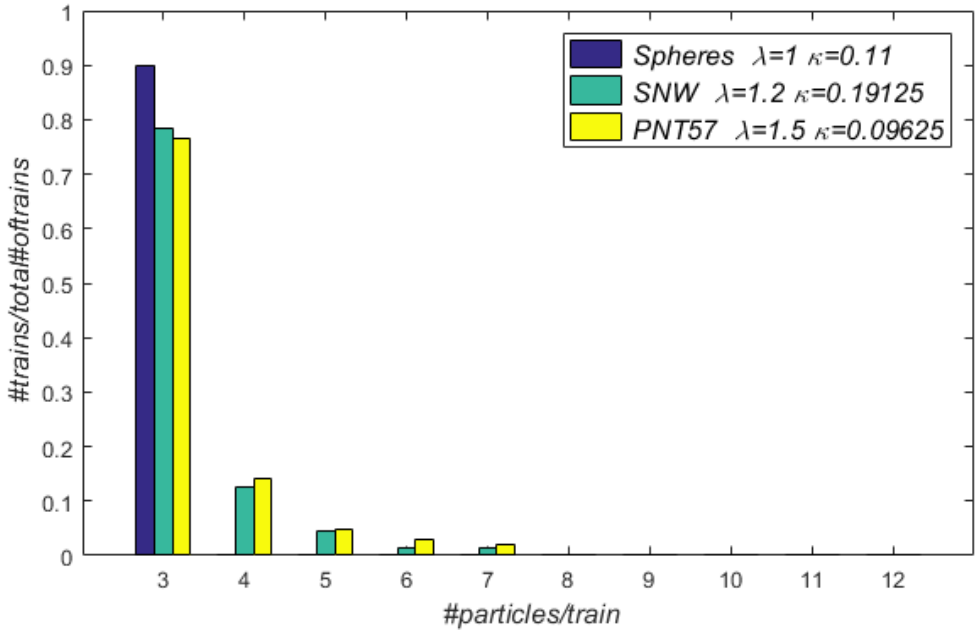

Figure 5.10. Fraction of trains as a function of the number of particles per train, for SNW ($\kappa = 0.19125$, $\lambda = 1.2$), $PNT57$ ($\kappa = 0.09625$, $\lambda = 1.5$), and spherical [67,93,159] particles. All the suspensions have the same equivalent concentration ($\Phi_{eq} = 0.05\%$), and flowing at $Re = 58$.

The $PNT57$ particles and the spheres have close values of κ but different λ. A clear drop in the fraction of three-particle trains is observed when λ is increased from 1 (spheres) to 1.5 ($PNT57$) (Figure 5.10). This shows an effect of λ on the train composition: an increase in λ increases the number of particles per train.

Based only on the effect of λ on the train composition, the fraction of three-particle trains for the SNW ($\lambda = 1.2$) particles would be lower than that of spheres ($\lambda = 1$) and higher than the fraction for $PNT57$ ($\lambda = 1.5$) particles. This is in agreement with what is observed on Figure 5.10.

However, the SNW particles have a greater κ ($\kappa = 0.19125$) than the studied spheres ($\kappa = 0.11$) and $PNT57$ ($\kappa = 0.09625$) particles. So, based only on the effect of κ on the train composition (Section 5.3.1), the fraction of three-particle trains for the SNW particles would be lower than that of the spheres and that of the $PNT57$ particles. This is not observed on Figure 5.10.

It should be mentioned that the shape of the particle might also have an effect on the length of the train. In fact, as explained earlier on the effect of λ on ψ, the asymmetry along one of the axes of the SNW might complexify the interactions with other particles, which reduces the possibility of forming long trains, increasing the fraction of three-particle trains.

So, the train composition is determined by the combined effect of the confinement ratio, the particle aspect ratio as well as the symmetry in the particle's geometry. However, with the experimental data that we possess, it is not possible to quantify the relative importance of these three effects.

5.3.3. Effect of fluid inertia Re

5.3.3.1. Fraction of particles in trains ψ

The effect of Re on ψ was described in Figure 5.2 of Section 5.2. In fact, ψ has a similar evolution as the focusing degree η: when Re increases, ψ increases to a maximum value, attained at a critical Re (same Re_{cr} for η), then decreases. This confirms the existence of a coupling between the longitudinal ordering and the lateral migration.

5.3.3.2. Normalized interparticle spacing l/d_{rot}

Figure 5.11 shows the normalized interparticle spacing as a function of Reynolds number, for a SNW suspension, at four different distances from the channel inlet.

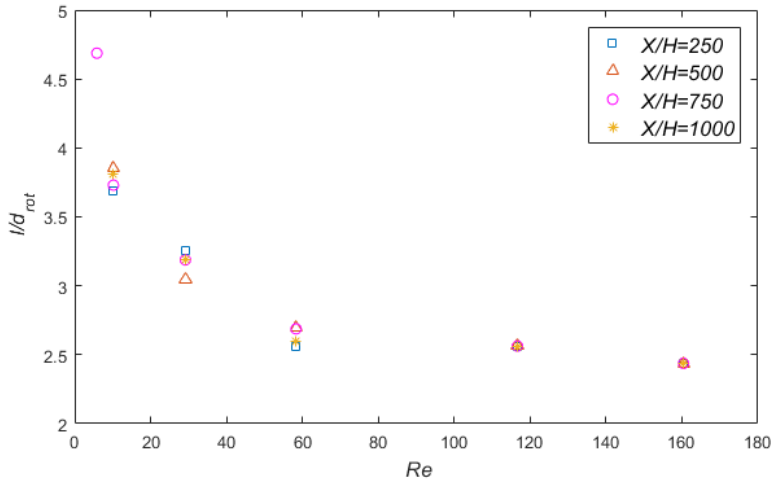

Figure 5.11. Evolution of the normalized interparticle spacing in function of Reynolds number, for a 0.05% suspension of SNW particles, at different distances from the channel inlet.

It can be observed that, regardless of X/H, l/d_{rot} decreases when fluid inertia is increased. This finding is similar to those obtained in the spherical case [67,71,79,81,159]. In fact, when fluid inertia increases, the recirculating zones get closer to the particle surface, which decreases the interparticle distance.

5.3.3.3. Train composition

Figure 5.12 shows the train composition for a $PNT57$ suspension, for seven different values of Reynolds number. It can be remarked that, increasing fluid inertia increases the fraction of long trains (4, 5 and 6 particles/train) and decreases the fraction of three-particle trains. This was also experimentally observed by Gao et al. [93] and numerically confirmed by Gupta et al. [159] in the spherical case. As explained in Section 5.3.1, [159] found that the length of a stable train is a function of κ and Re, and is approximately equal to the channel height. So, they deduced that the number of particles stable in a train increases when flow inertia is increased, mainly linked to the decrease in the interparticle spacing.

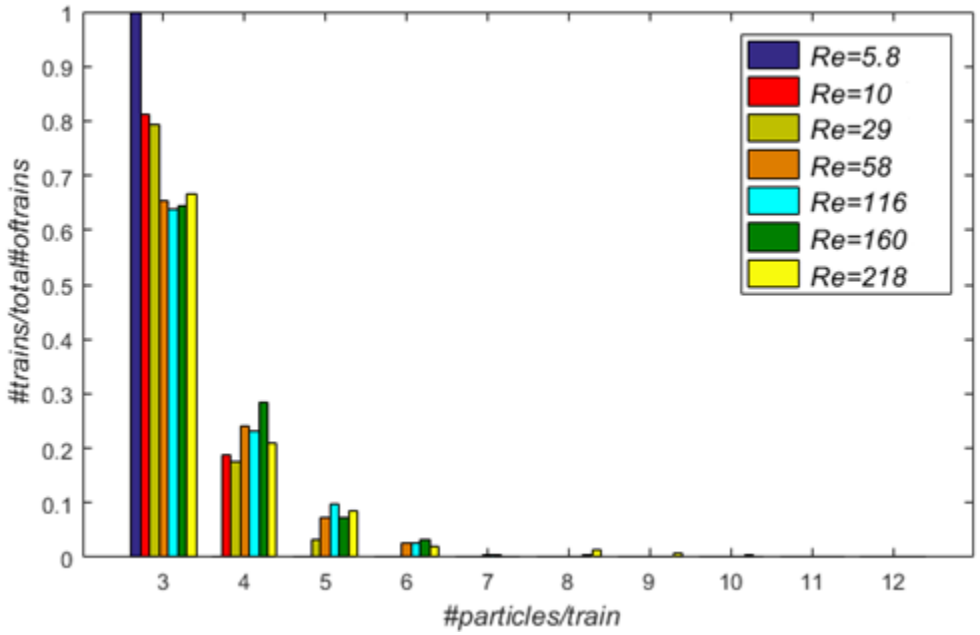

Figure 5.12. Fraction of trains as a function of the number of $PNT57$ particles per train, for seven values of Reynolds number.

5.3.4. Effect of the particle volume fraction Φ

5.3.4.1. Fraction of particles in trains ψ

As shown in Section 5.2, the fraction of particles in trains presents a parabolic evolution in function of Reynolds number (similar to η): ψ increases to a maximum value at a critical Reynolds number, then decreases. When suspensions of different concentrations are studied (Figure 5.13), the same curve is obtained, but with two main differences. The first one concerns the critical Reynolds number Re_{cr}, corresponding to the peak of the curve. It can be seen that Re_{cr} decreases when the concentration is increased. This is similar to what was found by Gao et al. [67,80] on spherical particles.

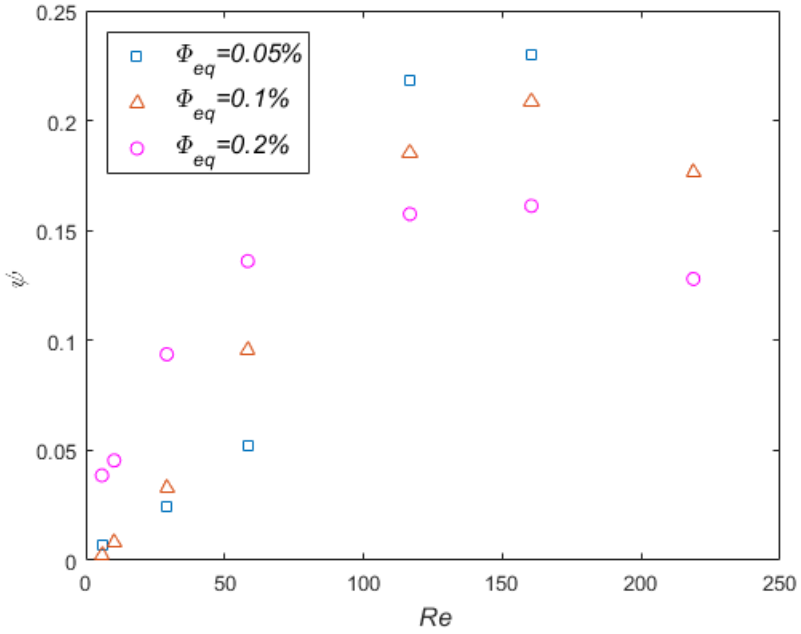

Figure 5.13. Evolution of the fraction of PNT57 particles in trains in function of Reynolds number, for three different particle volume fractions Φ.

The second effect of the concentration is on the maximum value of ψ, that decreases with an increasing concentration. This finding is different than the spherical results of Gao et al. [67,80], who found that an increase in the concentration increases the maximum fraction of particles in train.

This result confirms that the coupling between the longitudinal ordering and the lateral migration is complex and highly dependent from the flow conditions, as described in

Section 5.2, based on Figure 5.2. In fact, for $Re \leq 58$, when the concentration increases, the focusing degree decreases (c.f. Figure 3.10 in Section 3.2.4) and the fraction of particles in trains increases (Figure 5.13). However, for $Re > 58$, an increase in Φ decreases both η (c.f. Figure 3.10) and ψ (Figure 5.13).

5.3.4.2. Train composition

Figure 5.14 represents the train composition for three $PNT57$ suspensions, of different concentrations, at the same flow conditions. It can be observed that the particle volume fraction (0.05%,0.1% and 0.2%) does not seem to have an effect on the length of the train. The experimental study of [93] on spheres shows that, when the concentration increases from 0.05% to 1%, the percentage of three-particle trains decreases and longer trains are found. The reason behind the absence of this effect in this study might be linked to the narrow range of the studied concentration ($0.05\% < \Phi < 0.2\%$). The same study should be extended to a wider range of Φ.

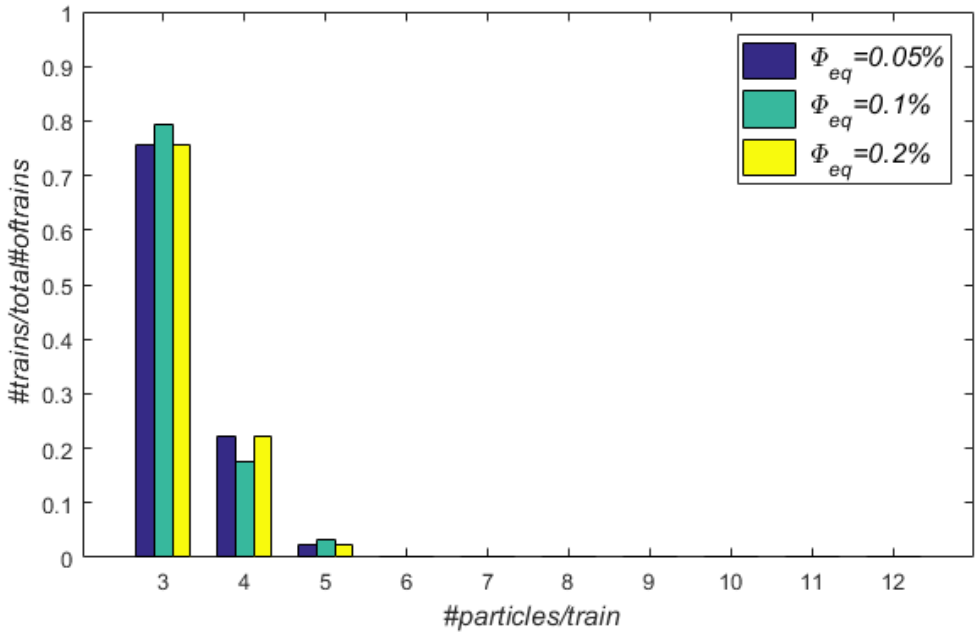

Figure 5.14. Fraction of trains as a function of the number of $PNT57$ particles per train, for three different equivalent particle volume fractions Φ_{eq} (0.05%, 0.1% and 0.2%), at $Re = 29$.

5.3.5. Effect of the distance from the channel inlet X/H

5.3.5.1. Fraction of particles in trains ψ

It has been shown in Section 5.2 (c.f. Figure 5.1) that, in a similar way to spheres [67,80], the fraction of particles in trains ψ increases with X/H, indicating that trains form progressively in the channel.

5.3.5.2. Normalized interparticle spacing l/d_{rot}

It can be remarked from Figure 5.10 (presented earlier) that the interparticle spacing in the case of SNW particles, seems to be independent from the distance from the channel inlet. In other words, the particles of the same train will conserve the distance between them along the channel. This result is similar to the one obtained in the spherical case by [67]. However, it is different from the findings of Lee et al. [68] on spheres, who showed that the peak of the interparticle spacing histogram continuously shift to larger distances further downstream. They attributed this increase in l/d_{rot} to residual viscous repulsive interactions.

5.3.5.3. Train composition

Figure 5.15 represents the train composition along the channel, for a $PNT57$ suspension flowing at $Re = 160$. It can be observed from Figure 5.15 that the train composition is roughly conserved along the channel, meaning that the number of particles per train is not modified while the train is flowing in the channel. This result is found for all the tested values of Reynolds number, and is coherent with the spherical results of Gupta et al. [159], who found that the length and the stability of the train are only a function of κ and Re, independently from X/H.

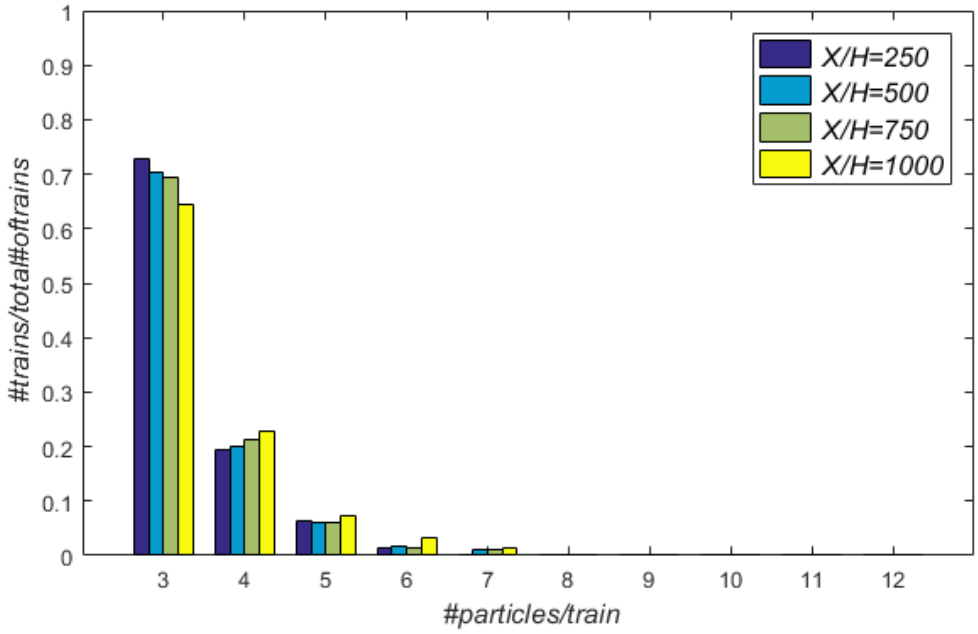

Figure 5.15. Fraction of trains as a function of the number of PNT57 particles per train, for different distances from the channel inlet, at $Re = 160$.

5.4. Longitudinal ordering and tumbling behavior

As explained in Section 5.2, the longitudinal ordering is a phenomenon that develops while the particles flow downstream in the channel. In the same time, the particles migrate towards the equilibrium positions where their rotational mode drifts to a tumbling mode (Chapter 4). The coupling between the lateral migration and the rotational behavior has been studied in Chapter 4. The coupling between the lateral migration and the longitudinal ordering was explained in Section 5.2. In this section, the relations that could exist between the train formation and the rotational mode are identified.

While studying the rotational behavior, using images captured at high frame rates (cf. Chapter 4), it has been noticed that pairs of particles had often in-phase rotations, as illustrated in Figure 5.16. This raised a question on whether or not particles get in phase rotation when they are in trains.

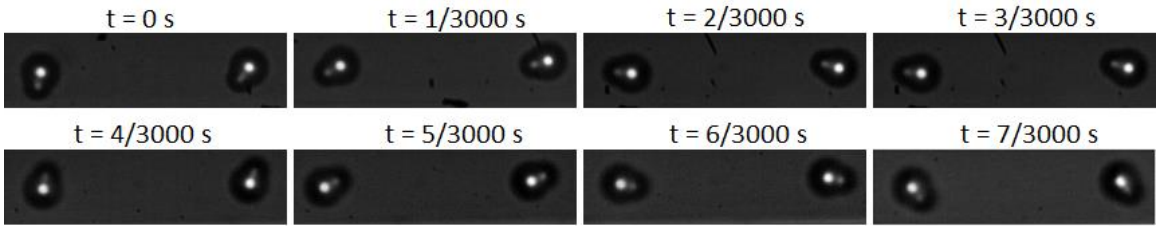

Figure 5.16. Eight consecutive captured images showing a pair of focused tumbling SNW particles in phase rotation.

To answer this question, a statistical analysis has been done on images taken by the Sensicam camera at the midplane of the channel, and only bright focused particles in trains have been considered. These particles have a tumbling behavior, since they are focused (cf. Chapter 4). In addition, the orientations of these particles can be easily detected, since the tumbling is done in the plane of the camera.

It should be also mentioned that the maximum Reynolds number investigated in this section is $Re = 58$, since it is the highest value attained in the case of high frame rate images, due to the drop in the luminosity and the image size at higher Re.

Once the orientations φ of the targeted particles are identified, the absolute value of the difference between the orientations of two consecutive particles of a train is calculated. This value, called $\Delta\varphi$, varies between 0° and 90°, where 0° means that the two particles have the same orientation and are in phase rotation, while 90° indicates that the main axes of the two particles are perpendicular. The distribution of $\Delta\varphi$ is then plotted for different configurations (Figure 5.17).

It can be clearly observed from Figure 5.17 that, in most of the cases, the highest bin corresponds to $\Delta\varphi$ between 0°and 10° (about one third of the number of particle pairs), and that the fraction corresponding to this bin increases with X/H. This suggests that consecutive particles of the same train tend to get into an in-phase rotation, established progressively along the channel.

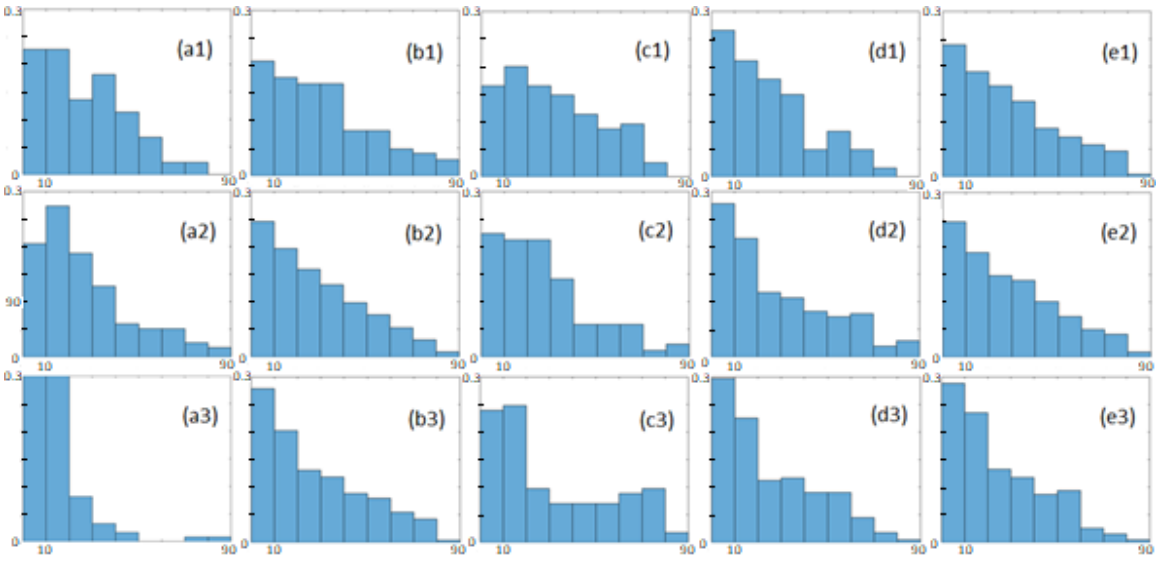

Figure 5.17. Distribution of Δφ for different configurations: (a) $PNT57$ at $Re = 29$, (b) $PNT57$ at $Re = 58$, (c) SNW at $Re = 10$, (d) SNW at $Re = 29$ and (e) SNW at $Re = 58$. The first line (1) corresponds to $X/H = 500$, the second line (2) is for $X/H = 750$, and the third line (3) represents tests done at $X/H = 1000$. The y-axis, representing the fraction of particles with a certain Δφ value, varies between 0 and 0.3, with a step of 0.05. The x-axis, corresponding to the value of Δφ, varies between 0° and 90°, with a bin width of 10°.

5.5. Summary and conclusions

The longitudinal ordering is a phenomenon that develops progressively in the channel, thanks to particle-particle interactions. It is conditioned by the lateral migration. Unlike the spherical case [67,80,93], the coupling between these two phenomena is complex and highly dependent on the flow conditions.

The longitudinal ordering is characterized by the fraction of particles in trains ψ , the normalized interparticle spacing l/d_{rot} and train composition, represented by the number of particles per train.

In this study, regardless of the experimental conditions (Re, λ, κ, Φ, X/H), the majority of the trains are formed of three particles, which is similar to the results of experimental and numerical works done on spherical particles with the same operating conditions [93,159].

In a similar way to the spherical case, increasing fluid inertia: (i) increases the fraction of particles in trains to a maximum value (at Re_{cr}) then decreases it, (ii) decreases the interparticle spacing, and (iii) increases the number of particles per train.

Concerning the effect of the confinement ratio κ on the longitudinal ordering, it has been found that increasing κ induces a decrease in the value of Re_{cr} and an increase in the values of ψ. These results are similar to the ones obtained in the spherical case [67,80]. In addition, when κ is increased, longer trains are found. This is different from the spherical results of Gupta et al. [159], and might be linked to the non-spherical geometry of the studied particles.

The particle aspect ratio λ has a clear effect on the train formation. An increase in the value of λ, decreases ψ and increases the number of particles per train. In addition, an increase in λ flattens the peak of the distribution of l/d_{rot}. This might be linked to the finding of Gao et al. [67,80] on spherical particles, where it has been found that the key distance is the one between the surfaces of the particles and not their centers.

It should be also mentioned that, the asymmetry of the SNW particles might be behind a decrease in the value of ψ and in the number of particles per train.

In the relatively small studied range of Φ, it has been shown that the particle volume fraction has major effects on the fraction of particles in trains. These effects are altered in function of the flow conditions. Concerning the train composition, no clear influence of Φ on the number of particles per train was observed.

It has been also found that, similarly to the spherical case [67,159], ψ increases with X/H, while the normalized interparticle spacing and the number of particles per train are conserved along the channel.

Finally, concerning the coupling between the longitudinal ordering and the rotational behavior, it has been observed that focused tumbling particles in trains appear to get into an in-phase rotation, established progressively along the channel.

6. Conclusions and Perspectives

6.1. Conclusions

The main goal of the present thesis was to experimentally investigate the lateral migration, rotational behavior, and longitudinal ordering of non-spherical particles flowing in square straight microchannels, as well as the possible couplings between these three phenomena.

An analysis, based on a deep bibliographical study, allowed the identification of essential unanswered questions in the literature. Then, the experimental setup and data processing technique, developed in this study, were presented. Thanks to this in-situ visualization technique, the lateral migration, the rotational behavior and the longitudinal ordering were characterized and evaluated.

The principal findings of this thesis work have been divided into three main parts, one for each of the phenomena mentioned above.

The major conclusions are as follows:

- ***Lateral migration:***

- At moderate fluid inertia ($5 < Re < 160$):
    - In a similar way to spheres, the studied non-spherical particles experience a two-stage migration to attain the four face-centered equilibrium positions in a square channel. In this regime, the migration's evolution with the operating conditions (fluid inertia, particle volume fraction, confinement ratio, …) is qualitatively similar to what was observed for spheres.
    - In the limited range covered by this study, the particle aspect ratio has no significant effect on the equilibrium position, which means that shape-based separation possibilities are limited.

  - Non-spherical particles focus in larger zones around the four equilibrium positions, when compared to spheres flowing at the same experimental conditions, which has also a limiting effect on the separation efficiency.
- At higher values of Reynolds number, like for spheres, a transition to a new migration regime occurs.
- At low fluid inertia ($Re \leq 5$), unlike spheres [67], the migration towards the channel centerline is not observed and the particles keep on migrating towards the face-centered equilibrium positions (even at $Re \approx 1$).

- ***Rotational behavior:***

- The rotational mode, observed up to $Re = 58$, is directly coupled to the lateral migration. A migrating particle has a kayaking mode, in which the orientation of the particle's major axis, with respect to the vorticity axis, is time-dependent. Once the particle attains its equilibrium position, a switch from the kayaking mode to a tumbling one occurs: the particle starts rotating about the axis passing by its centroid and parallel to the closest cross-sectional wall.
- The tumbling particle rotates at its minimum and maximum angular velocities when it is aligned with and perpendicular to the flow, respectively, as seen in the literature. The difference between the extreme values of the angular velocity, as well as the proportion of time (per one rotation) spent by the particle at the horizontal orientation, increase with Reynolds number. This last finding is interesting for applications where the orientation of the particles is critical.
- The tumbling period of rotation T decreases when fluid inertia is increased. In addition, in the conditions of this study (for $Re \leq 29$), Jeffery's theoretical expression of T [111] is valid, as long as the shear rate used in this equation is the one at the center of the particle on its equilibrium position.

- ***Longitudinal ordering:***

- In a similar way to spheres, flowing non-spherical particles form trains in the flow direction. The longitudinal ordering phenomenon develops progressively in the channel, due to particle-particle interactions.
- The non-spherical geometry of the particle influences the characteristics of the trains (fraction of particles in trains, interparticle spacing, train composition), as well as their dependence on the operating conditions, such as the confinement ratio and the particle volume fraction. One of the major observations concern the fraction of particles in trains, which is much lower in the non-spherical case.
- The longitudinal ordering phenomenon is conditioned by the lateral migration. Unlike the spherical case [67,80,93], the coupling between these two phenomena is complex and highly dependent on the flow conditions.
- Focused tumbling particles in trains appear to get into an in-phase rotation, established progressively along the channel.

6.2. Perspectives

Future works should be done in order to complete this study on the transport of non-spherical particles in microchannels:

- To verify if the distance between the surfaces of consecutive particles in trains is the key parameter characterizing the longitudinal ordering phenomenon, the existing processing code should be adapted in order to analyze this parameter on the already acquired image sets.
- To check if, in a similar way to spheres [93], at high fluid inertia, non-spherical particles migrate towards eight equilibrium positions (the four corners of the square channel and the four face-centered equilibrium positions), experiments should be done at high Reynolds number ($Re > 200$). This requires short exposure times and a powerful light source.
- To clearly isolate and characterize the influence of the particles' aspect and confinement ratios on their transport in the channel, an expansion of the variety of

the studied non-spherical geometries should be considered. It would be also interesting to test asymmetric particles, in order to investigate the influence of geometrical asymmetry on the particle's translational and rotational behaviors.

- In order to deepen the analysis on the rotational behavior (transition from kayaking to tumbling, in-phase rotation in trains, …), it would be necessary to make adjustments in the experimental setup, allowing a more precise acquisition of the particle's position and orientation (e.g., stereovision).

The long-time goal of this project is to predict the trajectories of microorganisms flowing in microchannels. Several steps, with rising complexity, have been determined to reach this objective (c.f. "About the thesis"). In the present thesis, the transport of rigid neutrally buoyant monodisperse non-spherical particles in straight microchannels has been studied. In the forthcoming works, the effect of the channel curvature on the transport of the particles will be investigated. This future work will be followed by the study of the transport of deformable particles and microorganisms, in dilute and moderately concentrated suspensions.

Appendix A: Particles geometrical properties

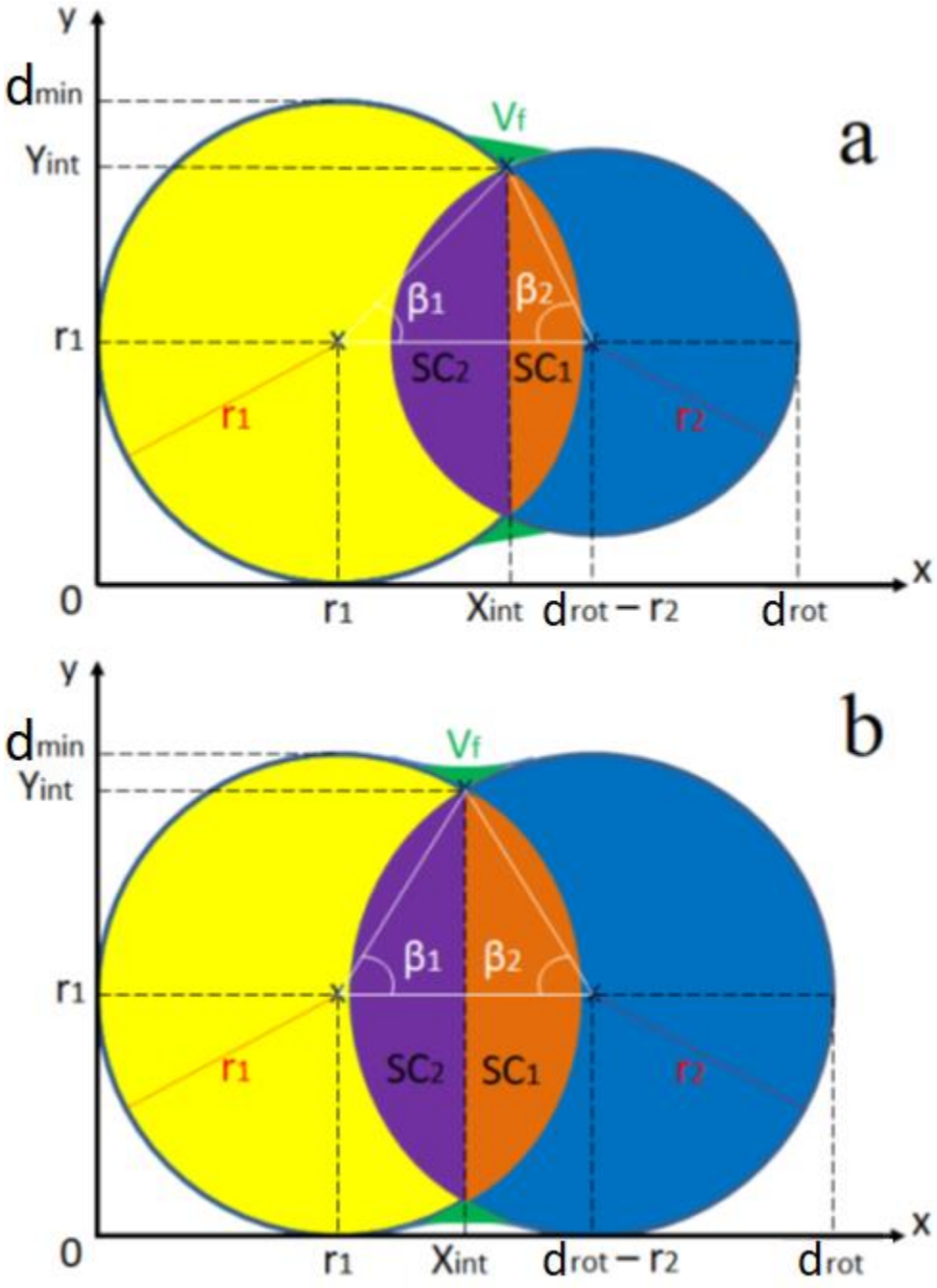

Figure A.1. Schematics showing (a) a SNW and (b) a PNT particle.

Table A.1. Necessary calculations to identify the volume of the particle, needed for the suspension calculation (Appendix B). The only dimensions given by the supplier are Dimension 1 and Dimension 2.

Parameter	Equation	$PNT57$	$PNT35$	SNW
Dimension 1 d_{rot} (μm)	given	7.7	5.1	15.3
Dimension 2 d_{min} (μm)	given	5.1	3.4	12.8
Aspect ratio λ (dimensionless)	d_{rot}/d_{min}	1.509	1.5	1.195*
Radius of sphere 1 r_1 (μm)	$d_{min}/2$	2.55	1.7	6.4
Radius of sphere 2 r_2 (μm)	$d_{min}/2$ for PNT, $d_{rot} - 2r_1$ for SNW**	2.55	1.7	2.5
X_{int}	$\frac{d_{rot}^2 - 2r_2 d_{rot}}{2(d_{rot} - r_1 - r_2)}$	3.85	2.55	12.31
Y_{int}	$\sqrt{r_1^2 - (X_{int} - r_1)^2} + r_1$	4.74	3.17	8.85
Angle of spherical cap 1 β_1 (radian)	$atan\frac{Y_{int} - r_1}{X_{int} - r_1}$	1.036	1.047	0.393
Angle of spherical cap 2 β_2 (radian)	$-atan\frac{Y_{int} - r_1}{X_{int} - d_{rot} + r_2}$	1.036	1.047	1.374
Maximum cross-sectional area A_{max} (μm^2)	$\pi r_1^2 + \pi r_2^2 - \frac{r_1^2(2\beta_1 - sin2\beta_1)}{2} - \frac{r_2^2(2\beta_2 - sin2\beta_2)}{2}$	33.09	14.61	139.31
…	…	…	…	…

Volume of sphere 1 V_{s1} (μm^3)	$\frac{4\pi r_1^3}{3}$	69.46	20.58	1098.07
Volume of sphere 2 V_{s2} (μm^3)	$\frac{4\pi r_2^3}{3}$	69.46	20.58	65.45
Volume of spherical cap 1 V_{sc1} (μm^3)	$\frac{\pi}{3} r_1^3 (2 + cos\beta_1)(1 - cos\beta_1)^2$	10.47	3.22	4.67
Volume of spherical cap 2 V_{sc2} (μm^3)	$\frac{\pi}{3} r_2^3 (2 + cos\beta_2)(1 - cos\beta_2)^2$	10.47	3.22	23.26
Intersection volume V_{int} (μm^3)	$V_{sc1} + V_{sc2}$	20.94	6.43	27.93
Fillet volume V_f (μm^3)	negligible	X	X	X
Particle total volume V_p (μm^3) (***)	$V_{s1} + V_{s2} - V_{int} + 2V_f$	117.97	34.73	1135.55

(*) In the calculation of λ for a SNW particle (*), it is assumed that the small sphere has a negligible size compared to the large sphere. For this reason, the rotational diameter was divided by $2r_1$ (and not $2r_2$) to obtain λ. (**) In the case of the asymmetric doublet (SNW), to simplify the calculation, it is assumed that the center of the small sphere is placed on the surface of the large sphere. This was also verified on images. (***) All the calculated volumes are verified to be a bit smaller than the volume of a prolate having its major and minor axes equal to d_{rot} and d_{min} respectively.

Appendix B: Suspension calculation and preparation

B.1. Suspension composition

To prepare $v\,mL$ of a suspension S with $\Phi\%$ solid volume fraction, a volume $v_p = \Phi \times v\,mL$ of particles is needed. However, the particles originally are in a suspension with a 10% solid content. This means that the volume needed to be extracted from the supplied suspension is $v_{ext} = 10 \times v_p\,mL$.

The suspension S is a mixture of particles and a suspending fluid. These two should have the same density ($\rho_p = \rho_f = 1050kg/m^3$), to respect the neutrally-buoyant condition. The fluid is a mixture of deionized water ($\rho_w = 998.3kg/m^3$) and glycerol ($\rho_g = 1260.4kg/m^3$) at a respective volume ratio 80.27%/19.73%(v/v):

$$\rho_{mixt} = 998.3 \times 80.27\% + 1260.4 \times 19.73\% = 1050kg/m^3 \qquad \text{(B.1)}.$$

So, thanks to this calculation, it can be deduced that a volume $v\,mL$ of a suspension S with $\Phi\%$ solid volume fraction contains: $v_{ext} = 10 \times \Phi \times v\,mL$ of the particles' original suspension, $v_w = (v - v_{ext}) \times 80.27\%\,mL$ of deionized water, and $v_g = (v - v_{ext}) \times 19.73\%\,mL$ of glycerol.

B.2. Suspension preparation

To prepare the suspension, the necessary tools and materials are: the polystyrene particles, deionized water, glycerol, a micropipette, a beaker, an electronic balance, and a syringe. First, the beaker is placed on the balance. Then, using the syringe, $0.9983 \times v_w$ grams of deionized water and $1.2604 \times v_g$ grams of glycerol are placed in the beaker. Next, using the micropipette, $v_{ext}\,mL$ of the particles' solution are added to the beaker. Finally, the mixture is swirled until all the solute is dissolved.

B.3. Equivalent concentration

To compare the behaviors of two suspensions S_1 and S_2, containing particles of different geometries and/or sizes, it was assumed that it is essential for them to have the same number of particles per unit volume.

The total volume of particles v_p in a suspension S can be calculated as follows:

$$v_p = \Phi \times v = N \times V_p \quad \text{(B.2)},$$

where Φ is the solid volume fraction, v the total volume of the suspension, N the number of particles in S, and V_p the volume of one particle of S. V_p can be identified from Appendix A in case of non-spherical particles, or calculated, if the particles are spheres ($V_p = \pi d_p^3/6$, with d_p being the diameter of the sphere).

Equation (B.2), applied to S_1 and S_2, gives:

$$v_{p1} = \Phi_1 \times v_1 = N_1 \times V_{p1} \quad \text{(B.3)},$$

$$v_{p2} = \Phi_2 \times v_2 = N_2 \times V_{p2} \quad \text{(B.4)}.$$

Since the number of particles per unit volume is the same for S_1 and S_2:

$$\frac{N_1}{v_1} = \frac{N_2}{v_2} \quad \text{(B.5)}.$$

It can be deduced from equations (B.3), (B.4) and (B.5) that:

$$\frac{\Phi_1}{V_{p1}} = \frac{\Phi_2}{V_{p2}} \quad \text{(B.6)}.$$

Knowing Φ_1, V_{p1} and V_{p2}, the solid volume fraction Φ_2 of S_2 can be calculated:

$$\Phi_2 = \frac{\Phi_1 \times V_{p2}}{V_{p1}} \quad \text{(B.7)}.$$

Appendix C: Theoretical prediction of the particle period of rotation

Jeffery [111] theoretically developed an expression for the period of rotation T:

$$T = \frac{2\pi}{\gamma}\left(\lambda + \frac{1}{\lambda}\right) \quad \text{(C.1)},$$

with λ being the particle aspect ratio and γ the shear rate at the particle centroid.

To find γ, the velocity profile in a plane Poiseuille flow is studied (Figure C.1).

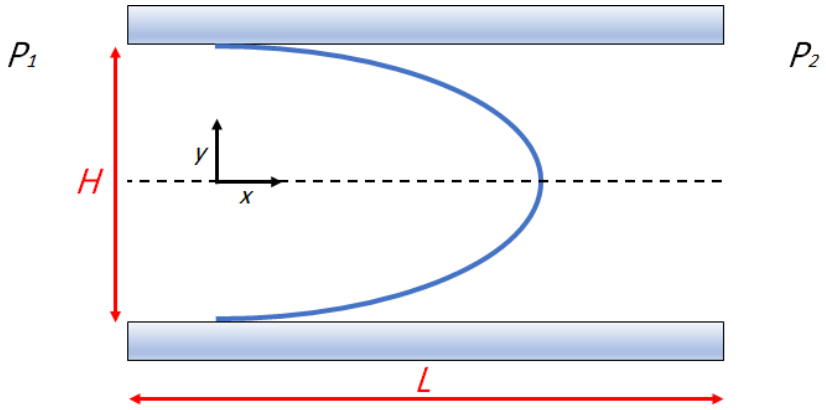

Figure C.1. The fluid velocity profile (in blue) in a plane Poiseuille flow, generated by a pressure gradient ($P_1 > P_2$).

Based on the projection of the momentum conservation equation (Navier-Stokes) along the flow axis, the equation describing the velocity profile can be obtained:

$$u(y) = \frac{1}{2\mu_f}\frac{\Delta P}{L}\left(y^2 - \frac{H^2}{4}\right) \quad \text{(C.2)},$$

with μ_f being the fluid viscosity and ΔP the pressure difference between the inlet and the outlet.

The value of the local shear rate γ, at a lateral position y^* (from the channel centerline), is the derivative of the velocity with respect to the position:

$$\gamma = |\frac{du}{dy}(y = y^*)| = |\frac{1}{\mu_f}\frac{\Delta P}{L}y^*| \quad \text{(C.3).}$$

The local shear rate can be also expressed in function of Reynolds number. In fact, in a square channel, $Re = \rho_f \bar{u} H/\mu_f$, where ρ_f is the density of the fluid and $\bar{u}$ is the average fluid velocity. This latter can be calculated as follows:

$$\bar{u} = \frac{\iint u(y)dS}{S} = \frac{-H^2}{12\mu_f}\frac{\Delta P}{L} \quad \text{(C.4),}$$

with S being the channel cross-sectional area. So, the expressions of Reynolds number and $\bar{u}$ transform Equation (C.3) to:

$$\gamma = |\frac{12\mu_f}{H^3\rho_f}y^* Re| \quad \text{(C.5).}$$

Based on Reynolds number and the particle equilibrium position from the channel wall (Y_{eq}/H) (Chapter 3), the shear rate is calculated at the centroid of the particle, with $y^* = H/2 - H * Y_{eq}/H$.

Finally, the period of rotation is calculated by inserting the corresponding γ in Equation (C.1).

References

1. Martel, J.M.; Toner, M. Inertial Focusing in Microfluidics. *Annu. Rev. Biomed. Eng.* **2014**, *16*, 371–396, doi:10.1146/annurev-bioeng-121813-120704.
2. Amini, H.; Lee, W.; Di Carlo, D. Inertial Microfluidic Physics. *Lab Chip* **2014**, *14*, 2739, doi:10.1039/c4lc00128a.
3. Gossett, D.R.; Tse, H.T.K.; Lee, S.A.; Ying, Y.; Lindgren, A.G.; Yang, O.O.; Rao, J.; Clark, A.T.; Di Carlo, D. Hydrodynamic Stretching of Single Cells for Large Population Mechanical Phenotyping. *Proceedings of the National Academy of Sciences* **2012**, *109*, 7630–7635, doi:10.1073/pnas.1200107109.
4. Dudani, J.S.; Gossett, D.R.; Tse, H.T.K.; Di Carlo, D. Pinched-Flow Hydrodynamic Stretching of Single-Cells. *Lab Chip* **2013**, *13*, 3728, doi:10.1039/c3lc50649e.
5. Tse, H.T.K.; Gossett, D.R.; Moon, Y.S.; Masaeli, M.; Sohsman, M.; Ying, Y.; Mislick, K.; Adams, R.P.; Rao, J.; Carlo, D.D. Quantitative Diagnosis of Malignant Pleural Effusions by Single-Cell Mechanophenotyping. *Science translational medicine* **2013**, *5*, 11, doi:10.1126/scitranslmed.3006559.
6. Lundell, F.; Söderberg, L.D.; Alfredsson, P.H. Fluid Mechanics of Papermaking. *Annu. Rev. Fluid Mech.* **2011**, *43*, 195–217, doi:10.1146/annurev-fluid-122109-160700.
7. Gossett, D.R.; Tse, H.T.K.; Dudani, J.S.; Goda, K.; Woods, T.A.; Graves, S.W.; Carlo, D.D. Inertial Manipulation and Transfer of Microparticles Across Laminar Fluid Streams. *Small* **2012**, *8*, 2757–2764.
8. Valsan, A.E.; Ravikrishna, R.; Biju, C.V.; Pöhlker, C.; Després, V.R.; Huffman, J.A.; Pöschl, U.; Gunthe, S.S. Fluorescent Biological Aerosol Particle Measurements at a Tropical High-Altitude Site in Southern India during the Southwest Monsoon Season. *Atmos. Chem. Phys.* **2016**, *16*, 9805–9830, doi:10.5194/acp-16-9805-2016.
9. Gascoyne, P.R.; Vykoukal, J. Particle Separation by Dielectrophoresis. *Electrophoresis* **2002**, *23*, 1973–1983.
10. Voldman, J. ELECTRICAL FORCES FOR MICROSCALE CELL MANIPULATION. *Annu. Rev. Biomed. Eng.* **2006**, *8*, 425–454.
11. Liu, C.; Stakenborg, T.; Peeters, S.; Lagae, L. Cell Manipulation with Magnetic Particles toward Microfluidic Cytometry. *Journal of Applied Physics* **2009**, *105*, 102014, doi:10.1063/1.3116091.
12. Miltenyi, S.; Müller, W.; Weichel, W.; Radbruch, A. High Gradient Magnetic Cell Separation with MACS. *Cytometry* **1990**, *11*, 231–238, doi:10.1002/cyto.990110203.
13. Zhao, Y.; Fujimoto, B.S.; Jeffries, G.D.; Schiro, P.G.; Chiu, D.T. Optical Gradient Flow Focusing. *Opt. Express* **2007**, *15*, 6167, doi:10.1364/OE.15.006167.
14. MacDonald, M.P.; Spalding, G.C.; Dholakia, K. Microfluidic Sorting in an Optical Lattice. *Nature* **2003**, *426*, 421–424, doi:10.1038/nature02144.
15. Petersson, F.; Åberg, L.; Swärd-Nilsson, A.-M.; Laurell, T. Free Flow Acoustophoresis: Microfluidic-Based Mode of Particle and Cell Separation. *Anal. Chem.* **2007**, *79*, 5117–5123, doi:10.1021/ac070444e.
16. Pamme, N. Continuous Flow Separations in Microfluidic Devices. *Lab Chip* **2007**, *7*, 1644, doi:10.1039/b712784g.
17. Lee, G.-B.; Chang, C.-C.; Huang, S.-B.; Yang, R.-J. The Hydrodynamic Focusing Effect inside Rectangular Microchannels. *J. Micromech. Microeng.* **2006**, *16*, 1024–1032, doi:10.1088/0960-1317/16/5/020.
18. Yang, R.-J.; Chang, C.-C.; Huang, S.-B.; Lee, G.-B. A New Focusing Model and Switching Approach for Electrokinetic FLow inside Microchannels. 9.

19. Howell Jr, P.B.; Golden, J.P.; Hilliard, L.R.; Erickson, J.S.; Mott, D.R.; Ligler, F.S. Two Simple and Rugged Designs for Creating Microfluidic Sheath Flow. *Lab Chip* **2008**, *8*, 1097, doi:10.1039/b719381e.
20. Huh, D.; Bahng, J.H.; Ling, Y.; Wei, H.-H.; Kripfgans, O.D.; Fowlkes, J.B.; Grotberg, J.B.; Takayama, S. Gravity-Driven Microfluidic Particle Sorting Device with Hydrodynamic Separation Amplification. 8.
21. Xuan, X.; Li, D. Focused Electrophoretic Motion and Selected Electrokinetic Dispensing of Particles and Cells in Cross-Microchannels. *Electrophoresis* **2005**, *26*, 3552–3560.
22. Mielnik, M.M.; Saetran, L.R. Selective Seeding for Micro-PIV. *Exp Fluids* **2006**, *41*, 155–159, doi:10.1007/s00348-005-0103-8.
23. Scott, R.; Sethu, P.; Harnett, C.K. Three-Dimensional Hydrodynamic Focusing in a Microfluidic Coulter Counter. *Review of Scientific Instruments* **2008**, *79*, 046104, doi:10.1063/1.2900010.
24. Watson, J.V. The Early Fluidic and Optical Physics of Cytometry. 13.
25. Schrum, D.P.; Culbertson, C.T.; Jacobson, S.C.; Ramsey, J.M. Microchip Flow Cytometry Using Electrokinetic Focusing. *Anal. Chem.* **1999**, *71*, 4173–4177, doi:10.1021/ac990372u.
26. McClain, M.A.; Culbertson, C.T.; Jacobson, S.C.; Ramsey, J.M. Flow Cytometry of *Escherichia Coli* on Microfluidic Devices. *Anal. Chem.* **2001**, *73*, 5334–5338, doi:10.1021/ac010504v.
27. Fu, L.-M.; Yang, R.-J.; Lin, C.-H.; Pan, Y.-J.; Lee, G.-B. Electrokinetically Driven Micro Flow Cytometers with Integrated Fiber Optics for On-Line Cell/Particle Detection. *Analytica Chimica Acta* **2004**, *507*, 163–169, doi:10.1016/j.aca.2003.10.028.
28. Takayama, S.; McDonald, J.C.; Ostuni, E.; Liang, M.N.; Kenis, P.J.A.; Ismagilov, R.F.; Whitesides, G.M. Patterning Cells and Their Environments Using Multiple Laminar Fluid Flows in Capillary Networks. *Proceedings of the National Academy of Sciences* **1999**, *96*, 5545–5548, doi:10.1073/pnas.96.10.5545.
29. Blankenstein, G.; Darling Larsen, U. Modular Concept of a Laboratory on a Chip for Chemical and Biochemical Analysis. *Biosensors and Bioelectronics* **1998**, *13*, 427–438, doi:10.1016/S0956-5663(97)00109-7.
30. Lee, G.-B.; Hung, C.-I.; Ke, B.-J.; Huang, G.-R.; Hwei, B.-H. Micromachined Pre-Focused 1 × N FLow Switches for Continuous Sample Injection. 8.
31. Lee, G.-B.; Hwei, B.-H.; Huang, G.-R. Micromachined Pre-Focused *M* × *N* Flow Switches for Continuous Multi-Sample Injection. *J. Micromech. Microeng.* **2001**, *11*, 654–661, doi:10.1088/0960-1317/11/6/306.
32. Fu, L.-M.; Yang, R.-J.; Lee, G.-B.; Pan, Y.-J. Multiple Injection Techniques for Microfluidic Sample Handling. *Electrophoresis* **2003**, *24*, 3026–3032, doi:10.1002/elps.200305528.
33. Fu, L.-M.; Yang, R.-J.; Lee, G.-B. Electrokinetic Focusing Injection Methods on Microfluidic Devices. *Anal. Chem.* **2003**, *75*, 1905–1910, doi:10.1021/ac020741d.
34. Knight, J.B.; Vishwanath, A.; Brody, J.P.; Austin, R.H. Hydrodynamic Focusing on a Silicon Chip: Mixing Nanoliters in Microseconds. *Phys. Rev. Lett.* **1998**, *80*, 3863–3866, doi:10.1103/PhysRevLett.80.3863.
35. Pollack, L.; Tate, M.W.; Darnton, N.C.; Knight, J.B.; Gruner, S.M.; Eaton, W.A.; Austin, R.H. Compactness of the Denatured State of a Fast-Folding Protein Measured by Submillisecond Small-Angle x-Ray Scattering. *Proceedings of the National Academy of Sciences* **1999**, *96*, 10115–10117, doi:10.1073/pnas.96.18.10115.
36. Hertzog, D.E.; Michalet, X.; Jäger, M.; Kong, X.; Santiago, J.G.; Weiss, S.; Bakajin, O. Femtomole Mixer for Microsecond Kinetic Studies of Protein Folding. *Anal. Chem.* **2004**, *76*, 7169–7178, doi:10.1021/ac048661s.

37. Huh, D.; Bahng, J.H.; Ling, Y.; Wei, H.-H.; Kripfgans, O.D.; Fowlkes, J.B.; Grotberg, J.B.; Takayama, S. Gravity-Driven Microfluidic Particle Sorting Device with Hydrodynamic Separation Amplification. *Anal. Chem.* **2007**, *79*, 1369–1376, doi:10.1021/ac061542n.
38. Loutherback, K.; Chou, K.S.; Newman, J.; Puchalla, J.; Austin, R.H.; Sturm, J.C. Improved Performance of Deterministic Lateral Displacement Arrays with Triangular Posts. *Microfluid Nanofluid* **2010**, *9*, 1143–1149, doi:10.1007/s10404-010-0635-y.
39. Devendra, R.; Drazer, G. Gravity Driven Deterministic Lateral Displacement for Particle Separation in Microfluidic Devices. *Anal. Chem.* **2012**, *84*, 10621–10627, doi:10.1021/ac302074b.
40. Huang, L.R. Continuous Particle Separation Through Deterministic Lateral Displacement. *Science* **2004**, *304*, 987–990, doi:10.1126/science.1094567.
41. Gossett, D.R.; Weaver, W.M.; Mach, A.J.; Hur, S.C.; Tse, H.T.K.; Lee, W.; Amini, H.; Di Carlo, D. Label-Free Cell Separation and Sorting in Microfluidic Systems. *Anal Bioanal Chem* **2010**, *397*, 3249–3267, doi:10.1007/s00216-010-3721-9.
42. Lapizco-Encinas, B.H. On the Recent Developments of Insulator-based Dielectrophoresis: A Review. *ELECTROPHORESIS* **2019**, *40*, 358–375, doi:10.1002/elps.201800285.
43. Coppola, L.; Gustafsson, Ö.; Andersson, P.; Axelsson, P. Fractionation of Surface Sediment Fines Based on a Coupled Sieve–SPLITT (Split Flow Thin Cell) Method. *Water Research* **2005**, *39*, 1935–1945, doi:10.1016/j.watres.2005.04.005.
44. Di Carlo, D. Inertial Microfluidics. *Lab Chip* **2009**, *9*, 3038, doi:10.1039/b912547g.
45. Poiseuille, J. Observations of Blood Flow. *Ann Sci Nat STrie* **1836**, *5*.
46. Segré, G.; Silberberg, A. Behaviour of Macroscopic Rigid Spheres in Poiseuille Flow Part 1. Determination of Local Concentration by Statistical Analysis of Particle Passages through Crossed Light Beams. *J. Fluid Mech.* **1962**, *14*, 115–135, doi:10.1017/S002211206200110X.
47. Segré, G.; Silberberg, A. Behaviour of Macroscopic Rigid Spheres in Poiseuille Flow Part 2. Experimental Results and Interpretation. *J. Fluid Mech.* **1962**, *14*, 136–157, doi:10.1017/S0022112062001111.
48. Bhagat, A.A.S.; Kuntaegowdanahalli, S.S.; Papautsky, I. Inertial Microfluidics for Continuous Particle Filtration and Extraction. *Microfluid Nanofluid* **2009**, *7*, 217–226, doi:10.1007/s10404-008-0377-2.
49. Choi, Y.-S.; Seo, K.-W.; Lee, S.-J. Lateral and Cross-Lateral Focusing of Spherical Particles in a Square Microchannel. *Lab Chip* **2011**, *11*, 460–465, doi:10.1039/C0LC00212G.
50. Di Carlo, D.; Irimia, D.; Tompkins, R.G.; Toner, M. Continuous Inertial Focusing, Ordering, and Separation of Particles in Microchannels. *Proceedings of the National Academy of Sciences* **2007**, *104*, 18892–18897, doi:10.1073/pnas.0704958104.
51. Kim, Y.W.; Yoo, J.Y. The Lateral Migration of Neutrally-Buoyant Spheres Transported through Square Microchannels. *J. Micromech. Microeng.* **2008**, *18*, 065015, doi:10.1088/0960-1317/18/6/065015.
52. Chun, B.; Ladd, A.J.C. Inertial Migration of Neutrally Buoyant Particles in a Square Duct: An Investigation of Multiple Equilibrium Positions. *Physics of Fluids* **2006**, *18*, 031704, doi:10.1063/1.2176587.
53. Abbas, M.; Magaud, P.; Gao, Y.; Geoffroy, S. Migration of Finite Sized Particles in a Laminar Square Channel Flow from Low to High Reynolds Numbers. *Physics of Fluids* **2014**, *26*, 123301, doi:10.1063/1.4902952.
54. Nakagawa, N.; Yabu, T.; Otomo, R.; Kase, A.; Makino, M.; Itano, T.; Sugihara-Seki, M. Inertial Migration of a Spherical Particle in Laminar Square Channel FLows from Low to High Reynolds Numbers. 18.

55. Rubinow, S.I.; Keller, J.B. The Transverse Force on a Spinning Sphere Moving in a Viscous Fluid. *J. Fluid Mech.* **1961**, *11*, 447, doi:10.1017/S0022112061000640.
56. Saffman, P.G. The Lift on a Small Sphere in a Slow Shear Flow. *J. Fluid Mech.* **1965**, *22*, 385–400, doi:10.1017/S0022112065000824.
57. Schonberg, J.A.; Hinch, E.J. Inertial Migration of a Sphere in Poiseuille Flow. *J. Fluid Mech.* **1989**, *203*, 517–524, doi:10.1017/S0022112089001564.
58. Asmolov, E.S. The Inertial Lift on a Spherical Particle in a Plane Poiseuille Flow at Large Channel Reynolds Number. 25.
59. Matas, Jp.; Morris, Jf.; Guazzelli, E. Lateral Forces on a Sphere. *Oil & Gas Science and Technology - Rev. IFP* **2004**, *59*, 59–70, doi:10.2516/ogst:2004006.
60. Feng, J.; Hu, H.H.; Joseph, D.D. Direct Simulation of Initial Value Problems for the Motion of Solid Bodies in a Newtonian Fluid. Part 2. Couette and Poiseuille Flows. *J. Fluid Mech.* **1994**, *277*, 271–301, doi:10.1017/S0022112094002764.
61. Zeng, L.; Najjar, F.; Balachandar, S.; Fischer, P. Forces on a Finite-Sized Particle Located Close to a Wall in a Linear Shear Flow. *Phys. Fluids* **2009**, 19.
62. Di Carlo, D.; Edd, J.F.; Humphry, K.J.; Stone, H.A.; Toner, M. Particle Segregation and Dynamics in Confined Flows. *Phys. Rev. Lett.* **2009**, *102*, 094503, doi:10.1103/PhysRevLett.102.094503.
63. Ho, B.P.; Leal, L.G. Inertial Migration of Rigid Spheres in Two-Dimensional Unidirectional Flows. *J. Fluid Mech.* **1974**, *65*, 365–400, doi:10.1017/S0022112074001431.
64. Matas, J.-P.; Morris, J.F.; Guazzelli, É. Inertial Migration of Rigid Spherical Particles in Poiseuille Flow. *J. Fluid Mech.* **2004**, *515*, 171–195, doi:10.1017/S0022112004000254.
65. Zhou, J.; Papautsky, I. Fundamentals of Inertial Focusing in Microchannels. *Lab Chip* **2013**, *13*, 1121, doi:10.1039/c2lc41248a.
66. Loth, E.; Dorgan, A.J. An Equation of Motion for Particles of Finite Reynolds Number and Size. *Environ Fluid Mech* **2009**, *9*, 187–206, doi:10.1007/s10652-009-9123-x.
67. Gao, Y. Inertial Migration of Particles in Microchannel Flows. Ph.D., Université de Toulouse: Toulouse, France, 2017.
68. Lee, W.; Amini, H.; Stone, H.A.; Di Carlo, D. Dynamic Self-Assembly and Control of Microfluidic Particle Crystals. *Proceedings of the National Academy of Sciences* **2010**, *107*, 22413–22418, doi:10.1073/pnas.1010297107.
69. Shichi, H.; Yamashita, H.; Seki, J.; Itano, T.; Sugihara-Seki, M. Inertial Migration Regimes of Spherical Particles Suspended in Square Tube Flows. *Phys. Rev. Fluids* **2017**, *2*, 044201, doi:10.1103/PhysRevFluids.2.044201.
70. Matas, J.-P.; Glezer, V.; Guazzelli, É.; Morris, J.F. Trains of Particles in Finite-Reynolds-Number Pipe Flow. *Physics of Fluids* **2004**, *16*, 4192–4195, doi:10.1063/1.1791460.
71. Haddadi, H.; Morris, J.F. Topology of Pair-Sphere Trajectories in Finite Inertia Suspension Shear Flow and Its Effects on Microstructure and Rheology. *Physics of Fluids* **2015**, *27*, 043302, doi:10.1063/1.4917030.
72. Kulkarni, P.M.; Morris, J.F. Suspension Properties at Finite Reynolds Number from Simulated Shear Flow. *Physics of Fluids* **2008**, *20*, 040602, doi:10.1063/1.2911017.
73. Humphry, K.J.; Kulkarni, P.M.; Weitz, D.A.; Morris, J.F.; Stone, H.A. Axial and Lateral Particle Ordering in FInite Reynolds Number Channel FLows. *Phys. Fluids* 4.
74. Kim, J.; Lee, J.; Wu, C.; Nam, S.; Di Carlo, D.; Lee, W. Inertial Focusing in Non-Rectangular Cross-Section Microchannels and Manipulation of Accessible Focusing Positions. *Lab Chip* **2016**, *16*, 992–1001, doi:10.1039/C5LC01100K.
75. Wu, L.; Guan, G.; Hou, H.W.; Bhagat, A.A.S.; Han, J. Separation of Leukocytes from Blood Using Spiral Channel with Trapezoid Cross-Section. *Anal. Chem.* **2012**, 8.

76. Martel, J.M.; Toner, M. Particle Focusing in Curved Microfluidic Channels. *Sci Rep* **2013**, *3*, 3340, doi:10.1038/srep03340.
77. Lee, W.C.; Bhagat, A.A.S.; Huang, S.; Van Vliet, K.J.; Han, J.; Lim, C.T. High-Throughput Cell Cycle Synchronization Using Inertial Forces in Spiral Microchannels. *Lab Chip* **2011**, *11*, 1359, doi:10.1039/c0lc00579g.
78. Di Carlo, D.; Edd, J.F.; Irimia, D.; Tompkins, R.G.; Toner, M. Equilibrium Separation and Filtration of Particles Using Differential Inertial Focusing. *Anal. Chem.* **2008**, *80*, 2204–2211, doi:10.1021/ac702283m.
79. Kulkarni, P.M.; Morris, J.F. Pair-Sphere Trajectories in Finite-Reynolds-Number Shear Flow. *J. Fluid Mech.* **2008**, *596*, 413–435, doi:10.1017/S0022112007009627.
80. Gao, Y.; Magaud, P.; Baldas, L.; Lafforgue, C.; Abbas, M.; Colin, S. Self-Ordered Particle Trains in Inertial Microchannel Flows. *Microfluid Nanofluid* **2017**, *21*, 154, doi:10.1007/s10404-017-1993-5.
81. Mikulencak, D.R.; Morris, J.F. Stationary Shear Flow around Fixed and Free Bodies at Finite Reynolds Number. *J. Fluid Mech.* **2004**, *520*, 215–242, doi:10.1017/S0022112004001648.
82. Leshansky, A.M.; Bransky, A.; Korin, N.; Dinnar, U. Tunable Nonlinear Viscoelastic "Focusing" in a Microfluidic Device. *Phys. Rev. Lett.* **2007**, *98*, 234501, doi:10.1103/PhysRevLett.98.234501.
83. D'Avino, G.; Maffettone, P.L.; Greco, F.; Hulsen, M.A. Viscoelasticity-Induced Migration of a Rigid Sphere in Confined Shear Flow. *Journal of Non-Newtonian Fluid Mechanics* **2010**, *165*, 466–474, doi:10.1016/j.jnnfm.2010.01.024.
84. D'Avino, G.; Romeo, G.; Villone, M.M.; Greco, F.; Netti, P.A.; Maffettone, P.L. Single Line Particle Focusing Induced by Viscoelasticity of the Suspending Liquid: Theory, Experiments and Simulations to Design a Micropipe Flow-Focuser. *Lab Chip* **2012**, *12*, 1638, doi:10.1039/c2lc21154h.
85. Villone, M.M.; D'Avino, G.; Hulsen, M.A.; Greco, F.; Maffettone, P.L. Simulations of Viscoelasticity-Induced Focusing of Particles in Pressure-Driven Micro-Slit Flow. *Journal of Non-Newtonian Fluid Mechanics* **2011**, *166*, 1396–1405, doi:10.1016/j.jnnfm.2011.09.003.
86. Yang, S.; Kim, J.Y.; Lee, S.J.; Lee, S.S.; Kim, J.M. Sheathless Elasto-Inertial Particle Focusing and Continuous Separation in a Straight Rectangular Microchannel. **2011**, 8.
87. Nam, J.; Lim, H.; Kim, D.; Jung, H.; Shin, S. Continuous Separation of Microparticles in a Microfluidic Channel via the Elasto-Inertial Effect of Non-Newtonian Fluid. *Lab Chip* **2012**, *12*, 1347, doi:10.1039/c2lc21304d.
88. Lim, H.; Nam, J.; Shin, S. Lateral Migration of Particles Suspended in Viscoelastic Fluids in a Microchannel Flow. *Microfluid Nanofluid* **2014**, *17*, 683–692, doi:10.1007/s10404-014-1353-7.
89. Lim, E.J.; Ober, T.J.; Edd, J.F.; Desai, S.P.; Neal, D.; Bong, K.W.; Doyle, P.S.; McKinley, G.H.; Toner, M. Inertio-Elastic Focusing of Bioparticles in Microchannels at High Throughput. *Nat Commun* **2014**, *5*, 4120, doi:10.1038/ncomms5120.
90. Seo, K.W.; Kang, Y.J.; Lee, S.J. Lateral Migration and Focusing of Microspheres in a Microchannel Flow of Viscoelastic Fluids. *Physics of Fluids* **2014**, *26*, 063301, doi:10.1063/1.4882265.
91. Ahn, S.W.; Lee, S.S.; Lee, S.J.; Kim, J.M. Microfluidic Particle Separator Utilizing Sheathless Elasto-Inertial Focusing. *Chemical Engineering Science* **2015**, *126*, 237–243, doi:10.1016/j.ces.2014.12.019.
92. Lim, E.J.; Ober, T.J.; Edd, J.F.; McKinley, G.H.; Toner, M. Visualization of Microscale Particle Focusing in Diluted and Whole Blood Using Particle Trajectory Analysis. *Lab Chip* **2012**, *12*, 2199, doi:10.1039/c2lc21100a.

93. Gao, Y.; Magaud, P.; Baldas, L.; Wang, Y. Inertial Migration of Neutrally Buoyant Spherical Particles in Square Channels at Moderate and High Reynolds Numbers. **2021**, 11.
94. Gao, Y.; Magaud, P.; Lafforgue, C.; Colin, S.; Baldas, L. Inertial Lateral Migration and Self-Assembly of Particles in Bidisperse Suspensions in Microchannel Flows. *Microfluid Nanofluid* **2019**, *23*, 93, doi:10.1007/s10404-019-2262-6.
95. Krishnan, G.P.; Beimfohr, S.; Leighton, D.T. Shear-Induced Radial Segregation in Bidisperse Suspensions. *J. Fluid Mech.* **1996**, *321*, 371–393, doi:10.1017/S0022112096007768.
96. Lyon, M.K.; Leal, L.G. An Experimental Study of the Motion of Concentrated Suspensions in Two-Dimensional Channel Flow. Part 2. Bidisperse Systems. *J. Fluid Mech.* **1998**, *363*, 57–77, doi:10.1017/S0022112098008829.
97. Vollebregt, H.M.; van der Sman, R.G.M.; Boom, R.M. Model for Particle Migration in Bidisperse Suspensions by Use of Effective Temperature. *Faraday Discuss.* **2012**, *158*, 89, doi:10.1039/c2fd20035j.
98. Hur, S.C.; Henderson-MacLennan, N.K.; McCabe, E.R.B.; Di Carlo, D. Deformability-Based Cell Classification and Enrichment Using Inertial Microfluidics. *Lab Chip* **2011**, *11*, 912, doi:10.1039/c0lc00595a.
99. Magnaudet, J.; Takagi, S.; Legendre, D. Drag, Deformation and Lateral Migration of a Buoyant Drop Moving near a Wall. *J. Fluid Mech.* **2003**, *476*, 115–157, doi:10.1017/S0022112002002902.
100. Hur, S.C.; Mach, A.J.; Di Carlo, D. High-Throughput Size-Based Rare Cell Enrichment Using Microscale Vortices. *Biomicrofluidics* **2011**, *5*, 022206, doi:10.1063/1.3576780.
101. Takagi, J.; Yamada, M.; Yasuda, M.; Seki, M. Continuous Particle Separation in a Microchannel Having Asymmetrically Arranged Multiple Branches. *Lab Chip* **2005**, *5*, 778, doi:10.1039/b501885d.
102. Sun, J.; Liu, C.; Li, M.; Wang, J.; Xianyu, Y.; Hu, G.; Jiang, X. Size-Based Hydrodynamic Rare Tumor Cell Separation in Curved Microfluidic Channels. *Biomicrofluidics* **2013**, *7*, 011802, doi:10.1063/1.4774311.
103. Morley, S.T.; Walsh, M.T.; Newport, D.T. The Advection of Microparticles, MCF-7 and MDA-MB-231 Breast Cancer Cells in Response to Very Low Reynolds Numbers. *Biomicrofluidics* **2017**, *11*, 034105, doi:10.1063/1.4983149.
104. Connolly, S.; McGourty, K.; Newport, D. The in Vitro Inertial Positions and Viability of Cells in Suspension under Different in Vivo Flow Conditions. *Sci Rep* **2020**, *10*, 1711, doi:10.1038/s41598-020-58161-w.
105. Connolly, S.; McGourty, K.; Newport, D. The Influence of Cell Elastic Modulus on Inertial Positions in Poiseuille Microflows. *Biophysical Journal* **2021**, *120*, 855–865, doi:10.1016/j.bpj.2021.01.026.
106. Di Carlo, D.; Irimia, D.; Tompkins, R.G.; Toner, M. Continuous Inertial Focusing, Ordering, and Separation of Particles in Microchannels. *Proceedings of the National Academy of Sciences* **2007**, *104*, 18892–18897, doi:10.1073/pnas.0704958104.
107. Bhagat, A.A.S.; Kuntaegowdanahalli, S.S.; Papautsky, I. Inertial Microfluidics for Continuous Particle Filtration and Extraction. *Microfluid Nanofluid* **2009**, *7*, 217–226, doi:10.1007/s10404-008-0377-2.
108. Lashgari, I.; Ardekani, M.N.; Banerjee, I.; Russom, A.; Brandt, L. Inertial Migration of Spherical and Oblate Particles in Straight Ducts. *J. Fluid Mech.* **2017**, *819*, 540–561, doi:10.1017/jfm.2017.189.
109. Nizkaya, T.V.; Gekova, A.S.; Harting, J.; Asmolov, E.S.; Vinogradova, O.I. Inertial Migration of Oblate Spheroids in a Plane Channel. *Physics of Fluids* **2020**, *32*, 112017, doi:10.1063/5.0028353.

110. Hur, S.C.; Choi, S.-E.; Kwon, S.; Carlo, D.D. Inertial Focusing of Non-Spherical Microparticles. *Appl. Phys. Lett.* **2011**, *99*, 044101, doi:10.1063/1.3608115.
111. Jeffery, G.B. The Motion of Ellipsoidal Particles Immersed in a Viscous Fluid. *Proc. R. Soc. Lond. A* **1922**, *102*, 161–179, doi:10.1098/rspa.1922.0078.
112. Bretherton, F.P. The Motion of Rigid Particles in a Shear Flow at Low Reynolds Number. *J. Fluid Mech.* **1962**, *14*, 284–304, doi:10.1017/S002211206200124X.
113. Saffman, P.G. On the Motion of Small Spheroidal Particles in a Viscous Liquid. *J. Fluid Mech.* **1956**, *1*, 540–553, doi:10.1017/S0022112056000354.
114. Leal, L.G. Particle Motions in a Viscous Fluid. *Annu. Rev. Fluid Mech.* **1980**, *12*, 435–476, doi:10.1146/annurev.fl.12.010180.002251.
115. Harper, E.Y.; Chang, I.-D. Maximum Dissipation Resulting from Lift in a Slow Viscous Shear Flow. *J. Fluid Mech.* **1968**, *33*, 209, doi:10.1017/S0022112068001254.
116. Ding, E.-J.; Aidun, C.K. The Dynamics and Scaling Law for Particles Suspended in Shear Flow with Inertia. *J. Fluid Mech.* **2000**, *423*, 317–344, doi:10.1017/S0022112000001932.
117. Qi, D.; Luo, L. Transitions in Rotations of a Nonspherical Particle in a Three-Dimensional Moderate Reynolds Number Couette Flow. *Physics of Fluids* **2002**, *14*, 4440–4443, doi:10.1063/1.1517053.
118. Qi, D.; Luo, L.-S. Rotational and Orientational Behaviour of Three-Dimensional Spheroidal Particles in Couette Flows. *J. Fluid Mech.* **2003**, *477*, doi:10.1017/S0022112002003191.
119. Yu, Z.; Phan-Thien, N.; Tanner, R.I. Rotation of a Spheroid in a Couette Flow at Moderate Reynolds Numbers. *Phys. Rev. E* **2007**, *76*, 026310, doi:10.1103/PhysRevE.76.026310.
120. Huang, H.; Yang, X.; Krafczyk, M.; Lu, X.-Y. Rotation of Spheroidal Particles in Couette Flows. *J. Fluid Mech.* **2012**, *692*, 369–394, doi:10.1017/jfm.2011.519.
121. Rosén, T.; Do-Quang, M.; Aidun, C.K.; Lundell, F. Effect of Fluid and Particle Inertia on the Rotation of an Oblate Spheroidal Particle Suspended in Linear Shear Flow. *Phys. Rev. E* **2015**, *91*, 053017, doi:10.1103/PhysRevE.91.053017.
122. Chwang, A.T. Hydromechanics of Low-Reynolds-Number Flow. Part 3. Motion of a Spheroidal Particle in Quadratic Flows. *J. Fluid Mech.* **1975**, *72*, 17–34, doi:10.1017/S0022112075002911.
123. Lundell, F.; Carlsson, A. Heavy Ellipsoids in Creeping Shear Flow: Transitions of the Particle Rotation Rate and Orbit Shape. *Phys. Rev. E* **2010**, *81*, 016323, doi:10.1103/PhysRevE.81.016323.
124. Zettner, C.M.; Yoda, M. Moderate-Aspect-Ratio Elliptical Cylinders in Simple Shear with Inertia. *J. Fluid Mech.* **2001**, *442*, 241–266, doi:10.1017/S0022112001005006.
125. Rosén, T.; Do-Quang, M.; Aidun, C.K.; Lundell, F. The Dynamical States of a Prolate Spheroidal Particle Suspended in Shear Flow as a Consequence of Particle and Fluid Inertia. *J. Fluid Mech.* **2015**, *771*, 115–158, doi:10.1017/jfm.2015.127.
126. Goldsmith, H.L.; Mason, S.G. Particle Motions in Sheared Suspensions XIII. The Spin and Rotation of Disks. *J. Fluid Mech.* **1962**, *12*, 88–96, doi:10.1017/S0022112062000051.
127. Karnis, A.; Goldsmith, H.L.; Mason, S.G. The Flow of Suspensions through Tubes: V. Inertial Effects. *Can. J. Chem. Eng.* **1966**, *44*, 181–193, doi:10.1002/cjce.5450440401.
128. Mason, S.G.; Manley, R.S.J. Particle Motions in Sheared Suspensions: Orientations and Interactions of Rigid Rods. *Proc. R. Soc. Lond. A* **1956**, *238*, 117–131, doi:10.1098/rspa.1956.0207.
129. Anczurowski, E.; Mason, S.G. The Kinetics of Flowing Dispersions. *Journal of Colloid and Interface Science* **1967**, *23*, 533–546, doi:10.1016/0021-9797(67)90200-7.
130. Anczurowski, E.; Cox, R.G.; Mason, S.G. The Kinetics of Flowing Dispersions. *Journal of Colloid and Interface Science* **1967**, *23*, 547–562, doi:10.1016/0021-9797(67)90201-9.

131. Candelier, F.; Einarsson, J.; Lundell, F.; Mehlig, B.; Angilella, J.-R. Role of Inertia for the Rotation of a Nearly Spherical Particle in a General Linear Flow. *Phys. Rev. E* **2015**, *91*, 053023, doi:10.1103/PhysRevE.91.053023.
132. Subramanian, G.; Koch, D.L. Inertial Effects on Fibre Motion in Simple Shear Flow. *J. Fluid Mech.* **2005**, *535*, 383–414, doi:10.1017/S0022112005004829.
133. Ku, X.K.; Lin, J.Z. Inertial Effects on the Rotational Motion of a Fibre in Simple Shear Flow between Two Bounding Walls. *Phys. Scr.* **2009**, *80*, 025801, doi:10.1088/0031-8949/80/02/025801.
134. Poe, G.G.; Acrivos, A. Closed-Streamline Flows Past Rotating Single Cylinders and Spheres: Inertia Effects. *J. Fluid Mech.* **1975**, *72*, 605–623, doi:10.1017/S0022112075003187.
135. Aidun, C.K.; Lu, Y.; Ding, E.-J. Direct Analysis of Particulate Suspensions with Inertia Using the Discrete Boltzmann Equation. *J. Fluid Mech.* **1998**, *373*, 287–311, doi:10.1017/S0022112098002493.
136. Trevelyan, B.J.; Mason, S.G. Particle Motions in Sheared Suspensions. I. Rotations. *Journal of Colloid Science* **1951**, *6*, 354–367, doi:10.1016/0095-8522(51)90005-0.
137. Kittipoomwong, P.; See, H.; Mai-Duy, N. Dynamic Simulation of Non-Spherical Particulate Suspensions. *Rheol Acta* **2010**, *49*, 597–606, doi:10.1007/s00397-009-0412-6.
138. Skjetne, P.; Ross, R.F.; Klingenberg, D.J. Simulation of Single Fiber Dynamics. *The Journal of Chemical Physics* **1997**, *107*, 2108–2121, doi:10.1063/1.474561.
139. Goldsmith, H.L.; Mason, S.G. THE MICRORHEOLOGY OF DISPERSIONS. In *Rheology*; Elsevier, 1967; pp. 85–250 ISBN 978-1-4832-2941-6.
140. Joung, C.G. Dynamic Simulation of Arbitrarily Shaped Particles in Shear Flow. *Rheol Acta* **2006**, *46*, 143–152, doi:10.1007/s00397-006-0110-6.
141. Gierszewski, P.J.; Chaffey, C.E. Rotation of an Isolated Triaxial Ellipsoid Suspended in Slow Viscous Flow. *Can. J. Phys.* **1978**, *56*, 6–11, doi:10.1139/p78-003.
142. Hinch, E.J.; Leal, L.G. Rotation of Small Non-Axisymmetric Particles in a Simple Shear Flow. *J. Fluid Mech.* **1979**, *92*, 591–607, doi:10.1017/S002211207900077X.
143. Wang, Q.; Yuan, D.; Li, W. Analysis of Hydrodynamic Mechanism on Particles Focusing in Micro-Channel Flows. *Micromachines* **2017**, *8*, 197, doi:10.3390/mi8070197.
144. Su, J.; Chen, X.; Hu, G. Inertial Migrations of Cylindrical Particles in Rectangular Microchannels: Variations of Equilibrium Positions and Equivalent Diameters. *Physics of Fluids* **2018**, *30*, 032007, doi:10.1063/1.5018714.
145. Pan, T.-W.; Chang, C.-C.; Glowinski, R. On the Motion of a Neutrally Buoyant Ellipsoid in a Three-Dimensional Poiseuille Flow. *Computer Methods in Applied Mechanics and Engineering* **2008**, *197*, 2198–2209, doi:10.1016/j.cma.2007.09.006.
146. Masaeli, M.; Sollier, E.; Amini, H.; Mao, W.; Camacho, K.; Doshi, N.; Mitragotri, S.; Alexeev, A.; Di Carlo, D. Continuous Inertial Focusing and Separation of Particles by Shape. *Phys. Rev. X* **2012**, *2*, 031017, doi:10.1103/PhysRevX.2.031017.
147. Hu, X.; Lin, J.; Guo, Y.; Ku, X. Inertial Focusing of Elliptical Particles and Formation of Self-Organizing Trains in a Channel Flow. *Physics of Fluids* **2021**, *33*, 013310, doi:10.1063/5.0035668.
148. Huang, Y.; Marson, R.L.; Larson, R.G. Inertial Migration of Neutrally Buoyant Prolate and Oblate Spheroids in Plane Poiseuille Flow Using Dissipative Particle Dynamics Simulations. *Computational Materials Science* **2019**, *162*, 178–185, doi:10.1016/j.commatsci.2019.02.048.
149. Li, M.; Muñoz, H.E.; Goda, K.; Di Carlo, D. Shape-Based Separation of Microalga Euglena Gracilis Using Inertial Microfluidics. *Sci Rep* **2017**, *7*, 10802, doi:10.1038/s41598-017-10452-5.

150. Einarsson, J.; Mihiretie, B.M.; Laas, A.; Ankardal, S.; Angilella, J.R.; Hanstorp, D.; Mehlig, B. Tumbling of Asymmetric Microrods in a Microchannel Flow. *Physics of Fluids* **2016**, *28*, 013302, doi:10.1063/1.4938239.
151. Einarsson, J.; Johansson, A.; Mahato, S.K.; Mishra, Y.N.; Angilella, J.R.; Hanstorp, D.; Mehlig, B. Periodic and Aperiodic Tumbling of Microrods Advected in a Microchannel Flow. *Acta Mech* **2013**, *224*, 2281–2289, doi:10.1007/s00707-013-0924-0.
152. Mach, A.J.; Di Carlo, D. Continuous Scalable Blood Filtration Device Using Inertial Microfluidics. *Biotechnol. Bioeng.* **2010**, *107*, 302–311, doi:10.1002/bit.22833.
153. Lafforgue-Baldas, C.; Magaud, P.; Schmitz, P.; Zhihao, Z.; Geoffroy, S.; Abbas, M. Study of Microfocusing Potentialities to Improve Bioparticle Separation Processes: Towards an Experimental Approach. *Journal of Flow Chemistry* **2013**, *3*, 92–98, doi:10.1556/JFC-D-13-00010.
154. Barrot-Lattes, C.; Newport, D.; Chiavaroli, S.; Morini, G.L.; Baldas, L.; Colin, S. 3-D Reconstruction of Velocity Profiles in Rectangular Microchannels. **2008**, *26*, 153–159.
155. Heller, W. Remarks on Refractive Index Mixture Rules. *J. Phys. Chem.* **1965**, *69*, 1123–1129, doi:10.1021/j100888a006.
156. Tasadduq, B.; Wang, G.; El Banani, M.; Mao, W.; Lam, W.; Alexeev, A.; Sulchek, T. Three-Dimensional Particle Tracking in Microfluidic Channel Flow Using in and out of Focus Diffraction. *Flow Measurement and Instrumentation* **2015**, *45*, 218–224, doi:10.1016/j.flowmeasinst.2015.06.018.
157. Pan, Z.; Zhang, R.; Yuan, C.; Wu, H. Direct Measurement of Microscale Flow Structures Induced by Inertial Focusing of Single Particle and Particle Trains in a Confined Microchannel. *Physics of Fluids* **2018**, *30*, 102005, doi:10.1063/1.5048478.
158. Yuan, C.; Pan, Z.; Wu, H. Inertial Migration of Single Particle in a Square Microchannel over Wide Ranges of Re and Particle Sizes. *Microfluid Nanofluid* **2018**, *22*, 102, doi:10.1007/s10404-018-2120-y.
159. Gupta, A.; Magaud, P.; Lafforgue, C.; Abbas, M. Conditional Stability of Particle Alignment in Finite-Reynolds-Number Channel Flow. *Phys. Rev. Fluids* **2018**, *3*, 114302, doi:10.1103/PhysRevFluids.3.114302.